

Catalytic Reforming of Fuels Over Noble Metal-Coated Honeycomb Monoliths: Capillary-Based In-Situ Sampling Technique

Zur Erlangung des akademischen Grades eines
DOKTORS DER NATURWISSENSCHAFTEN
(Dr. rer. nat.)

Fakultät für Chemie und Biowissenschaften
Karlsruher Institut für Technologie (KIT) - Universitätsbereich
genehmigte

DISSERTATION

von
Dipl.-Chem. Claudia Diehm

aus
Karlsruhe

Dekan: Prof. Dr. Peter Roesky

Referent: Prof. Dr. Olaf Deutschmann

Korreferent: Prof. Dr. Jan-Dierk Grunwaldt

Tag der mündlichen Prüfung: 20.12.2013

“In the middle of difficulty lies opportunity.”

Albert Einstein

*“The clock is running. Make the most of today.
Time waits for no man.
Yesterday is history. Tomorrow is a mystery.
Today is a gift. That’s why it is called the present.”*

Alice Morse Earle

Acknowledgements

I am very grateful to many people for their help and support during my time as a PhD student. I would like to thank

my supervisor Prof. Dr. Olaf Deutschmann. He provided me with a topic that I could relate to and was inspired by. The faith he had in me and my research skills were essential during my eventful journey as a PhD student.

Prof. Dr. Alessandra Beretta, who treated me as one of her own PhD students during my three-months stay at the Laboratory of Catalysis and Catalytic Processes (LCCP) at Politecnico di Milano. My gratitude is extended to Prof. Dr. Gianpiero Groppi for fruitful discussions and to all the members of LCCP, who were always helpful and made me feel welcome.

Dr. Dario Livio for the scientific exchange and the collaboration during the construction of the setup.

Sven Lichtenberg, Hans Weickenmeier, Jörg Finsterle, Ingrid Zeller and the whole staff of the workshop for their help during the construction and the maintenance of the experimental setup. My gratitude is extended to Leonhard Rutz for IT support. Especially, I would like to thank Azize Ünal for her commitment to and help with the experimental work.

Prof. Dr. Jan-Dierk Grunwaldt for agreeing to be my co-supervisor.

Dr. Matthias Hettel, Julian Bär, and Rebecca Klinkig for proof-reading of my thesis.

the investigators of the Helmholtz Research School “Energy-Related Catalysis” for giving me the opportunity to be a member of this graduate school, especially to Prof. Dr. Roland Dittmeyer for

being my co-supervisor in the school. My gratitude is extended to the Helmholtz Association for financial funding and for the transferable skill courses. I am very thankful to Dr. Steffen Tischer for the organization and to all the members of the school for the fruitful discussion, sense of community, and the fun times.

the KIC InnoEnergy for financial support within the SynCon project and all the researchers in the SynCon project for interesting discussions.

Umicore AG & Co. KG and Delphi Inc. for the provision of the model catalysts.

Within the research group, I owe many thanks to my colleagues. I am grateful for all the discussions, scientific as well as personal, the times spent together in the “Kaffeecke”, and the readiness to help. I would like to thank Ursula Schwald and Evangelia Mina for the great support with administration. I am grateful to my former colleagues Dr. Marco Hartmann, Dr. Torsten Kaltschmitt and Dr. Willi Boll, who remained helpful and supportive even after they left our research group. Special thanks go to Dr. Matthias Hettel for the numerical simulations that complete my experimental work, and for being willing to listen and to give advice in any situation. It is a great pleasure to thank my colleagues who became more than that, and are friends now: Julian, Lea, Denise, Meike, and Yvonne.

I owe sincere and earnest gratitude to Simone Anderhub, who helped me find a way through the challenges in my life.

My friends and family played an important part in the completion of this thesis. I am lucky to have my friends, who supported me through all this time, in particular Bettina, Benny, Michi, and Ronja. I am very thankful to my parents and my brother for their support and understanding. Especially, I would like to thank David, my boyfriend, for always being there for me.

List of Abbreviations

approx.	approximately
APU	Auxiliary Power Unit
ATR	Autothermal Reforming
BHS	Back Heat Shield
BTL	Biomass-To-Liquids
CFD	Computational Fluid Dynamics
CPOX	Catalytic Partial Oxidation
cpsi	channels per square inch
DR	Dry Reforming
DUO	codes DETCHEM Und (German for “and”) OpenFOAM
e.g.	“exempli gratia” meaning “for example”
FFV	Flexible Fuel Vehicles
FHS	Front Heat Shield
FTIR	Fourier-Transform Infrared Spectroscopy
GC-MS	Gas Chromatography - Mass Spectrometry
gen.	general or generally
GHSV	Gas Hourly Space Velocity (calculated for open volume of the catalyst at $T = 298$ K and $p = 1.013$ bar)
I.D.	Inner Diameter
i.e.	“id est”, meaning “that is to say”
LIF	Laser Induced Fluorescence
LPG	Liquefied Petroleum Gas

MFC	Mass Flow Controller
NI	Normal liter (at $T = 273$ K and $p = 1.013$ bar)
O.D.	Outer Diameter
PAH	Polycyclic Aromatic Hydrocarbons
ppi	pores per inch
RBM	Radial Breathing Mode
RON	Research Octane Number
SEM	Scanning Electron Microscopy
SLPM	Standard Liter Per Minute (at $T = 298$ K and $p = 1.013$ bar)
SOFC	Solid-Oxide Fuel Cell
SR	Steam Reforming
WGS	Water-Gas Shift
w.r.t.	with regards to
XRD	X-Ray Diffraction

List of Symbols

Latin Symbols

Symbol	Unit	Description
a	$[\text{mol}^{-1}]$	slope
A	$[\text{m}^2]$	area
c	$[\text{mol}-\text{m}^{-3}]$	concentration of species in the gas and in the liquid phase
c	$[\text{mol}-\text{m}^{-2}]$	concentration of surface species
d	$[\text{m}]$	diameter
d_h	$[\text{m}]$	hydraulic diameter
D	$[-]$	dispersion
$F_{\text{cat,geo}}$	$[-]$	ratio of catalytic to geometric surface area
h	$[\mu\text{m}]$	free height of a quadratic single channel
H	$[\text{J mol}^{-1}]$	enthalpy
$\Delta_{\text{R}}H^{\ominus}$	$[\text{J mol}^{-1}]$	standard reaction enthalpy
k	(mol,m,s)	rate coefficient
L	$[\text{m}]$	length
n	$[\text{mol}]$	amount of substance
\dot{n}	$[\text{mol min}^{-1}]$	molar flow rate
N	$[-]$	number of species
p	$[\text{bar}]$	pressure
r	$[\text{m}]$	radius

R	$[J K^{-1} mol^{-1}]$	ideal gas constant
S_τ	$[-]$	source term of residence time equation
S_i	$[-]$	sticking coefficient for species i
T	$[K]$	temperature
u	$[m s^{-1}]$	velocity
V	$[m^3]$	volume
\dot{V}	$[m^3 min^{-1}]$	volume flux
x	$[-]$	mole fraction
X	$[-]$	conversion
Y	$[-]$	yield
z	$[m]$	axial coordinate

Greek Symbols

Symbol	Unit	Description
α	$[-]$	thermal efficiency
β	$[-]$	temperature coefficient
Γ	$[mol m^{-2}]$	surface-site density
Δ	$[-]$	difference
ε	$[J m^{-2}]$	activation energy dependent on surface coverage
θ	$[rad]$	angle of diffraction
Θ	$[-]$	surface coverage
μ	$[kg s^{-1} m^{-1}]$	dynamic viscosity
μ_k	$[-]$	change of the rate of reaction
ν	$[-]$	stoichiometric coefficient
Φ	$[-]$	porosity of the washcoat
ρ	$[kg m^{-3}]$	density
σ	$[-]$	number of surface sites covered by a species
τ	$[s]$	residence time

Indices

Symbol	Description
C	based on C atoms
equil	equilibrium value
exp	experimental value
g	gas phase
H	based on H atoms
<i>i</i>	species <i>i</i>
<i>j</i>	species <i>j</i>
<i>k</i>	reaction <i>k</i>
probe	channel with probe
ref	reference channel
<i>r</i>	reactant <i>r</i>
s	surface
0	at time t=0
⊖	standard conditions

Abstract

Hydrogen is applicable to many processes, e.g. as a basic chemical for the production of value-added chemicals and as a direct fuel in fuel cells for power generation. The production of hydrogen is possible from various feedstocks, both fossil and renewable. For on-board hydrogen production, e.g. in airplanes and vehicles, rapid start-up, transient response, and compact reactor design are important criteria. Reformers on the basis of catalytic partial oxidation (CPOX) meet these requirements and therefore represent an attractive option for on-board applications.

This work focuses on high-temperature catalysis ($T = 900 - 1200$ K) in CPOX reactors with short contact times ($\tau \approx 10$ ms). The performance of CPOX reformers was investigated for a broad range of fuels: methane (main component of natural gas), propane (main component of LPG - Liquefied Petroleum Gas), ethanol (renewable fuel), and 95 RON gasoline and E 85 (ethanol-blended gasoline). The catalyst used in these investigations was a Rh-coated honeycomb monolith. An additional study on CPOX of methane was performed on a two-stage catalyst based on Pd and Rh. For a detailed insight into the reaction network during CPOX of the different fuels, an in-situ sampling technique was constructed. With this technique, axial concentration and temperature profiles are detectable in one channel of the honeycomb monolith. The investigated channel is freely selectable from all channels of the monolith. Thus, the influence of heat loss on the system can be studied in detail. However, the in-situ technique influences the measured data because of the positioning of the probe in the channel. To evaluate the influence of the probe on the collected data, CFD (Computational Fluid Dynamics) simulations were performed. These investigations revealed the source of the measuring error and made it possible to quantify the error.

For all investigated fuels, the applicability in a CPOX reformer was verified. The C/O ratios (molar carbon-to-oxygen ratio) with the best performance, i.e. both high fuel conversion and hydrogen yield, were identified for all fuels. By using of the sampling technique, a separation of the reaction sequence in the channel into two zones was demonstrated. The first zone covers the first millimeter of the catalyst, while molecular oxygen is present. In this zone, the oxy-reforming zone, total oxidation, partial oxidation, and steam reforming proceed simultaneously. Thus, H₂O and CO₂ as well as the desired synthesis gas (H₂ + CO) are formed. A hot spot is observed on the catalytic surface. In the second zone, the reforming zone, all oxygen has already been consumed. Steam reforming is the predominant reaction, consuming water and unconverted fuel to yield further synthesis gas. As steam reforming is an endothermic reaction, the surface temperature decreases in the reforming zone.

The high impact of heat transfer in the CPOX process became apparent in these investigations. The high surface temperatures during the CPOX lead to radial heat loss and heat radiation from both the front and the back face of the monolith. Furthermore, the materials in a CPOX reformer are exposed to high thermal stress. Material properties such as heat conductivity and thermal expansion become important factors. The spatially-resolved profiles collected in different channels revealed that the radial heat loss has a negative influence on the performance. At the outlet of the channels that are positioned close to the reactor wall, lower rates of fuel consumption and hydrogen yield are observed.

The occurrence of axial diffusion at the catalyst inlet was proven by a combination of measurements of the axial profiles and CFD simulations. In the inlet region, large concentration gradients and high temperatures make axial diffusion a significant transport process. For ethanol, homogeneous gas-phase reactions occur upstream of the catalyst, leading to the formation of acetaldehyde and water.

Ethanol/iso-octane blends are proposed as model fuels for ethanol-blended gasoline due to the similar performance for these fuels in a CPOX reformer. Thus, two-component blends can be used to reproduce results for complex commercial fuels.

Based on the mechanistic insights gained from the spatial profiles, a staged catalytic reactor containing Pd and Rh was investigated. The Pd-Rh catalyst is not beneficial for the performance of a CPOX reformer. However, the measurement of the axial profiles in the two-stage catalyst made it possible to draw new mechanistic conclusions for CPOX on Pd.

At elevated pressures (2-4 bar), nearly no alteration of the gas composition at the reactor outlet was observed for CPOX of propane over Rh. The coke, which forms during operation at 4 bar, was analyzed and possible causes were explored.

Kurzfassung

Wasserstoff findet in vielen Prozessen Verwendung, z. B. als Grundchemikalie in der Produktion höherwertiger Chemikalien und als Kraftstoff in Brennstoffzellen zur Stromerzeugung. Die Wasserstoffherstellung kann aus verschiedenen Rohstoffen erfolgen, wobei sowohl fossile, als auch nachwachsende Rohstoffe verwendet werden können. Zur mobilen Erzeugung von H_2 , z. B. in Fahrzeugen und Flugzeugen, sind schnelles Zündverhalten und zeitnahe Anpassung an veränderte Betriebsbedingungen sowie eine kompakte Bauweise wichtige Kriterien. Reformier, die auf der katalytischen Partialoxidation (CPOX, Catalytic Partial Oxidation) basieren, erfüllen diese Anforderungen und sind somit für mobile Anwendungen attraktiv.

In dieser Arbeit wurde ein breites Spektrum an möglichen Kraftstoffen für CPOX-Reformer untersucht: Methan (als Hauptkomponente von Erdgas), Propan (als Hauptkomponente von LPG – Liquefied Petroleum Gas), Ethanol (als erneuerbarer Kraftstoff) und ethanolhaltiges Benzin (Super Benzin und E 85). Als Katalysator wurde ein mit $Rh/\gamma-Al_2O_3$ beschichteter monolithischer Wabenkörper verwendet. Für CPOX von Methan wurde zusätzlich ein zweistufiger Katalysator, bestehend aus Pd und Rh, getestet. In allen durchgeführten Messungen wurden extrem kurze Verweilzeiten ($\tau \approx 10$ ms) am verwendeten Katalysator realisiert. Als ein Teilbereich der Hochtemperaturkatalyse läuft die CPOX bei Temperaturen von $T = 900 - 1200$ K ab. Um ein tiefergehendes Verständnis des während der CPOX auftretenden Reaktionsnetzwerkes zu erreichen, wurde eine in-situ Probentechnik aufgebaut. Mit dieser Technik können axiale Konzentrations- und Temperaturprofile in einem Kanal eines monolithischen Wabenkörpers detektiert werden. Die Profile können in einem beliebigen Kanal des Monolithen gemessen werden. Dadurch können makroskopische Einflüsse, wie der Wärmeverlust des Reformers an die Umgebung, analysiert werden. Die gemessenen Werte werden allerdings durch die Positionierung der Probensonde im Katalysatorkanal beeinflusst.

Zur Beurteilung dieses Einflusses wurden in der vorliegenden Arbeit CFD-Simulationen (Computational Fluid Dynamics) durchgeführt. Anhand dieser Untersuchungen konnte die Herkunft des inhärenten Messfehlers erklärt und quantifiziert werden.

Für alle untersuchten Kraftstoffe konnte ein C/O-Verhältnis (molares Kohlenstoff-zu-Sauerstoff-Verhältnis) gefunden werden, bei dem ein hoher Umsatz und eine hohe Wasserstoffausbeute erreicht werden. Somit ist eine Verwendung dieser Kraftstoffe in einem CPOX-Reformer möglich. Anhand der Probentechnik konnte eine Aufteilung der in einem Kanal auftretenden Reaktionen in zwei Zonen gezeigt werden. Die erste Zone deckt lediglich den ersten Millimeter eines Kanales ab. Es handelt sich um den Bereich, in dem noch molekularer Sauerstoff vorhanden ist. In dieser Zone, der Oxy-Reformierungszone, laufen Totaloxidation, Partialoxidation und Wasserdampfreformierung (SR – Steam Reforming) parallel ab. Es werden H_2O , CO_2 und Synthesegas ($\text{H}_2 + \text{CO}$) gebildet. Ein Maximum der Wandtemperatur wird in dieser Zone beobachtet. In der zweiten Zone, der Reformierungszone, ist kein molekularer Sauerstoff mehr vorhanden. Die vorherrschende Reaktion ist die SR, in der Wasser und Kraftstoff zu weiterem Synthesegas umgesetzt werden. Da es sich bei der SR um eine endotherme Reaktion handelt, sinkt die Wandtemperatur in dieser Zone.

Aufgrund der durchgeführten Untersuchungen konnte der hohe Stellenwert des Wärmetransports für den Gesamtprozess innerhalb des CPOX-Reaktors verdeutlicht werden. Die hohen Oberflächentemperaturen verursachen radialen Wärmeverlust und Wärmestrahlung an den Stirnseiten des Katalysators. Durch die hohe thermische Belastung, der die verwendeten Materialien ausgesetzt sind, spielen Materialeigenschaften, wie Wärmeleitfähigkeit und thermische Ausdehnung, eine wichtige Rolle. Die Messungen der ortsaufgelösten Profile in verschiedenen Kanälen zeigten eine Auswirkung des radialen Wärmeverlusts auf den Kraftstoffumsatz und die Produktverteilung. In

den Kanälen nahe der Reaktorwand werden ein geringerer Kraftstoffumsatz und eine niedrigere Wasserstoffausbeute erreicht.

Die Messungen orts aufgelöster Profile führten in Kombination mit CFD-Simulationen zum Nachweis der axialen Diffusion am Katalysatoreingang. Durch die großen Konzentrationsgradienten und hohen Temperaturen trägt die Diffusion in diesem Bereich signifikant zum Massentransport bei. Für Ethanol wurden bereits vor dem Eintritt des reaktiven Gases in den Katalysator homogene Gasphasenreaktionen beobachtet. In diesem Bereich werden vor allem Wasser und Acetaldehyd gebildet.

Ethanol/iso-Oktan-Mischungen können als Modellkraftstoffe für die untersuchten, ethanolhaltigen Benzine verwendet werden. Die für die kommerziellen Kraftstoffe gemessenen Gaszusammensetzungen und Temperaturen können durch die Zwei-Komponenten-Mischungen in ähnlicher Form reproduziert werden.

Die Erkenntnisse bezüglich des Mechanismus auf Rh führten zu Untersuchungen der CPOX von Methan an einem Pd-Rh-Katalysator. Für den Zwei-Stufen-Katalysator wurden ein geringerer Umsatz und eine niedrigere Wasserstoffausbeute beobachtet als für einen einstufigen Rh-Katalysator. Aus den Messungen konnten jedoch neue Schlussfolgerungen bezüglich des CPOX-Mechanismus auf Pd gezogen werden.

Bei Untersuchungen der CPOX von Propan zwischen 2 und 4 bar zeigte sich nur eine geringfügige Änderung der Gaszusammensetzung am Reaktorausgang. Der gebildete Kohlenstoff wurde analysiert und mögliche Ursachen der Kohlenstoffbildung aufgezeigt.

Contents

List of Abbreviations	V
List of Symbols	VII
1 Introduction	1
1.1 On-Site Production and Application of Hydrogen	1
1.2 Objectives	4
1.2.1 Setup and Application of In-Situ Sampling Techniques .	5
1.2.2 Fuels and Catalysts to Be Studied	6
1.2.3 Critical Evaluation of the Sampling Technique	7
2 Fundamentals	9
2.1 Fuel Reforming to Synthesis Gas	9
2.1.1 Catalytic Partial Oxidation	10
2.1.2 Steam Reforming	14
2.1.3 Autothermal Reforming	15
2.1.4 Comparison of the Reforming Processes for their Ap- plicability in Mobile and Decentralized Applications . .	15
2.2 Parameters Influencing the CPOX Process	17
2.2.1 Catalysts	17
2.2.2 Fuels	21
2.2.3 Pressure	25
2.3 In-Situ Techniques	26

2.3.1	Non-Invasive In-Situ Techniques: Laser and X-Ray Spectroscopy	26
2.3.2	Invasive In-Situ Techniques: Capillary Sampling	28
2.4	Modeling of Heterogeneous Catalysis	31
2.4.1	Fundamentals of Heterogeneous Catalysis	31
2.4.2	Numerical Modeling	35
3	Methods and Materials	41
3.1	Lab-Scale Reactor	42
3.1.1	Dosing System	43
3.1.2	Reactor and Catalysts	46
3.1.3	Analytical Methods	47
3.2	In-Situ Sampling Technique	55
3.3	Investigated Systems	65
3.3.1	General Measuring Conditions	66
3.3.2	Methane	67
3.3.3	Ethanol	68
3.3.4	Commercial Fuels	70
3.3.5	Propane CPOX at 2-4 bar	73
3.4	Error Analysis	76
3.5	Mathematical Modeling	80
3.5.1	Calculation of Thermodynamic Equilibrium	80
3.5.2	Calculation of Concentration Profiles in a Single Channel	81
3.5.3	Thermal Efficiency	83
3.5.4	CFD Modeling for Evaluating the Influence of the Sampling Technique	84
3.5.5	CFD Modeling of the Entire Monolith	89
4	CPOX of Methane and Ethanol over Rh/Al₂O₃	95
4.1	Methane	95
4.1.1	Spatial Profiles in a Single Channel	96
4.1.2	Influence of Radial Position of Channel	99

4.1.3	Evaluation of the Sampling Technique	109
4.1.4	Modeling of the Entire Monolith	125
4.1.5	Summary for Methane	127
4.2	Ethanol	129
4.2.1	Spatial Profiles in a Single Channel	129
4.2.2	Effect of C/O on Spatial Profiles	137
4.2.3	Influence of Radial Position of Channel	151
4.2.4	Summary for Ethanol	159
5	CPOX of Ethanol-Blended Gasoline Over Rh/Al₂O₃	161
5.1	Gasoline with 5 % Ethanol	163
5.2	Gasoline with 85 % Ethanol	167
5.3	Summary	168
6	CPOX of CH₄ Over Staged Pd-Rh Catalyst	171
6.1	Spatial Profiles in a Single Channel for Pd-Rh	172
6.2	Pd-Rh vs. Rh	175
6.3	Summary	181
7	CPOX of Propane at Elevated Pressures over Rh/Al₂O₃	183
7.1	Operation at 2-4 bar	184
7.1.1	Summary for Operation at Elevated Pressures	192
7.2	Coke Formation at 4 bar	193
7.2.1	Summary for Coke Formation	198
8	Conclusion	201
	References	XXIII

Chapter 1

Introduction

1.1 On-Site Production and Application of Hydrogen

Hydrogen is discussed as an energy carrier due to its applicability in a number of processes such as power generation (Figure 1.1). The production of hydrogen is not dependent on the limited resources of fossil fuels; it can also be based on renewable resources, which makes hydrogen a very flexible energy carrier. However, storage and transportation of hydrogen are inefficient due to the element's low volumetric energy density. The on-site production of hydrogen from logistic hydrocarbon fuels, e.g. natural gas, LPG (Liquefied Petroleum Gas), ethanol, or gasoline, provides an efficient alternative to centralized hydrogen production as hydrocarbon fuels have a higher volumetric energy density.

Hydrogen or synthesis gas (short “syngas”), a mixture of hydrogen and carbon monoxide, is produced from hydrocarbon fuels by reforming. Different approaches can be taken for hydrogen generation: i) steam reforming, in which steam is used as the oxidizing agent, ii) partial oxidation, in which molecular

1. Introduction

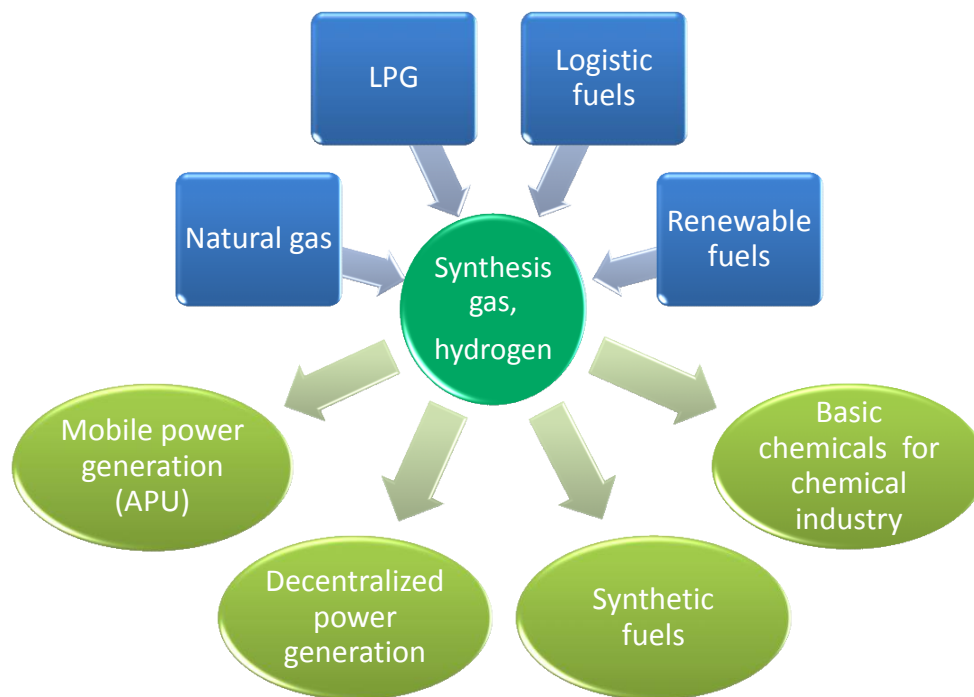


Figure 1.1: Schematic representation of synthesis gas production and application.

oxygen is employed, iii) autothermal reforming, a combination of steam reforming and partial oxidation, and iv) dry reforming, in which carbon dioxide is used. These four reforming processes yield syngas with different H_2 -to-CO ratios. The choice of the right reforming process is mainly dependent on the required H_2/CO ratio for the downstream application. However, for mobile applications, requirements such as fast start-up and compact reactor design need to be taken into consideration.

Endothermic steam reforming is used industrially to produce hydrogen, mostly from natural gas [1], due to the highest hydrogen yield per mole fuel. However, downscaling is difficult because of the heat management necessary to generate steam and to maintain the reforming reaction in the reactor [2]. Dry reforming is also a highly endothermic process, thus downscaling and heat management are similarly problematic as for steam reforming. Autothermal reforming combines positive features of steam reforming and CPOX, e.g. high hydrogen yields (higher than for CPOX) and autothermal operation [3]. How-

ever, for mobile application, the required steam represents a major disadvantage. Catalytic partial oxidation (CPOX) is an attractive possibility, especially for small-scale applications, as CPOX reformers operate autothermally, i.e. no external heat supply is necessary after ignition [4] and a supply of steam is not needed.

As catalysts, noble metals, such as Rh and Pt, are frequently employed [2, 3, 5]. For steam reforming, Ni is a common choice in industrial applications [3]. Foams and monolithic honeycombs, a structure based on a large number of small (hydraulic diameter $d_h \leq 1$ mm) straight channels, are often used as catalyst carriers.

As displayed in Figure 1.1, syngas can be formed from a variety of feedstocks and is applied in a broad range of applications, which also depends on the raw material. The utilization of CPOX reformers for syngas formation is widely discussed, especially in mobile applications but also in other processes [4], as pointed out below.

In mobile applications, hydrogen produced on-board is often employed as a fuel in fuel cells for power generation. Mobile applications, such as APUs (Auxiliary Power Unit) – consisting of fuel reformer and fuel cell –, can be used in trucks to provide the electricity for on-board devices with logistic fuels. Also, an application for power generation in airplanes is possible. Here, an APU can replace the additional turbine which is commonly used to produce electricity in airplanes. For mobile applications, an advantage of on-board hydrogen generation is the applicability of logistic fuels such as gasoline or diesel. No additional tank needs to be carried along in the vehicle as the same fuel is used for engine and APU. Also, the already existing infrastructure for the logistic fuels can be exploited. As an additional feature of the application of APUs in vehicles, a part of the produced hydrogen can be applied to reduce exhaust-gas emissions from the engine [4].

1. Introduction

Besides mobile applications, larger outputs are also feasible for decentralized power generation in remote areas. Here, the utilization of logistic fuels, such as LPG or natural gas, and renewable fuels, such as ethanol, is reasonable. A similar setup to that of APUs, with a fuel reformer and a downstream fuel cell, can be chosen for decentralized power generation.

Another potential application is the reforming of natural gas to syngas as the first step in the supply chain of more valuable chemicals and synthetic fuels [1, 6]. Also, in biomass-to-liquids (BTL) processes, CPOX reformers are taken into consideration for syngas formation from biomass [4].

1.2 Objectives

For a successful application of CPOX reformers, a profound understanding of the reaction network for the respective fuel is advantageous. Furthermore, for technical applications, catalyst deactivation, formation of carbonaceous deposits, and heat management [4] need to be understood to guarantee a reliable performance of the reformer. Experimental as well as numerical studies have been performed for different fuels in catalytic partial oxidation, mostly using rhodium as the catalytically active material on foams and monoliths. Methane, the main component of natural gas, has been widely studied [6–12]. Also, the CPOX of propane [13, 14], a main component of LPG, and ethanol [15–18], an alternative fuel produced from biomass, were studied. Regarding gasoline, surrogates, e.g. iso-octane [19–22] and iso-octane toluene mixtures [23, 24] as well as the actual commercial gasoline [25–27] were studied for hydrogen production by CPOX.

Still, there are many unsolved questions concerning different fuels, catalytically active materials, and operating conditions in CPOX reformers. A broadening of the fundamental knowledge about different applications of CPOX reformers is a major goal of this work.

1.2.1 Setup and Application of In-Situ Sampling Techniques

In ex-situ measurements, important information on the axial profiles of gas composition and temperature along the catalyst is missing. The emergence of in-situ sampling techniques made it possible to detect spatially-resolved concentration and temperature profiles in channels of honeycomb catalysts and drilled holes in foam monoliths. Applying in-situ sampling techniques to methane CPOX, the interaction between heterogeneous chemistry and physical processes, such as mass and heat transport, was experimentally investigated [28–31] and important insights into the sequence of reactions were gained [28–31]. Moreover, guidelines were developed for the reduction of the hot spot observed at the catalyst inlet [32].

Apart from methane, CPOX of propane was investigated by means of an in-situ method [33, 34]. These investigations showed that for propane, contrary to methane, homogeneous gas-phase reactions occur in the channel of the catalyst and lead to the formation of by-products, e.g. ethane, ethylene, and propylene. Since these by-products are consumed again in heterogeneous reforming reactions on the catalytic surface, their presence would not have been foreseeable from ex-situ measurements.

For detailed investigations of further fuels, catalysts, and operating parameters in CPOX, an in-situ sampling technique is constructed in our laboratory at KIT within the scope of this work. An additional feature of this setup is the possibility to carry out measurements not only in a central channel of a monolithic catalyst but also in channels with different radial positions across the catalyst, e.g. at the periphery of the monolith. This feature makes it possible to examine potential deviations in the performance for different channels. Thus, the overall performance of the reformer can be assessed more accurately.

1. Introduction

1.2.2 Fuels and Catalysts to Be Studied

The reforming of fuels related to different applications and with different levels of complexity are experimentally investigated in a CPOX reformer using a Rh-coated catalyst.

CPOX of Methane is investigated in three channels differently positioned across the monolithic catalyst to explore the influence of heat loss on the system.

Ethanol is chosen as a fuel originating from renewable resources. However, in contrast to methane, homogeneous gas-phase reactions occur in ethanol CPOX, which increase the complexity of the investigated system. Different feed compositions in a central channel as well as different channels for a fixed feed composition are examined for CPOX of ethanol.

The investigation of ethanol-blended gasoline (95 RON gasoline and E 85) lead to even higher complexities. Different feed compositions are examined to find inlet conditions which yield high amounts of hydrogen and lead to low rates of by-product formation. Additionally, similar measurements are performed for ethanol/iso-octane mixtures to study the applicability of simple two-component blends as model fuels for complex ethanol-blended gasoline.

Based on the results for methane CPOX on Rh catalysts, the catalyst composition is varied. Consequently, a two-stage catalyst composed of Pd and Rh is examined in CPOX of methane.

The last parameter which is varied in this work is the operating pressure. For elevated pressures, higher throughput can be achieved compared to ambient pressure. To investigate the effect of pressure on syngas formation, the CPOX of propane is studied on Rh/Al₂O₃ at 2 to 4 bar during an external stay at Politecnico di Milano. Additionally, carbon formation is studied during operation at 4 bar, and the deposited coke is analyzed.

1.2.3 Critical Evaluation of the Sampling Technique

The influence of the in-situ setup on the collection of the axial profiles has not been sufficiently clarified; a detailed evaluation is missing. For honeycomb monoliths, a capillary is inserted into one of the channels, which could cause a deviation of the flux in this channel compared to the channels without a capillary. In this work, CFD (Computational Fluid Dynamics) simulations are performed to evaluate the effect of the capillary and to be able to quantify the systematic error of the sampling technique.

Aside from the evaluation studies, a combination of 2D and 3D simulations is performed with a newly developed tool to numerically study the effects in a CPOX reformer, while taking the entire monolithic catalyst into consideration.

Chapter 2

Fundamentals

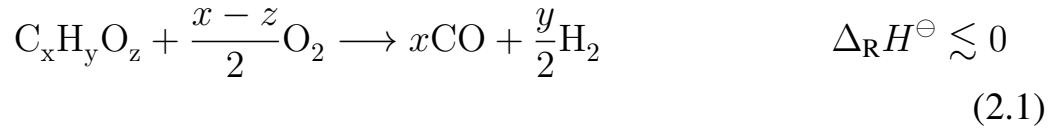
In this chapter, after an introduction to fuel reforming, a short overview of the research activities on CPOX concerning different fuels, catalysts and operating conditions is given. Additionally, the state of the art is presented for in-situ techniques in this field. In the final section, the modeling fundamentals are briefly summarized for heterogeneous catalysis applied in this work.

2.1 Fuel Reforming to Synthesis Gas

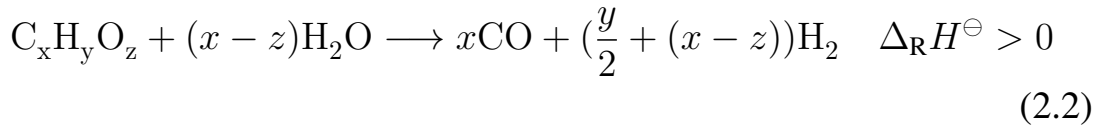
Several routes exist for synthesis gas (or hydrogen) formation from hydrocarbon fuels, such as partial oxidation, steam reforming (SR), autothermal reforming (ATR), and dry reforming (DR). These processes are described with the reaction equations shown in Equations (2.1) to (2.4) for an (oxygenated) hydrocarbon $C_xH_yO_z$. The following paragraphs deal with CPOX, SR, and ATR separately. A detailed discussion concerning DR can be found in [35, 36]. This section is concluded with a comparison of the applicability of the different methods for mobile and decentralized applications.

2. Fundamentals

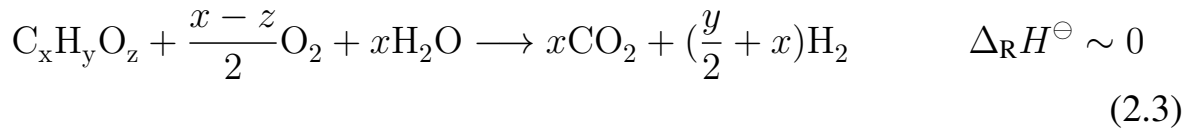
Partial Oxidation



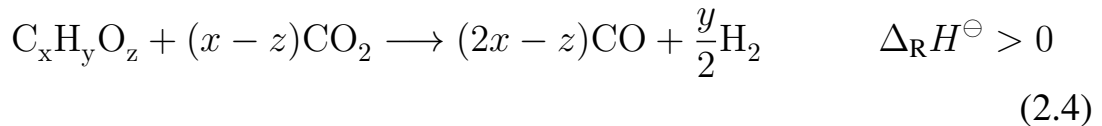
Steam Reforming



Autothermal Reforming



Dry Reforming

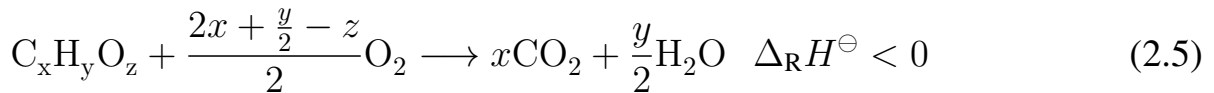


2.1.1 Catalytic Partial Oxidation

In the catalytic partial oxidation process, synthesis gas is produced from a hydrocarbon fuel and oxygen in a heterogeneously catalyzed gas-phase reaction (see Section 2.4.1 for fundamentals of heterogeneous catalysis). Many different processes occur simultaneously and successively on the catalytic surface. Adsorption and desorption of reactants, intermediates, and products as well as surface reactions have a major influence on the CPOX. Thus, the actual reaction network inside a CPOX reformer is composed of dozens to hundreds of elementary-step reactions. However, for simplification, global reactions can

be formulated. The global reaction for catalytic partial oxidation of (oxygenated) hydrocarbons ($C_xH_yO_z$) to synthesis gas is shown in Equation (2.1). The stoichiometric composition for partial oxidation is reached at $C/O = 1.0$ for all fuels (see Equation (3.8) for definition of C/O ratio). The other important reactions which occur during CPOX are described with the global reactions in Equations (2.2) and (2.4) to (2.9). In the CPOX process, after ignition, no external heat needs to be supplied. A CPOX reformer operates autothermally [4].

Total Oxidation



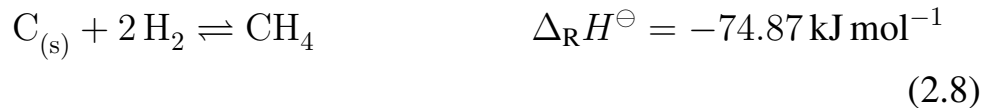
Water-Gas Shift Reaction



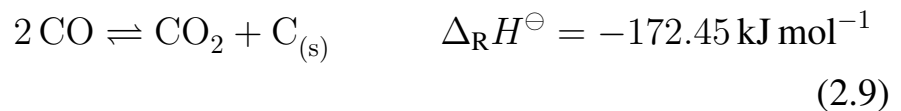
Methanation



Coke Hydrogenation



Boudouard Reaction



2. Fundamentals

For the majority of fuels, partial oxidation of a fuel with oxygen is an exothermic reaction (see Table 2.1). It represents a direct way of syngas formation. However, in a CPOX reformer, syngas is additionally formed via another route. At the catalyst inlet, while the oxygen concentration in the feed is still high, total oxidation (Equation (2.5)) of the hydrocarbon fuel occurs [10], which is a highly exothermic reaction (see Table 2.1). The formed total oxidation products, H_2O and CO_2 , can be consumed again together with unconverted fuel in reforming reactions [10]. These reforming reactions are the steam reforming reaction, converting fuel and H_2O to syngas (Equation (2.2)), and the dry reforming reaction, consuming fuel and CO_2 to yield syngas (Equation (2.4)). These endothermic reactions consume part of the heat released from total oxidation [10]. The partial and total oxidation products, CO , H_2 , H_2O , and CO_2 , are connected through the water-gas shift (WGS) reaction (Equation (2.6)). The WGS is an equilibrium reaction which can proceed in both ways, WGS and reverse WGS, depending on the concentrations of the species involved. Thus, it can be beneficial for hydrogen yield or have an opposing effect [37].

Methane is a by-product which can be formed on the catalytic surface independently of the employed fuel in the CPOX process. Methane formation can occur from synthesis gas in methanation (Equation (2.7)) and from solid carbon on the catalytic surface and hydrogen in coke hydrogenation (Equation (2.8)) [2, 24]. In both cases, the yield of the desired product hydrogen decreases due to these side reactions. On the catalytic surface, carbon formation is possible due to the disproportionation of carbon monoxide in the Boudouard reaction (Equation (2.9)) and methane decomposition (reverse reaction of coke hydrogenation Equation (2.8)) [2, 39]. Another pathway to carbon formation is the deposition of olefins and molecular-growth products such as aromatics and polycyclic aromatic hydrocarbons (PAH) from the gas phase [20, 40–42]. The formation of carbon can lead to lower catalytic activity and even complete catalyst deactivation, depending on the amount of solid carbon on the surface [39, 43]. Also, as mentioned above, the formed coke can lead to hydrogen

Fuel	Reaction	Standard reaction enthalpy $\Delta_{\text{R}}H^{\ominus}$ [kJ mol ⁻¹]
Methane	Partial Oxidation	-35.66
	Total Oxidation	-802.30
	Steam Reforming	+206.17
	Dry Reforming	+247.32
Propane	Partial Oxidation	-226.89
	Total Oxidation	-2043.15
	Steam Reforming	+498.60
	Dry Reforming	+622.05
Ethanol	Partial Oxidation	+12.94
	Total Oxidation	-1278.51
	Steam Reforming	+254.77
	Dry Reforming	+295.92
iso-Octane	Partial Oxidation	-660.14
	Total Oxidation	-5100.45
	Steam Reforming	+1274.50
	Dry Reforming	+1603.70

Table 2.1: Standard reaction enthalpies for the fuels which were investigated in this work. For gasoline, iso-octane is displayed as a surrogate. The standard reaction enthalpies were calculated from the enthalpies of formation of gas, which were taken from [38]. $C_{(s)}$ is the only exception; here graphite was chosen as the allotrope of solid carbon.

consumption if it reacts according to Equation (2.8).

The interplay of the reactions and the extent to which they occur depend on the catalytically active material. The employed fuel also has an influence on

2. Fundamentals

the reaction network. Additional reactions occur, e.g. homogeneous gas-phase reactions. For the CPOX process, which is the investigated process in this thesis, the influence of different parameters on the reaction network is discussed later in this chapter. Section 2.2.1 focuses on different catalysts and the mechanistic insights for Rh and Pd. The influence of different fuels is explained in Section 2.2.2. Another influencing parameter is the pressure, which is discussed in Section 2.2.3.

2.1.2 Steam Reforming

In steam reforming, hydrocarbons react with steam, usually on a heterogeneous catalyst (Ni, Rh, Pt), to yield synthesis gas with a high hydrogen content. This process is used industrially for large-scale production of hydrogen, mostly from natural gas [1]. The overall SR reaction equation is shown in Equation (2.2) for a general hydrocarbon fuel. It is an endothermic reaction, i.e. for high rates of fuel conversion, high operation temperatures are necessary. External heat supply and heat management are crucial factors in an SR reactor. Besides Equation (2.2), the WGS reaction (WGS, Equation (2.6)) and the methanation (Equation (2.7)) are part of the reaction network during SR [44]. These reactions lead to the formation of carbon dioxide and methane as additional products during the SR process.

Industrially, Ni catalysts are mainly used due to the low price of the metal. An excess of steam is employed in the large-scale applications with a steam-to-carbon ratio of 2.5 to suppress coke formation [3]. Carbon deposition originates from processes which can be described with the Boudouard reaction (Equation (2.9)) and methane decomposition (reverse of Equation (2.8)).

2.1.3 Autothermal Reforming

In the ATR process, the fuel is converted heterogeneously with oxygen and steam to yield hydrogen and carbon dioxide. Autothermal reforming is a combination of the CPOX process and the SR process [3, 44]. The global reaction equation is shown in a general form in Equation (2.3). As for CPOX and SR, the WGS reaction (Equation (2.6)) influences the product composition [3]. Also, coke formation according to Equation (2.9) and reverse reaction of Equation (2.8) and methane formation according to Equations (2.7) and (2.8)) can occur [44]. After ignition, the process needs no external heating of the reactor due to the exothermic reactions (partial oxidation Equation (2.1) and total oxidation Equation (2.2)) which proceed while oxygen is present. These provide the heat for downstream reforming processes [3]. However, heat is required for the evaporation of water.

2.1.4 Comparison of the Reforming Processes for their Applicability in Mobile and Decentralized Applications

The different reforming approaches have their specific advantages and disadvantages. The requirements of the application, in which the reformer should be employed, determine the best choice for a reforming system. The main requirement is the H_2/CO ratio in the produced syngas, which is different for all reforming methods. However, for mobile application, additional demands need to be taken into consideration when deciding on a process. These requirements relate to the reactor design, e.g. space and weight are major limitations in mobile applications, as well as operating claims, such as fast start-up and transient response to load changes.

2. Fundamentals

Steam reforming is a mature technology for large-scale applications [2]. Also, it provides the highest hydrogen yield of all three processes under similar conditions [44]. However, for small-scale or mobile applications, the employment of steam reforming is difficult. Fast start-up and frequent load changes are not feasible when using steam reforming due to the heat-transfer limitation [2, 3, 44]. A strong load change could lead to catalyst overheating, which would cause sintering [3]. Furthermore, water needs to be supplied and evaporated, which extends the space and weight of the system.

Autothermal reforming includes positive properties similar to those of CPOX, i.e. fast start-up and good transient response [3]. However, steam needs to be provided, which requires an additional tank and an additional evaporation unit for water. This makes the system more complex than the CPOX process.

The CPOX process provides fast start-up and a quick response to load changes because of the autothermal operation of the reformer and the fast exothermic reaction [44]. As reactants, only the hydrocarbon fuel and air need to be provided. Thus, a compact reactor design is feasible. Nevertheless, a lower hydrogen yield than for SR and ATR is achieved under similar conditions [44]. Also, safety issues need to be taken into consideration in CPOX reformers, as the formation of explosive mixtures from the reactants is possible.

Taking all these advantages and disadvantages into consideration, CPOX is an attractive choice for mobile as well as decentralized applications due to its rapid start-up and transient response, and the simplicity and compactness of the reformer system.

2.2 Parameters Influencing the CPOX Process

2.2.1 Catalysts

Rhodium and platinum are mostly used as catalytically active material in CPOX [2, 3, 5, 29]. Also, for other metals, such as Pd, Ni, Ir, and Ru, activity for partial oxidation was reported in literature [9, 45–51]. Ni catalysts are often investigated [50, 52–55], as they would represent a low-priced alternative to Rh and Pt. However, the application of Ni is problematic as fast catalyst deactivation occurs during operation. The loss in activity is due to sintering of the Ni particles and carbon formation on the catalytic surface [39, 56–58]. Alternative catalysts with no or very low noble metal content are also investigated, e.g. noble metal-doped hexaaluminates [59], noble metal-substituted pyrochlores [47, 60], and group-6 metal carbides [61]. However, the noble metal catalysts still show the highest reforming activity and catalyst stability.

The catalytically active material is often deposited on a catalyst carrier. As catalyst carriers, foams and honeycomb monoliths are employed [29, 32, 62]. These structured carriers provide the advantage of low pressure drops and a high geometric surface area [63–65]. The honeycomb monoliths which are used in this work consist of a high number of straight, quadratic channels which are separated by thin walls.

Often, a highly porous material, called a “washcoat”, e.g. γ -Al₂O₃, is applied to the catalyst carrier. The washcoat is impregnated with the catalytically active material either before or after deposition on the catalyst carrier. The washcoat increases the geometric surface area and the dispersion of the catalytic metal and inhibits sintering during operation. These characteristics can lead to higher syngas formation [11, 66–68].

2. Fundamentals

In this work, the experimental investigations were performed on Rh/ γ -Al₂O₃ and Pd/ γ -Al₂O₃ honeycomb catalysts. For this reason, a closer look on the mechanism of CPOX on these two metals is taken in Sections 2.2.1.1 and 2.2.1.2, respectively.

2.2.1.1 Rhodium

Rhodium has been widely studied as a catalyst in partial oxidation of methane [6, 10, 29, 31, 32, 69, 70] and other fuels, such as ethanol [15], ethanol-blended gasoline [16], propane [71], and n-butane [72]. In studies comparing the reforming activity of different metals of the groups 8-10, e.g. Rh, Pt, Pd, Ir, and Ni, the highest syngas formation and stability was observed for Rh [43, 73]. Rh also showed only a very low tendency to coke formation for methane CPOX [39] and ethanol CPOX [43].

Methane CPOX is the simplest of the investigated systems, as only heterogeneous reactions occur at ambient pressure [6, 32, 69, 70] and it only yields H₂, CO, H₂O, and CO₂. Nevertheless, an ongoing discussion of the mechanism of methane CPOX on Rh can be found in literature [57, 74–78]. For other fuels, similar mechanistic uncertainties are present. Additionally, homogeneous gas-phase reactions and further heterogeneous reactions need to be considered, which further increases the complexity of the system (see Section 2.2.2). For this reason, the discussion of the mechanism on Rh is restricted to methane CPOX in this section.

Two mechanisms have been proposed for CPOX of methane on Rh. One is the indirect formation of synthesis gas by a sequence of total oxidation (Equation (2.5)) and steam reforming (Equation (2.2)), with steam reforming setting in when all molecular oxygen is consumed. The other one is the direct formation of synthesis gas in partial oxidation (Equation (2.1)) in the presence of molecular oxygen. There are studies favoring the indirect formation [74, 75] as well as the direct formation [76–78]. Also, a combination of the mechanisms

has been proposed [10, 79]. Additionally, the support material seems to play a role for the formation of synthesis gas on Rh [57, 75, 80, 81].

The in-situ spectroscopic investigation of the oxidation state of Rh during CPOX of methane at low temperatures (573-673 K) [7] showed oxidized Rh particles on the first part (approx. 1 mm) of the catalyst and reduced particles in the second, larger part (approx. 2 mm) of the catalyst. Here, an indirect mechanism is observed, but this could also be due to the low temperatures [7, 82].

The axial concentration and temperature profiles detected by Horn et al. [12, 29] for foams and by Beretta et al. [32] for honeycomb monoliths show H₂ and CO formation starting at the catalyst inlet, when molecular oxygen is still present. A hot spot occurs in this zone on the catalyst surface due to the concurrently occurring total oxidation. This zone is the oxy-reforming zone, where total oxidation, partial oxidation, and steam reforming seem to occur simultaneously. After all oxygen has been consumed, steam reforming of methane takes place. This second zone is the reforming zone. A drop in the surface temperature due to endothermic steam reforming is detected. Dry reforming does not seem to take place on Rh catalysts [37]. The WGS equilibrium influences the gas composition [37]. Also, in the investigations for methane CPOX in this work (see Sections 3.3.2 and 4.1), similar spatially-resolved profiles were observed.

These observations suggest a direct formation of synthesis gas in the first zone of the catalyst and indirect formation in the second zone. However, the spatially-resolved profiles cannot be used to directly identify the ongoing elementary-step reactions [29]. It has to be taken into consideration that a radial gradient is present in the channels of the monolith, especially near the inlet, due to external diffusion limitation. Therefore, it is possible that a species is detected in the gas composition with the in-situ sampling technique but is not present close to the channel wall at this axial position. The gas sample sucked

2. Fundamentals

into the probe will probably consist of a mixture of the gas compositions at different radial positions. In the collected gas samples, oxygen and hydrogen are present in parallel within the first millimeter of the channel. However, the concentration of oxygen close to the channel wall is probably lower and might even be zero, so that hydrogen formation on the surface might occur while no oxygen is present. Thus, it is not possible to draw a conclusion on direct and indirect mechanism for syngas formation based on the measured concentration profiles.

2.2.1.2 Palladium

Palladium has been studied as a CPOX catalyst for methane [48, 49, 73, 83, 84] and other fuels such as ethanol [43, 85]. Complete conversion of the fuels and high hydrogen yields can be reached by reforming over Pd [45, 48]. Nevertheless, lower syngas yields were observed compared to Rh under similar conditions [43]. Additionally, Pd seemed prone to coking [39, 73], which even caused extinction of the reaction in some cases [43]. However, the extent of coking seemed to depend strongly on the support, as a higher amount of solid carbon was observed on Pd/Al₂O₃ than on Pd/xCeO₂-Al₂O₃ [48].

For Pd, the two mechanisms for syngas formation in methane CPOX also have been discussed (see Section 2.2.1.1). However, the indirect route [86] is not proposed as often as the direct one [48, 49, 83]. To the best of the author's knowledge, no spatially-resolved profiles of concentration and temperature for CPOX over Pd were published in literature yet. Thus, the development of the gas composition along the catalyst is unknown. However, this information would help to understand the prevalent reactions in CPOX on Pd. In Chapter 6 of this work, spatial profiles are presented for a two-stage Pd-Rh catalyst. New insights into the CPOX mechanism on Pd are also discussed in Chapter 6.

For Pd, oscillatory behavior for methane CPOX was observed and studied [87–89]. However, under the operating conditions employed in this work, these

oscillations did not occur. Therefore, no discussion of this behavior is presented herein.

2.2.2 Fuels

Schmidt and his co-workers showed that CPOX of a variety of feedstocks is possible in millisecond contact time on heterogeneous catalysts [6,9,11,90,91]. For the main reactions (Equations (2.1), (2.2), (2.4) and (2.5)), the standard reaction enthalpies are displayed in Table 2.1. As mentioned above, methane CPOX at ambient pressure provides the simplest system, as the complete process is covered by Equations (2.1), (2.2) and (2.4) to (2.9) and no homogeneous gas-phase reactions occur [6, 32, 69, 70]. For other fuels, additional reactions to the ones shown in Equations (2.1), (2.2) and (2.4) to (2.9) are possible. Sections 2.2.2.1 to 2.2.2.3 discuss the characteristics of the fuels investigated in this work. Methane CPOX was already explained above (Sections 2.2.1.1 and 2.2.1.2).

2.2.2.1 Ethanol

Ethanol is one of the few fuels for which the catalytic partial oxidation reaction is slightly endothermic (see Table 2.1). Nevertheless, autothermal operation of the CPOX reformer is also observed for ethanol [15].

CPOX of ethanol has been studied for different combinations of catalytically active material and washcoat material such as Rh/Al₂O₃ [15], Rh/CeO₂ [17, 92], Pt/Al₂O₃ and Pt/ZrO₂ [93], NiO/Al₂O₃ [50], and Ni/La₂O₃ [55]. Besides methane, typical side-products in ethanol CPOX are acetaldehyde [55,85,94], ethylene [43,93], and diethylether [15]. The selectivity to the products is highly influenced by the chosen metal [85]. The deviation in selectivity is caused by different adsorbed species on the catalytic surface for the differ-

2. Fundamentals

ent metals. For example, on Rh, an ethoxy species is formed as the first step after ethanol adsorption [43, 95]. It should be noted that the resolution of the elementary-step reactions is beyond the scope of this work.

The washcoat material plays an important role in ethanol CPOX. For example, the acid sites of γ -Al₂O₃ can catalyze dehydration of ethanol to ethylene (Equation (2.12)) [96] and diethylether (Equation (2.13)) [97]. For acetaldehyde formation from dehydrogenation (Equation (2.10)), γ -Al₂O₃ [98] as well as Rh [99] and Pt [85] were identified as catalytically active materials. Also, acetaldehyde decomposition to carbon monoxide and methane (Equation (2.14)) can occur on the Rh surface [100].

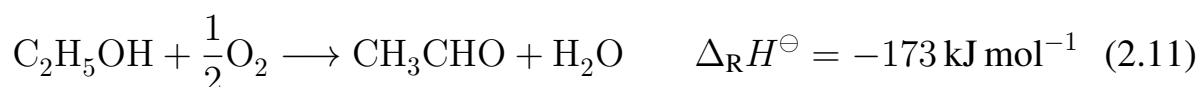
Besides heterogeneous catalyzed side-reactions by metal or washcoat, homogeneous gas-phase reactions can occur. Acetaldehyde, ethylene, and diethylether formation may also occur in the gas phase [101].

In this work, ethanol CPOX is investigated for the first time by means of an in-situ sampling technique (see Sections 3.3.3 and 4.2). The results were also published in [102]. From the axial profiles, new insights into the interaction of homogeneous and heterogeneous gas-phase reactions are gained (Section 4.2).

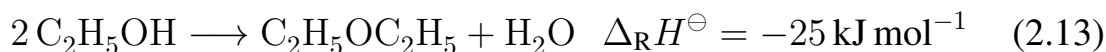
Dehydrogenation



Oxidative Dehydrogenation



Dehydration



Acetaldehyde Decomposition



2.2.2.2 Propane

Huff et al. studied partial oxidation of C_3H_8 over a range of metals of the groups 8-10 [54]. Over Pt, C_2H_4 formation was observed, whereas Rh showed high selectivities to syngas and no C_2H_4 formation [54]. Studies in a microstructured reactor with Rh [14] as well as performance and stability tests on Rh-coated foams [13] were published. Mechanistic investigations on Rh were performed in an annular reactor [103] and recently also using an in-situ sampling technique for propane CPOX over Rh-coated honeycomb catalysts [71, 104]. The in-situ investigations revealed the formation of by-products such as CH_4 , C_2H_4 , C_3H_6 , and C_2H_6 in homogeneous gas-phase reactions at the catalyst inlet. The homogeneous gas-phase reactions are favored at the catalyst inlet due to the high temperatures in this region. Propane cracking to CH_4 and C_2H_4 (Equation (2.15)) as well as dehydrogenation to C_3H_6 (Equation (2.16)), which are likely the proceeding reactions [81], are endothermic reactions. Only the hydration of C_2H_4 to C_2H_6 (Equation (2.17)) is an exothermic reaction. Except for methane, these by-products are completely consumed again in heterogeneous steam reforming [71]. Thus, for propane CPOX, a combination of heterogeneous and homogeneous processes occurs [71].

In this work, the influence of pressure on propane CPOX was examined (see Section 3.3.5 and chapter 7), as this was expected to have significant

2. Fundamentals

influence on the homogeneous gas-phase reactions. The results were also published [81].

Propane Cracking



Dehydrogenation



Hydration of Ethylene



2.2.2.3 Ethanol-Blended Gasoline

Ethanol-blended gasoline, which was studied in this work, consists of hundreds of different hydrocarbon species, e.g. alkanes, alkenes, cycloalkanes, and aromatic hydrocarbons [105]. Furthermore, the exact composition of the fuels is not known and can vary due to different origins and regulations. For this reason, model fuels consisting of one or two components in known concentrations are often studied. Iso-octane is frequently used as a surrogate for gasoline. Several studies of iso-octane CPOX on Rh catalysts can be found in literature [19, 20, 42, 66]. In all these investigations, formation of coke-precursors, such as ethylene, were observed, especially at fuel-rich conditions. Besides iso-octane, other hydrocarbon species representing different classes of hydrocarbons in logistic fuels [23, 62] and two-component mixtures were examined [16, 22, 23]. These investigations showed that the performance of the mixture is not the averaged performance of the single component. However, the

performance of commercial gasoline was also studied based on the gas composition at the catalyst outlet [25]. In this investigation, a breakthrough of the fuel was observed. Still, data on logistic fuels are scarce. Results for two kinds of ethanol-blended gasoline, 95 RON gasoline and E 85, are presented in this work in Chapter 5 and were also published in [16].

2.2.3 Pressure

Operation of CPOX reformers at elevated pressures has not been extensively studied experimentally. Most investigations were based on methane [69,80,106–108] or natural gas [109]. Stable performance of Rh-based catalysts was reported at elevated pressures as well [109]. The conversion of methane decreased with increasing pressure in some of these studies [107, 108]. However, in the in-situ investigations presented by Bitsch-Larsen et al. [69] for a Rh-coated foam monolith, only small changes in methane conversion and syngas yield were observed. Mass-transfer limitation for the reactants was indicated as the reason for these observations. Furthermore, only little indication of homogeneous gas-phase reactions was found for methane CPOX up to 11 bar [69]. Quiceno et al. [110] showed a numerical study of the CPOX of methane over Pt gauzes up to 10 bar. Even though an increase in C_2H_6 yield with rising pressures was observed in the simulations, the overall amount of products formed in homogeneous gas-phase reactions was still low.

However, the increase of pressure also increases the reaction rate of gas-phase reactions, as the reaction rates are proportional to p^2 (for bimolecular homogeneous reactions) [106]. For fuels such as ethanol and propane, an increase of homogeneous gas-phase reactions with increasing pressure is expected, as homogeneous reactions are already observed at ambient pressure.

Propane CPOX (see Section 3.3.5 and chapter 7) was investigated at 2 to 4 bar with the in-situ sampling technique to evaluate the extent of homogeneous

2. Fundamentals

gas-phase reactions at elevated pressures. The results were also presented in [81].

2.3 In-Situ Techniques

From Section 2.1.1 it becomes apparent that the partial oxidation of fuels is a complex combination of a large number of reactions. For the design and optimization of CPOX reformers, a profound knowledge of the reaction network is desirable. To achieve this knowledge, the examination of the process under operating conditions as close to technical ones as possible is necessary [29]. However, common monitoring of concentration and temperature at the catalyst outlet of the operating catalyst cannot provide enough information for mechanistic insights into the system. The evolution of the catalyst structure, gas composition, and temperature along the catalyst is very useful information for understanding the mechanism. To fill this gap in knowledge, in-situ techniques have recently been developed to obtain highly resolved spatial data during operation of a catalyst. A short overview of the application of these techniques in CPOX is given in the following sections. The in-situ techniques are divided into two different types, non-invasive and invasive. Here, invasive means the insertion of a probe into the catalytic system for determining local concentrations or temperatures.

2.3.1 Non-Invasive In-Situ Techniques: Laser and X-Ray Spectroscopy

In non-invasive techniques for in-situ investigations, optically accessible reactors are necessary [111]. Mantzaras and co-workers have developed an optically accessible channel-flow reactor, in which 2D laser induced fluorescence (LIF) and 1D Raman spectroscopy are employed to measure concentrations of trace

species and stable gas-phase species, respectively [111, 112]. The channel consists of two horizontal plates which are coated with the catalyst and placed in a way that results in a free space of 7 mm between the plates. Devices for heating and cooling of the plates are present. Temperature profiles are obtainable from thermocouples which are placed along the channel length beneath the catalytic surface. Additionally, this reactor is also applicable for operation at elevated pressures [111]. Employing this reactor, Schneider et al. [113, 114] investigated CPOX of methane over Rh/ZrO₂ from 4 to 10 bar with H₂O and CO₂ dilution. A small increase in methane conversion and syngas yield was observed for higher pressures. The obtained concentration profiles also showed higher hydrogen yields for H₂O addition and nearly no impact on the profiles for CO₂ addition [114].

A similar setup for 2D LIF spectroscopy was recently completed at KIT [115], which can also be used for the investigation of trace species in CPOX.

Besides concentration profiles, structural changes of the catalyst surface during operation can be determined with non-invasive techniques along the catalyst length. This was presented by Grunwaldt et al. for CPOX of methane over Rh and Pt-Rh [7, 116, 117]. For this method, in-situ X-ray absorption spectroscopy in an in-situ spectroscopic cell is employed [7]. The measurements were performed at a synchrotron. As described above (Section 2.2.1.1), in methane CPOX on Rh/Al₂O₃ at low temperatures, oxidized Rh species were detected in the first part (0 to approx. 1 mm) of the catalyst and reduced Rh species in the second part (1 mm to 3 mm) during operation [7, 116].

With non-invasive techniques, the catalytic system is not disturbed by a probe as is the case for invasive techniques. However, the non-invasive methods are very demanding due to their requirement of laser setups or beam time at a synchrotron. Furthermore, the optical accessibility restricts the operation conditions that can be investigated. For the concentration profiles, a single channel is formed by two catalyst-coated plates. Thus, the heat management is different

2. Fundamentals

than during autothermal operation of a CPOX reactor with a honeycomb catalyst.

2.3.2 Invasive In-Situ Techniques: Capillary Sampling

Lyubovsky et al. [80] presented one of the first studies on CPOX including concentration and temperature profiles. This technique was based on stacking of microlith screens, in between which thermocouples and $\frac{1}{16}$ inch tubing for gas sampling were placed. With this setup, a resolution of 2 mm was obtained. However, this resolution is not high enough for the separation of the different zones, oxy-reforming and reforming zone (see Sections 2.2.1.1 and 4.1.1), in catalytic partial oxidation that were discovered with the more recent in-situ techniques.

Another possibility for the measurement of axial concentration profiles in honeycomb monoliths is the application of an isothermal flat-bed reactor, as presented for NO_x catalysts in exhaust-gas after-treatment for diesel engines [118]. Here, the catalyst is made up of thin slices of monolith which are arranged successively. After each slice, a gas sample can be withdrawn to obtain concentration profiles along the catalyst. However, the resolution is limited by the length of the employed slices ($L = 40$ mm in the study shown in [118]). This technique has not been used for the study of CPOX to the best of the author's knowledge.

In a capillary-based technique, which was used extensively in the last years, the catalytic system is investigated by inserting a movable probe into the catalyst for concentration and/or temperature measurements along the catalyst length. Horn et al. [12, 119] have developed an in-situ sampling technique for foam catalysts. For this technique, a capillary is inserted into a channel which is drilled through the center of the foam in axial direction. The capillary is sealed at the upper end and a small orifice at the side of the capillary is

used to sample the gases [120], so that the channel in the foam is not left open when the capillary is pulled out. A thermocouple is placed inside the capillary to detect temperature profiles simultaneously with the concentration profiles. Many studies have been performed on this setup for partial oxidation over Pt and Rh, mainly with methane [29, 67, 69, 119, 120], but also with ethane [121] as fuel. The sampling setup was further improved by Horn et al. [122] to make the operation with pressures up to 45 bar and with temperatures up to 1573 K possible. Further studies on methane partial oxidation over Rh- and Pt-coated foams were presented, also at higher pressures [123]. From the investigations with the in-situ sampling technique, the separation of the Rh catalyst into the oxy-reforming and the reforming zone, as already described in Section 2.2.1.1, was revealed [123]. This was also confirmed in the measurements performed in this work on a Rh/Al₂O₃ honeycomb catalyst (Section 4.1.1).

Also, for Pt, a two-zone structure of the concentration profiles over the catalyst length was observed [124]. However, oxygen consumption in CPOX on Pt is mainly kinetically controlled in contrast to oxygen consumption in CPOX on Rh, where mass-transfer limitation occurs [123].

Donazzi et al. [33, 71] have adapted the in-situ sampling setup for honeycomb catalysts. A very thin capillary (diameter = 340 μm) is used inside the channel ($d_h \leq 1$ mm). For the temperature profile, two different temperature probes were inserted separately into the channel. For the gas-phase temperature, a thermocouple was used. The surface temperature was detected by a side-looking optical fiber connected to a pyrometer [33]. The CPOX of propane was studied over a Rh/Al₂O₃ monolith, which led to the discovery of the combined homogeneous-heterogeneous reaction network for propane [71], already described in Section 2.2.2.2. For methane as well as propane, the in-situ investigations led to guidelines for the hot-spot reduction at the catalyst inlet [32, 34]. The in-situ sampling technique was modified to make an operation up to 4 bar possible, and investigation of methane and propane CPOX up to 4 bar were

2. Fundamentals

performed [81]. The results for propane CPOX at elevated pressures were part of this work and are discussed in Section 7.1.

Patridge et al. [125] presented a capillary-based sampling technique, called “SpaciMS”, in which several capillaries are inserted simultaneously into different channels of a honeycomb monolith. The gas samples are analyzed by mass spectrometry. Mostly, catalytic processes for exhaust-gas after-treatment were studied, e.g. the regeneration mechanism of a NO_x storage-reduction catalyst [126]. The SpaciMS technique is now commercially available from HIDEN Analytical Ltd. [127].

The spatially-resolved profiles which are obtained with the in-situ sampling techniques make it possible to gain a profound knowledge of the investigated system. An in-situ sampling technique was constructed during this work to further broaden the knowledge on various fuels. The sampling system is based on the in-situ techniques by Horn et al. and Donazzi et al. and is described in detail in Section 3.2.

With the in-situ sampling techniques, a honeycomb catalyst can be employed in the same form it would have in a CPOX reformer. No adjusting of structure or form is necessary. Thus, operation close to technical conditions is achieved. However, the inserted probe influences the investigated catalytic system, which affects the detected concentration and temperature profiles.

To the best of the author’s knowledge, the influence of the probe on the measured concentration profiles has only been studied by Sá et al. [128]. The simulations were based on the experimental SpaciMS technique presented in [125]. CO oxidation was studied experimentally with 16 capillaries in 16 channels of a honeycomb monolith and numerically using CFD simulations. They discovered a negligible influence of the probe when the capillary was in the corner of a channel and an increase of velocity for the channel with the probe. However, the volume flux was the same for all channels in their simulations, which seems to deviate from experimental conditions [129]. In this work, a

detailed evaluation of the experimentally employed in-situ technique by CFD simulations is presented (see Section 4.1.3).

Stagnation-flow reactors can also be used to obtain concentration profiles as a function of the distance from the catalytic surface [130–132]. In a stagnation-flow reactor, a flat catalyst-coated disc is employed. The flow is oriented perpendicular to the catalyst surface. For the in-situ measurements, gas samples can be collected in the reactor with a quartz microprobe. The probe can be moved relative to the catalyst in radial and axial direction [130–132]. Recently, a simulation tool was presented which makes it possible to simulate the experiments and which takes external as well as internal mass-transfer limitations into account [133]. However, as the setup of a stagnation-flow reactor is far away from the one for technical reactors, this method is not further discussed herein.

2.4 Modeling of Heterogeneous Catalysis

2.4.1 Fundamentals of Heterogeneous Catalysis

A catalyst is a component which takes part in a chemical reaction without being consumed in the reaction and which increases the reaction rate of the reaction [134,135]. This definition is a translated, slightly varied version of the definition given by Wilhelm Ostwald in 1909, which still covers the essential points of catalysis.

A catalyst can have various forms and shapes; however, a subdivision of catalysis into three categories is common [134, 135]:

- Homogeneous catalysis, in which the reactants and the catalyst are in the same phase, i.e. all components are either in the gas phase or in the liquid phase.

2. Fundamentals

- Biocatalysis, in which enzymes are the catalysts in chemical reactions in living cells and organisms [134].
- Heterogeneous catalysis, in which the reactants and the catalyst are in different phases. The catalyst is a solid and the reactants are either in the gas or in the liquid phase.

In this work, heterogeneous gas-phase reactions are studied. Thus, all further explanations and discussions are based on these reactions. Since the catalyst is a solid in heterogeneous catalysis, the catalytic reaction takes place at the surface. Often, expensive noble metals are used. As described in Section 2.2.1, porous washcoats are used to obtain high surface areas.

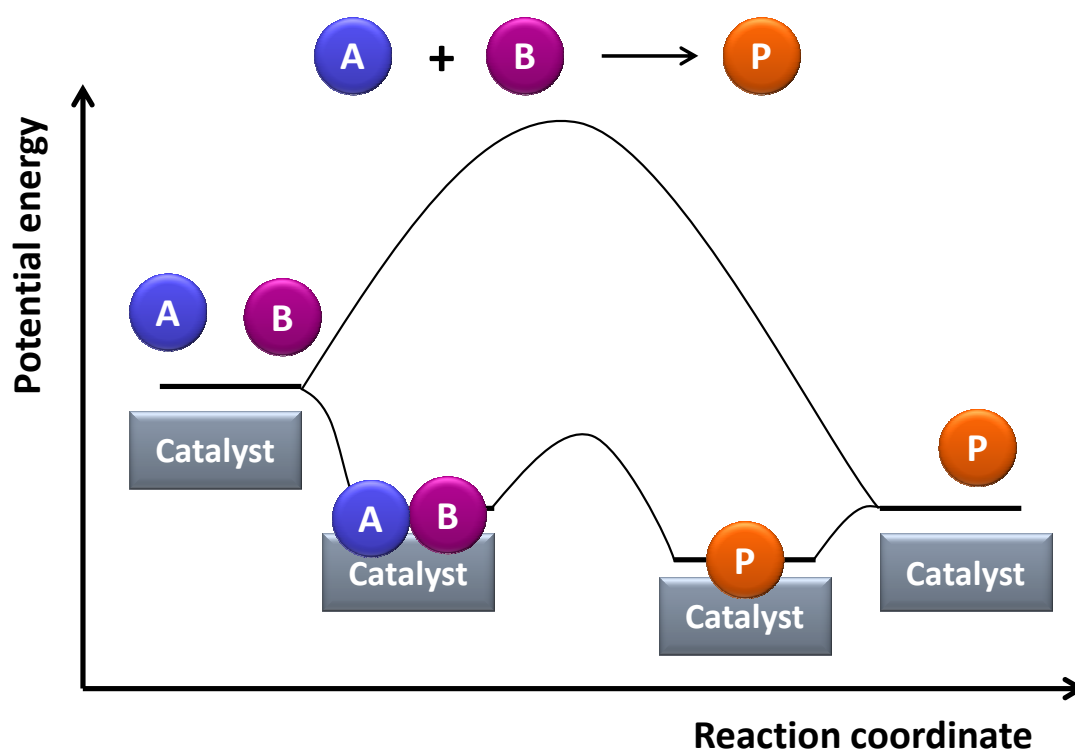


Figure 2.1: Diagram of potential energy for a catalyzed and an uncatalyzed reaction. Adapted from [135].

Figure 2.1 displays a diagram of the potential energy for the reaction $A + B \rightarrow P$ as a catalyzed and an uncatalyzed reaction. In the non-catalytic reaction, the gaseous reactants A and B have to overcome the activation barrier to

form the gaseous product P. A different pathway is used in the catalytic reaction. As a first step, the reactants adsorb on the surface. The adsorbed species can react to the adsorbed product when they overcome the activation barrier. Nevertheless, the activation barrier is smaller than for the non-catalytic reaction. In the last step, the adsorbed product desorbs from the surface. Figure 2.1 shows that the change in Gibbs free energy between reactants and product is the same for catalyzed and uncatalyzed reactions. Thus, the thermodynamic equilibrium of the reaction is not affected by the catalyst. Nevertheless, due to the lower activation barriers, the reaction rate of the reaction is increased by the use of a catalyst [134–136].

This is a simplified description of a catalyzed reaction based on the Langmuir-Hinshelwood mechanism [135, 136]. However, other mechanisms such as the Eley-Rideal mechanism can occur, depending on the considered reaction [135, 136]. Nevertheless, the depiction is sufficient for the basic understanding of heterogeneously catalyzed gas-phase reactions.

Heterogeneous catalysis is composed of a high number of interacting chemical and physical processes. Figure 2.2 sketches a single channel of a honeycomb catalyst with the occurring chemical and physical processes. In the channel, the transport of momentum, energy, and species occurs in axial direction by convective diffusive flow. However, mass transport also occurs in radial direction by diffusion of the reactants to the catalyst-coated channel wall and diffusion of the products from the wall. The species can adsorb on and desorb from the catalyst surface, and with the adsorbed species (or adsorbed fragments), surface reactions can take place. In CPOX, high temperatures are commonly reached inside the catalyst. Thus, homogeneous gas-phase reactions also need to be considered as a chemical process inside the channel of the catalyst.

Often, porous washcoat materials are employed, on which the catalytically active material is dispersed. Diffusion in and out of the pores affects the

2. Fundamentals

ongoing chemical reactions as the mass transport of the species to the active sites becomes an important step in the process. Additionally, the catalytic surface consists of different active sites as the surface of the particles consists of terraces, kinks, steps, and edges.

The temperature field inside the channel of a honeycomb catalyst is influenced by many processes. Heat is released as well as consumed in chemical reactions. In the fluid, convective and conductive heat transfer take place. For the solid, heat transport occurs in the channel wall. Additionally, heat transfer by thermal radiation from the channel wall exists.

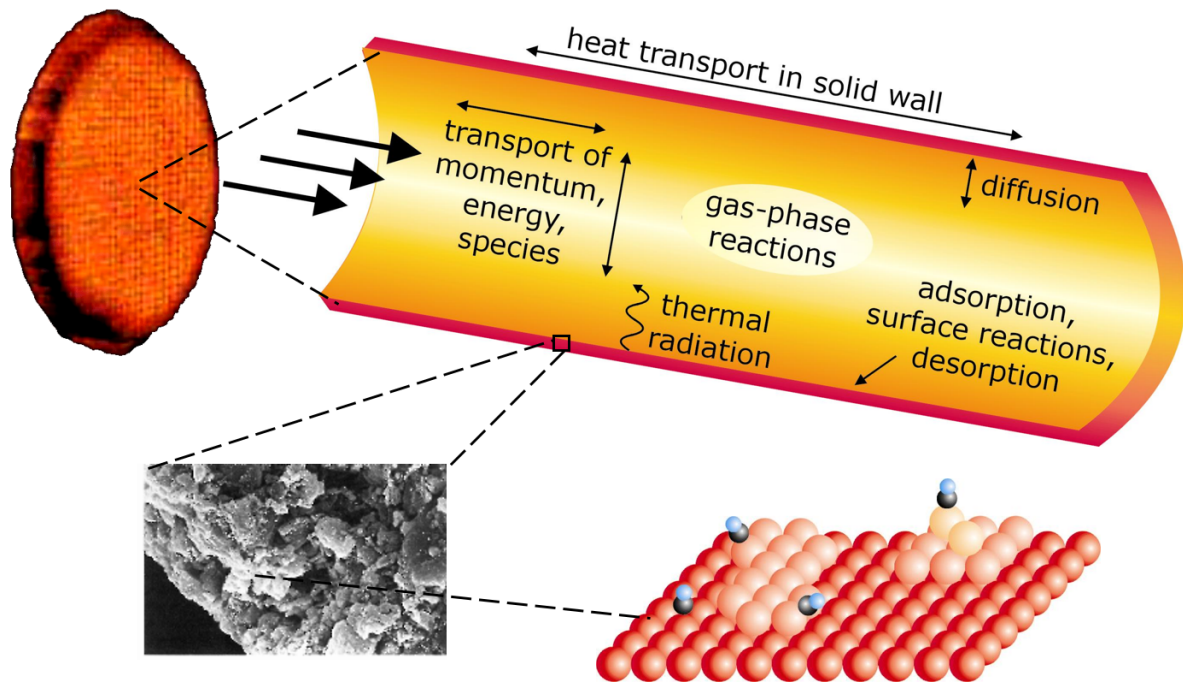


Figure 2.2: Interaction of chemical and physical processes inside a channel of a catalytic honeycomb monolith. Taken from [137].

As the main focus of this work is on experimental investigations, only a brief introduction into numerical simulations is given with a focus on the methods used in this work. For a more detailed description of the underlying fundamentals and equations, it is referred to [137, 138].

2.4.2 Numerical Modeling

2.4.2.1 Detailed Modeling

The three-dimensional problem presented by the complex interaction of various chemical and physical processes in a channel of a monolith, is a challenging task for numerical modeling. For the laminar, reactive flow inside the channel, transport equations for mass, momentum, and energy need to be solved. Furthermore, for each gas-phase species, an additional transport equation needs to be included. In the equations for the species, the formation and consumption in the gas phase have to be considered. Thus, a detailed mechanism, i.e. consisting of elementary steps, for the homogeneous gas-phase reactions is desired. Furthermore, the chemical reactions on the surface need to be coupled with the flow field. For this, a detailed mechanism for the heterogeneous reactions is desired as well. Additionally, the diffusive flux at the fluid-surface boundary caused by adsorption and desorption of the present species has to be considered. Moreover, internal mass-transfer limitation due to the diffusion in the washcoat has to be taken into consideration.

For the detailed mechanisms, the most accurate approach would be to include the elementary steps and to consider all different kinds of crystallographic structures present in the catalytic particle. However, this approach requires a high amount of information about the various possible structures of the particle. More importantly, the complexity for a real catalytic system like CPOX of fuels would be excessive. To make surface-reaction mechanisms applicable to real systems, the mean-field approximation is a prevalent choice for an assumption. In this approach, the catalytic surface is separated into computational cells which originate from the flow-field simulation. In the computational cell, a mean value is assumed for the state of the active surface. A uniform surface with a random adsorbate distribution is the basic assumption. Thus, a description of the catalytic surface is possible by the temperature and the surface coverages Θ

2. Fundamentals

for the present species [137]. Therefore, the concentration of a surface species i can be described by Equation (2.18). The surface-site density Γ represents the total number of surface sites on which species can be adsorbed. The coordination number σ_i describes the number of surface sites required for a species i to adsorb on the surface [137].

$$c_i = \frac{\Theta_i \Gamma}{\sigma_i} \quad (2.18)$$

c_i : concentration of surface species i

Θ_i : surface coverage for surface species i

Γ : surface-site density

σ_i : coordination number for surface species i

Based on these assumptions, the production rate \dot{s}_i of a surface species i can be calculated with Equation (2.19).

$$\dot{s}_i = \sum_{k=1}^{K_s} \nu_{ik} k_{f_k} \prod_{j=1}^{N_g+N_s} c_j^{\nu'_{jk}} \quad (2.19)$$

\dot{s}_i : molar net production rate

ν_{ik} : stoichiometric coefficient for species i in reaction k

k_{f_k} : rate coefficient for reaction k

K_s : total number of surface reactions

N_s : number of adsorbed species

N_g : number of gaseous species

c_j : concentration of species j

ν'_{jk} : stoichiometric coefficient of species j in reaction k

For the rate coefficient k_{f_k} , an Arrhenius expression is used (Equation (2.20)) [137]. The rate coefficient of surface reactions is commonly dependent on the surface coverage. This is taken into account by employing the parameters μ_{i_k}

and ε_{i_k} in the expression for the rate coefficient.

$$k_{f_k} = A_k T^{\beta_k} \exp \left[-\frac{E_a}{RT} \right] \prod_{i=1}^{N_s} \Theta_i^{\mu_{i_k}} \exp \left[\frac{\varepsilon_{i_k} \Theta_i}{RT} \right] \quad (2.20)$$

A_k : pre-exponential factor

E_a : activation energy

R : ideal gas constant

T : temperature

β_k : temperature coefficient

μ_{i_k} : change of the rate of reaction

ε_{i_k} : activation energy, dependent on surface coverage

In the description of adsorption reactions, sticking coefficients S_i are commonly used. The sticking coefficient quantifies the probability that a gas-phase species i , which hits the surface, is adsorbed on it. The value of the sticking coefficient is between 0 and 1. A transformation of the sticking coefficient to a rate coefficient is possible using Equation (2.21) [137].

$$k_{f_k}^{\text{ads}} = \frac{S_i^0}{\Gamma \tau} \sqrt{\frac{RT}{2\pi M_i}} \quad (2.21)$$

S_i^0 : initial sticking coefficient for species i

M_i : molar mass of species i

with

$$\tau = \sum_{j=1}^{N_s} \nu'_{jk} \quad (2.22)$$

Assuming that detailed mechanisms for gas-phase and surface reactions, based on the mean-field approximation, are available and coupled with the governing equations, the solution of such an equation system would still be challenging.

2. Fundamentals

The high number of equations, which need to be solved, and the different time scales, which have to be covered for the chemical reactions, require excessive CPU time [4].

2.4.2.2 Approaches to Simplify the System

Simplifications need to be employed to reach reasonable computing times. In this work, three different approaches are chosen to simplify the system. One approach is the reduction of the size of the considered system (see Section 3.5.4 for detailed description and Section 4.1.3 for results). In this case, a complex 3D flow field as well as a detailed reaction mechanism were employed. However, only nine partially-sliced channels were considered in the simulations. The reduction of the investigated part of the monolith to a considerably smaller sector makes it possible to achieve feasible computing times (one simulation took approx. 24 h of real time).

The second approach to simplify the system is to make assumptions about the flow, which lead to two- or one-dimensional flow fields, and keep a detailed reaction mechanism. This approach is used to simulate the behavior in one channel of the monolith with very short computing times in the range of minutes (see Section 3.5.2 for detailed description of the simulations and Section 4.1.2 for results). This approach is further discussed in Section 2.4.2.3.

Another possible simplification is to look at a complex 3D flow field with as little chemistry as possible, i.e. no elementary-step reaction mechanisms and only the most relevant reactions are considered. This approach is reasonable for systems in which chemistry can be neglected or plays only a minor role. In this work, this approach is chosen for the region upstream of the catalyst and is combined with a 2D approach with detailed chemistry in the channels of the monolith. The influx region upstream of the catalyst ($L = 5$ mm) and the entire monolith are included in these simulations (see Section 4.1.4 for results). Computing times corresponding of 24 h real time are necessary to complete one

simulation. A discussion of this method can be found in Section 2.4.2.4 and a detailed description of the performed simulations is given in Section 3.5.5.

2.4.2.3 Two-Dimensional Simulations with Detailed Chemistry

The DETCHEM^{CHANNEL} code [139] is chosen here as an example for numerical modeling employing a 2D flow field and detailed chemistry. This code was also applied for numerical simulations in this thesis (Sections 3.5.2 and 4.1.2).

For the simulations, detailed gas-phase as well as surface-reaction mechanisms are applicable. The channel of the catalyst is approximated by a cylindrical geometry. This is reasonable due to the washcoat layer, which is thicker in the corners of the channel. The assumption of a cylindrical channel leads to a two-dimensional flow, for which axial and radial positions are independent variables [137]. To further simplify the flow field, the boundary-layer approximation is applied. In this approach, the axial flow caused by diffusion is assumed to be negligible compared to the convective flow [140, 141]. The assumption is valid for high fluid velocity or small channel diameters.

To account for the washcoat layer, two different models are available in the DETCHEMTM software package [139]. One is a time-consuming, detailed washcoat model, in which the solution of the reaction-diffusion equations for all species in the washcoat is included [141]. The second model is the effectiveness-factor model. The factor is based on the Thiele module which considers washcoat thickness, concentration of the species at the boundary between fluid and washcoat, an effective diffusion coefficient, and the ratio of catalytic to geometric surface area [137]. In the model, the effectiveness factor is calculated for the limiting species, which determines overall reactivity [137]. The factor is then applied to all chemical species, which leads to very fast calculations.

2. Fundamentals

2.4.2.4 Coupling of 2D and 3D

The aim of modeling the entire monolith is to understand the behavior of the entire monolith. This behavior is influenced by the flow upstream of the catalyst, by the heat transfer between the flow inside the channels and the solid structure, and by heat transfer between the monolith and the surroundings. The investigation and development of reformer systems using solely a common CFD code is not practical. Direct coupling of chemistry at a detailed level greatly exceeds the capability of CFD models. Common CFD models can treat geometric complexity but not in combination with complex chemistry, this is not possible in reasonable calculation times.

To overcome this problem, the software tool DUO was used in Section 4.1.4. DUO stands for the coupling of the two computer codes DETCHEMTM and OpenFOAM [142]. Using DUO, the flow upstream of the monolith is calculated with the CFD code OpenFOAM, which essentially handles arbitrary geometry. In addition to the outer fluid flow, the code also solves the conjugated heat transfer in the solid structure of the monolith. This implies the handling of the heat transfer between the solid and fluid regions as well as the exchange of heat with the external environment. In the flow regions upstream of the catalyst, the chemistry can be fully neglected. The flow inside the channels is calculated with DETCHEM^{CHANNEL} by applying detailed gas-phase and surface chemistry. As the flow is handled as a two-dimensional flow, only a simple grid is used. This makes the calculation fast and makes it possible to simulate the entire monolith.

Chapter 3

Methods and Materials

During the work presented herein, an experimental setup was designed, constructed and successfully used for ex-situ as well as in-situ studies of reforming reactions. The special feature of this setup is an in-situ technique, which allows for a much more detailed investigation of reactions in monolithic catalysts than with ex-situ methods.

Beside the newly built setup, an already existing setup (described in [24]) was used for ex-situ measurements. This setup was also one of the two setups on which the design of the new setup was based. Additionally, in-situ measurements were performed on a setup at Politecnico di Milano during a stay as a guest scientist.

To gain a deeper understanding of the experimentally obtained values, different simulation tools were employed as described below. CFD simulations as well as 2D-simulations and thermodynamic equilibrium calculations were carried out.

3. Methods and Materials

3.1 Lab-Scale Reactor¹

The experimental setup shown in Figure 3.1 was designed and built within this thesis. In this work, the experimental setup is referred to as “CPOX 3”.



Figure 3.1: Picture of the fully assembled reactor setup CPOX 3.

¹Parts of this section have been taken from [16, 102, 129]. Reprinted (adapted) from Applied Catalysis A: General, 467, D. Livio, C. Diehm, A. Donazzi, A. Beretta and O. Deutschmann, Catalytic partial oxidation of ethanol over Rh/Al₂O₃: Spatially resolved temperature and concentration profiles, 530 - 541, Copyright (2013), with permission from Elsevier. Reprinted (adapted) from Catalysis Today, 216, M. Hettel, C. Diehm, B. Torkashvand and O. Deutschmann, Critical evaluation of in situ probe techniques for catalytic honeycomb monoliths, 2 - 10, Copyright (2013), with permission from Elsevier. Reprinted (adapted) from Catalysis Today, 197, C. Diehm, T. Kaltschmitt and O. Deutschmann, Hydrogen production by partial oxidation of ethanol/gasoline blends over Rh/Al₂O₃, 90-100, Copyright (2012), with permission from Elsevier.

The design of CPOX 3 was based on the already existing experimental setups [24, 143] (“CPOX 1” and “CPOX 2”) so it would be possible to compare the measurements performed with the different setups. The unique feature of the new setup is the spatially resolved sampling technique (see Section 3.2), with which axial concentration and temperature profiles can be detected inside a monolithic channel.

3.1.1 Dosing System

The flow diagram of the experimental setup CPOX 3 is shown in Figure 3.2. For the feeding of the gaseous components, mass flow controllers (MFC, Bronkhorst) are used. Up to 10 gaseous components (5 shown in the flow diagram) can be fed simultaneously to the reactor.

It is possible to feed two different streams of pre-evaporated components. One is dosed (named “Fuel” in Figure 3.2) from a tank under He-pressure with a Cori-Flow (Bronkhorst), a controlled evaporation mixer (CEM, Bronkhorst) and an inert N₂ flow. As fuel, liquid hydrocarbons, e.g. iso-octane, oxygenates, e.g. ethanol, and two-component mixtures of liquid species, can be employed. The pre-evaporated fuel is fed to the reactor inlet through different lines than the gaseous reactants (inlet marked with “Fuel” in Figure 3.3). More details about the delivery system of liquid hydrocarbons can be found elsewhere [16, 20].

Water is the second pre-evaporated component, which is dosed from a second tank under He-pressure with a Liqui-Flow (Bronkhorst), a pre-evaporator (University of Stuttgart) and an inert N₂ flow. Water is fed to the reactor inlet together with the gaseous components (inlet marked with “Syn. Air” in Figure 3.3).

The reactor inlet shown in Figure 3.3 was designed for CPOX 3. The inlet system with the opposing feed lines and the dosing of the pre-evaporated fuel into the stream of synthetic air leads to a quick mixing of the components.

3. Methods and Materials

This was also confirmed by CFD simulations performed by Matthias Hettel. As fuel, a pre-evaporated liquid fuel in N₂, such as ethanol, can be supplied. If a gaseous reactant, such as methane is fed, it will be fed through the “Syn. Air” inlet together with the other gaseous components.

The purities for the chemicals used in the different studies performed during this work are shown in Table 3.1.

Chemical	Purity
Methane	2.5
Ethanol	99.9 %
Propane	97.8 %
2,2,4-trimethylpentane	99 %
Oxygen	3.5
Argon	4.6
Nitrogen	5.0
CO	3.7
CO ₂	4.5
Hydrogen	5.0
Water	Conductivity < 20 μ S cm ⁻¹

Table 3.1: Purities of the chemicals utilized. Purities of gases given as industrial code: first digit stands for number of “nines”, second digit for the first digit deviating from nine, e.g. 2.5 ≡ 99.5 %. The purity of water is given as conductivity.

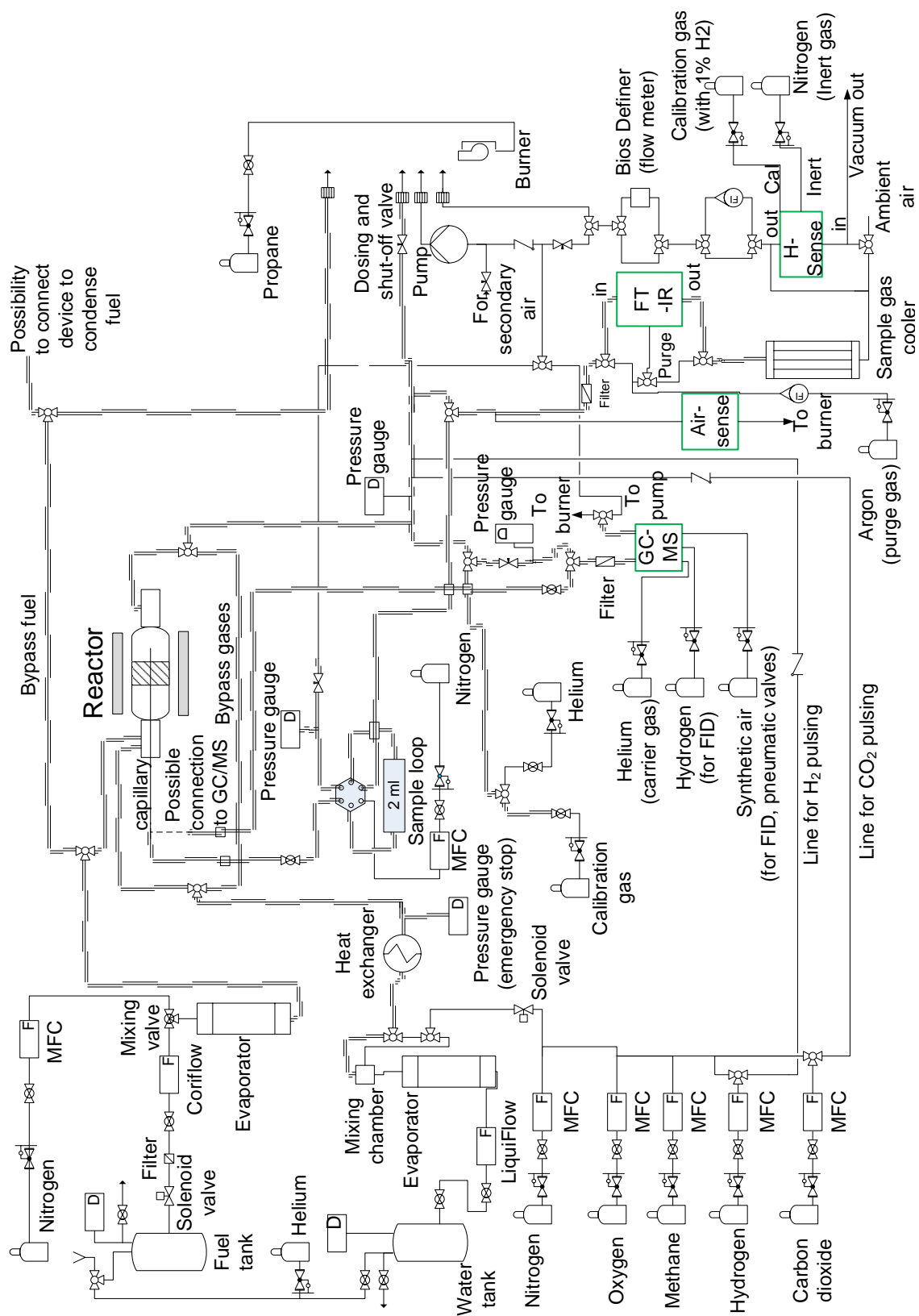


Figure 3.2: Flow diagram of the experimental setup; analytical instruments are highlighted with a green frame.

3. Methods and Materials

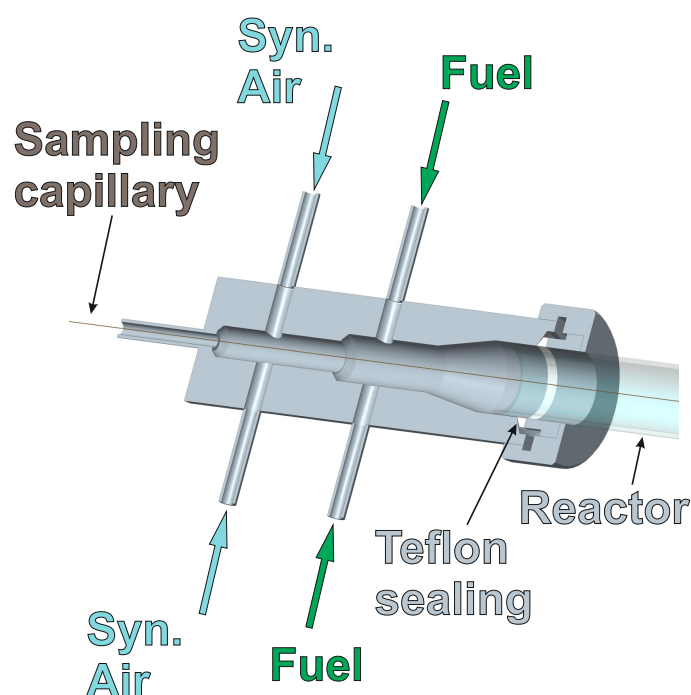


Figure 3.3: Cross section of the reactor inlet designed for CPOX 3; shown with capillary (without connection between capillary and inlet). As fuel, a pre-evaporated liquid fuel in N_2 , such as ethanol, can be supplied. If a gaseous reactant, such as methane is fed, it will be fed through the “syn. Air” inlet together with the other gaseous components.

3.1.2 Reactor and Catalysts

Partial oxidation experiments were performed in a lab-scale reformer consisting of a quartz tube (length = 62 cm, inner diameter (I.D.) = 20 mm) placed in an oven for thermal insulation and reaction light-off.

The monolithic honeycomb catalyst (diameter = 19 mm, variable length) is placed 230 mm downstream of the reactor inlet. For increased insulation, the part of the reactor tube, in which the catalyst is positioned, is wrapped with a 1 cm thick layer of quartz wool. Uncoated monoliths up- and downstream of the catalyst are employed as heat shields (front heat shield (FHS) and back heat shield (BHS), respectively). The FHS also serves as support for the probe applied in the sampling technique (Section 3.2). To prevent a gas by-pass between

monoliths and quartz tube, the heat shields and the catalyst are wrapped with a ~ 1 mm thick layer of ceramic fiber paper.

For the investigations, different catalysts were used. All of them were supported on a honeycomb monolith made of cordierite. In the following sections, the catalysts will be named by labels. Table 3.2 lists all the different catalysts with label and specifications. In the calculation of the catalyst loading, the cylindrical volume of the catalyst, calculated from the diameter and the length of the entire monolith, is used.

3.1.3 Analytical Methods

The total gas flow from the reactor outlet is monitored on-line by an FTIR analyzer (MKS Multigas 2030) and an EI-MS (V&F, H-sense). The FTIR is operated at a cell temperature of 463 K. The IMR-MS (V&F, Airsense) displayed in Figure 3.2 was only used in the sampling system, as complete oxygen conversion is expected at the reactor outlet. A sample gas cooler is installed between FTIR and EI-MS to protect the EI-MS from excessive amounts of water in the gas composition. The sample gas cooler is set to 278 K to remove water and other species, e.g. unconverted hydrocarbons, which condense at these conditions. The total gas flow is fully oxidized in the flame of a bunsen burner after it left the analytics.

3.1.3.1 Fourier-Transform Infrared Spectroscopy

In infrared spectroscopy, IR-active components are excited by IR-light at wave numbers in the range of 400 to 4000 cm^{-1} , leading to a change in the vibrational and rotational state of the compound. IR-active components are molecules with a permanent (e.g. H_2O) or induced dipole moment (e.g. CO_2) which changes during the excitation of the vibrational state. A change in vibrational state is

3. Methods and Materials

Label (gen. M _{psi})	Catalytically active material	Catalyst loading [mg cm ⁻³]	Cell density [cpsi]	Channel wall thick- ness [μm]	Washcoat	BET surface area [m ² g ⁻¹]	Washcoat thickness [μm]	Hydraulic diameter (open channel) [μm]	Manufac- turer
Rh ₄₀₀	Rh	1.38	400	170	α-Al ₂ O ₃	10	18	1064	Prepared at Politecnico di Milano
Rh ₆₀₀	Rh	4.23	600	80	γ-Al ₂ O ₃	28	40	880	Delphi Inc.
Rh ₉₀₀	Rh	1.48	900	60	γ-Al ₂ O ₃	52	10	770	Umicore AG & Co. KG
Pd ₆₀₀	Pd	1.06	600	100	γ-Al ₂ O ₃	28	30	880	Umicore AG & Co. KG

Table 3.2: Details for the catalysts used in the investigations shown in this work. The labels are used in the rest of the text to refer to the respective catalysts.

always accompanied by a change in rotational state and only certain transitions are possible due to the selection rules of quantum mechanics [136]. The transition energy between one vibrational-rotational state and another is always a discrete energy according to quantum mechanics. Thus, the excitation of the molecule is only possible for characteristic, discrete energies of the light, i.e. characteristic wave lengths.

In a Fourier-transform infrared spectroscopy (FTIR) analyzer, a light source containing the full range of frequencies necessary for the measurement, i.e. a black-body source, is used [144]. The infrared light is shone on a Michelson interferometer, which is shown in Figure 3.4. The interferometer consist of a beam splitter and two mirrors. The beam hits the beam splitter, which divides the beam into two beams. One beam hits a fixed mirror, the other one hits a movable mirror. The beam is recombined again, leading to an interference of the waves, and sent through the sample at the detector. Different positions of the movable mirror lead to different interferences [145]. An interferogram is formed, which shows the intensity of the beam as a function of the mirror position. With this layout, all frequencies can be measured at the same time, which leads to very fast measurements in the range of seconds. The Fourier transform is used to obtain a spectrum of absorption from the raw data as a function of the wavelength. The He-Ne-Laser, which is shown in Figure 3.4, emits a single wavelength beam and is employed to calculate the exact position of the movable mirror from the monochromatic interference [144, 145]. The FTIR used in this work is a MKS Multigas 2030.

3.1.3.2 Mass Spectrometry

Two different sets of mass spectrometers are used for the gas analysis. One electron pulse ionization mass spectrometer (EI-MS, H-Sense) for measuring the hydrogen concentration and one ion-molecule reaction mass spectrometer (IMR-MS, Airsense) for oxygen analysis.

3. Methods and Materials

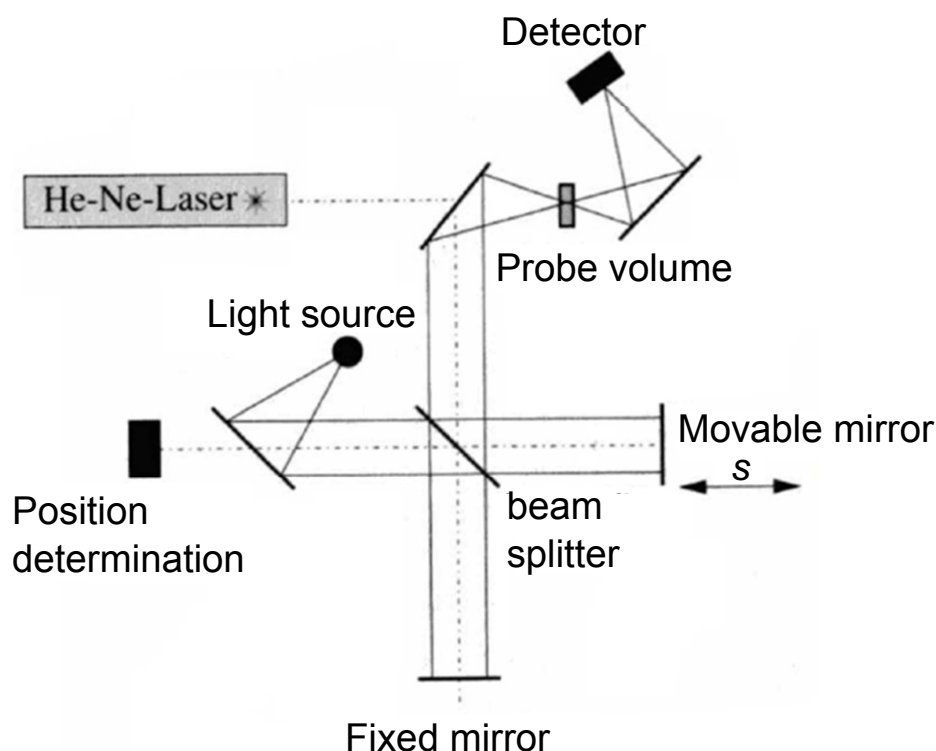


Figure 3.4: Scheme of Michelson interferometer (adapted from [146]).

In mass spectrometry, the molecules in a gas sample are ionized and the ratio of mass to charge of the ions is measured. Different ionization methods exist. From the mass-to-charge ratio, the present molecules in the gas sample can be determined [144]. In the EI-MS, the ions necessary for the measuring method are formed by electron ionization. In the ion source, electrons are produced by electrically heating a wire filament. The electrons are accelerated to 70 eV and focused into a beam by the attraction to the trap electrode. The gas sample, which is to be analyzed, is inserted perpendicular to the electron beam, and when a molecule is hit by an electron, a molecule-ion is formed [144, 145]. The formed ions are focused and enter a magnetic sector (see Figure 3.5), which leads to separation of the different ions due to different trajectories of the ions in the sector field. In the H-sense, the magnetic sector field is constructed to let only hydrogen and helium reach the detector. The quantification is possible by correlating the intensity of the detector signal with the concentration of the considered species.

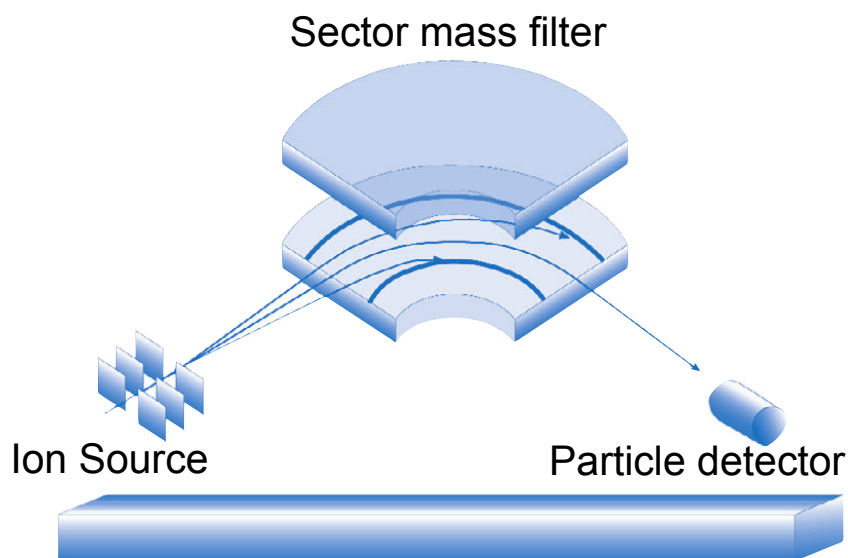


Figure 3.5: Scheme of sector field mass spectrometer, adapted from [147].

In the IMR-MS (see Figure 3.6 for setup scheme), the gas molecules, which are supposed to be analyzed, are ionized by collision with primary ions with low energies (10 to 14 eV). The primary ions are chosen depending on the molecule that is supposed to be analyzed [144]. For oxygen, Xe is used. The Xe atoms are ionized in an ion source and the Xe ions are focused into a beam by the octopole separation device. The gas sample is fed perpendicular to the ion beam. A reaction between primary ions and the molecules in the sample leads to ionization of the molecules. A quadrupole mass filter leads to separation of the different ions, which are then detected. The quantification is also possible by using the intensity of the detector signal.

3. Methods and Materials

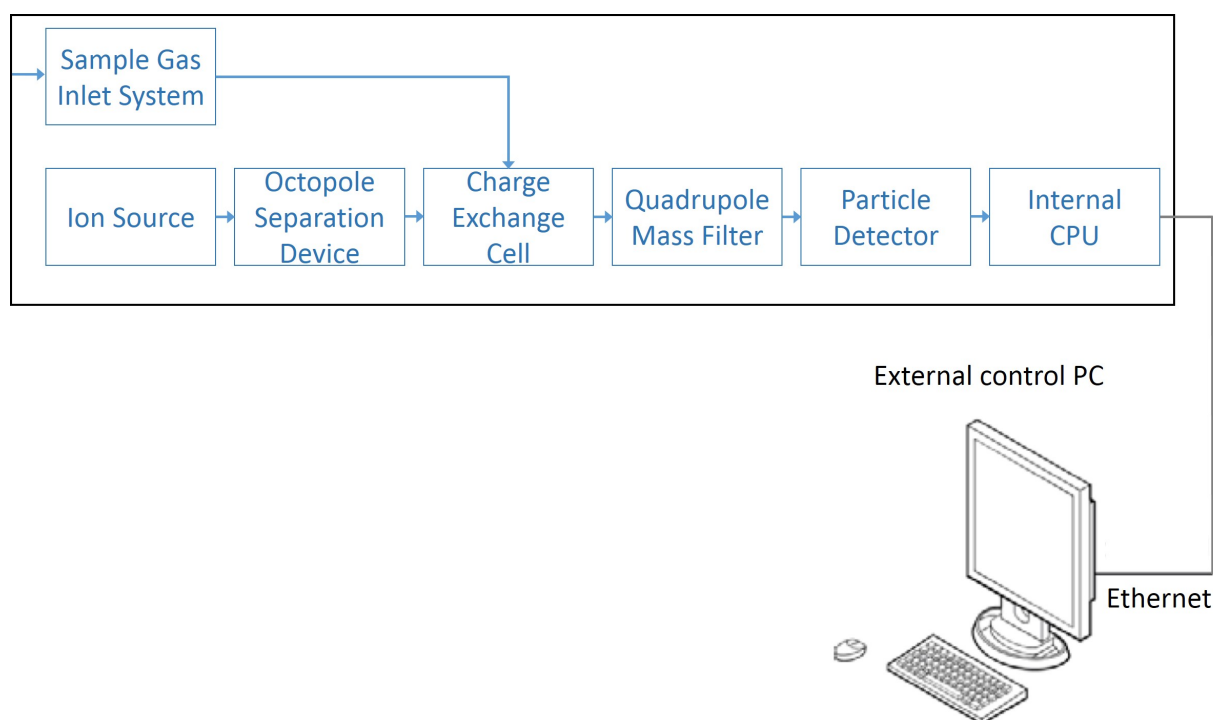


Figure 3.6: Scheme of setup of IMR-MS, adapted from [148].

3.1.3.3 Gas Chromatography

Gas chromatography (GC) can be used to separate and analyze different components of a gas mixture. In this method, a mobile phase, which consists of a carrier gas and the gas sample, and a stationary phase, which is a liquid or polymer film, exist. As carrier gas, inert gases such as He or N₂ are used. The mobile phase flows through a column which is coated with the stationary phase. The molecules from the gas sample interact differently with the stationary phase, depending on their chemical and physical properties. For each compound, it takes a characteristic time, the retention time, to elute from the column. The retention time can be used to identify the components under constant method conditions. The molecules are detected after they leave the column [144]. Different types of detectors are available, the most common of which are FID (Flame Ionization Detector) and TCD (Thermal Conductivity Detector). An FID is based on the ionization of an organic compound in a hydrogen flame. The flame is set be-

tween two electrodes and the ions formed in the flame hit the electrode above the flame, inducing a current which is measured [144]. The number of carbon atoms in the compound determines the response of the detector. The FID is highly sensitive to hydrocarbon species and has a high range of detection of 10^7 orders of magnitude. A TCD is mostly used to detect permanent gases and CO_2 . The TCD is based on the measurement of the thermal conductivity of the eluate from the column in comparison to a reference gas flow [144]. Every substance with a thermal conductivity different than the reference gas can be detected. In this work, beside the use of FID and TCD, a combination of GC and mass spectrometry (GC-MS) was used. Here, the eluate from the column is sent to an MS which is used to detect the separated components (see Section 3.1.3.2 for basics of mass spectrometry).

A chromatograph is gained, which is a diagram of the detector response as a function of the retention time with the differently eluted components visible as peaks. Quantification is possible as the peak area is correlated to the amount of component in the gas sample. A calibration is necessary to determine the calibration curve for a compound under the given method conditions and to calculate the concentration in the gas sample.

The GC-MS (6890N, Agilent) used for the investigations of the commercial fuel (see Section 3.3.4) consisted of a three-column arrangement including a DB-5ms, a HP-Plot/Q and a HP Molesieve 5A (part of CPOX 1 as described in [149]). As detectors, a FID, TCD and a mass spectrometer were used. The mass spectrometer was connected downstream of the TCD.

The micro-GC used in this work for propane CPOX at higher pressures (see Section 3.3.5) contained two different columns to make the separation of H_2 , N_2 , CH_4 , CO on one column (Molecular sieve column) and hydrocarbon species on another column (Plot-Q-Column) possible. Both columns are connected to a TCD detector.

3. Methods and Materials

3.1.3.4 Determination of Total Gas Flow

To quantify the total gas flow that reaches the FTIR, an adapted external standard method is used. As this method is already extensively explained in [24, 143, 149], only a short explanation shall be provided here. It is necessary to determine the total gas flow, as a volume increase occurs in the CPOX reformer due to the break down of fuel molecules, e.g. C_2H_5OH , into a higher number of smaller molecules, e.g. H_2 and CO . As the volume concentration of the detected species shall be converted to a molar flow rate, the total volume flux \dot{V}_{total} is needed:

$$\dot{n}_i = \dot{V}_{total} \cdot c_i \quad (3.1)$$

\dot{n}_i : molar flow rate of species i

\dot{V}_{total} : total volume flux

c_i : concentration of species i

The following procedure is applied: after steady state is reached in the reformer, a known amount of carbon dioxide (250 ml min^{-1}) is added to the total gas flow downstream of the reactor for short periods of time. This leads to “steps” in the concentration-over-time diagram for CO_2 . From the change in CO_2 concentration measured in the FTIR, the total gas flow can be calculated.

3.1.3.5 Calculation of Conversion and Yield

The determined molar flow rate of the species i is used to calculate the yield Y_i . The yields Y_i^H and Y_i^C are calculated based on H and C atoms in the species i , respectively, as shown in Equations (3.2) and (3.3). For the reactant r , the conversion X_r is calculated using Equation (3.4).

$$Y_i^{\text{H}} = \frac{\nu_i^{\text{H}} \dot{n}_i}{\nu_r^{\text{H}} \dot{n}_{r,0}} \quad (3.2)$$

$$Y_i^{\text{C}} = \frac{\nu_i^{\text{C}} \dot{n}_i}{\nu_r^{\text{C}} \dot{n}_{r,0}} \quad (3.3)$$

Y_i^{H} : yield of species i based on H atoms

Y_i^{C} : yield of species i based on C atoms

ν_x^{H} : number of H atoms present in component x

ν_x^{C} : number of C atoms present in component x

$\dot{n}_{r,0}$: molar flow rate of reactant r at time $t = 0$

$$X_r = \frac{\dot{n}_{r,0} - \dot{n}_r}{\dot{n}_{r,0}} \quad (3.4)$$

X_r : Conversion of reactant r

$\dot{n}_{r,0}$: molar flow rate of reactant r at time $t = 0$

\dot{n}_r : molar flow rate of reactant r at time t

3.2 In-Situ Sampling Technique²

The experimental setup CPOX 3 includes the in-situ sampling technique, which represents a unique feature of CPOX 3 compared to CPOX 1 and 2. The sampling system was set up during this work together with Dario Livio, a visiting PhD student from Politecnico di Milano. In Figure 3.7 (a), a close-up of the reactor with the capillary for temperature profiles is displayed. The FHS, the

²Parts of this section have been taken from [102]. Reprinted (adapted) from Applied Catalysis A: General, 467, D. Livio, C. Diehm, A. Donazzi, A. Beretta and O. Deutschmann, Catalytic partial oxidation of ethanol over Rh/Al₂O₃: Spatially resolved temperature and concentration profiles, 530 - 541, Copyright (2013), with permission from Elsevier.

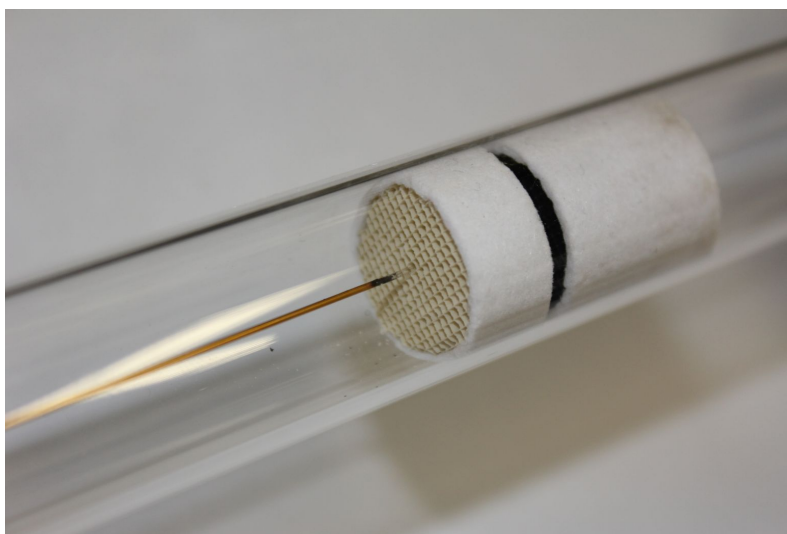
3. Methods and Materials

capillary inserted into one channel and the ceramic fiber paper covering FHS, catalyst, and BHS are visible. The setup can be used for in-situ measurements, where axial temperature and concentration profiles can be detected from one channel of the monolithic catalyst. Figure 3.7 (b) shows the microvolume tee mounted onto the motorized linear stage used for moving the capillary.

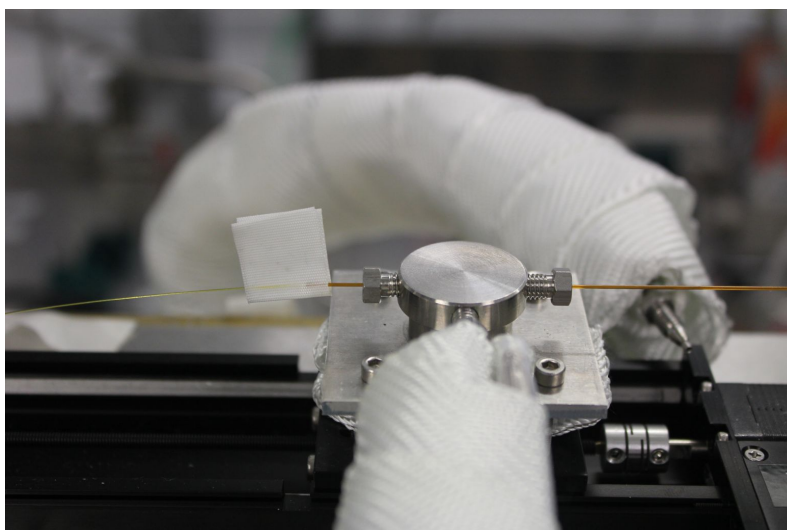
The setup used to collect axial profiles of temperature and composition in CPOX reactors is similar to the one introduced for foam monoliths by Horn et al. [12, 119] and then adapted to honeycomb monoliths by Donazzi et al. [33, 71]. The additional feature of the sampling system of CPOX 3 is the ability to maintain spatial concentration and temperature profiles in channels differently positioned across the monolith, e.g. a channel close to the periphery of the monolith.

The cross section of the reactor setup used for the sampling technique is shown in Figure 3.8 for sampling from a central channel. The catalytic monolith (~ 19 mm in diameter, variable length, cell density ≥ 600 cpsi corresponding to a hydraulic diameter $d_h \geq 880 \mu\text{m}$) is placed between two uncoated cordierite honeycomb monoliths (same diameter and cell density as the catalytic module, $L = 10$ mm) to minimize axial heat losses. A void space of ~ 5 mm is kept between the front inert monolith and the catalyst to avoid flow disturbance at the catalyst entrance due to partial occlusion of the channels by misalignment of the front heat shield.

The temperature probes consist of a thin K-type thermocouple (Omega Engineering Inc., diameter = $250 \mu\text{m}$) and a VIS-IR optical fiber (Leoni, core diameter = $200 \mu\text{m}$, clad diameter = $220 \mu\text{m}$, outer diameter (O.D.) = $245 \mu\text{m}$) connected to an infrared narrow band pyrometer (LumaSense Technologies GmbH, IGA LO-50 plus). The IR detector is an InGaAs photodiode with a spectral range of $1.45\text{-}1.8 \mu\text{m}$. With this spectral range, temperatures between 623.15 K and 2073.15 K can be detected. As previously shown for a similar setup [33], the tip of the optical fiber is industrially polished at an angle of $\sim 45^\circ$ in order



(a) Reactor with capillary for T profile



(b) Microvolume tee with capillary for T profile

Figure 3.7: Picture of (a) the reactor with capillary for temperature profiles and (b) the microvolume tee, with the connected capillary, mounted onto the miniature motorized linear stage (black part below). The thin yellow fiber coming out of the back of the capillary is the VIS-IR optical fiber.

to guarantee the local measurement of the temperature. The connector of the optical fiber to the pyrometer is equipped with an anti-twist protection to avoid measurement bias due to fiber misalignment. Previous works [30, 33] reported

3. Methods and Materials

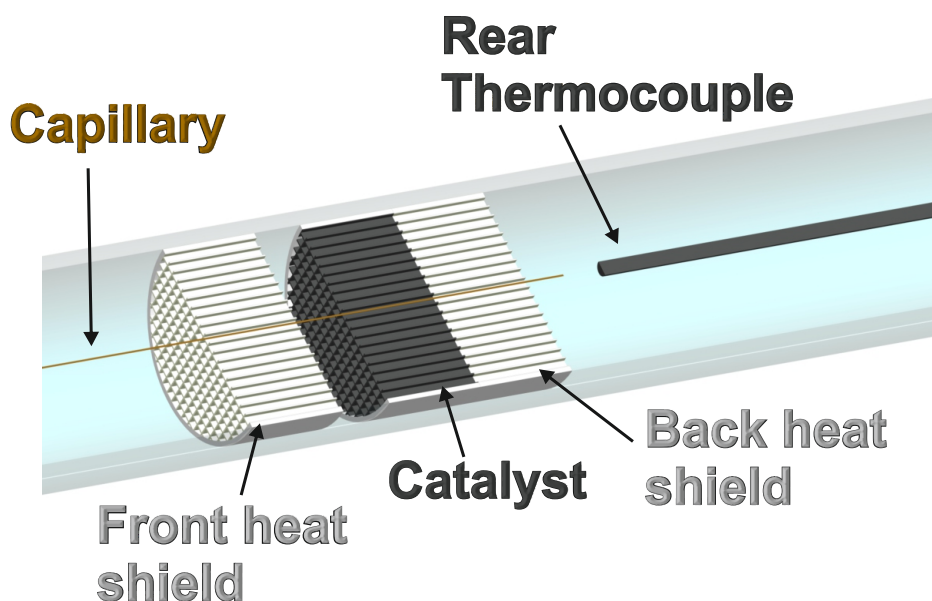


Figure 3.8: Cross section of reactor with front heat shield, catalyst, back heat shield, sampling probe, and rear thermocouple.

that the temperature measured by thermocouple and the optical fiber were representing the temperature of the gas phase and the surface, respectively. Both temperature probes are inserted into a deactivated, fused silica capillary (I.D. = $570\ \mu\text{m}$, O.D. = $630\ \mu\text{m}$), which serves as a protection sheath. The distal end of the capillary is sealed by melting the capillary to isolate the temperature probe from the reacting system, while the proximal end is connected to a microvolume tee (see Figure 3.7 (b)) and is moved with a constant velocity of $0.009\ \text{cm s}^{-1}$ along the monolith channels (channel diameter = $876\ \mu\text{m}$) through a miniature motorized linear stage (Zaber Technologies, T-LSM100A) with very high spatial resolution. As a sealing between reactor inlet, which ends in a 1/16 inch connection, and capillary, a graphite ferrule is used inside the stainless steel nut. The tightening of the sealing system with ferrule and nut is limited as the capillary still needs to be movable. Small leakages at this point of the reactor are possible. For the temperature profiles, the measurements can be performed during both, pulling the capillary out of the reactor and pushing it back in. There is no visible difference in the arising profiles.

During the temperature profile measurements, the total gas flow from the reactor outlet is monitored on-line by the FTIR analyzer (MKS Multigas 2030) and the EI-MS (V&F, H-sense) (see Section 3.1.3). The flow diagram for the experimental setup is shown in Figure 3.2. With the data on the outlet composition, the performance of the catalyst over time is observed and the achieving of steady state is confirmed.

To measure the axial profile of the gas composition, an analogous sampling probe to the one used for the temperature profiles is applied. The dimension of the capillary (I.D. = 100 μm , O.D. = 170 μm) was chosen so that the disturbance of the probe on the flow field inside the channel (channel diameter = 880 μm) is as small as possible and the capillary is relatively simple to handle. The capillary is flexible and bends due to gravity. The radial position of the capillary inside the channel is not controllable, but the capillary will most likely be leaning on a channel wall. The gas is sampled from the capillary tip at a low sucking rate and is sent to the analytics section via a 6-port valve and a pump (see Figure 3.9).

For reliable results, a flow rate for the analytics of at least 1000 ml min^{-1} is required, whereas only around 2.0 ml min^{-1} are sucked from the channel of the catalyst. With the 6-port-valve, a constant flow of 1000 ml min^{-1} is achievable for the analytics even with a sucking flow rate of 2 ml min^{-1} from the channel. The two different configurations of the 6-port valve, “load” and “inject”, are shown in Figure 3.10 (a) and (b), respectively. In the load position, the sample is sucked from the capillary through a sample loop with a fixed volume of 2 ml to a pump and finally a burner. The analytic section is purged by 1000 ml min^{-1} N_2 . The pressure inside the sampling loop is measured by a pressure gauge. The pump is set to continuous mode; the sucking flow rate can be influenced via a secondary air metering valve. By partially closing the secondary air valve, the pressure in the sample loop decreases and a higher sucking flow rate from the reactor is achieved. During a measurement, the pressure is kept constant at ~ 610 mbar corresponding to a sucking flow rate of ~ 0.6 to 1.1 ml min^{-1} .

3. Methods and Materials

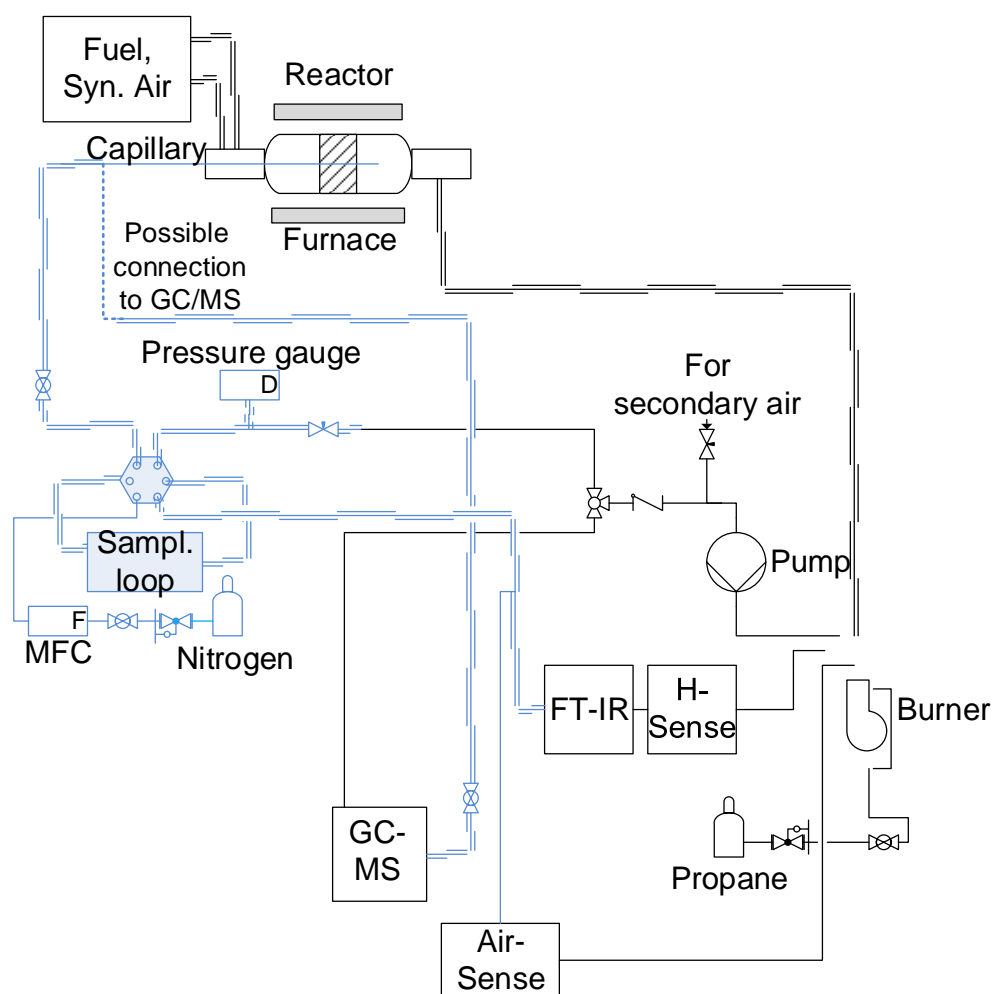


Figure 3.9: Simplified section of the flow diagram (Figure 3.2) showing the configuration used for concentration profiles. The sample gas cooler and the connection between in- and outlet of the H-sense is not used in this configuration to avoid fluctuations during the sampling for concentration profiles.

The sample loop and the 6-port valve are kept at a constant temperature of 363 K through the use of heating tapes (set to 393 K) and a heating block (set to 423 K), respectively. When switching to the inject position, the gas in the sample loop is injected into the analytics by the nitrogen flow. In the inject position, the sample flow from the reactor is directly connected to the pump and burner. When switching from inject to load position, 5 min of waiting are necessary before another sample can be injected to the analytics, as a complete

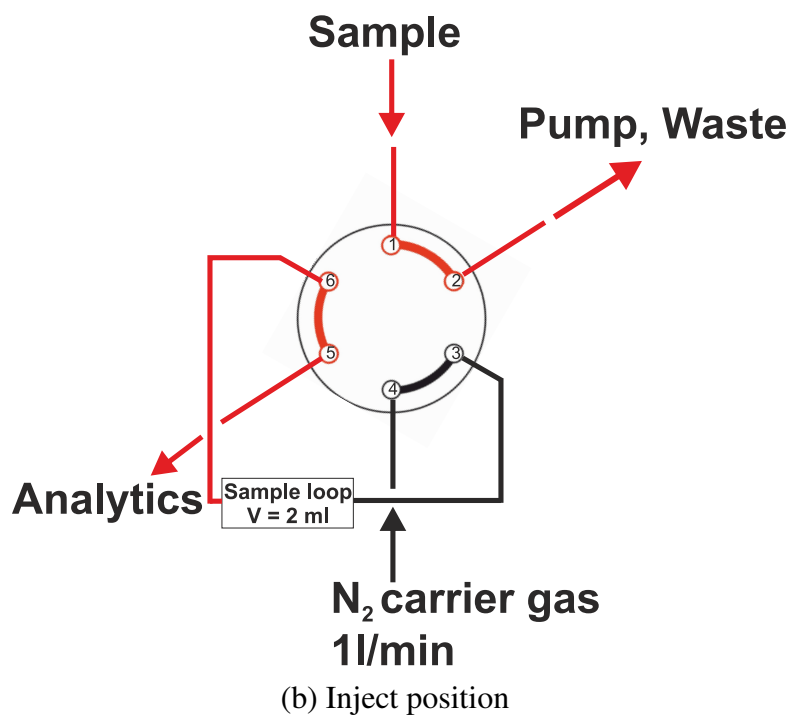
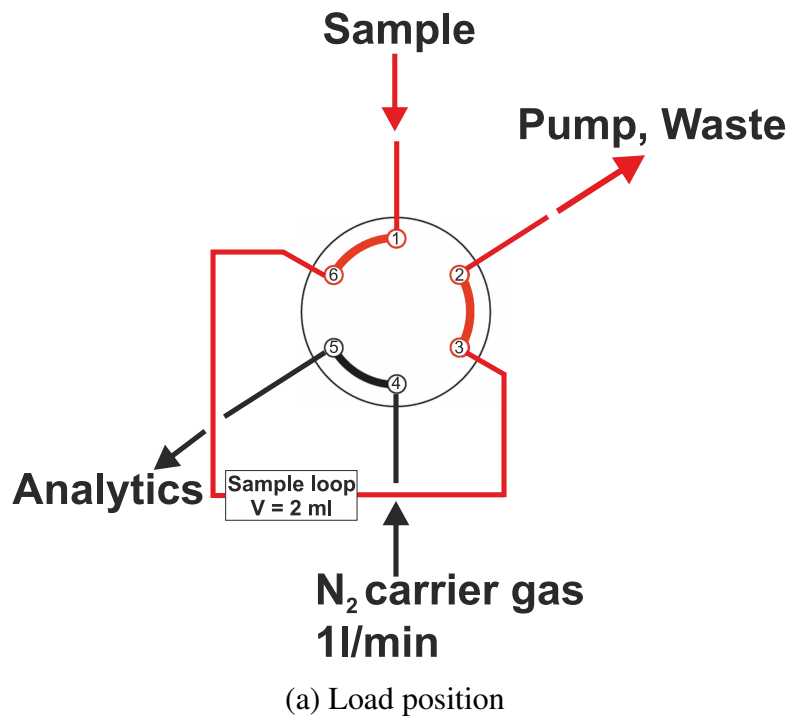


Figure 3.10: Scheme of the two different settings of the 6-port valve used for the sampling technique, load position (a) and inject position (b). Adapted from [150].

3. Methods and Materials

gas exchange in the line connecting the capillary and the sample loop and in the sample loop itself must be ensured. For the experiments, a sucking flow rate of $\sim 0.6 - 1.1 \text{ Nml min}^{-1}$ was chosen, so that the contact time inside the channel with the probe is very close to that inside a channel without a probe. Besides, it was considered to be a good compromise between the influence of a high sucking rate on the flow field and the occurrence of homogeneous reactions inside the capillary at a low sucking rate. For the same reason, the gas is drawn from the reactor inlet (cold side) counter-currently to the reacting flow. However, gas-phase reactions in the probe cannot be completely ruled out. The analytics section consists of the FTIR analyzer (MKS Multigas 2030), the IMR-MS (V&F, Airsense 500), and the EI-MS (V&F, H-sense) (see Section 3.1.3). The sample gas cooler, normally installed between FTIR and H-sense (see Figure 3.2), was not connected during the measurements of the concentration profiles as it causes fluctuations which interferes with the injected sample. The IMR-MS is used for the determination of the oxygen concentration in the concentration profile. The IMR-MS is not used for the total outlet measurements as described above. Also, another modification to the flow scheme shown in Figure 3.2 was necessary to guarantee proper functioning of the sampling system. There is no bridging connection between the inlet and outlet line of the H-sense.

The sampling system is capable of the simultaneous detection of a wide spectrum of gaseous species potentially produced in the CPOX of higher hydrocarbons. The lower detection limit of a species is between 50 and 100 ppm regarding the concentration in the sample loop, depending on the species. This limit is due to the dilution of the sample with $1 \text{ NL min}^{-1} \text{ N}_2$. At each axial position, three measurements were repeated and mass balances typically closed within 5 to 10 % error, depending on the investigated system. The different axial positions of the capillary tip are controlled by the miniature motorized linear stage (Zaber Technologies, T-LSM100A). An axial resolution of 0.25 mm could be achieved. As a sealing between capillary and reactor inlet, a graphite ferrule is used, which is similar to the one for the temperature profiles but was fitted

to the smaller diameter of the sampling capillary. Also here, a small leakage at the connection between reactor inlet and capillary is possible. The capillary that is used for the measurement of the concentration profiles is very thin (O.D. = 170 μm) and bends easily. For this reason, this capillary can only be pulled out of the reactor.

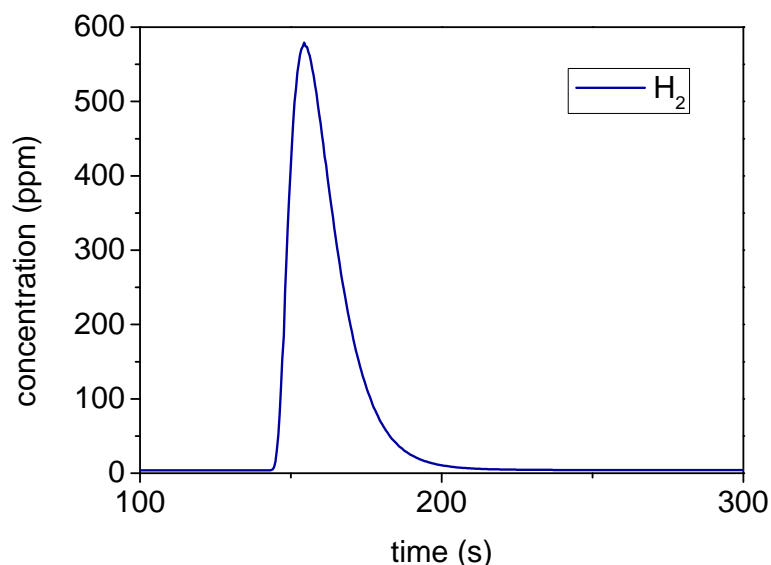


Figure 3.11: Peak for hydrogen from injecting sample from sample loop into the analytics section.

With the in-situ sampling technique, the gas is injected into the analytics section. This leads to peaks for the species in the analytical instruments (see Figure 3.11 for an example). From the peak area, the mole fraction of the species can be calculated after an appropriate calibration. The calibration is performed by feeding a gas mixture with known amounts of the particular reactants (e.g. in the case of CH_4 -CPOX methane and oxygen) and expected products (e.g. H_2 , CO , CO_2 , and H_2O) to the reactor using the MFC (Bronkhorst) and the pre-evaporation system for H_2O . The reactor contains an uncoated monolith and a sampling capillary in one of the channels of the monolith (channel position not relevant in the calibration). The sample loop and all the lines are heated as they would be during the experiments. The furnace is heated to 523 K to prevent condensation of components and to supply already preheated gas for

3. Methods and Materials

the suction of the gas sample into the sample loop. The pressure in the sample loop is changed stepwise from ~ 650 mbar to 60 mbar. At each pressure, three samples are injected into the analytics, with 5 min in between the injections for purging the sample loop. When changing the pressure, a waiting period of 10 min is applied to make sure that the gas in the lines leading to the sample loop is exchanged several times. The stepwise decrease in pressure results in lower peak areas as smaller amounts of substance are being injected into the analytics. The total amount of substance can be calculated using the ideal gas law with the given values:

$$n_{\text{total}} = \frac{p_{\text{loop}} \cdot V_{\text{loop}}}{R \cdot T_{\text{loop}}} \quad (3.5)$$

n_{total} : total amount of substance in the sample loop

p_{loop} : pressure measured in the sample loop, varied in calibration

V_{loop} : volume of sample loop, fixed value of 2 ml

R : ideal gas constant

T_{loop} : temperature of the sample loop

The amount of substance can be calculated using Equation (3.5) and the known mole fraction of the species in the gas mixture:

$$n_i = n_{\text{total}} \cdot x_i \quad (3.6)$$

n_i : amount of substance for species i

x_i : mole fraction of species i

From a graph with the peak area as a function of n_i , a linear calibration curve (Equation (3.7)) is obtained. With this calibration curve, the peak

areas obtained in the experiments can be related to the amount of substance for species i by simply solving Equation (3.7) for n_i and using peak area $_{i,exp}$, which is obtained from integrating the experimentally measured peak.

$$\text{peak area}_i = a \cdot n_i \quad (3.7)$$

peak area $_i$: Peak area for species i

a : slope

The mole fraction of species i at the measured point can be calculated by solving Equation (3.6) for x_i and inserting Equation (3.5) for n_{total} using the values from the experiments, i.e. $T_{\text{loop, exp}}, p_{\text{loop, exp}}$.

3.3 Investigated Systems

During this work, different fuels were investigated for the production of hydrogen for fuel cells by catalytic partial oxidation. An overview of all investigated systems is given in Table 3.3. The details of the experiments for each system are given in the subsections below.

Fuel	Setup
Methane	CPOX 3
Ethanol	CPOX 3
Propane	Politecnico di Milano
Commercial fuels	CPOX 1

Table 3.3: Investigated systems with setups on which the studies have been performed.

3. Methods and Materials

3.3.1 General Measuring Conditions³

Typically, the experiments were performed at 4 SLPM (standard liters per minute, standard refers to standard conditions, $T = 298$ K and $p = 1.013$ bar), yielding a GHSV (Gas Hourly Space Velocity) of $120\,000\text{ h}^{-1}$ (referred to open volume of the catalyst, calculated for standard conditions, $T = 298$ K and $p = 1.013$ bar) for a typical catalyst (diameter = 19 mm, length = 11 mm, 600 channels per square inch (cps)) used in this work. Very short residence times τ in the range of $\tau \approx 10$ ms (at $T \approx 800$ K) were reached in a channel of the catalyst. All experiments were carried out at 80 % N_2 dilution. Such a N_2 dilution is required for safety reasons in order to avoid the operation within the flammability region of the reacting mixture. The gases were preheated to 463 K. For light-off, the furnace was heated to 523 K and a diluted mixture of H_2 and O_2 was fed until a temperature of 563 K was measured downstream of the back heat shield. After this temperature was reached, the inlet composition was switched to fuel and O_2 in nitrogen. The furnace was kept at 523 K to maintain a steady temperature around the reactor tube, leading to quasi-autothermal operation.

The measuring conditions are defined by the C/O ratio, which is the ratio of the total number of carbon atoms and the total number of oxygen atoms in the reactant feed. In Equation (3.8), the definition of the C/O ratio for a fuel molecule $\text{C}_x\text{H}_y\text{O}_z$ is given. A C/O ratio of 1.0 corresponds to the stoichiometry of partial oxidation (syngas formation) and a C/O ratio of 0.5 to the stoichiometry of total oxidation. Conditions with $\text{C/O} < 1.0$ are called fuel-lean, the ones with $\text{C/O} > 1.0$ fuel-rich. Since the experiments were performed at a constant N_2 molar fraction in the inlet mixture, an increase of the C/O ratio results in an increase of ethanol and a decrease of molecular oxygen in the feed stream.

³Parts of this section have been taken from [102]. Reprinted (adapted) from Applied Catalysis A: General, 467, D. Livio, C. Diehm, A. Donazzi, A. Beretta and O. Deutschmann, Catalytic partial oxidation of ethanol over Rh/Al₂O₃: Spatially resolved temperature and concentration profiles, 530 - 541, Copyright (2013), with permission from Elsevier.

$$\frac{C}{O} = \frac{x \cdot n(C_x H_y O_z)}{z \cdot n(C_x H_y O_z) + 2 \cdot n(O_2)} \quad (3.8)$$

3.3.2 Methane⁴

The catalytic partial oxidation of methane was investigated under the conditions shown in Table 3.4. Methane was chosen as a fuel for several reasons. As the main component of natural gas, it is a very widely available compound and likely to be applied in decentralized CPOX reformers. Additionally, the CPOX of methane has been studied numerically for over 15 years, yielding sophisticated mechanisms, e.g. [10, 130]. Thus, the experimental results can be compared to simulations, allowing us to gain a deeper understanding, to evaluate the used in-situ technique (see Section 3.5.4), and to look at the global effects in a complete monolith (see Section 3.5.5).

Experiment	Method	C/O	Channel	Catalyst	p [bar]
Radial heat loss	in-situ	1.0	central, middle, outer	Rh ₆₀₀ , $L = 11$ mm	1
Two-stage catalyst	in-situ	1.0	central	Pd ₆₀₀ $L = 2$ mm, Rh ₆₀₀ $L = 8$ mm	1

Table 3.4: Experimental conditions investigated for CPOX of CH₄.

For an investigation of the radial heat loss, concentration and temperature profiles for three different channels of the monolith, one central channel (referred to as “central”), one channel between center and periphery of the mono-

⁴Parts of this section have been taken from [129]. Reprinted (adapted) from Catalysis Today, 216, M. Hettel, C. Diehm, B. Torkashvand and O. Deutschmann, Critical evaluation of in situ probe techniques for catalytic honeycomb monoliths, 2 - 10, Copyright (2013), with permission from Elsevier.

3. Methods and Materials

lith (referred to as “middle”, radial position $r = \frac{1}{2}r_{\text{Monolith}}$), and one channel close to the periphery of the monolith (referred to as “outer”) were obtained. The catalyst used was one piece of a honeycomb monolith coated with Rh/ γ -Al₂O₃. A C/O ratio of 1.0 was chosen.

Besides the investigations for the Rh catalyst, CPOX of methane was also investigated on a staged catalyst, consisting of a slice of monolith coated with Pd/ γ -Al₂O₃ ($L = 2$ mm, 600 cpsi) and a slice of monolith coated with Rh/ γ -Al₂O₃ ($L = 8$ mm, 600 cpsi). Palladium is known to be a good total oxidation catalyst for methane [151]. The configuration with Pd followed by Rh was employed to gain a deeper insight into the different reaction zones that are observed for a single Rh slice (see Section 4.1.1). For the investigation of the two-stage catalyst with Pd₆₀₀ and Rh₆₀₀, the spatial resolution of gas composition and temperature was measured inside a central channel and a C/O ratio of 1.0 was chosen. For the temperature profiles, only the gas-phase temperature was detected.

Steady state was achieved after 60 min in both studies. Then, the collection of the data for the axial profiles, temperature or composition, was started.

3.3.3 Ethanol⁵

Table 3.5 contains an overview of the operating conditions for the different experiments performed for ethanol CPOX. Ethanol is an alternative fuel produced from renewable resources like biomass. In Germany, it is mainly used as a fuel additive in automotive fuels, e.g. 95 RON (Research Octane Number) gasoline containing 5 vol-% ethanol. In countries with large ethanol production, e.g. Federative Republic of Brazil, ethanol itself is used as an automotive fuel.

⁵Parts of this section have been taken from [102]. Reprinted (adapted) from Applied Catalysis A: General, 467, D. Livio, C. Diehm, A. Donazzi, A. Beretta and O. Deutschmann, Catalytic partial oxidation of ethanol over Rh/Al₂O₃: Spatially resolved temperature and concentration profiles, 530 - 541, Copyright (2013), with permission from Elsevier.

Therefore, studying the applicability of ethanol in CPOX reformers and understanding the mechanism is an important step towards the development of reformers for mobile and decentralized power generation.

Experiment	Method	C/O	Channel	Catalyst	p [bar]
C/O dependency	in-situ	0.65-0.85	central, middle, outer	Rh ₆₀₀ , $L = 11$ mm	1
Radial heat loss	in-situ	0.75	central, middle, outer	Rh ₆₀₀ , $L = 11$ mm	1
<i>blank</i>	in-situ	0.75	central	uncoated monolith, $L = 11$ mm	1

Table 3.5: Experimental conditions investigated for CPOX of ethanol.

The measurements of concentration and temperature profiles for CPOX of ethanol were performed in collaboration with Dario Livio. The performance of the ethanol reformer was studied in a central channel of the monolith at varying C/O ratios ($C/O = 0.65 - 0.85$). This investigation was performed to find the ideal operating conditions in a CPOX reformer for ethanol. At the higher C/O ratio tested herein, a 10 % defect error on the C mass balance was obtained in the first millimeter of the channel of the honeycomb. This indicates the formation of other species, such as diethyl ether or carbon deposits, which could not be detected by our analytic system.

In addition, the temperature and concentration profiles were investigated in three channels, which were differently-positioned across the monolith, at $C/O = 0.75$. This study made it possible to gain insight into radial concentration and temperature gradients across the monolith.

3. Methods and Materials

The reactor reached a steady state approx. 30 min after light-off; then axial profiles of temperature and composition were collected.

Besides the catalytic tests, isothermal *blank* experiments were carried out, in which the catalyst was replaced by an uncoated monolith. These measurements were performed to examine the possibility of gas-phase reactions upstream of the catalyst in the studies mentioned above. The same inlet conditions were chosen for the other experiments, i.e. 4 SLPM, 80 vol % N₂ dilution, preheating of gases to 463 K. A C/O ratio of 0.75 was chosen and temperatures from 473 K to 873 K were investigated.

3.3.4 Commercial Fuels⁶

The commercial fuels 95 RON gasoline and E 85 were studied. These logistic fuels contain 5 and 85 vol-% ethanol, respectively, and were purchased from a German gas station (ZG Raiffeisen Tankstation Karlsruhe). The fuels were chosen as representatives for a common logistic fuel (95 RON gasoline called “Super Benzin” in Germany) and a fuel with high ethanol content (E 85) which is also available at certain gas stations. Thus, the applicability of these fuels, which provide an already existing infrastructure, for mobile hydrogen generation was investigated.

To be able to calculate the C/O ratio for the commercial fuels, the C/H/O content of the fuels was determined by elemental analysis, and an averaged molecular composition was calculated, yielding C_{7.5}H_{13.6}O_{0.2} for 95 RON gasoline and C_{2.5}H₇O₁ for E 85. In the investigations, the commercial fuels were compared to a model system composed of ethanol and iso-octane. A blend composed of only two components as a model system for a commercial fuel, which

⁶Major parts of this section have been taken from [16]. Reprinted (adapted) from Catalysis Today, 197, C. Diehm, T. Kaltschmitt and O. Deutschmann, Hydrogen production by partial oxidation of ethanol/gasoline blends over Rh/Al₂O₃, 90-100, Copyright (2012), with permission from Elsevier.

represents a very complex mixture of over a hundred different hydrocarbon species, would make a fundamental understanding possible and guarantee reproducibility. Iso-octane is standardly used as a surrogate for gasoline [23, 24]. To match with the ethanol concentration in the commercial fuels, model fuels with 5 and 85 vol-% ethanol were investigated. The exact concentrations were determined by NMR spectroscopy.

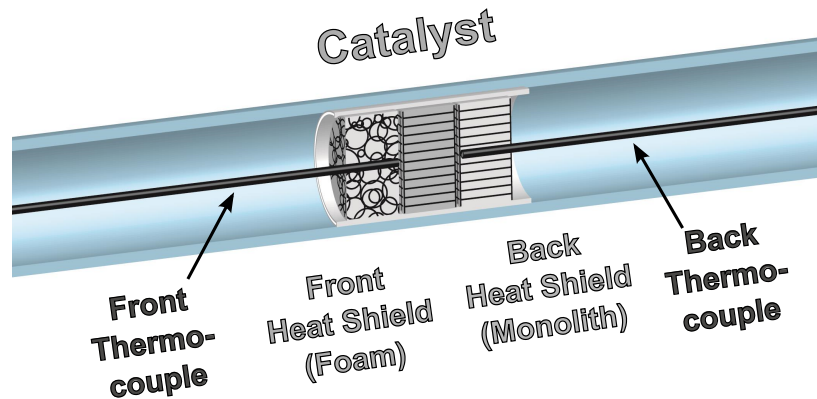


Figure 3.12: Cross section of reactor in CPOX 1 with front heat shield, catalyst, back heat shield, and thermocouples. Adapted from [24].

The investigations (see Table 3.6 for an overview) were performed on the setup CPOX 1. This reactor setup is similar to the part of CPOX 3 for ex-situ measurements. The reactor setup used for the measurements is shown in Figure 3.12. The position of the catalyst (Rh_{900}) in the reactor was 200 mm downstream of the mixture inlet. As heat shields, differing from the other investigated systems, an uncoated $\gamma - \text{Al}_2\text{O}_3$ foam monolith (85 ppi, pores per inch) was placed directly upstream of the catalyst. The BHS was an uncoated monolith (600 cps). Both heat shields, also serving as fixations for thermocouples, had a diameter of 19 mm and a length of 10 mm. For the analysis of the outlet gas composition, the same analytics as in CPOX 3 were used. A detailed description of the experimental setup can be found elsewhere [20, 62].

Measurements were performed from fuel-lean ($\text{C/O} = 0.6$) to fuel-rich ($\text{C/O} = 1.5$) conditions by gradual variation of the inlet mixture. By screening a range of feed compositions, the composition with the highest hydrogen

3. Methods and Materials

Experiment	Method	C/O	Channel	Catalyst	p [bar]
95 RON gasoline	ex-situ	0.6-1.5	–	Rh ₉₀₀ , $L = 8.5$ mm	1
E 85	ex-situ	0.6-1.5	–	Rh ₉₀₀ , $L = 8.5$ mm	1
Ethanol iso-Octane blend, 5% w.r.t. ethanol	ex-situ	0.6-1.5	–	Rh ₉₀₀ , $L = 8.5$ mm	1
Ethanol iso-Octane blend, 85% w.r.t. ethanol	ex-situ	0.6-1.5	–	Rh ₉₀₀ , $L = 8.5$ mm	1

Table 3.6: Experimental conditions investigated for CPOX of commercial fuels.

yield and lowest by-product formation for each fuel can be determined. To ensure reproducibility, each measurement was performed twice. The results for the measurements were compared and averaged as only slight differences were observable. A total flow rate of 4.5 SLPM was used for each measurement, corresponding to a gas hourly space velocity (GHSV) of $105\,600\text{ h}^{-1}$ (at standard conditions). For each C/O ratio, experimental data were collected for at least 15 min. The total flow rate was determined by the method described in Section 3.1.3. For each C/O ratio, after steady state was reached, one sample was analyzed by GC/MS (6890N, Agilent). After one set of measurements reaching from fuel-lean to fuel-rich conditions, the catalyst was regenerated. The regeneration was conducted by temperature-programmed oxidation with synthetic air, in particular to burn off carbon deposits on the catalyst surface. Additionally, the amount of carbon deposited on the surface was quantified by monitoring the CO and CO₂ flux.

3.3.5 Propane CPOX at 2-4 bar⁷

In this study, CPOX of C_3H_8 was studied at elevated pressures in the range of 2 to 4 bar (see Table 3.7). Propane is a component of LPG (Liquefied Petroleum Gas). LPG is a generic term for a composition with concentrations varying between pure propane, a mixture of propane and butane and pure butane. It can be easily stored and distributed, which makes its application in decentralized power generation attractive. These small-scale applications are favorably performed under pressure as this leads to an intensified process for the same reactor size as operation at ambient pressure. The influence of pressure was studied with the in-situ sampling technique in a central channel. Additionally to the spatial profiles, the coking during CPOX of C_3H_8 at 4 bar was investigated. Carbon formation needs to be taken into account at elevated pressures as gas-phase reactions are favored at these conditions, which could lead to the formation of soot. Downstream equipment can be blocked and damaged by the carbon particles, thus their formation needs to be monitored, understood, and, if possible, suppressed.

The measurements were performed during a stay as guest scientist at Politecnico di Milano together with Mattia Bogotto and Marco Dellavedova, using the available in-situ sampling technique which allowed for investigations under pressure [152]. The characteristics and differences to the setup CPOX 3 are pointed out in the following section.

Experiment	Method	C/O	Channel	Catalyst	p [bar]
Increased pressure	in-situ	0.8	central	Rh ₄₀₀ , $L = 26$ mm, $\varnothing = 24$ mm	2-4

Table 3.7: Experimental conditions investigated for CPOX of propane.

⁷Measurements performed during my visit at Politecnico di Milano; the study is published in [81].

3. Methods and Materials

3.3.5.1 Measuring Conditions and Setup Characteristics at Politecnico di Milano

The experiments were performed at 10 NI min^{-1} (NI – normal liters, normal refers to normal conditions, $T = 273 \text{ K}$ and $p = 1.013 \text{ bar}$), i.e. at a constant molar flow, with 77 % N_2 dilution and a C/O ratio of 0.8. For the ignition, the catalyst was preheated by feeding hot N_2 ($T = 773 \text{ K}$) to the reactor until the catalyst reached a temperature of 623 K. At this temperature, the feed stream was switched to the unheated gas mixture containing propane and oxygen in nitrogen. The gases were not pre-heated for safety reasons and were fed separately at 298 K. A FeCrAlloy[®] foam (100 ppi, $L = 2.2 \text{ cm}$) was used for mixing the gases. The catalyst was placed inside a quartz tube which was in turn placed inside a stainless steel tube. The stainless steel tube was insulated by quartz wool. Heat shields were placed upstream and downstream of the catalyst with a void space of 10 mm at the catalyst inlet and outlet (see Figure 3.13, similar configuration without filters).

To be able to perform in-situ investigations under pressure, the sealing system for the capillary was different to the one in CPOX 3. The capillary enters the reactor through a piece of 1/16 inch tubing connected to a piece of 1/4 inch tubing, both filled with high vacuum grease (Dow Corning). The reactor pressure was measured at the reactor inlet and was controlled by a metering valve downstream of the reactor. For safety reasons, the reactor part upstream of the catalyst was equipped with a pressure release valve.

For the temperature profiles, a very similar assembly to the one described in Section 3.2 was used. For the concentration profiles, a capillary with O.D. = $350 \mu\text{m}$ and I.D. = $200 \mu\text{m}$ was used. The axial profiles were performed in the central channel. A flow of 2 ml min^{-1} was sucked from the channel of the catalyst and analyzed by a micro-GC (Agilent 3000).

The mixture at 3 and 4 bar was within the flammability limits [153], but no gas-phase reactions upstream of the catalyst were observed.

For all the experiments performed at Politecnico di Milano, a catalyst (Rh_{400}) prepared at Politecnico di Milano was used. Contrary to all other catalysts used, the washcoat was $\alpha\text{-Al}_2\text{O}_3$ instead of $\gamma\text{-Al}_2\text{O}_3$. The preparation of the catalyst is described elsewhere [81].

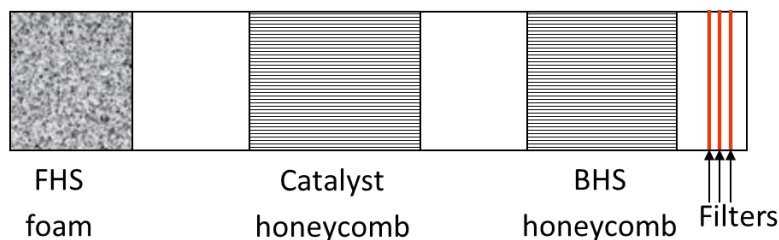


Figure 3.13: Scheme of the reactor setup used to collect coke samples from CPOX of propane at 4 bar.

For the collection of solid carbon, a reactor configuration as shown in Figure 3.13 was adopted. Downstream of the back heat shield, filters were placed to collect the carbon particle. Different kinds of filter materials were used to rule out catalytic activity of the filter material itself. The following materials were used:

- FeCrAlloy[®] micro-fiber mat, calcined at 1223 K
- FeCrAlloy[®] micro-fiber mat, calcined at 1373 K
- FeCrAlloy[®] micro-fiber mat, coated with $\gamma\text{-Al}_2\text{O}_3$
- Glass fabric tape

The FeCrAlloy[®] micro-fiber mat has a thickness of 1.0 mm and the following composition: Fe > 70 %, Cr: 20 – 24 %, Al: 4.8 – 5.5 %, traces of Y [154].

For the calcination, the filters were cleaned in an ultrasound bath in ethanol for 10 min and dried at 383 K for 2 h. The calcination was then performed at 1223 K under air circulation for 10 h (time for heating up not included, temperature ramp 5 K min^{-1}). The amount of Al_2O_3 formed during the calcination

3. Methods and Materials

process was equivalent to 3.5 wt %. To prepare the filters calcined at 1373 K, already at 1223 K calcined filters were used and calcined again at 1373 K under air circulation. Here, the formed Al_2O_3 -layer amounted to 6.7 wt %.

The filter coated with $\gamma\text{-Al}_2\text{O}_3$ was coated by the following process. The filter was saturated with a 10 wt % Disperal[®] solution, which was prepared 48 h in advance. The excess solution was drained from the filter by placing the filter into a Büchner funnel on top of a side-arm flask and connecting a vacuum pump. Following this, the filter was dried at 383 K for 1 h and calcined at 973 K for 10 h (time for heating up not included, temperature ramp 2 K min^{-1}). The Al_2O_3 -layer formed on the three coated filter amounted to 14.9 wt %, 16.6 wt %, and 16.7 wt %.

For the glass fabric tape, the reactor configuration was adjusted. The back heat shield was used as a support for the glass fabric tape.

Every filter was used for at least 6 h in CPOX of C_3H_8 at 4 bar with a total flow of 10 Nl min^{-1} and with $\text{C/O} = 0.80$.

3.4 Error Analysis

The error by feeding of the gases and liquids needs to be taken into consideration in the interpretation of the measured data. The accuracies for MFCs, Cori-Flow (for liquid components except water) and Liqui-Flow (for water) are given in Table 3.8. For the calibration of the gas flow of the MFCs, a primary flow meter (Definer 220L for $0\text{-}500\text{ ml min}^{-1}$ and Definer 220H for $300\text{-}30\,000\text{ ml min}^{-1}$, DryCal, Bios) was used (for accuracy see Table 3.8). For the Cori-Flow and the Liqui-Flow, the calibrations provided by the manufacturer were applied.

Table 3.9 shows the deviation for the C/O ratio based on the accuracies for the dosing devices. For gaseous fuels, an error of $\Delta\frac{\text{C}}{\text{O}} \leq 0.02$ is possible

Feeding of gases and liquids

Device	Error
MFC, Bronkhorst	$\pm 0.5\%$ from measured value plus $\pm 0.1\%$ from the end value
Cori-Flow, Bronkhorst	$\pm 0.2\%$ from measured value
Liqui-Flow, Bronkhorst	$\pm 1\%$ from end value
Definer 220 DryCal, Bios	1 % of standardized value

Analytical instruments

Device	Error
FTIR multigas analyzer 2030, MKS	$\pm 2\%$ from the measured value
H-sense, MS4	$\pm 2\%$
Airsense, V&F	$\pm 2\%$

In-situ sampling devices

Device	Error
High-temperature precision pressure sensor Type P320T, Wagner Mess- und Regeltechnik GmbH	0.1 %
Thermocouple Type K, Omega Engineering Inc.	$\pm 2.2\text{ K}$ plus $\pm 0.75\%$ from the measured value
Pyrometer IGA LO-50 plus, LumaSense Technologies GmbH	0.3 % from the measured value in $^{\circ}\text{C}$ plus $1\text{ }^{\circ}\text{C}$

Table 3.8: Values for accuracy as declared by the manufacturers.

3. Methods and Materials

for all investigated C/O ratios. For liquid fuels, the evaporating system has to be taken into account, which consists of a Cori-Flow (Bronkhorst), an MFC (Bronkhorst), and a controlled evaporator mixer (Bronkhorst). The deviation is $\Delta \frac{C}{O} < 0.03$ for all investigated C/O ratios. For the commercial fuels, the deviation in C/O ratio is calculated based on the assumed molecular composition. The error from the elemental analysis (1 % of the amount of each element) has to be taken into account additionally.

Fuel	$\Delta \frac{C}{O}$
Methane	0.01
Ethanol	0.02
Propane	0.01
95 RON gasoline	0.02 w.r.t. the averaged molecular composition $C_{7.5}H_{13.6}O_{0.2}$
E 85	0.02 w.r.t. the averaged molecular composition $C_{2.5}H_7O_1$
Ethanol iso-octane blend with 5 vol % ethanol	0.02
Ethanol iso-octane blend with 85 vol % ethanol	0.02

Table 3.9: Deviation of the C/O ratio for the investigated fuels.

The accuracies of the analytical instruments as given by the manufacturers are listed in Table 3.8. These apply for the ex-situ measuring method (Section 3.1). Additionally to these, an error occurs due to the quantification of the total flow rate by use of an adapted external standard method (Section 3.1.3).

For the in-situ sampling technique, additional errors have to be taken into consideration. The errors from the used equipment and setup for the sampling technique are discussed here. For the evaluation of the method concerning the influence of the capillary on the processes in the analyzed channel, see Sec-

tion 4.1.3. In the in-situ experiments, the pressure in the sample loop (see Section 3.2) is determined by a high-temperature precision sensor (P320T, Wagner Mess- und Regeltechnik) with a deviation of only 0.1 % from the measured value. However, the pressure value fluctuates within 2.5 %, which results from the layout of the in-situ sampling technique, i.e. the pulsing of the connected pump is visible. This fluctuation will also have an influence on the peak area detected in the analytical instruments as the averaged pressure is used to calculate the mole fractions based on the integrated peak areas. Also, the separate calibration of the analytics for the sampling method (see Section 3.2) needs to be taken into account. Here, the error of the pressure sensor also plays a role. As the gas composition for the calibration is obtained by using the different MFCs and the evaporating system, the errors for the dosing of gases and liquids (discussed above) have to be taken into account. The variance for the calibration is 3.8 % regarding the amount of substance of a calibrated species. For the experiments, this leads to a variance in mole fraction of 4.8 % (calculated by the propagation of errors).

For the temperature profiles, the different methods used contain different errors. For the gas-phase temperature, the measurements with the thermocouple include the error shown in Table 3.8 (declared by the manufacturer). Additionally, another source of deviation is possible as the thermocouple is inside a sealed capillary and thus only the temperature of the gas inside the capillary can be detected. Nevertheless, only small amounts of gas are inside the capillary, leading to a fast adjustment to the gas-phase temperature outside of the capillary. For the surface temperature, the error of the pyrometer has to be taken into account, which is given by the manufacturer as shown in Table 3.8. The optical fiber with a 45° polished tip, which is connected to the pyrometer (see Section 3.2), also has an influence on the measured wall temperature. As described in [33, 155], the optical fiber is a side-looking probe, with a primary acceptance cone perpendicular to the fiber axis and close to the fiber tip, with the highest contribution to the measured temperature, and a secondary acceptance cone,

3. Methods and Materials

which is in front of the fiber tip and has a minor contribution. The secondary acceptance cone will probably become important in the inlet and outlet region of the monolithic channels, leading to a temperature deviation in these areas. Nevertheless, this deviation should be small as the secondary contribution is only about 10 % of the relative intensity of the primary one [33, 155]. Also, defects on the polished, beveled surface of the fiber could also have an influence, but this is described as negligible in literature [33].

3.5 Mathematical Modeling

3.5.1 Calculation of thermodynamic equilibrium⁸

For the fuels methane, ethanol, and propane, the thermodynamic equilibrium compositions were calculated using DETCHEM^{EQUIL} [139]. The measured inlet gas composition and the gas-phase temperature at the catalyst outlet were used in the calculations. Solid carbon was included in the calculations in the form of graphitic carbon, with thermodynamic data from [156]. The gas-phase species considered at equilibrium for the different fuels are listed below:

- for methane: H_2 , O_2 , OH , H_2O , H , O , $\text{C}_2\text{H}_5\text{OH}$, CH_4 , CO_2 , CO , N_2 , C_2H_4 , C_3H_6 , CH_2O , CH_3CHO , C_2H_2
- for ethanol: H_2 , O_2 , OH , H_2O , H , O , $\text{C}_2\text{H}_5\text{OH}$, CH_4 , CO_2 , CO , N_2 , C_2H_4 , C_3H_6 , CH_2O , CH_3CHO , C_2H_2 , C_2H_6
- for propane: H_2 , O_2 , OH , H_2O , H , O , $\text{C}_2\text{H}_5\text{OH}$, CH_4 , CO_2 , CO , N_2 , C_2H_4 , C_3H_6 , CH_2O , CH_3CHO , C_2H_2 , C_3H_8 , C_2H_6

⁸Major parts taken from [102]. Reprinted (adapted) from Applied Catalysis A: General, 467, D. Livio, C. Diehm, A. Donazzi, A. Beretta and O. Deutschmann, Catalytic partial oxidation of ethanol over Rh/Al₂O₃: Spatially resolved temperature and concentration profiles, 530 - 541, Copyright (2013), with permission from Elsevier.

For propane, a pressure of 2 to 4 bar was chosen, fitting the pressure in the experiments. The gas-phase temperature used for the simulations was the one determined not directly at the catalyst outlet, but further upstream at 20 mm. The reason for this choice is a decrease of the temperature within the last millimeters of the catalyst, which is only present in the configuration without a BHS.

For all examined fuels, the thermodynamic equilibrium compositions are shown in addition to the axial concentration profiles of each species as lines at the catalyst outlet (see Sections 4.1.2, 4.2.1 and 4.2.3 and chapters 6 and 7). For ethanol, a discussion of the equilibrium composition as a function of the C/O ratio can be found in Section 4.2.2.

3.5.2 Calculation of Concentration Profiles in a Single Channel

The DETCHEM^{CHANNEL} code [139] was used to simulate the 2D reactive gas flow in a cylindrical channel with a Rh-coated wall. The simulations were performed for methane CPOX, using the measured gas-phase temperature at the catalyst inlet and the surface temperature profile along the channel as the inlet and the boundary condition, respectively. A surface-reaction mechanism was used, including 6 gas-phase species and 12 surface species [130]. A mechanism for the gas-phase reactions was not employed as these are not likely to occur under the operating conditions for methane CPOX.

In the simulations, the effectiveness factor model was applied, choosing O₂ as the rate-limiting species (see Section 2.4.2.3). Further parameters used in the calculations are shown in Table 3.10. The ratio of catalytic to geometric surface area, $F_{\text{cat,geo}}$, was calculated with Equation (3.9). For the calculation of $F_{\text{cat,geo}}$, the dispersion D_{Rh} was experimentally determined by chemisorption measurements (performed by Kathrin Schäfer). For the active-site density of

3. Methods and Materials

Rh, a value from literature [157], $\Gamma = 2.72 \cdot 10^{-9} \text{ mol cm}^{-2}$, was chosen. The total number of channels, N_{channels} , was calculated from the cell density and the area of the front face of the catalyst. The values for porosity and tortuosity given in Table 3.10 were estimated. For the channel radius, the half of the hydraulic diameter, d_h , was used. The velocity u_{in} was calculated for $T_{\text{in}} = 797.51 \text{ K}$ assuming a cylindrical channel and an equal distribution of the total flow (4 SLPM) among all channels of the monolith.

$$F_{\text{cat,geo}} = \frac{\frac{D_{\text{Rh}}}{\Gamma} \cdot \text{cat.loading} \cdot V_{\text{Monolith}}}{(\pi \cdot d_h \cdot L_{\text{Monolith}}) \cdot N_{\text{channels}}} \quad (3.9)$$

D_{Rh} : dispersion of Rh

Γ : surface-site density

cat.loading : catalyst loading

V_{Monolith} : volume of the monolith

d_h : hydraulic diameter

L_{Monolith} : length of the monolith

N_{channels} : total number of channels in the monolith

The simulations were performed for the three differently-positioned channels, which were investigated for CPOX of methane. For the outer channel, a velocity of 0.896 m s^{-1} was used, according to 80 % of the velocity for the central and middle channel. This condition was chosen to take into account the lower velocity close to the reactor wall, which is due to the formation of a boundary layer. However, the associated increase in velocity for the other channels was not considered. The results of these simulations are discussed in Section 4.1.2.

Parameter	Value
$F_{\text{cat,geo}}$	185
Porosity	0.5
Tortuosity	3
Pore diameter [m]	2.38×10^{-8}
Channel radius [m]	0.0004384
p [bar]	1.00
$x_{\text{CH}_4,\text{in}}$	0.133
$x_{\text{O}_2,\text{in}}$	0.667
T_{in} [K]	797.51
Velocity u_{in} [m s^{-1}]	1.12

Table 3.10: Values used for simulations with DETCHEM^{CHANNEL}.

3.5.3 Thermal Efficiency⁹

The thermal efficiency, α , is an indication for the extent of adiabatic operation of the reactor and was evaluated as follows:

$$\alpha = \frac{T_{\text{EXP}}^{\text{OUT}} - T_{\text{EXP}}^{\text{IN}}}{T_{\text{ADIABATIC}}^{\text{OUT}} - T_{\text{EXP}}^{\text{IN}}} \quad (3.10)$$

In Equation (3.10), $T_{\text{EXP}}^{\text{IN}}$ was the temperature measured by the thermocouple approximately 1 cm upstream of the front heat shield, $T_{\text{EXP}}^{\text{OUT}}$ was the temperature measured by the thermocouple at the exit of the catalyst-coated channel, and $T_{\text{ADIABATIC}}^{\text{OUT}}$ was the adiabatic temperature calculated with the composition

⁹Major parts taken from [102]. Reprinted (adapted) from Applied Catalysis A: General, 467, D. Livio, C. Diehm, A. Donazzi, A. Beretta and O. Deutschmann, Catalytic partial oxidation of ethanol over Rh/Al₂O₃: Spatially resolved temperature and concentration profiles, 530 - 541, Copyright (2013), with permission from Elsevier.

3. Methods and Materials

of the inlet and outlet gas mixture and the inlet gas temperature by using routines from the DETCHEM library. The thermal efficiency was calculated for ethanol CPOX.

3.5.4 CFD Modeling for Evaluating the Influence of the Sampling Technique¹⁰

The in-situ technique used in this work is an invasive technique, in which the probe inside the channel will influence the velocity and species profiles. To be able to evaluate the measured profiles, CFD simulations were performed as described below. The simulations have been performed by Matthias Hettel and Bentolhoda Torkashvand.

3.5.4.1 CFD Code

The CFD (Computational Fluid Dynamics) code FLUENT [158] was applied for the numerical simulation of the three-dimensional flow field in the monolithic structure. Transport processes in the solid structure were not included in the computations.

3.5.4.2 Chemical Reaction Mechanism

A detailed surface-reaction mechanism was used for the partial oxidation of methane over rhodium [79]. The mechanism includes 20 species and 38 reactions. It can be imported into FLUENT in the format of the CHEMKIN database. The mean-field approximation was applied for modeling the surface chemistry (see Section 2.4.2 and, e.g., [159]). For the active-site density of

¹⁰Taken from [129]. Reprinted (adapted) from Catalysis Today, 216, M. Hettel, C. Diehm, B. Torkashvand and O. Deutschmann, Critical evaluation of in situ probe techniques for catalytic honeycomb monoliths, 2 - 10, Copyright (2013), with permission from Elsevier.

rhodium, a value of $2.72 \cdot 10^{-9} \text{ mol cm}^{-2}$ was chosen [157]. In these simulations, the influence of the internal mass transfer was not covered by the employed CFD code. Thus, $F_{\text{cat,geo}}$ was reduced to a value of 5 to account for the mass-transfer limitations in the washcoat layer. No gas-phase reaction mechanism was employed, as it was already shown in literature that reactions in the gas phase can be neglected for the given operational conditions [6, 32, 69, 70] which was also proven by additional calculations.

3.5.4.3 Transport Equation for Residence Time

In addition to the transport equations for mass, momentum, and enthalpy, a transport equation for each of the eight gas-phase species CH_4 , O_2 , N_2 , H_2O , CO_2 , H_2 , CO has to be solved. To analyze the residence time τ of the fluid, an additional transport equation was implemented into the CFD code by implementing user-defined functions. The appropriate transport equation reads [160]:

$$\frac{\partial(\rho \cdot \tau)}{\partial t} + \text{div}(\rho \cdot u \cdot \tau) = \text{div} \left(\frac{\mu}{Sc} \cdot \text{grad}\tau \right) + \rho \cdot S_\tau \quad (3.11)$$

τ may be regarded as the mean value of the residence times of molecules which are transported and exchanged according to convection and diffusion. ρ is the density, u is the velocity vector, μ the dynamic viscosity, and Sc is the Schmidt number of the mixture ($Sc = 0.7$). The source term S_τ is set to 1 (one second residence time per second physical time). To integrate the residence time inside the channels, the source term was only active downstream of $z = 0$ mm. Therefore, the residence time may also be interpreted as the local “age” of fuel with respect to its “birth” at the entrance into a channel.

3. Methods and Materials

3.5.4.4 Computational Domain and Grid

The computations were performed for a typical monolithic honeycomb as used in the experiments described above. For simplicity, the rounding of the channel edges due to the washcoat was neglected. The free height of a quadratic single channel is $h = 795 \mu\text{m}$.

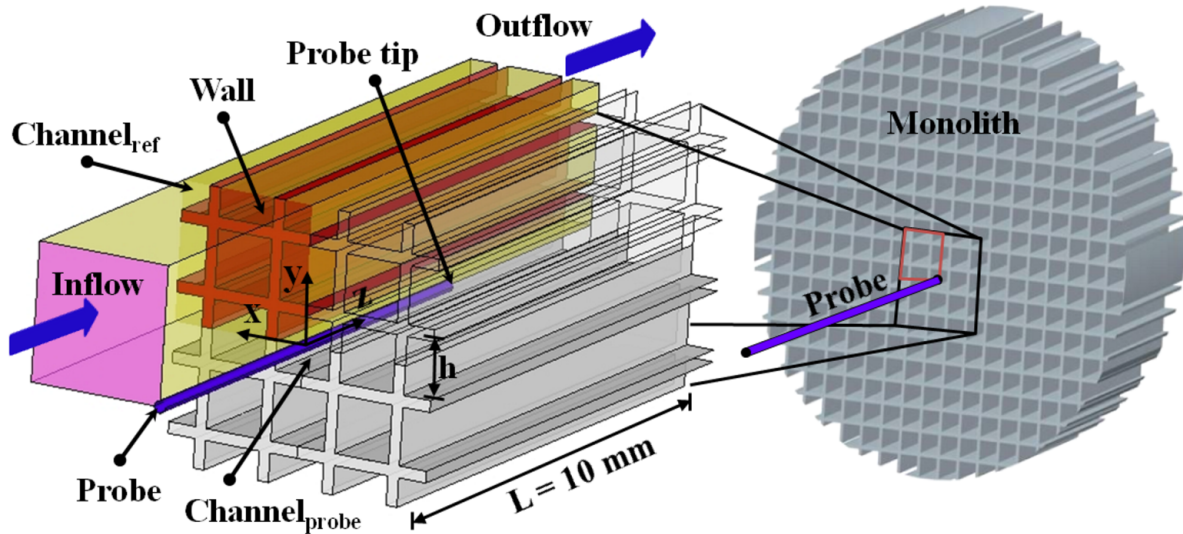


Figure 3.14: Calculation domain and boundary conditions.

The calculation domain comprises only a part of the monolith, including one channel with the probe and several channels without a probe. Figure 3.14 (left) shows a part of the monolith for the configuration in which the probe is positioned in the center of a channel and in which the tip of the probe is at $z_{\text{probe}} = 5 \text{ mm}$. In this case, the flow domain includes nine partially sliced channels. It was verified that the amount of calculated channels is large enough to guarantee a negligible influence of the size of the calculation domain on the results. The solid was not included in the calculations.

The fluid enters on the left side (magenta), 5 mm upstream of the monolith, and leaves the channels on the right side. Part of the fluid is sucked in at the tip of the probe which is colored blue. The probe points into the z direction and is perpendicular to the xy plane. The outer diameter of the probe is $O.D. =$

170 μm , the inner diameter is $I.D. = 100 \mu\text{m}$. First, four different positions of the probe in the xy plane were examined, while the probe was fully inserted into the channel. Second, for the case in which the probe is in the center of a channel, nine axial positions of the probe tip were explored (see Section 4.1.3). For each configuration, a block-structured grid with a typical size of 700,000 prism cells was generated. The grid for the configuration given in Figure 3.14 is shown from the backside in Figure 3.15. The two zoomed zones indicate the high resolution of the grid. On the lower left side, the region near the capillary tip is magnified, including the region, in which the volume flux is sucked. On the lower right side, the outlet of the channel with the probe at the end of the monolith is enlarged.

In Section 4.1.3, the conditions in the channel with the probe (subscript “probe”) and in a reference channel without a probe (subscript “ref”) are compared. The reference channel is the channel without a probe, which is the farthest from the channel with the probe and, therefore, the influence of the probe was expected to be the smallest. However, the difference of the volume fluxes in the various empty channels is very small (below 1 %). For this reason and for the sake of simplicity, it is not referred to *the* reference channel in Section 4.1.3, but to *a* reference channel, which can refer to every channel without a probe.

3.5.4.5 Boundary Conditions and Parameters

In the simulations, two sets of parameters were used. For all calculations *parameter set 1* was used. The only exception is the comparison with the experiments, in which *parameter set 2* was used. For *parameter set 1*, the conditions at the flow inlet were: velocity $u_{\text{in}} = 0.72 \text{ m s}^{-1}$, pressure $p_{\text{in}} = 1 \text{ bar}$, temperature $T_{\text{in}} = 873 \text{ K}$, mole fraction of methane in air $x_{\text{CH}_4, \text{in}} = 0.133 \text{ mole mole}^{-1}$ (C/O ratio = 1.0). Due to acceleration (area reduction and temperature rise), the velocity at the entrance of a channel without a probe was approximately $u = 1.3 \text{ m s}^{-1}$, which was equal to a volume flux of about 49 ml min^{-1} . As

3. Methods and Materials

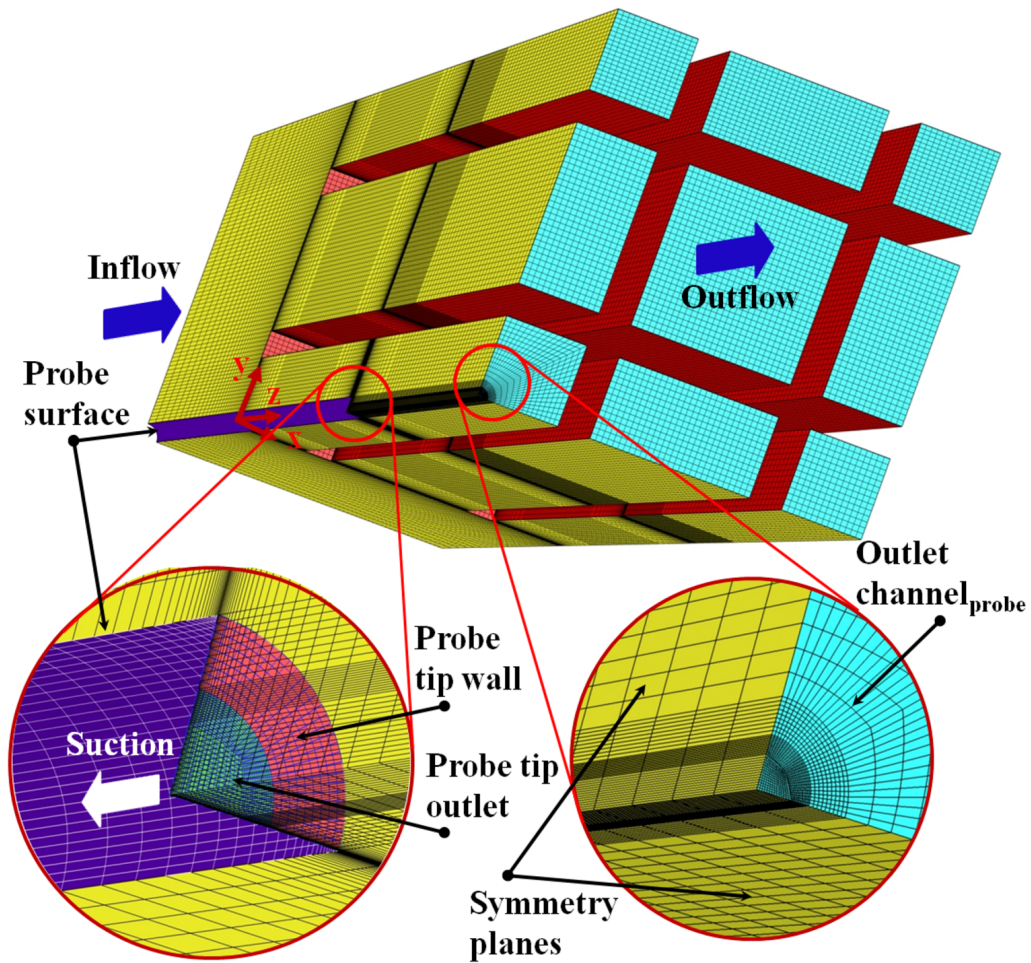


Figure 3.15: Typical calculation grid, here for case A (see Figure 4.6) and $z_{\text{probe}} = 5 \text{ mm}$.

in the experiments, the volume flux sucked through the probe tip was approx. 2 ml min^{-1} , leading to a suction velocity of ca. 2 m s^{-1} at the probe tip. At the channel walls, the temperature was fixed to be $T_{\text{wall}} = 973 \text{ K}$.

For the calculations which were done for the comparison with the measurements (see Section 4.1.3.4), *parameter set 2* was used, implying two changed conditions. The inlet velocity was $u_{\text{in}} = 0.68 \text{ ml s}^{-1}$ and, for the temperature at the channel walls, the experimentally determined wall temperature was applied (see Figure 4.1). The Reynolds number was always lower than 40 and, thus, the flow was laminar.

3.5.5 CFD Modeling of the Entire Monolith

In Section 3.5.4, the modeling of the influence of the sampling technique was described. Therefore, the three-dimensional flow including detailed chemistry in nine channels of the monolith was calculated applying the CFD code FLUENT [158]. In the present section, the calculation of the entire monolith is described. The usage of a three-dimensional grid for the entire calculation domain would lead to excessive calculation times. Therefore, a rather new approach was chosen, applying the simulation tool DUO. The simulations were performed by Matthias Hettel.

DUO stands for the coupling of the two computer codes DETCHEM Und (German for “and”) OpenFOAM. OpenFOAM [142] is an open source CFD tool which makes the calculation of three-dimensional fluid and solid regions possible. DETCHEM [139] is a package of software tools specifically designed for the modeling and simulation of reacting flows, in particular for heterogeneous systems such as catalysis, materials synthesis and fuel cells. The simulation tool DUO is the symbiosis of the two codes.

Figure 3.16 explains the functionality of DUO, showing a schematic drawing of a monolith with some channels located in a surrounding flow field. Using DUO, the flow outside of the monolith is calculated with the CFD code OpenFOAM, which handles essentially arbitrary geometrical structures. In the outer flow regions, the chemistry is often simple or can be fully neglected. In addition to the outer fluid flow, the code also solves the conjugate heat transfer in the solid walls of the monolith. This implies the handling of the heat transfer between the solid and fluid regions as well as the exchange of heat with the external environment. The flow inside the channels is calculated with DETCHEM codes by applying detailed surface chemistry. As the flow is handled as a one- or two-dimensional flow, solving the boundary layer equations, the calculation is fast.

3. Methods and Materials

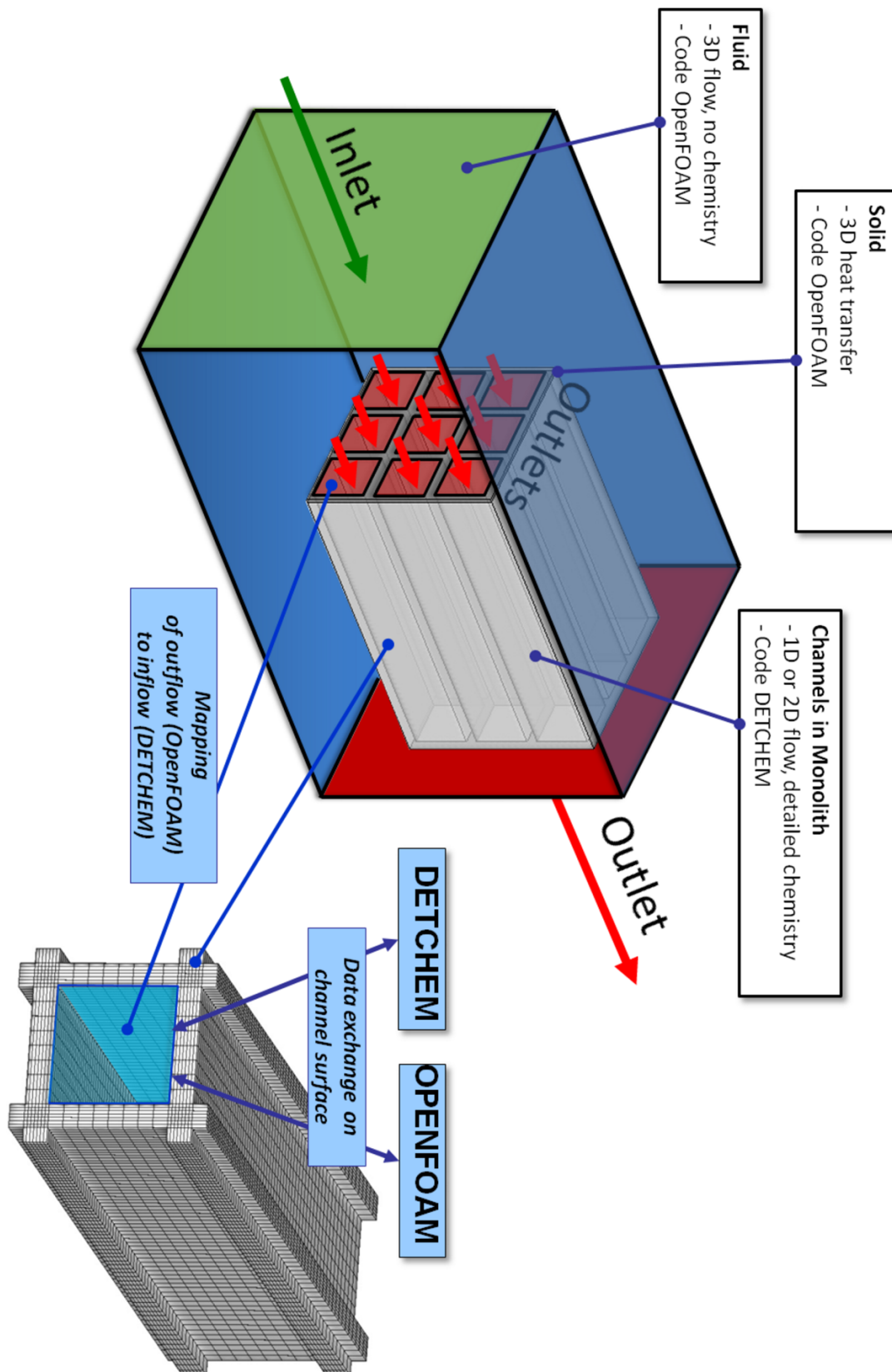


Figure 3.16: Typical calculation domain; here nine channels located in a surrounding flow field.

DUO controls the exchange of data at the inner surface of the channels between the two codes and provides the interface between the geometrically complex three-dimensional outer mesh and the two-dimensional axial mesh for the catalyst tubes (see Figure 3.17). The internal chemistry problem is solved using axial wall temperature profiles that are specified by OpenFOAM. Tube-wall heat-fluxes are predicted as a result of the chemically reacting flow problem within the tubes. These flux profiles are supplied to OpenFOAM by DETCHEM. OpenFOAM then solves the external problem using the tube-wall heat fluxes as boundary conditions. The outer flow solution provides new tube-wall temperature profiles, which are used to solve the chemistry problem. The iterative process continues until convergence between the inner and outer problems is achieved.

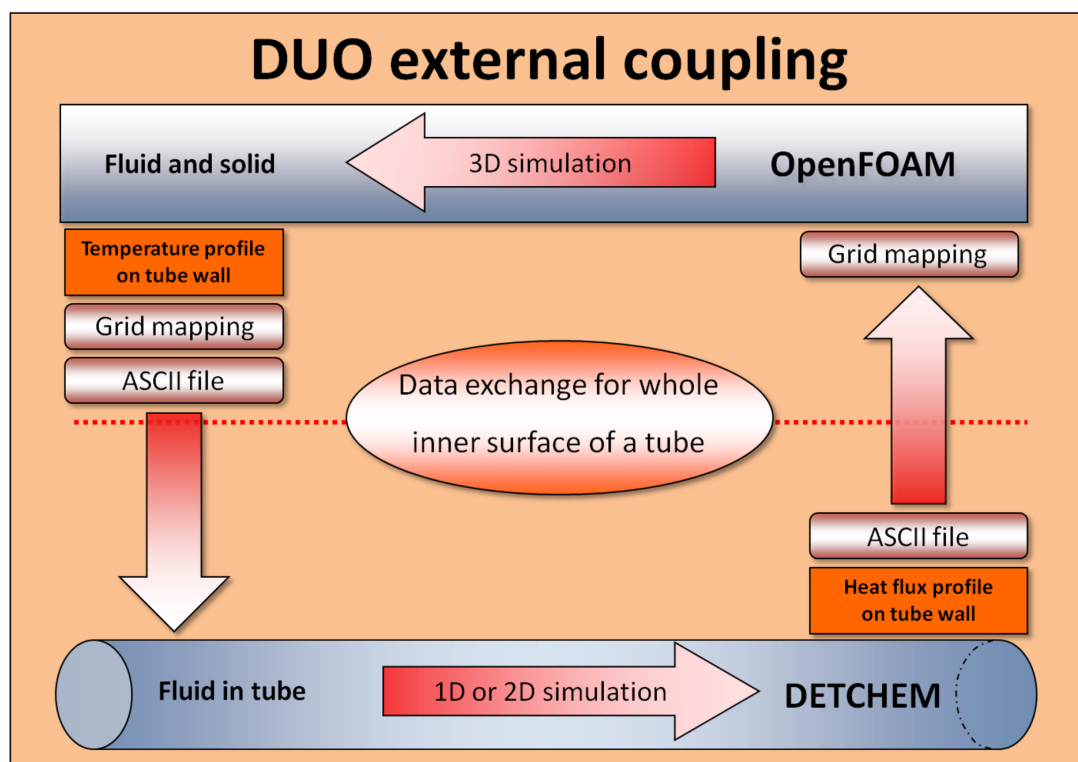


Figure 3.17: Schematic representation of the communication between DETCHEM and OpenFOAM.

The calculations with DUO include the solid part of the monolith. Contrary to the approach explained in the previous section, no measured temperature

3. Methods and Materials

profiles have to be used as boundary conditions along the inner walls of the channels. However, as the heat losses at the front and the back side of the monolith are unknown, the temperatures at these two surfaces were set to be constant using measured values.

The calculation domain for OpenFOAM includes the solid part of one quarter of the monolith. The flow region between the outlet of the FHS and the monolith was also included. The geometry was discretized with a block-structured grid with approx. 2 mio. cells.

The flow in the 76 channels was calculated with the 2D code DETCHEM^{CHANNEL}.

The code DUO makes the mapping of the channels possible. This means that for channels with the same boundary conditions, only one representative channel is solved and the result (the wall heat flux) is applied for all other channels of the group. It was found that 5 channels at 5 different radial positions are sufficient. Each of these channels represents all channels, which can be found in an annulus with the height of 2 mm. The annuli divided the monolith ($r = 10$ mm) in five regions.

The free height of a channel was $876 \mu\text{m}$. As a reaction mechanism, a detailed surface-reaction mechanism for the partial oxidation of methane over rhodium was used [130], containing 6 gas-phase and 12 surface species. Gas-phase reactions were not considered. The following boundary conditions were used for the simulations: velocity $u_{\text{in}} = 0.427 \text{ m s}^{-1}$, pressure $p_{\text{in}} = 1 \text{ bar}$, gas-phase temperature $T_{\text{gas,in}} = 600 \text{ K}$, solid temperature $T_{\text{solid,in}} = 1026 \text{ K}$, $T_{\text{solid,out}} = 906 \text{ K}$, mole fraction of methane $x_{\text{CH}_4,\text{in}} = 0.13 \text{ mole mole}^{-1}$, mole fraction of oxygen $x_{\text{O}_2,\text{in}} = 0.13 \text{ mole mole}^{-1}$ (C/O ratio = 1.0), ratio of catalytic to geometric surface $F_{\text{cat,geo}} = 185$, porosity of washcoat $\Phi = 0.5$, tortuosity is 3, pore diameter $2.3 \times 10^{-8} \text{ m}$. The effectiveness factor model was used with O_2 as the rate-limiting species to account for diffusion limitations (see Section 2.4.2.3). Adiabatic conditions were chosen at the reactor wall. For the

solid material cordierite, a thermal conductivity of $2 \text{ W m}^{-1} \text{ K}^{-1}$, a heat capacity of $900 \text{ kJ kg}^{-1} \text{ K}^{-1}$, and a density of 2100 kg m^{-3} were used.

Chapter 4

CPOX of Methane and Ethanol over Rh/Al₂O₃

The focus of this work is the mobile and decentralized hydrogen production in compact devices by catalytic partial oxidation for production of hydrogen-rich syngas for fuel cell applications. Different fuels were investigated, representing different fields of application. Here, the results for the single-component fuels methane and ethanol are described and discussed.

4.1 Methane¹

Methane is the main component of natural gas (70-99 %). There is a wide pipeline distribution network of natural gas in Europe as well as the USA. It is utilized for domestic, e.g. central heating and cooking, as well as industrial

¹Parts of this section have been taken from [129]. Reprinted (adapted) from Catalysis Today, 216, M. Hettel, C. Diehm, B. Torkashvand and O. Deutschmann, Critical evaluation of in situ probe techniques for catalytic honeycomb monoliths, 2 - 10, Copyright (2013), with permission from Elsevier.

4. CPOX of Methane and Ethanol over Rh/Al₂O₃

uses, e.g. heat supply for thermal processes [1]. Also the application as fuel for vehicles is realized. The production of hydrogen from natural gas by steam reforming is industrially established but only on a large scale, as small scale processes are not efficient. A CPOX reformer with methane as fuel can also be efficient on a small scale in mobile or decentralized applications as the reformer operates autothermally.

4.1.1 Spatial Profiles in a Single Channel

The catalytic partial oxidation of methane on Rh₆₀₀ at C/O = 1.0 was experimentally studied using the in-situ sampling technique of CPOX 3. For detailed operating conditions, see Section 3.3.2. Figure 4.1 shows the axial temperature profiles for the gas phase and the solid phase in a channel, which is situated between the center and the periphery of the monolith. For the surface temperature measured by the pyrometer, no data are depicted in the void space between FHS and catalyst (axial coordinate $z = -5.5 - 0$ mm), as no solid exists close to the position of the tip of the optical fiber. Also, between catalyst and BHS, a small gap (≈ 0.6 mm) is present, which leads to the local minimum at $z = 11$ mm.

Within the first millimeter of the catalyst-coated channel, the surface temperature shows a hot spot of 990 K. This maximum is followed by a steep decrease in temperature to 922 K after half of the channel ($z = 5$ mm) and further downstream by a much slower decline to 903 K at the end of the channel ($z = 11$ mm). For the gas phase, the temperature rises from 799 K at the catalyst entrance ($z = 0$ mm) to 928 K at 2.6 mm and declines to 891 K at the outlet of the catalyst ($z = 11$ mm). The highest temperature of the gas phase is shifted further downstream in the channel compared to the hot spot on the surface. Inside the catalyst, a thermal equilibrium between gas and solid is reached towards the end of the channel. In methane CPOX, it is very likely no gas-phase reactions occur [6, 32, 69, 70]. Thus, the gas temperature is not influenced by gas-phase reactions.

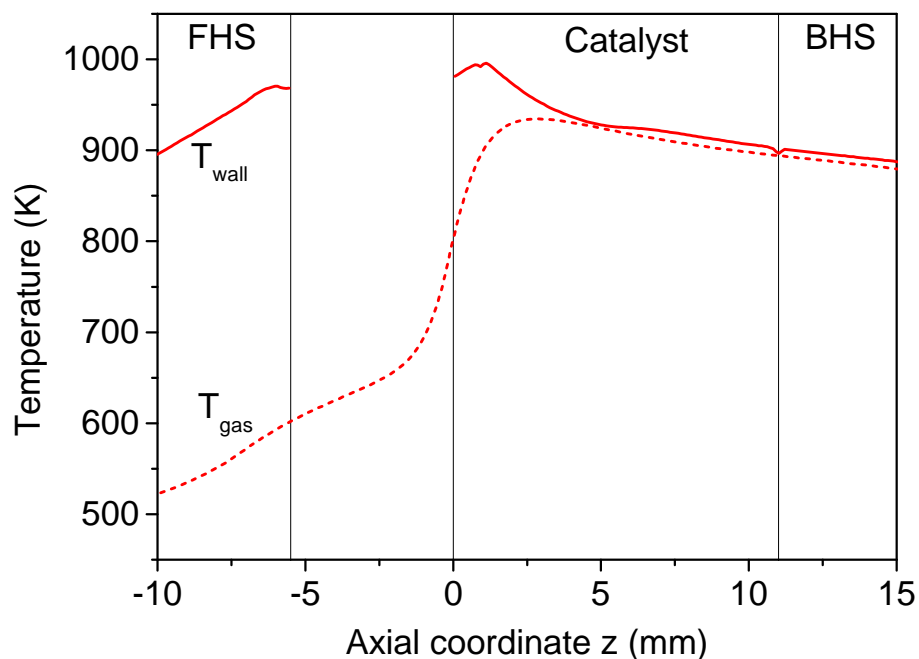


Figure 4.1: Measured temperature of the gas phase and surface as a function of the axial coordinate for CPOX of CH_4 over $\text{Rh}/\text{Al}_2\text{O}_3$ at $\text{C}/\text{O} = 1.0$.

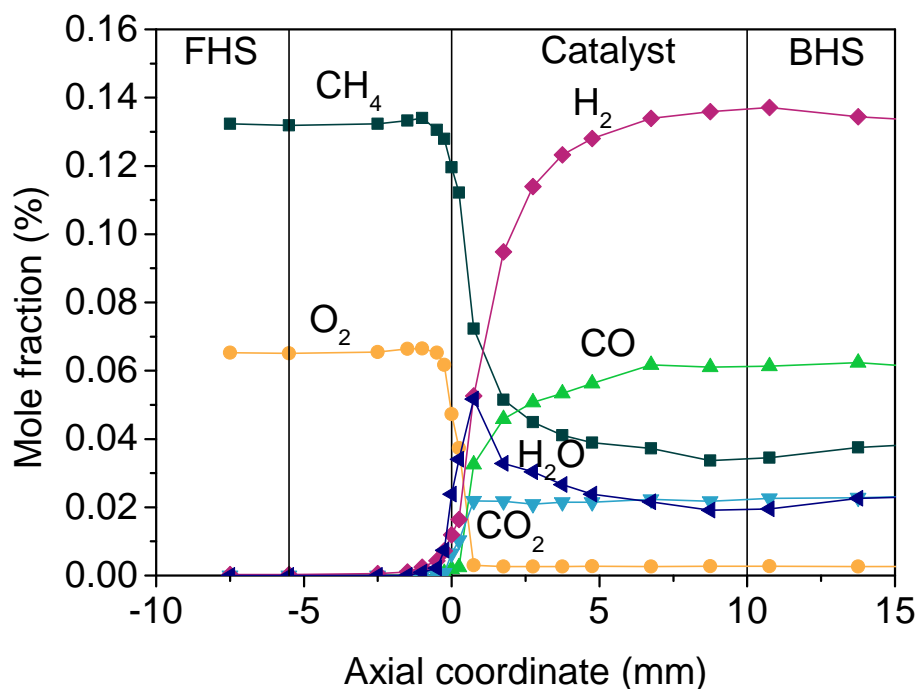


Figure 4.2: Measured mole fractions of CH_4 , O_2 , H_2 , H_2O , CO , and CO_2 as a function of the axial coordinate for CPOX of CH_4 over $\text{Rh}/\text{Al}_2\text{O}_3$ at $\text{C}/\text{O} = 1.0$.

4. CPOX of Methane and Ethanol over Rh/Al₂O₃

The concentration profiles of the reactants and products are displayed in Figure 4.2. The temperature and concentration profiles clearly indicate that the CPOX proceeds in two steps. The first zone of the catalyst (0 – 1 mm) is the oxy-reforming zone. In the first part of the channel, exothermic total oxidation is the determining processes, leading to the temperature hot spot at the channel wall. Oxygen is completely converted after 1 mm. The main consumption of methane from mole fraction of $x(\text{CH}_4) = 0.131$ to $x(\text{CH}_4) = 0.046$ occurs upstream of an axial position of 3.5 mm, followed by a much slower consumption to $x(\text{CH}_4) = 0.039$ at the end of the catalyst. For water, a maximum is detected at $z = 0.5$ mm. Simultaneously, partial oxidation and reforming reactions take place, leading to the formation of hydrogen and carbon monoxide and the consumption of water. Carbon dioxide is formed within the first millimeter and nearly no change in mole fraction is observed throughout the rest of the channel of the catalyst. It seems CO₂ is mainly formed in total oxidation in the oxy-reforming zone and is neither consumed in dry reforming or WGS nor formed in reverse WGS or other reactions. Several articles in literature suggested that dry reforming is not taking place in a CPOX reformer under similar conditions [10, 12, 29].

The second zone ($z = 1 - 11$ mm) is the reforming zone. The endothermic process predominates after all oxygen has been consumed, thus leading to the steep decrease in surface temperature and a further consumption of methane and water as well as formation of hydrogen and carbon monoxide. These findings support former studies of CPOX of CH₄ over Rh [10, 12, 33]. The formation of syngas seems to occur on Rh by a combination of direct and indirect routes (see Section 2.2.1.1), as already proposed in literature [12]. Nevertheless, as discussed in Section 2.2.1.1, it is not possible to infer the concentrations close to the catalytic surface from the gas composition measured with the in-situ technique.

Upstream of the catalyst, diffusion influences the concentration profiles (see Section 4.1.3.4). The concentration of the reactants start to decrease and of

the products H_2 and H_2O start to increase at -1.5 mm.

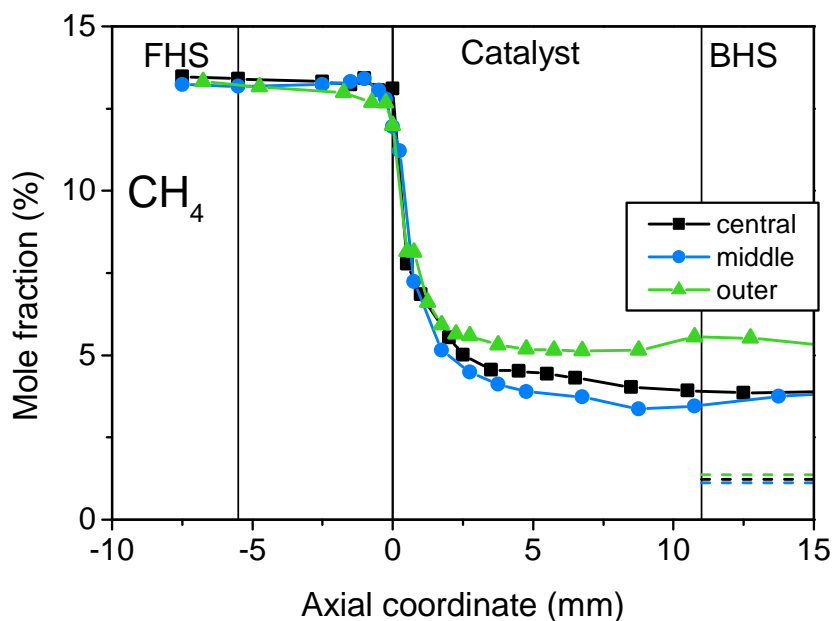
4.1.2 Influence of Radial Position of Channel

The in-situ sampling technique of CPOX 3 at KIT provides the feature to measure concentration and temperature profiles in different channels across the monolith. In order to examine, if there are changes in temperature and composition for different radial positions across the monolith, three channels were investigated for $\frac{C}{O} = 1.0$ on Rh_{600} (see Section 3.3.2 for detailed operating conditions). One channel in the center of the monolith (referred to as “central”), one in the middle between center and periphery of the monolith (referred to as “middle”), and one close to the periphery of the monolith (referred to as “outer”). In Figure 4.3, the methane and oxygen mole fractions as well as gas and wall temperatures are shown for all three channels. The concentration profile for oxygen for the central channel is not shown due to problems in the measurement with the baseline in the IMR-MS, which led to corrupted values. A shape of the concentration profile similar to the one shown for the middle channel is expected. The products of methane CPOX, H_2 , CO , CO_2 , and H_2O are shown in Figure 4.4.

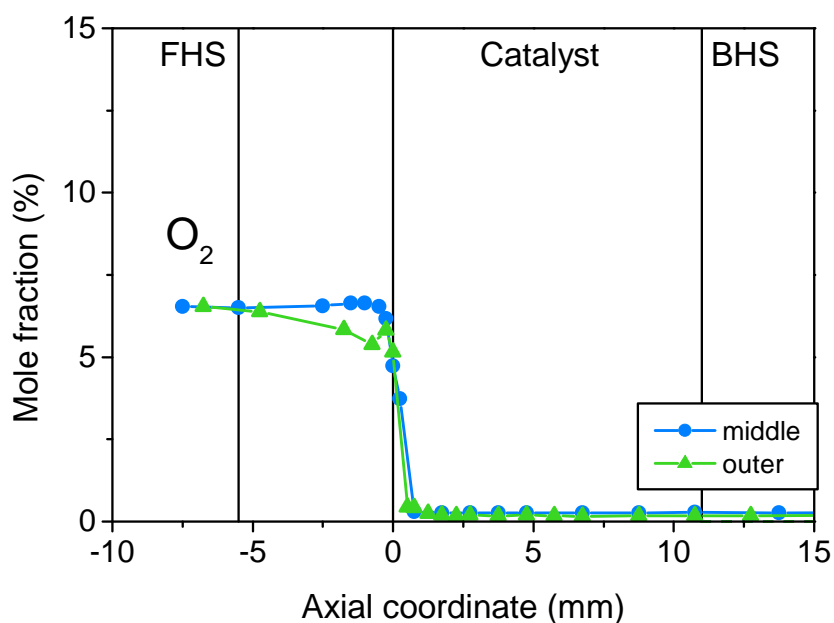
In general, it is observed that the detected concentration and temperature profiles are very similar for the central and middle channel. A detailed discussion of these axial profiles is already given in Section 4.1.1. For the outer channel, deviations are observed, which are pointed out and discussed in the following section.

Upstream the outer channel, a decrease in reactant concentrations and an increase in product concentrations is already detected at a position of -5 mm. Different reasons are conceivable. The velocity of the gas close to the reactor wall is lower than in the center of the reactor due to the boundary layer, which develops close to the wall. Thus, the effect of diffusion is stronger

4. CPOX of Methane and Ethanol over Rh/Al₂O₃

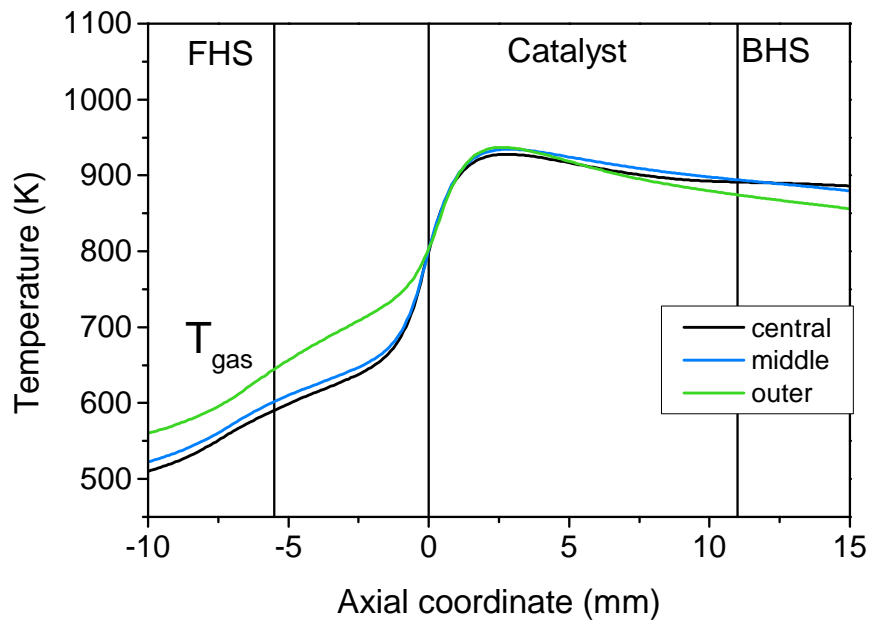


(a) Mole fraction of CH₄

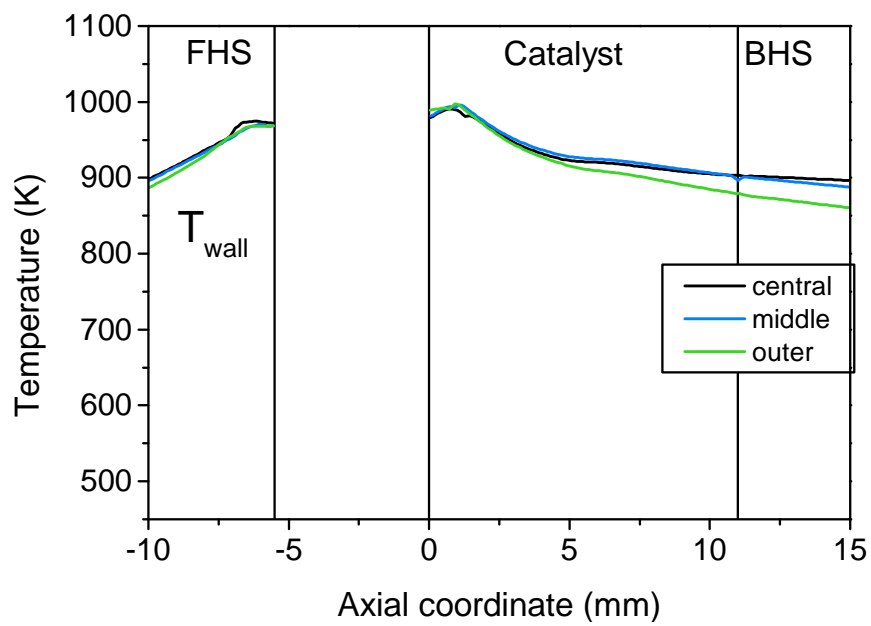


(b) Mole fraction of O₂

Figure 4.3: Mole fractions of the reactants, CH₄ (a) and O₂ (b), gas-phase temperature (c), and surface temperature (d) as a function of the axial coordinate for CPOX of CH₄ over Rh/Al₂O₃ at C/O = 1.0 in three different channels. One central channel (referred to as central), one channel at an intermediate position between the center and the periphery of the monolith (middle), and one channel close to the periphery of the monolith (outer). The dashed lines represent equilibrium concentrations. For oxygen, the equilibrium concentrations are zero.



(c) Gas-phase temperature



(d) Surface temperature

Figure 4.3: Continued.

4. CPOX of Methane and Ethanol over Rh/Al₂O₃

close to the reactor wall as the conductive flux is lower. Also, the temperature of the gas phase was at least 40 K higher in this region compared to a more central region. Simulations (not shown) using a gas-phase mechanism [161] with DETCHEM^{BATCH} [139] were performed to check for the possibility of gas-phase reactions. For the gas-phase temperature $T_{gas} = 722$ K (at $z = -1.85$ mm), residence times of ≥ 3 s are necessary in the simulations to observe gas-phase reactions. In the experiments, an average residence time of 13 ms is calculated at 722 K. The residence time in the boundary layer close to the wall is predicted by CFD simulations (not shown) to be ten times higher, i.e. 130 ms. This is still an order of magnitude smaller than the time necessary for gas-phase reactions to occur under the given conditions. Investigations are still ongoing, employing further CFD simulations to gain a deeper insight into the reasons for the detected profiles.

Inside the channel of the catalyst, the first part up to $z = 1.75$ mm shows very similar behavior for all three investigated channels. In this part, total oxidation partial oxidation and steam reforming are the predominant reactions. The oxy-reforming zone does not seem to be affected by the changes due to the different channel positions. This is the case even though the inlet conditions are not the same for all channels due to the deviation in concentration profiles upstream of the outer channel (see paragraph above).

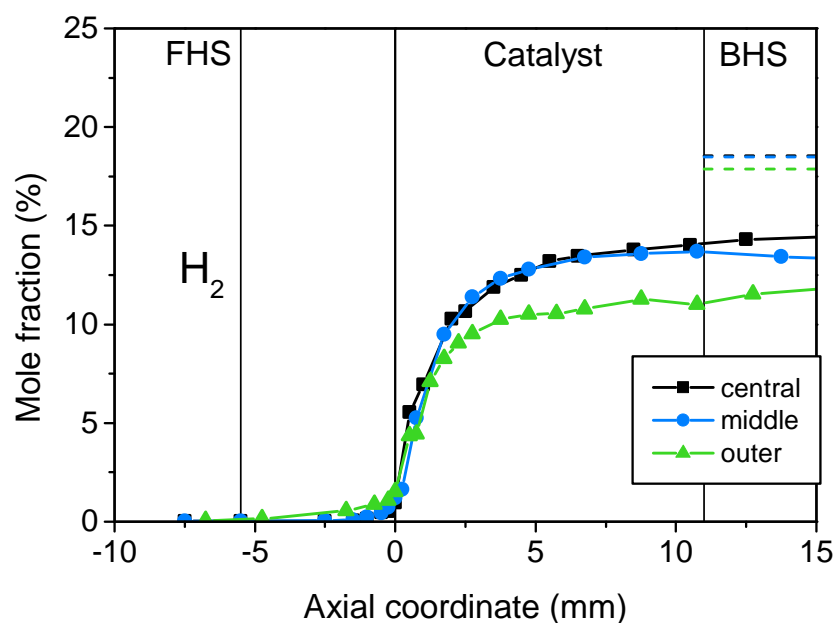
After all oxygen is consumed, endothermic steam reforming is the prevalent reaction. This is also the region, in which a difference in behavior for the outer channel compared to central and middle channel is recognizable. In the concentration profiles, it is clearly observable, that steam reforming occurs to a lesser extent in the outer channel. For methane, the outer channel shows a higher mole fraction at the outlet ($x_{CH_4} = 5.6\%$ compared to $x_{CH_4} = 3.9\%$ for the central channel; $\Delta x_{CH_4} = 1.7$ percentage points). The unit “percentage point” is used in this work for the difference between two values, which are given as percentages. The H₂O concentration decreases not as steeply as for the other two channels after the maximum at 0.75 mm. At the catalyst outlet, the

water concentration is 1 percentage point higher for the outer channel. The hydrogen concentration increases only slightly after 1.75 mm and reaches a value of approx. 11 % at the catalyst outlet, which is 3 percentage points lower than for central and middle channel. Accordingly, the rise in CO concentration is slower than for central and middle channel. At the catalyst outlet, a concentration of 4.5 % for the outer channel and 6.1 % for central and middle channel is observed. Concerning CO₂, a slight increase along the length of the outer channel is observed, leading to a concentration at the catalyst outlet of 2.7 % compared to 2.2 % for central and middle channel. It might be that under the conditions given in the outer channel, reverse WGS is favored. Especially the longer residence time in the outer channel would be beneficial for reverse WGS. Also for ethanol CPOX (see Section 4.2.3), it is observed that different channel positions influence the behavior in the reforming zone.

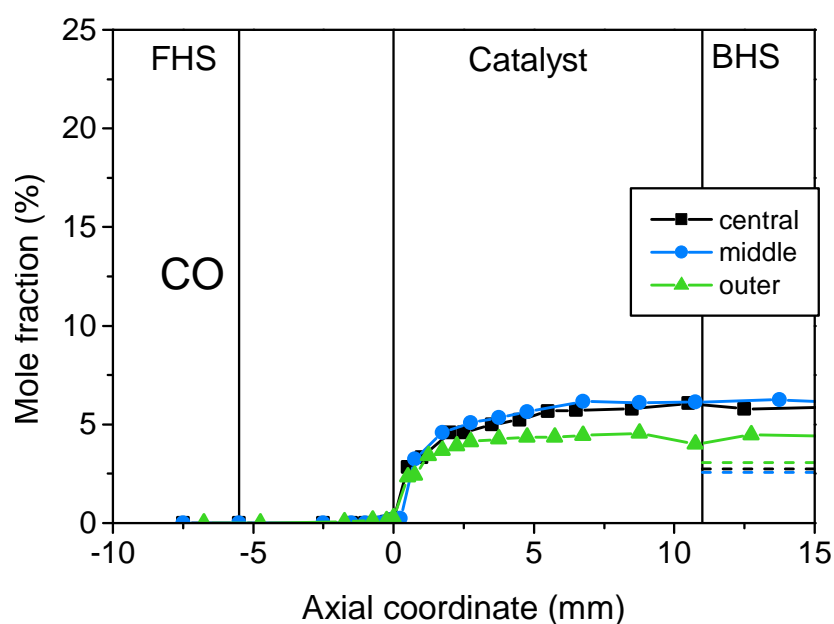
The temperature profiles also reveal a different behavior of the outer channel compared to the other investigated channels. A stronger decrease in surface temperature after the hot spot along the channel of the catalyst is observed for the outer channel ($T = 880$ K) than for middle and central channel ($T = 900$ K). The gas-phase temperature shows an according trend with the strongest decrease after the maximum for the outer channel to 873 K at the catalyst outlet (compared to 893 K for central and middle channel). These observations also fit with the lower extent of steam reforming in the outer channel, as endothermic steam reforming is less favored at lower temperatures.

One of the reasons for the lower temperature in the outer channel could be radial heat loss. The insulation of the reactor with quartz wool might not be sufficient to prevent radial heat radiation at the high surface temperatures of $T \geq 900$ K inside the furnace with a temperature of $T = 523$ K. The effect will be the strongest for the outer channel, which is closest to the reactor wall. Even though a higher residence time is expected in the outer channel, which would be favorable for reforming reactions, the lower temperature seems to outweigh the higher residence time.

4. CPOX of Methane and Ethanol over Rh/Al₂O₃



(a) Mole fraction of H₂



(b) Mole fraction of CO

Figure 4.4: Mole fractions of the main products hydrogen (a), carbon monoxide (b), water (c), and carbon dioxide (d) as a function of the axial coordinate for CPOX of CH₄ over Rh/Al₂O₃ at C/O = 1.0 in three differently-positioned channels. See Figure 4.3 for explanation of the channel positions. For hydrogen, equilibrium concentration for central channel is covered by the one for the middle channel.

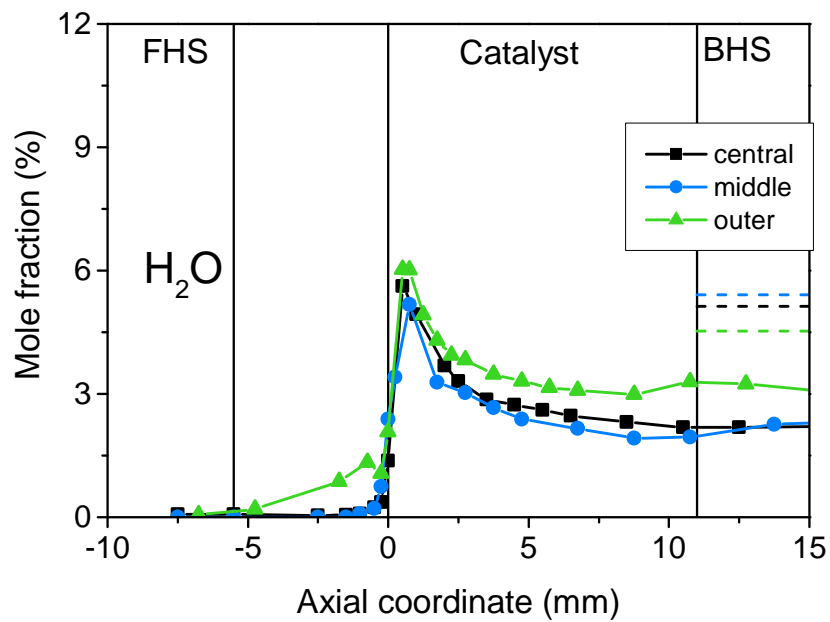
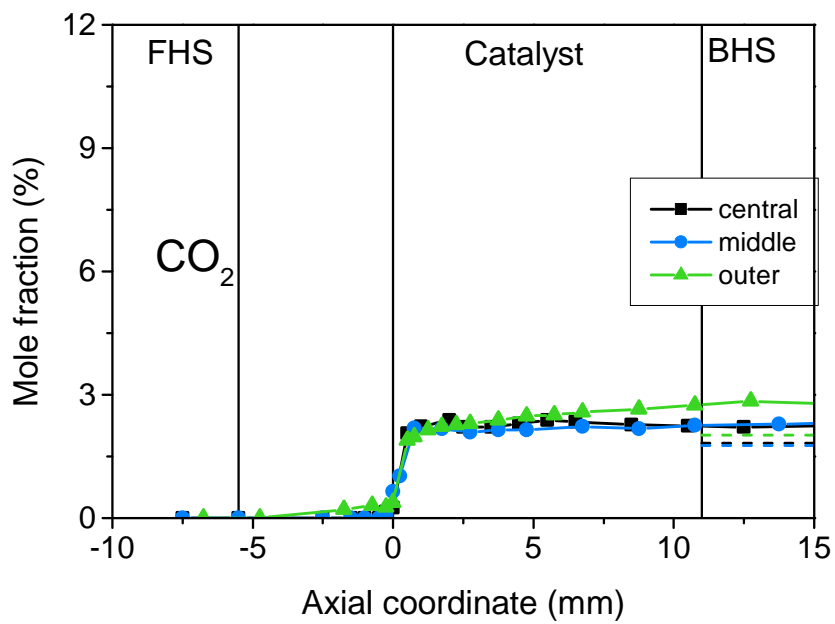
(c) Mole fraction of H_2O (d) Mole fraction of CO_2

Figure 4.4: Continued.

4. CPOX of Methane and Ethanol over Rh/Al₂O₃

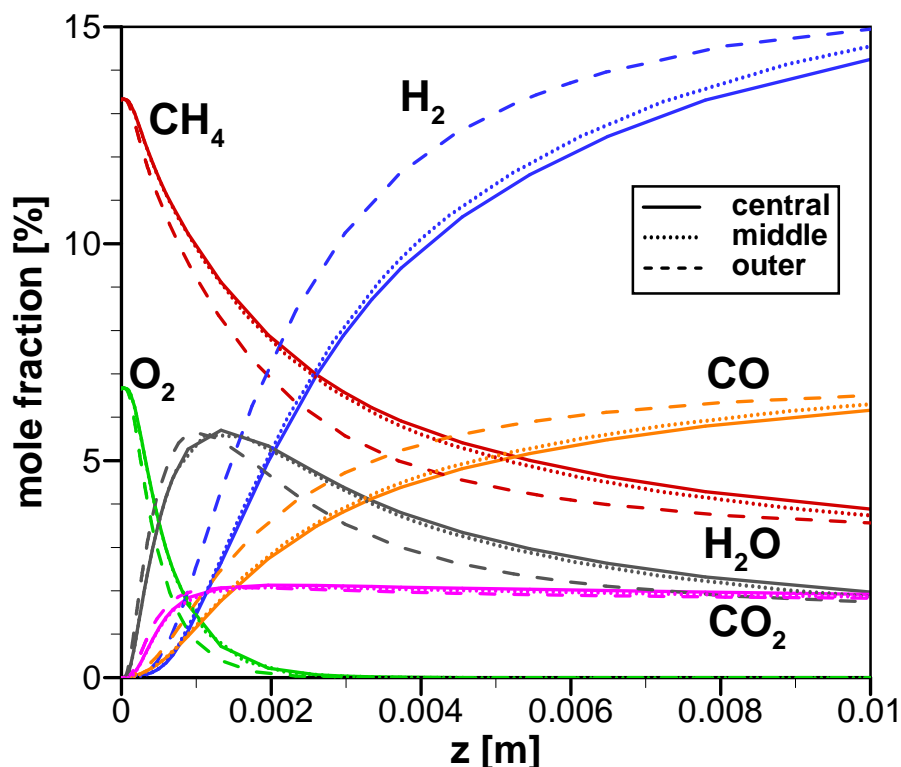


Figure 4.5: Mole fractions of reactants and products simulated by DETCHEM^{CHANNEL} as a function of the axial coordinate for CPOX of CH₄ over Rh/Al₂O₃ at C/O = 1.0 using the measured temperature profiles of the three differently positioned channels. From the 2D simulations, the values from the channel center are shown for each channel. Solid lines represent the values for the central channel, dotted lines for the middle channel and dashed lines for the outer channel. A lower velocity was employed for the outer channel (corresponding to 80 % of the one used for central and middle channel).

Simulations with the DETCHEM^{CHANNEL} code were performed for the three investigated channels (see Section 3.5.2). The measured gas-phase temperature at the catalyst inlet and the surface temperature profiles along the channels were used for the simulations. For the outer channel, a lower velocity, which corresponds to 80 % of the velocity in the central and middle channel, was applied. The lower velocity in the outer channel was applied to account for the boundary layer, which forms close to the channel wall and

which will also influence the flux into the outer channel. The simulation results displayed in Figure 4.5 show an opposite trend to the one observed in the experiments. The higher residence time causes higher hydrogen formation and higher methane and water conversion in the outer channel compared with to the same position in the central or middle channel. The highest difference of ≈ 1.9 percentage points for hydrogen mole fraction is noticeable at $z = 4$ mm. At positions $> z = 4$ mm, the difference between the concentrations of the outer and the other two channels decreases, with the result that the difference at the catalyst outlet is small, ≤ 0.4 percentage points depending on species. The temperature profile, on which also the simulations are based, is very similar for the three channels up to $z = 4$ mm. Therefore, the higher residence time at the same temperature leads to a higher conversion. Along the channel, syngas production decreases for the outer channel, probably due to the decrease in temperature, which becomes more prominent towards the catalyst outlet ($\Delta T = 20$ K at $z = 10$ mm). The reason for the different trends observed in experiment and simulation are not yet fully understood and further investigations are necessary to get a deeper insight.

4.1.2.1 Equilibrium Considerations

The equilibrium concentrations are shown as dashed lines in Figure 4.3 and Figure 4.4. At thermodynamic equilibrium, the methane concentration is very similar for all three channels with a value of $x_{\text{CH}_4, \text{equil}} \approx 1.4\%$. This shows that the lower temperature at the catalyst outlet for the outer channel ($\Delta T = 20$ K compared to central and middle channel) does not have a major influence on the equilibrium composition at the given conditions. Compared to the equilibrium, the experimentally measured concentration at the catalyst outlet is higher with a value of at least $x_{\text{CH}_4, \text{exp}} = 3.5\%$ (for the middle channel). Furthermore, a noticeable difference of the outer channel ($x_{\text{CH}_4, \text{exp}} = 5.6$ at 11 mm) to the other two channels is observed in the experiments as described above. The thermodynamic values of oxygen are all zero, which fits with the experimentally

4. CPOX of Methane and Ethanol over Rh/Al₂O₃

determined complete consumption of oxygen. Nevertheless, thermodynamic equilibrium is not reached for the investigated catalyst, as can be seen from the methane concentrations.

For the products, a difference in equilibrium composition is visible for the three different channels. Especially the outer channel deviates from the other two investigated channels, with lower H₂ and H₂O and higher CO and CO₂ concentrations. Nevertheless, the deviations are small, only in the range of 0.5 percentage points when comparing outer to central and middle channel. Compared to the experimental concentrations, the equilibrium concentrations of water and hydrogen are higher and the ones of CO and CO₂ are lower. As mentioned in Section 3.5.1, solid carbon in the form of graphite is included in the thermodynamic equilibrium calculations. A yielded amount of $\approx 28\%$ graphite is present in the equilibrium composition for all channels. Carbon formation was not monitored during the experiments. However, only small amounts of carbon formation are expected in the experiments, as the catalyst performance reaches a steady value for the performed measurements. Also the carbon balances closed within 10%, therefore, if carbon is formed, it will only be in small amounts.

The calculation of the thermodynamic equilibrium was also performed without the consideration of solid components (not shown). As for the calculations with graphite, only small deviations are observed at thermodynamic equilibrium for the different channels. The comparison of the experimental values and the equilibrium concentrations (for the calculation without solid carbon) shows higher H₂ and CO concentrations and lower H₂O and CO₂ concentrations at thermodynamic equilibrium. The mole fraction of methane at the equilibrium ($x_{\text{CH}_4, \text{equil}} \approx 2.6\%$ for the middle channel) is lower than the experimentally measured one ($x_{\text{CH}_4, \text{exp}} = 3.5\%$ for the middle channel). Thermodynamic equilibrium is not reached for the investigated catalyst, also in the case, for which solid carbon is not considered in the equilibrium calculations.

4.1.3 Evaluation of the Sampling Technique

The sampling capillary is placed inside the channel of the catalyst from the upstream side and thus affects the gas flux into the channel. As discussed in Section 3.2, this placement was chosen to avoid gas-phase reactions inside the sampling capillary. The colder area of the reactor is reached after a much shorter distance than for sampling from the downstream side of the catalyst. Nevertheless, even if gas-phase reactions are avoided in the capillary, the impact of the sampling probe in the investigated channel needs to be considered. For this evaluation, CFD simulations have been performed as described in Section 3.5.4. The simulations have been performed by Matthias Hettel and Bentolhoda Torkashvand. The investigations with the CFD calculations of the system started without reaction to see the influence on the volume flux for different axial and radial positions of the probe inside the channel. Furthermore, calculations with reaction have been performed for an insight into the effect on the reaction network. Finally, a comparison of the experimental and simulation results is accomplished.

4.1.3.1 Calculation without Reaction

Variation of Probe Position in the xy Plane

First, the influence of the position of the probe in the xy plane was investigated. Four different configurations are compared. Figure 4.6 shows the velocity in the z direction at the outlet of a reference channel (for case A) and at the outlet of channel_{probe} for each configuration. In configuration A, the probe is placed in the channel center, and in B midway between channel center and a corner. In D and E, the probe is positioned in the center of a wall and in a channel corner, respectively. For the last two configurations, the shape of the probe was varied to guarantee a block-structured grid with good quality. This variation slightly increases the cross-sectional area of the probe which is a conservative

4. CPOX of Methane and Ethanol over Rh/Al₂O₃

approximation with respect to the volume flux reduction in channel_{probe}. In all configurations, the probe tip is at $z_{\text{probe}} = 10$ mm, which means that the probe is completely launched into the monolith (Figure 4.7).

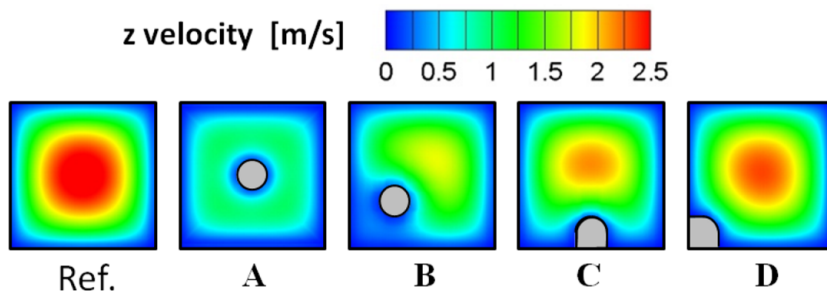


Figure 4.6: Z velocity in the xy plane at the outlet of channel_{ref} and four different configurations of the probe in channel_{probe} ($z_{\text{probe}} = 10$ mm).

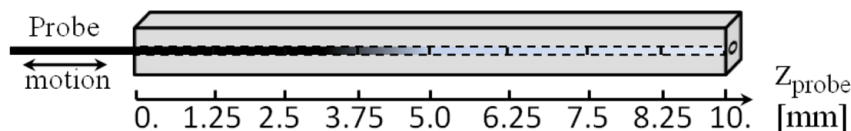


Figure 4.7: Positions of the probe tip z_{probe} used in the calculations.

In Table 4.1, the results for the different configurations are compared. The area-averaged velocity at the outlet of the channel with a probe $u_{\text{out,probe}}$ is strongly dependent on the probe position and decreased from D to A. The area-averaged velocity at the outlet of a reference channel $u_{\text{out,ref}}$ slightly changes vice versa, because the reduction of volume flux in channel_{probe} is distributed to the empty channels. From configuration A over B and C to D, the probe is positioned closer and closer to the corner of the channel. As the velocity profiles in the channels develop fast (see Figure 4.8), the channels are “filled” with boundary. Hence, the probe lies more and more in the area of influence of the channel walls where the velocity decreases to zero (see channel_{ref}). The smaller the original velocity inside channel_{ref}, the smaller is the effect of the blocking and of the additional adhesion at the wall of a capillary which is inserted into this

region. In case A, the ratio of the volume fluxes in $\text{channel}_{\text{ref}}$ and $\text{channel}_{\text{probe}}$ is approx. 46 %, in case D only approx. 9 %. The appropriate field of the velocity in z direction can be seen in Figure 4.6.

	$u_{\text{out,ref}}$ [m s ⁻¹]	$u_{\text{out,probe}}$ [m s ⁻¹]	$\frac{\dot{V}_{\text{channel,probe}}}{\dot{V}_{\text{channel,ref}}}$ [%]
A	1.29	0.62	46
B	1.28	0.82	62
C	1.22	1.12	79
D	1.18	1.00	91

Table 4.1: Velocities and ratio of volume fluxes for different configurations.

Variation of Probe Position in z Direction

For the case in which the probe is positioned in the center of the xy plane (configuration A in Figure 4.6), the influence of the position of the probe tip in the z direction was evaluated. Nine different positions ($z_{\text{probe}} = 0/1.25/2.5/3.75/5/6.25/7.5/8.25/10$ mm) of the probe tip were explored (Figure 4.7).

In Figure 4.8 the field of z velocity for the tip position $z_{\text{probe}} = 5$ mm is plotted. The viewpoint is the same as in Figure 3.15. The velocity versus the wall of the channels and also versus the probe surface decreases to zero. If the probe is launched into $\text{channel}_{\text{probe}}$ a part of the volume flux of the formerly empty channel cannot flow through this channel anymore, because it is blocked by the probe. Therefore, the velocity in $\text{channel}_{\text{probe}}$ is smaller than in the other channels. As a consequence, the velocity in all other channels increases slightly compared to a calculation where no probe would be considered. However, the velocity distribution in all channels without a probe is the same and not dependent from the distance to $\text{channel}_{\text{probe}}$. This indicates that the volume flux blocked by the probe is equally distributed to all other empty channels.

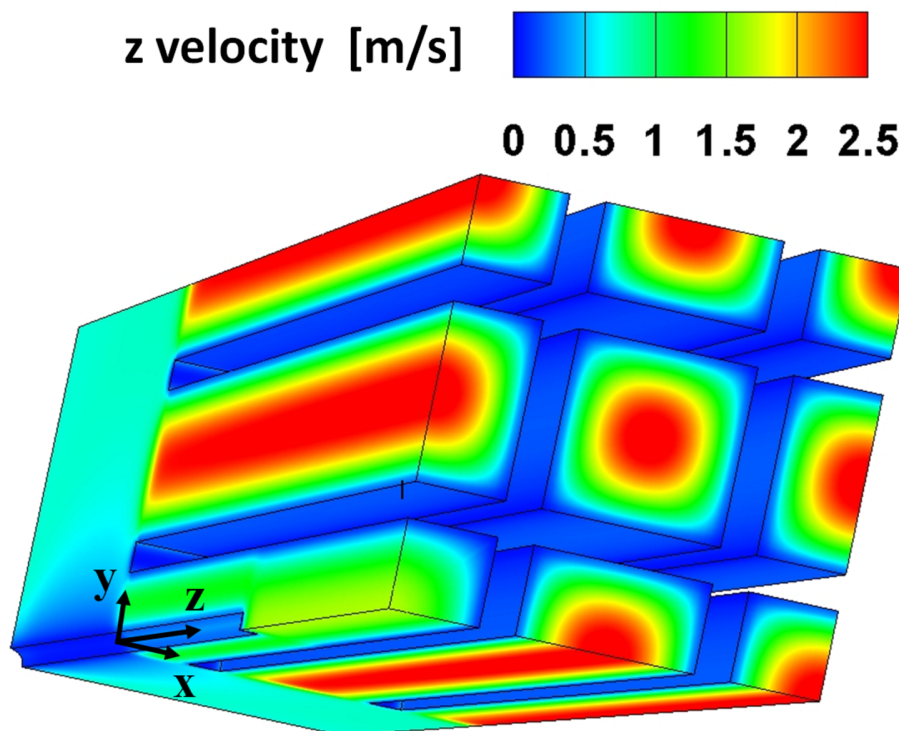


Figure 4.8: Z velocity for case A (see Figure 4.6) and $z_{\text{probe}} = 5$ mm.

Figure 4.9 shows isoplots of the velocity in the z direction in the yz plane through the center of the channels (left symmetry side of the calculation domain in Figure 3.14) including a region of 2 mm upstream of the monolith for three different z positions of the probe tip (from top to bottom: $z_{\text{probe}} = 0/5/10$ mm). The fluid flows from left to right. The white blocks indicate the solid parts of the monolith.

The velocity profile in the channels is completely developed after a distance of approx. 0.5 mm. As expected, the velocity in the channel with the probe is smaller, the deeper the probe is launched into the channel.

In Table 4.2, the results are given in detail. The values indicate that the deeper the probe is inserted into the channel, the smaller are the averaged velocity and the volume flux at the outlet of $\text{channel}_{\text{probe}}$. If the probe tip is at $z_{\text{probe}} = 0$ mm, the volume flux in $\text{channel}_{\text{probe}}$ is approx. 96 % of the volume flux in $\text{channel}_{\text{ref}}$. If the probe is inserted up to the end of the channel

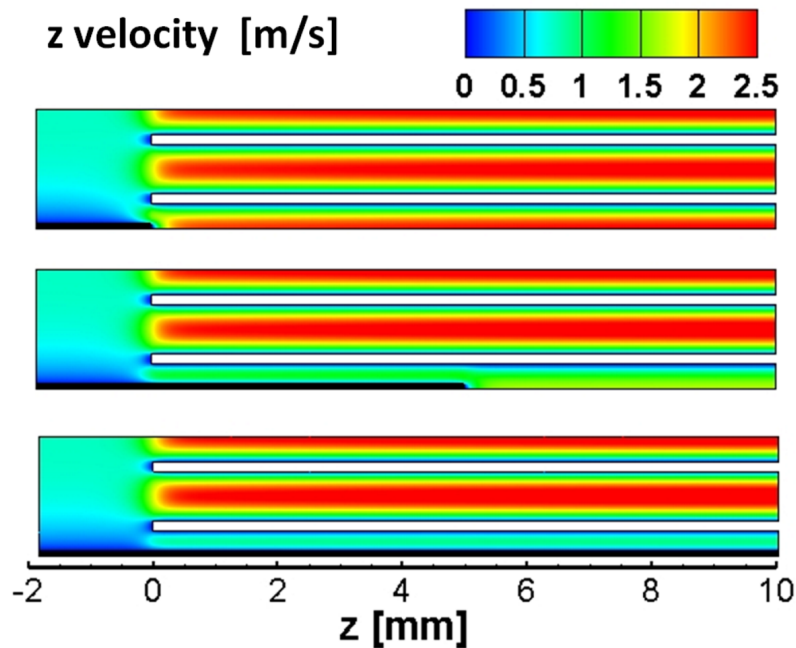


Figure 4.9: Z velocity for case A in the yz plane for three different positions $z_{\text{probe}} = 0/5/10$ mm (from top to bottom).

($z_{\text{probe}} = 10$ mm), the volume flux in channel probe is only approx. 46 % of the volume flux in channel_{ref}. In spite of that, the cross sectional area of channel_{probe} is only approx. 3.5 % smaller than that of channel_{ref}. The reason for the large impact of the probe on the volume flux is the boundary layer which develops at the outer wall of the probe inside and already upstream of the channel. The velocity at the outlet of channel_{ref} slightly increases with z_{probe} , because the volume flux which does not pass channel_{probe} is distributed among the other channels.

Influence of Operational Conditions

Additional calculations were performed in which the boundary conditions varied compared to the values given in Section 3.5.4.5. It is observed that the ratio of the volume fluxes in the channel with probe and in the reference channel is rather independent from the inflow velocity and the wall temperature. This means that for a larger flow rate at the inlet, the velocities in all channels

4. CPOX of Methane and Ethanol over Rh/Al₂O₃

z_{probe} [mm]	$u_{\text{out,ref}}$ [m s ⁻¹]	$u_{\text{out,probe}}$ [m s ⁻¹]	$\frac{\dot{V}_{\text{channel,probe}}}{\dot{V}_{\text{channel,ref}}}$ [%]
0.0	1.27	1.22	96
1.25	1.27	1.05	82
2.50	1.27	0.96	75
3.75	1.28	0.87	68
5.00	1.28	0.80	62
6.25	1.28	0.74	57
7.50	1.29	0.69	52
8.75	1.29	0.64	49
10.0	1.29	0.62	46

Table 4.2: Averaged velocities and ratios of volume fluxes for a reference channel and the channel with probe for different z positions of the probe tip z_{probe} .

increase, but the ratio remains the same. Also, the suction at the probe tip has a negligible influence, even if the volume flux sucked is increased to 5 ml min⁻¹. The reason for this is that only a small portion of the volume flux of the entire channel is sucked in.

4.1.3.2 Calculation with Reaction

Figure 4.10 shows distributions of different quantities for configuration A for $z_{\text{probe}} = 5$ mm in the same yz plane as in Figure 4.9. The concentrations of methane (a) and oxygen (b) decrease relatively fast due to total oxidation of methane, which forms water (c) with a maximum at ca. 2 mm. Afterwards, the water is consumed by endothermic steam reforming, which yields hydrogen (d)

and carbon monoxide (not shown). The comparison of the concentrations in the different channels shows that the entire process takes place earlier (in terms of the z position) in the channel with the probe than in a channel without a probe. The reference to the real time can be seen in the plot of the residence time τ (e). As the velocity in $\text{channel}_{\text{probe}}$ is smaller than that in $\text{channel}_{\text{ref}}$, the residence time increases faster in the z direction. Therefore, at the same z position, the reaction progress in $\text{channel}_{\text{probe}}$ is advanced further than in $\text{channel}_{\text{ref}}$. The entire process is dominated by the given wall temperature (part (f)), as the wall temperature is fixed and the velocity is relatively slow. Except for the first millimeter, all quantities are mainly homogeneous in the cross-sectional area of each channel, i.e. that strong radial mass-transfer limitation of the reaction rate occurs only in the entrance zone.

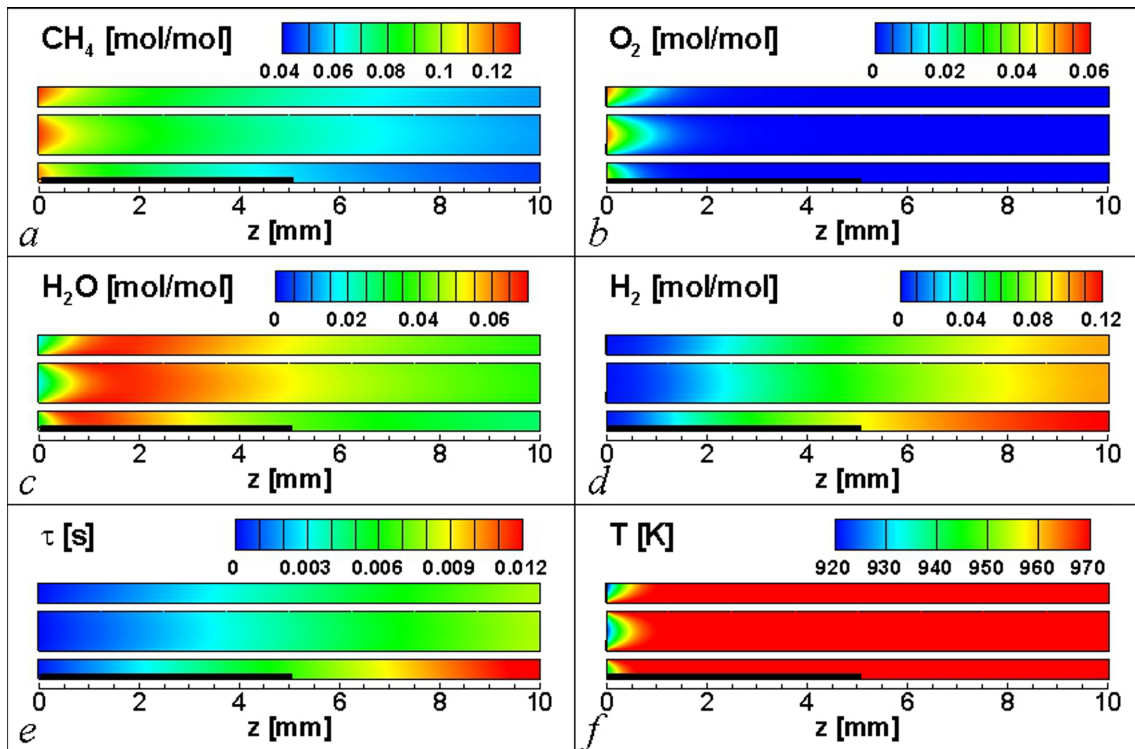


Figure 4.10: Calculated concentrations of CH_4 (a), O_2 (b), H_2O (c), H_2 (d), residence time τ (e), and temperature T (f) in the yz plane through channel centers (case A, $z_{\text{probe}} = 5$ mm, *parameter set 1*).

4. CPOX of Methane and Ethanol over Rh/Al₂O₃

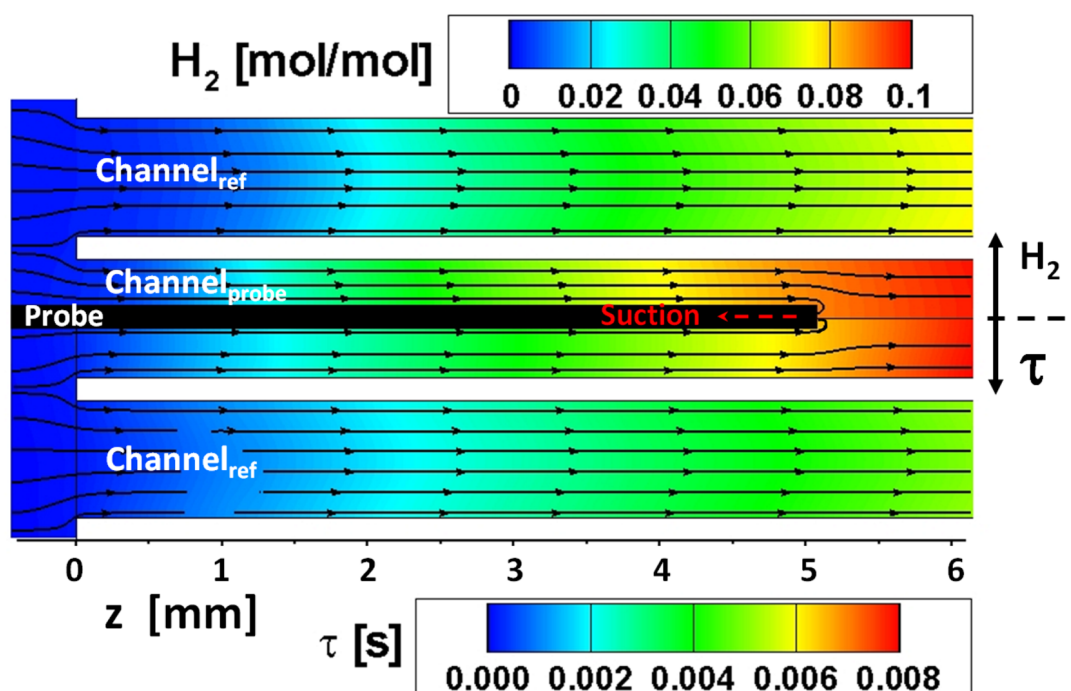


Figure 4.11: Calculated distributions of H₂ (upper half) and residence time (lower half) in the yz plane through channel centers (case A, $z_{\text{probe}} = 5 \text{ mm}$, *parameter set 1*).

Figure 4.11 shows an enlargement of the region near the probe tip in Figure 4.10 for the quantities H₂ concentration (upper half) and residence time τ (lower half). The flow is from left to right. The streamlines depict the direction of the flow and show the suction of the capillary. The reduced volume flux in channel_{probe} leads to a residence time of $\tau \approx 7 \text{ ms}$ for the fluid at the probe tip ($z = 5 \text{ mm}$) versus a value of $\tau \approx 4 \text{ ms}$ at the same axial position in channel_{ref}. Therefore, the concentration of the hydrogen sucked in at the probe tip is higher than that in the reference channel (8 % versus 6 %).

4.1.3.3 Analysis of Residence Time

Figure 4.12 shows the analysis of the residence times along the channel axis. The residence time of channel_{ref} increases nearly linearly in time (solid blue line) along the z position of the channel. The solid red line shows the residence

time in $\text{channel}_{\text{probe}}$ for a varying position of the probe tip z_{probe} . For example, for $z_{\text{probe}} = 5 \text{ mm}$, the residence time at the probe tip is $\tau \approx 6.8 \text{ ms}$, whereas at the equivalent z position in $\text{channel}_{\text{ref}}$, it is $\tau \approx 4 \text{ ms}$ (black dotted lines with arrows). The difference between the residence times at the probe tip and the residence time at the same z position in an open channel increases as the probe is launched deeper into the channel. Therefore, the difference of the reaction progresses at the same z position of the two channels also increases. The two calculated curves can be fitted with the following equations (see dashed blue and dashed red line in diagram):

$$\tau_{\text{channel,ref}}(z) = 7.8 \cdot 10^{-4} \cdot z + 2 \cdot 10^{-4} \quad (4.1)$$

$$\tau_{\text{channel,probe}}(z_{\text{probe}}) = 6.61 \cdot 10^{-5} \cdot z_{\text{probe}}^2 + 1 \cdot 10^{-3} \cdot z_{\text{probe}} + 2 \cdot 10^{-4} \quad (4.2)$$

Development of a Conversion Function

Figure 4.13 shows the mole fractions of three species sucked from $\text{channel}_{\text{probe}}$ at different axial positions of the probe tip z_{probe} (dashed lines) and the concentrations at equivalent positions z at the axis of a channel without a probe, $\text{channel}_{\text{ref}}$ (solid lines). For each axial position z_{probe} , the concentration of H_2 is larger and the concentration of CH_4 and H_2O are smaller than at z_{ref} . Hence, in an equivalent experiment, the data collected on the basis of suction in $\text{channel}_{\text{probe}}$ would be defective. The further downstream the location of the tip is, the more overrated the progress of conversion at each tip position would be. For example, for $z_{\text{probe}} = 5 \text{ mm}$, the concentration of the hydrogen sucked from $\text{channel}_{\text{probe}}$ is approx. 8.5 %, and the one in $\text{channel}_{\text{ref}}$ would be only approx. 6 %. The aim is to find a corresponding position z in $\text{channel}_{\text{ref}}$ that exhibits the same residence time for every axial position of the probe tip z_{probe} . Equating Equations (4.1) and (4.2) leads to

4. CPOX of Methane and Ethanol over Rh/Al₂O₃

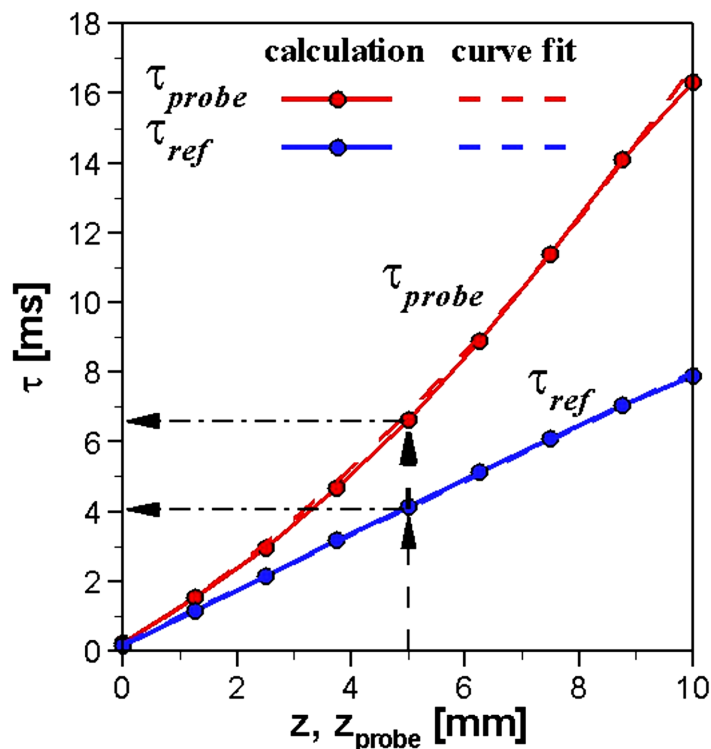


Figure 4.12: Calculated residence time along channel axis for channel with and without probe (case A, parameter set I).

$$z = 0.0847 \cdot z_{\text{probe}}^2 + 1.28 \cdot z_{\text{probe}} \quad (4.3)$$

If the two positions z and z_{probe} exhibit the same residence time, it can also be expected that the reaction progress and beyond that also the species concentrations are the same.

As long as only two channels (with and without probe) of the monolith, excluding the part upstream of the monolith, are compared, the function is independent of the flow conditions (volume flux and temperature of gas) and only dependent on geometry. This was also proven based on analytical considerations. Due to the influence of the part of the probe which lies upstream of the monolith, a weak dependency on the boundary conditions can be observed in the numerical calculations.

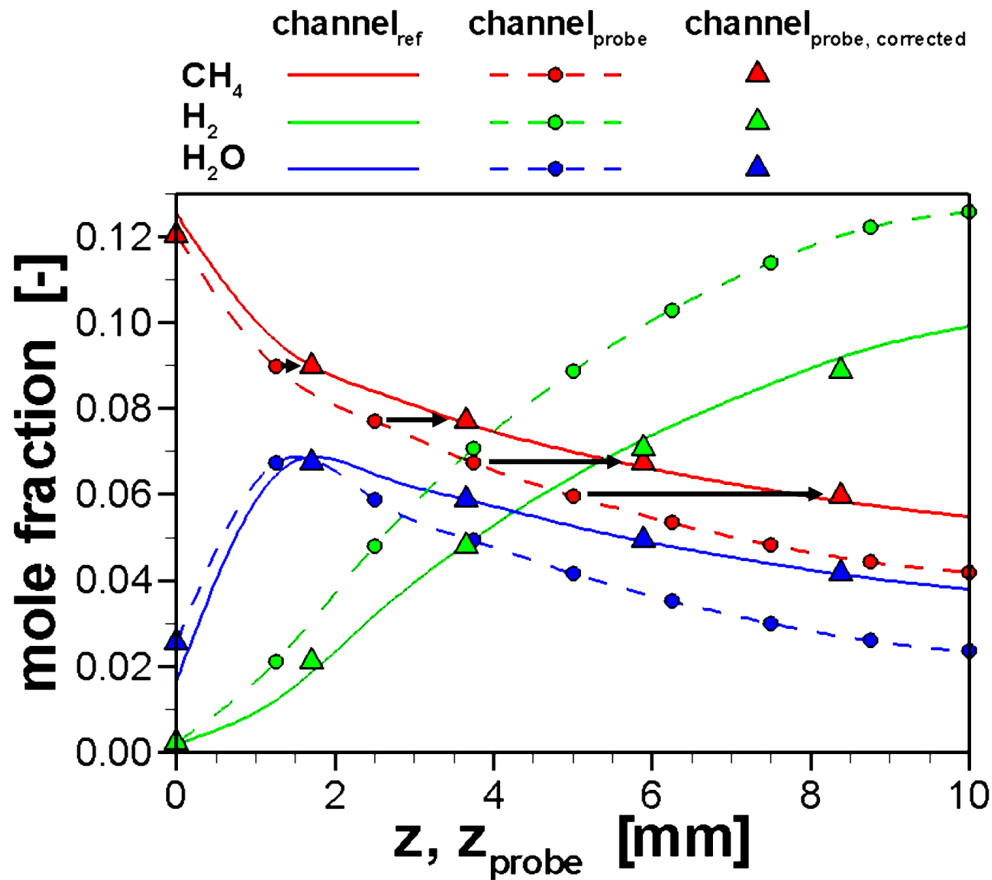


Figure 4.13: Comparison of calculated concentrations for a channel without probe, with probe, and corrected values for channel with probe for the species CH₄, H₂O, and H₂ along channel axis (case A, *parameter set 1*).

The deduction of a conversion function for the *parameter set 2* (see Section 3.5.4.5) used in Section 4.1.3.4 leads to z values which differed up to a maximum of 5% from the values calculated using the function above. Therefore, Equation (4.3) is also applied in Section 4.1.3.4.

Application of the Conversion Function

The triangles referred to as $\text{channel}_{\text{probe, corrected}}$ in Figure 4.13 represent the values which were yielded after transformation of the values of $\text{channel}_{\text{probe}}$ by applying the correction function. This leads to an axial shift of the values. For

4. CPOX of Methane and Ethanol over Rh/Al₂O₃

clarity, the result of the application of the conversion function is marked with black arrows for the H₂ concentration at four different positions of the probe tip ($z_{\text{probe}} = 0/1.25/2.5/3.75/5$ mm). It can be seen that, for each species, the concentrations after the shift (triangles) coincide very well with the values in channel_{ref} without a probe (solid lines). This data would be of interest in a comparable measurement because they are not influenced by the probe.

The application of this approach is only feasible if the time scale of convection is large compared to the time scales of reaction and radial diffusion (no mass-transfer limitation). Then, the radial gradients of all quantities are small. Additionally, the temperature gradient along the channel should be small (here, constant), and the process should be isothermal to a large extent. If not, the result of a comparison of two channels with regard to the local reaction progress would not be dependent on residence time only but also on the local gas temperature.

This approach shows that measured data (collected in a channel with probe) can in principle be compared with the results of 1D or 2D calculations (calculated for a channel without probe), even if it is falsified by the influence of the probe. If the process is largely isothermal, the use of the conversion function will lead to a correction of the measuring error. However, for different geometrical structures or positions of the probe in the xy plane (e.g., cases B, C, and D), a new conversion function has to be developed by applying CFD calculations.

4.1.3.4 Comparison of Experiment and Simulation

The calculations shown in this section were done using *parameter set 2* (see Section 3.5.4.5). First, the applicability of the conversion function (Equation (4.3)) on the calculated results is discussed and, second, the calculation is compared to the measurements.

As Figure 4.13 already showed for the *parameter set 1* (see Section 3.5.4.5), the comparison of three different species (CH_4 , H_2O and H_2) along the channel axis for $\text{channel}_{\text{ref}}$ (solid lines) and for nine different positions of the probe tip in $\text{channel}_{\text{probe}}$ (dashed lines) is plotted in Figure 4.14 for the *parameter set 2*. If the probe tip is, for example, located at $z_{\text{probe}} = 5$ mm, the concentrations of CH_4 and H_2 are larger and the concentration of H_2O is smaller than those/those at the same axial position in the reference channel. The residence time in $\text{channel}_{\text{probe}}$ is larger than the residence time of $\text{channel}_{\text{ref}}$, leading to a larger reaction progress at the same axial position of the probe tip in $\text{channel}_{\text{probe}}$ compared to the same z position in $\text{channel}_{\text{ref}}$.

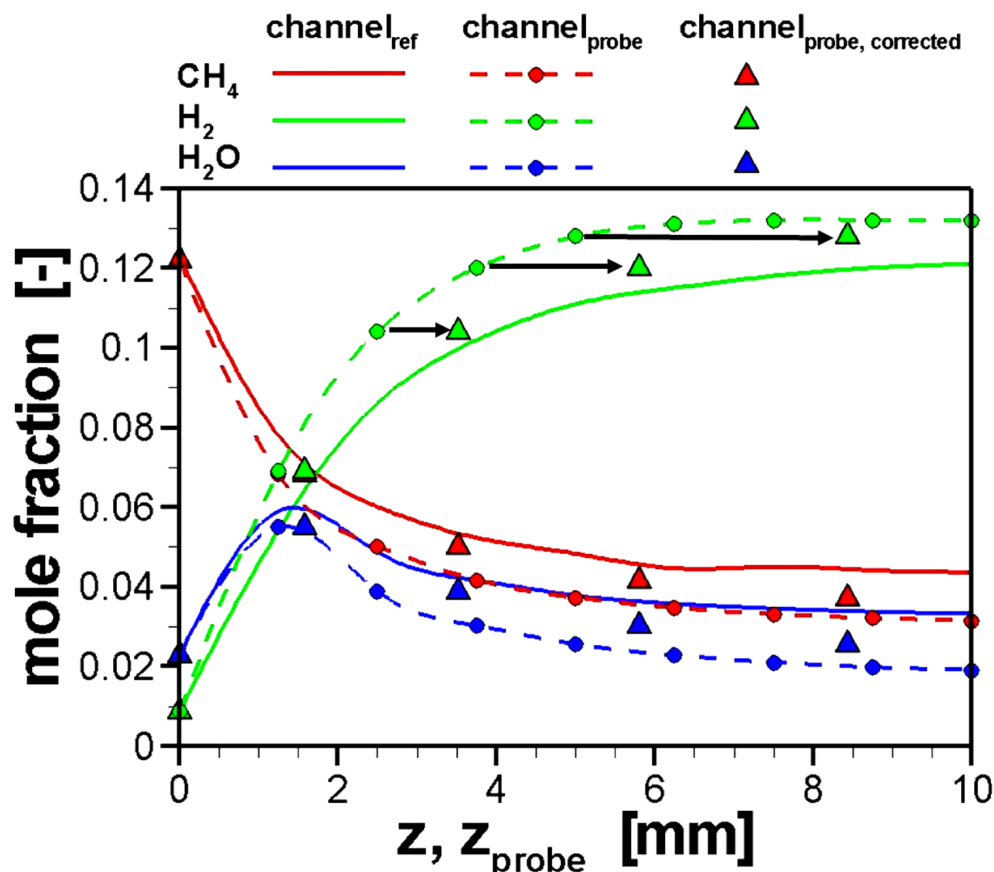


Figure 4.14: Comparison of calculated concentrations for a channel without probe, with probe, and corrected values for channel with probe for the species CH_4 , H_2O , and H_2 along channel axis (case A, *parameter set 2*).

4. CPOX of Methane and Ethanol over Rh/Al₂O₃

Again, the triangles referred to as $\text{channel}_{\text{probe,corrected}}$ represent the values which are yielded after transformation of the values of $\text{channel}_{\text{probe}}$ by applying the correction function (Equation (4.3)). For each species, the concentration values are shifted to larger z positions, and thus, towards the values which refer to an empty channel. For three values of the H₂ concentration, the shift is additionally marked with black arrows. However, contrary to the results in Figure 4.13, the values of $\text{channel}_{\text{ref}}$ and $\text{channel}_{\text{probe,corrected}}$ differ more when the z position is larger.

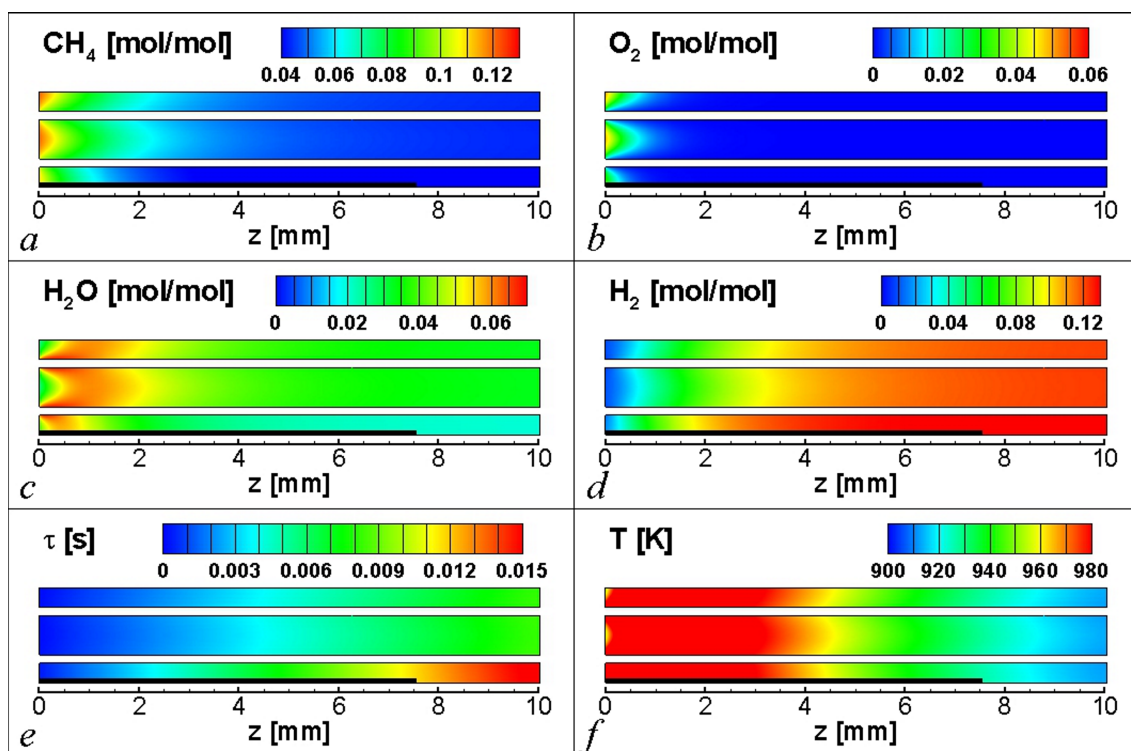


Figure 4.15: Calculated concentrations of CH₄ (a), O₂ (b), H₂O (c), H₂ (d), residence time τ (e), and temperature T (f) in the yz plane through channel centers (case A, $z_{\text{probe}} = 7.5$ mm, *parameter set 2*).

To explain this, the distributions of different quantities (for $z_{\text{probe}} = 7.5$ mm) are shown in Figure 4.15. The fields of the concentrations and the residence time are qualitatively the same as in the calculation with a constant wall temperature (Figure 4.10). Apart from the inlet region, the radial gradients are relatively small. The isoplot of the temperature denotes that the gas temper-

ature is nearly isothermal up to approx. $z = 3$ mm. Hence, for the first three probe positions ($z_{\text{probe}} = 0/1.25/2.5$ mm), the correction function is applicable, leading to a good agreement between the values of $\text{channel}_{\text{probe,corrected}}$ and those in $\text{channel}_{\text{ref}}$ (see Figure 4.14). Downstream, the gas temperature decreases and the values corrected with the conversion function differ more and more from the values in $\text{channel}_{\text{ref}}$. The reason for this is that the reaction progress is not dependent on residence time only. In this case, it is also dependent on the local gas temperature.

This means that, for non-isothermal conditions, the measuring error due to the influence of a probe could not be corrected retrospectively. To compare experimental data with simulations, the probe has to be taken into account in the simulations. The measured values could not be reproduced by applying a one- or two-dimensional calculation.

As the position of the probe in the xy plane is not clearly defined in the experiments, the results of the simulation of case A were chosen for the sake of comparison. For this position, the probe has the largest influence.

In Figure 4.16, the measured data is plotted together with the calculated concentration profiles in the center of the channels with and without a probe starting upstream of the catalyst at $z = -2.5$ mm up to the end at $z = 10$ mm. Inside the channel of the catalyst ($z = 0 - 10$ mm), the values for the empty $\text{channel}_{\text{ref}}$ (solid lines) differ from the measured data (square symbols). In contrast, the concentrations for the different positions of the probe tip in $\text{channel}_{\text{probe}}$ (dashed lines) agree very well with the measured values. Only the position of the maximum of H_2O is a little bit further downstream in the calculation compared to the measurement. The important statement that can be gained from this plot is the general influence of a probe, which is positioned in the channel center, on the data.

In the region upstream of the catalyst, the influence of the capillary on the concentration profiles is negligible. Nevertheless, an interesting shape of the

4. CPOX of Methane and Ethanol over Rh/Al₂O₃

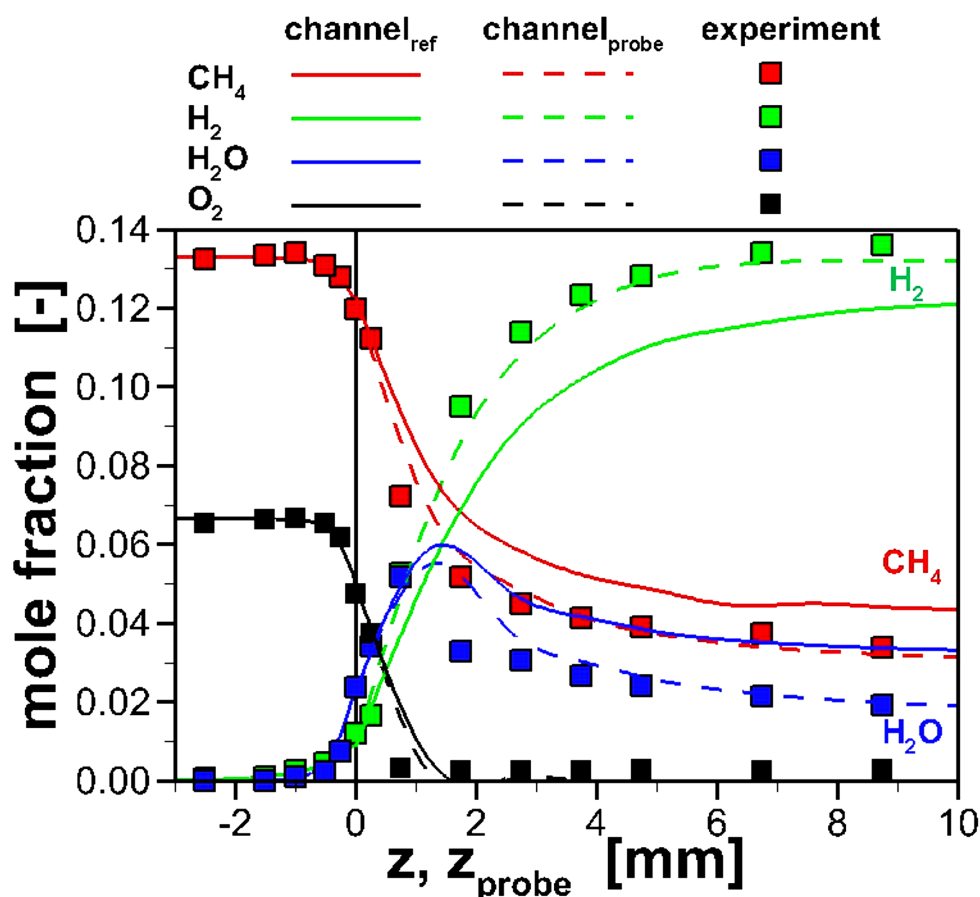


Figure 4.16: Comparison of calculated (with and without probe) and measured concentrations for the species CH₄, O₂, H₂O, and H₂ as function of axial coordinate (case A, *parameter set 2*).

concentration profiles can be observed. For the calculations as well as for the experiments, the concentrations of oxygen and methane start to show a decrease already at $z = -0.5$ mm and the concentrations of water and hydrogen begin to increase from $z = -1$ mm.

In the CFD simulations shown in Figure 4.16, gas-phase reactions are not enabled in the calculation method used. This leaves diffusion as source for the decrease in reactants and increase in products upstream of the catalyst in the simulations. The operating conditions in the region between $-1 < z < 1$ mm, e.g. high temperature ($T = 690$ K) and large concentration gradients, favor diffusion effects. In this region, the diffusive flux of the species is in the same

order of magnitude than the convective flux. The close fit between measured and calculated data upstream of the catalyst is a piece of evidence that also in the experiments, no gas phase reactions take place. Additionally, simulations including a gas phase mechanism [161] using DETCHEM^{BATCH} [139] did not show a conversion of gas phase species for the reaction conditions given in this region, as mentioned in Section 4.1.2.

4.1.4 Modeling of the Entire Monolith

This section aims for a more global consideration of the monolith using simulation tools. The newly developed code DUO (see Section 3.5.5) was used to compute the behavior in a quarter of a monolith including the solid body for catalytic partial oxidation of methane at $C/O = 1.0$. DUO simulations were performed by Matthias Hettel. A quarter of a monolith was sufficient to represent a complete monolith due to symmetry conditions (see Section 3.5.5). This approach combines 3D simulation of the flow upstream of the catalyst with 2D simulation inside the channel of the monolith. This combination leads to a reasonable computing time, which allows for the examination of global effects, such as heat dissipation from the front face of the catalyst.

Figure 4.17 displays the simulated temperature distribution in the monolith. The temperature is fixed to 1026 K at the front face of the catalyst and 906 K at the back face. A decrease in temperature is observed in the channel of the honeycomb catalyst, reaching values close to the outlet value at $z = 4$ mm. A part upstream of the catalyst ($L = 5$ mm) has also been taken into consideration, showing a preheating of the gas by the hot surface of the catalyst front. This effect is stronger for the channels close to the reactor wall, as a boundary layer with a lower velocity forms close to the wall. Furthermore, the channels closest to the wall, which are partially sliced, are blocked for gas flux, leading to an even lower velocity in this region. This condition was chosen, to represent the experimental conditions, where ceramic fiber paper is wrapped around the

4. CPOX of Methane and Ethanol over Rh/Al₂O₃

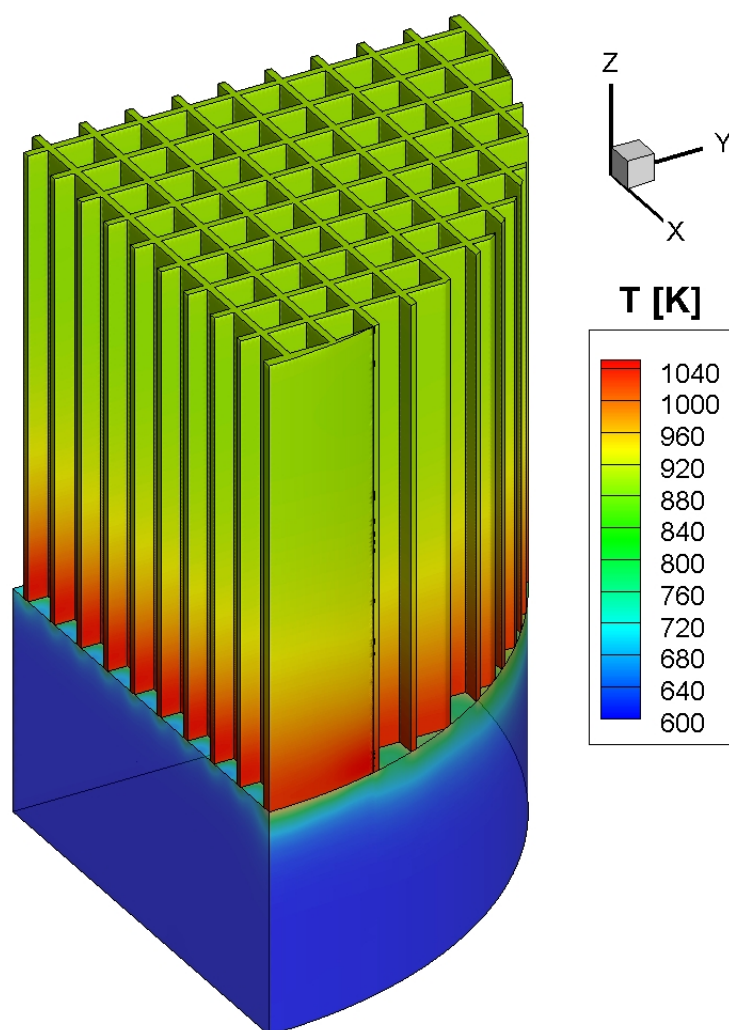


Figure 4.17: 3D temperature distribution in 1/4 of the monolith for CPOX of CH₄ over Rh/Al₂O₃ at C/O = 1.0.

monolith to prevent gas by-pass and which will block the flow in the partially sliced channels. Gas-phase reactions are not taken into consideration for the calculation, as it is commonly agreed in literature upon an absence of gas-phase reactions in methane CPOX [6, 32, 69, 70].

A comparison of experimental and calculated mole fractions of reactants and products is shown in Figure 4.18. It has to be taken into account that these are the first results with the newly developed DUO, leaving room for further improvement. Moreover, the influence of the capillary is not taken into considera-

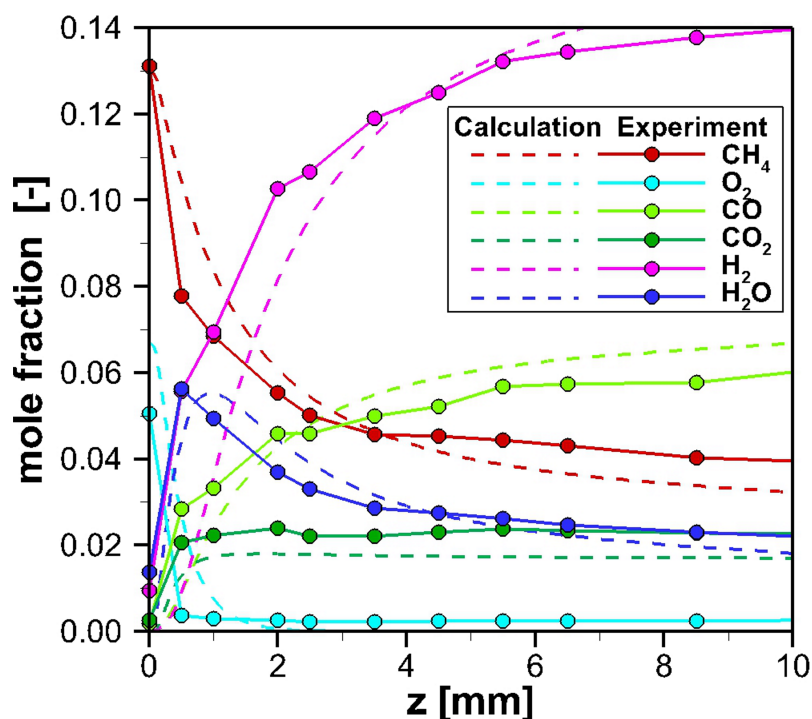


Figure 4.18: Mole fractions of reactants and products as a function of the axial coordinate for CPOX of CH_4 over $\text{Rh}/\text{Al}_2\text{O}_3$ at $\text{C}/\text{O} = 1.0$. Experimental results are shown for a central channel and are displayed as symbols connected with lines. Simulation results for a central channel are shown as dashed lines and are taken from a 3D simulation as shown in Figure 4.17.

tion in these simulations. Nevertheless, the simulation results closely resemble the experimental results. Thus, using DUO for the prediction of global effects is reasonable.

4.1.5 Summary for Methane

Spatially-resolved concentration and temperature profiles were used to understand the reaction network in catalytic partial oxidation of methane over $\text{Rh}/\text{Al}_2\text{O}_3$. The investigations show that the channel of the honeycomb catalyst can be split into two different zones, the oxy-reforming zone and the reforming zone. The oxy-reforming zone is located on the first millimeter of the catalyst

4. CPOX of Methane and Ethanol over Rh/Al₂O₃

and is dominated by total oxidation. Partial oxidation and steam reforming also proceed. All available molecular oxygen is consumed in this zone. The reforming zone starts, when all oxygen has been depleted. Here, steam reforming is the prevalent reaction. This behavior also agrees with literature reports [10, 12, 33]. Three different channels in a catalytic monolith were investigated in this work, to gain an insight into the influence of the channel position in the monolith on the gas composition and temperature distribution. The study reveals that the oxy-reforming zone is not affected by the channel position, but the reforming zone is. Less steam reforming occurs in an outer channel, which is positioned close to the periphery of the monolith, where a lower gas and wall temperature is detected and a lower gas velocity is suspected. Radial heat losses at the reactor wall could be, at least partially, responsible for the lower temperature in the outer channels.

It is very important to know the influence of the sampling technique on the detected data. CFD simulations with nine channels, including the capillary inside one of the channels, were performed to be able to compare the behavior of a channel with and without probe. The results reveal a distinct difference for the channel with capillary, which is the stronger, the further the capillary is inserted into the channel. The residence time is higher inside the channel with probe, leading to an upstream shift of the concentration profiles for this channel compared to a channel without probe. This deviation has to be taken into consideration, for quantitative interpretation of the values obtained with the sampling technique. CFD simulations including the probe, as done here, are necessary to quantify the influence.

To investigate global effects in the monolith, very detailed CFD simulations demand high computation times. Thus, a more time efficient method was developed. In this method, a quarter of a monolith is simulated by DUO, a gateway between a CFD software and the software DETCHEMTM. An overall reasonable reproduction of the experimental results is possible with this newly developed tool.

For the design of a CPOX reformer, the radial heat loss needs to be taken into account. The hot outlet gas of the downstream fuel cell could be used for heat recovery by designing a concentric tube reactor with the outlet gas in the outer ring, flowing counter-currently to the gas inside the reactor tube. Furthermore, for methane, a C/O ratio < 1.0 should be chosen, to reach higher conversion of methane and higher hydrogen yields.

4.2 Ethanol²

Ethanol is an alternative fuel produced from biomass. Often, mixtures of ethanol and gasoline are used as automotive fuels, e.g. E 10 and E 85 with 10 vol-% and 85 vol-% ethanol, respectively. 95 RON gasoline (“Super Benzin”) also contains 5 vol-% ethanol to increase the octane number and the knock resistance of the fuel.

4.2.1 Spatial Profiles in a Single Channel

In this section, typical characteristics of the concentration and temperature profiles for a C/O ratio of 0.75 are discussed. The spatial sampling technique was applied to gain insight into the CPOX of ethanol on Rh₆₀₀ under autothermal conditions (see Section 3.3.3 for detailed operating conditions). The axial temperature profiles collected in the central channel of the catalytic monolith are reported in Figure 4.19 (a). The gas-phase temperature measured by the thermocouple shows a steep rise from 771 K to 950 K in the first part of the catalyst until reaching 956 K at 3 mm, then a slight decrease to 943 K occurs towards the end of the monolith. Differently from the thermocouple data, the temperature

²Major parts of this section have been taken from [102]. Reprinted (adapted) from Applied Catalysis A: General, 467, D. Livio, C. Diehm, A. Donazzi, A. Beretta and O. Deutschmann, Catalytic partial oxidation of ethanol over Rh/Al₂O₃: Spatially resolved temperature and concentration profiles, 530 - 541, Copyright (2013), with permission from Elsevier.

4. CPOX of Methane and Ethanol over Rh/Al₂O₃

measured by the pyrometer exhibits a hot spot of 993 K exactly at the catalyst entrance, and then the temperature drops until it matches the temperature measured by the thermocouple. At the end of the catalyst, thermal equilibrium between the gas and the solid phase is reached. The maximum trend of the temperature profiles is in line with other findings in the literature [20, 28, 33]. The hot-spot formation is a result of the balance between the heterogeneous exothermic oxidation reaction, which is controlled by the rate of O₂ consumption, and the heterogeneous endothermic steam reforming reaction, which is controlled by the rate of fuel consumption.

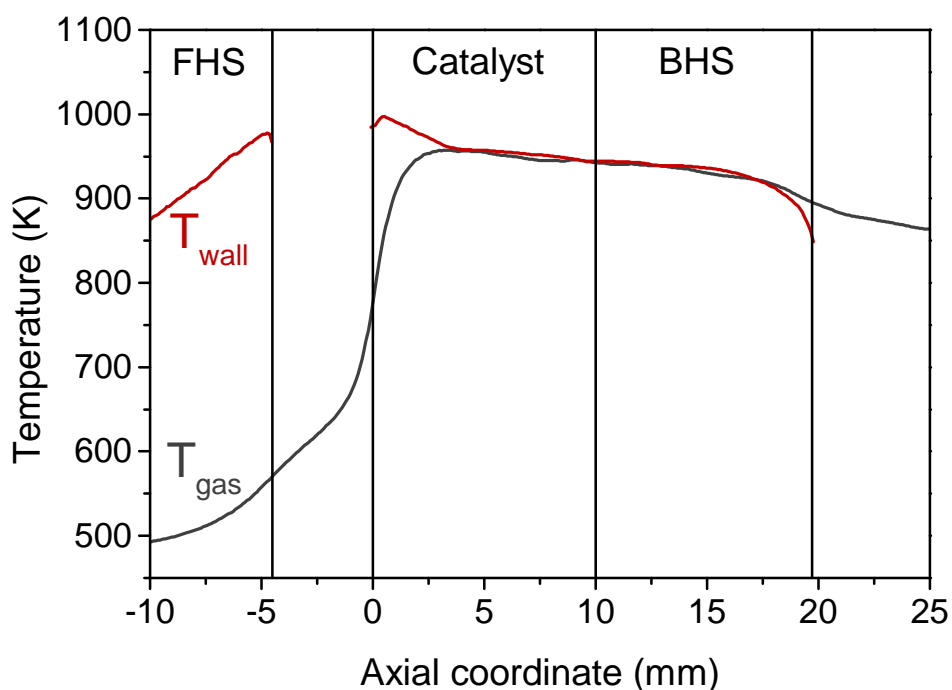
The pyrometer measure in the void space upstream of the catalyst (axial coordinate $z = -5 \text{ mm} - 0 \text{ mm}$) is not displayed because of optical artifacts that affected the measurement. As previously shown by Donazzi et al. [33], the optical fiber with a tip angled at 45° primarily behaves like a side-looking probe, but also presents a secondary acceptance cone that collects radiation in front of the optical fiber tip (see also Section 3.2). Even though this cone has a negligible impact on the measurement within the honeycomb channel, it may become important upstream of the catalyst ($z < 0 \text{ mm}$), where the primary acceptance cone collects radiation from the quartz wall of the reactor, which is at a much lower temperature than the front face of the monolith. A similar bias effect cannot be completely ruled out for the last portion of the FHS.

The concentration profiles of the reactants and the main products are plotted in Figure 4.19 (b) and (c), respectively. A conversion rate of ethanol of approximately 5 % is observed upstream of the catalyst with formation of water and acetaldehyde as main products (Figure 4.19 (d)). Traces of ethylene and hydrogen are also found. This can be explained by gas-phase reactions occurring in the last part of the front heat shield and in the void space between the front heat shield and the catalyst. The onset of such homogeneous reactions is likely due to the heat radiated from the front face of the catalytic monolith to the back face of the front heat shield. Besides the gas-phase reactions, diffusion has to be taken into account in the region between $z = -1 \text{ mm}$ and 1 mm . CFD simu-

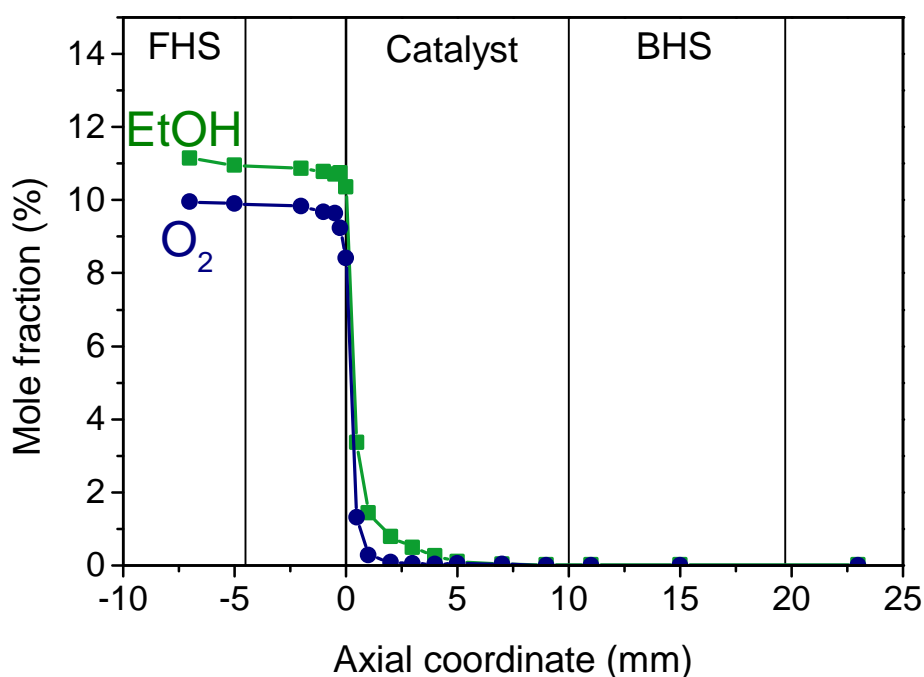
lations for the catalytic partial oxidation of methane (see Section 4.1.3.4) show that diffusion cannot be neglected under the given operating conditions. To clarify the origin of the behavior upstream of the catalyst for CPOX of ethanol, additional CFD simulations, similar to those shown in section 4.1.3.4, would be necessary. For those simulations, a heterogeneous reaction mechanism for CPOX of ethanol would be required, which is not published in literature yet. Nevertheless, the high temperature and high concentration gradients on a short distance are favorable for diffusion. For ethanol, a combination of gas-phase reactions and diffusion is expected to be responsible for the shape of the profiles directly upstream the catalyst. Within the channel of the catalyst, oxygen is completely converted within 2 mm, while the complete consumption of ethanol takes place within a longer portion of the monolith. The main products are hydrogen and carbon monoxide, which are steadily produced over the entire length of the catalyst; water exhibits a maximum at 1 mm, which is in line with its formation by oxidation reactions and consumption by steam reforming. The formation of carbon dioxide takes places mostly in the first part of the channel but the CO_2 concentration slightly increases along the catalyst.

Figure 4.19 (d) shows the axial concentration profiles of acetaldehyde, ethylene, and methane, which are the only detected by-products under the operating conditions explored herein. Additionally, Hebben et al. [15] measured diethyl ether at the reactor outlet at $\text{C/O} > 0.80$. Such a species was not detectable by the analytics used in this study, but the error on the C atom balance is always within ± 5 percent (10 % for the first millimeter of the channel at the higher C/O ratios), indicating that, even if diethyl ether is formed, it would be produced only in small amounts. The production of acetaldehyde mostly takes place upstream of the catalyst ($z < 0$ mm), whereas ethylene is mainly formed in the channel of the catalyst ($z > 0$ mm). For both species, complete consumption occurs within $z = 5$ mm, mainly by steam reforming, as the decrease of water concentration indicates. The profile of methane shows a different trend: no traces are found upstream of the catalyst and its formation starts at the catalyst

4. CPOX of Methane and Ethanol over Rh/Al₂O₃

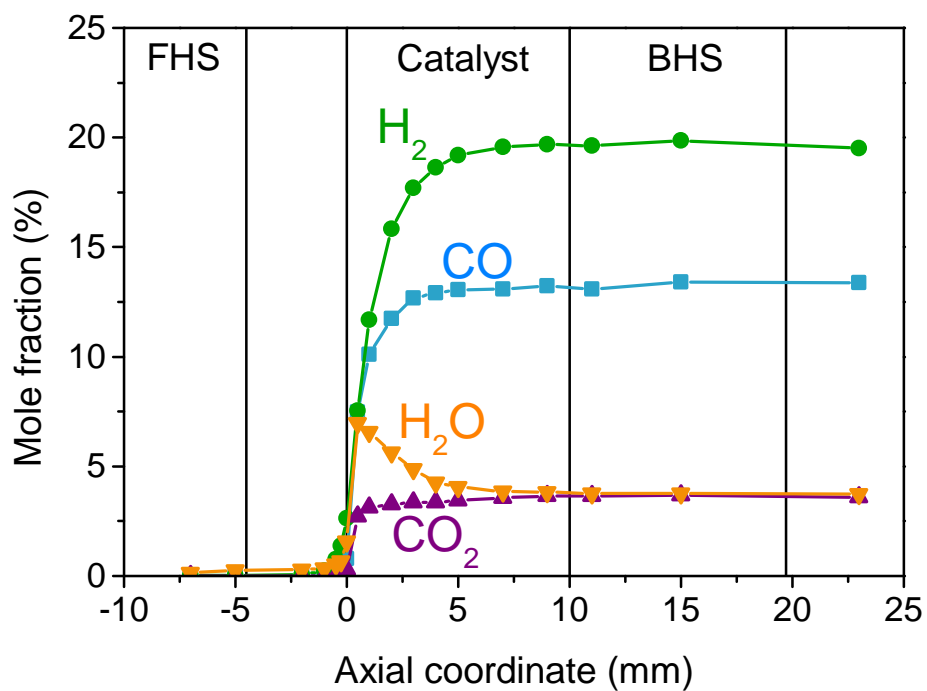


(a) Gas-phase (T_{gas}) and surface (T_{wall}) temperature

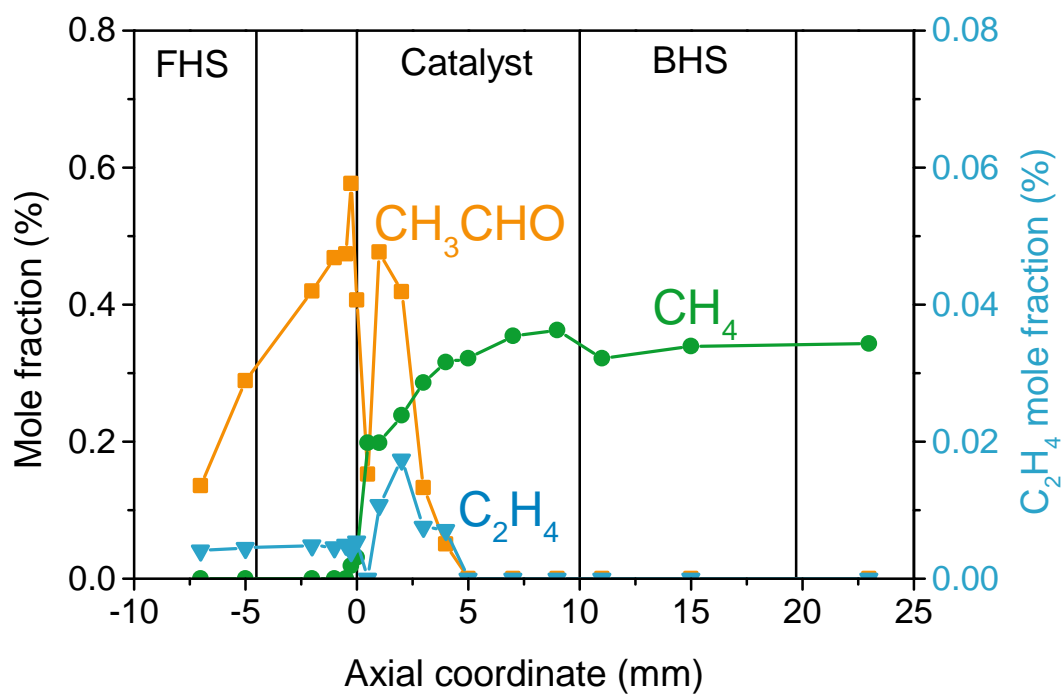


(b) Mole fractions of reactants

Figure 4.19: Temperature of the gas phase (T_{gas}) and surface (T_{wall}) as a function of the axial coordinate (a). Mole fractions of reactants (b), main products (c), and by-products (d) as a function of the axial coordinate for CPOX of C₂H₅OH over Rh/Al₂O₃ at C/O = 0.75.



(c) Mole fractions of main products



(d) Mole fractions of by-products

Figure 4.19: Continued.

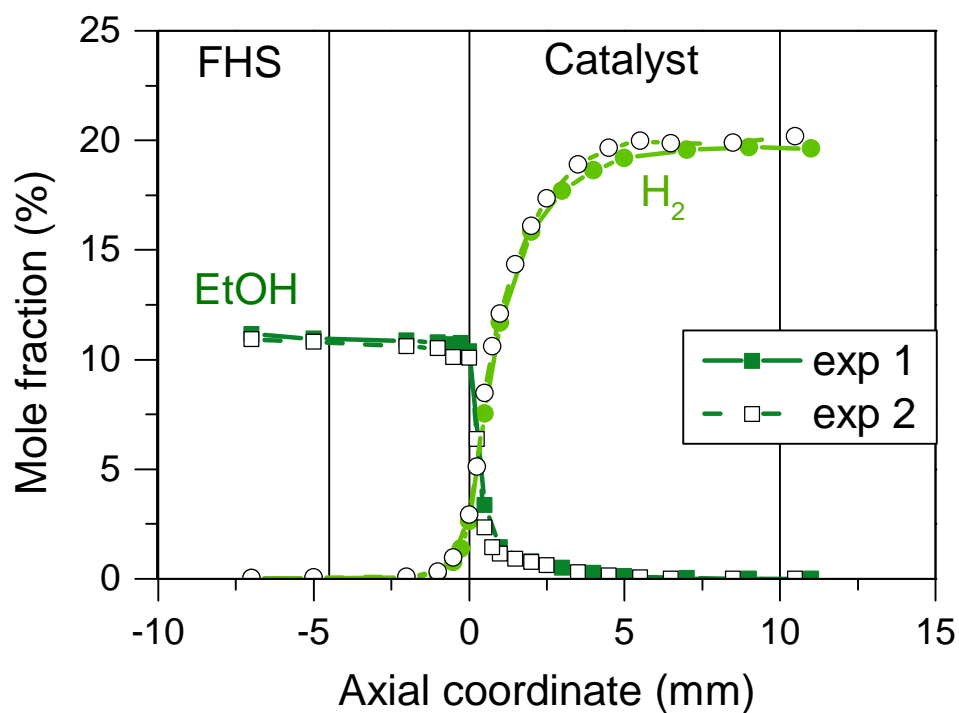
4. CPOX of Methane and Ethanol over Rh/Al₂O₃

entrance with a steep rise. After that, the concentration of methane remains almost constant within the first millimeter and gradually grows again along the channel of the catalyst. Several reactions can play a role in determining the complex evolution of methane, i.e. decomposition of ethanol and acetaldehyde, CO_x methanation, steam reforming, or homogeneous cracking reactions. More details on the pathway of methane formation are given in Section 4.2.2.

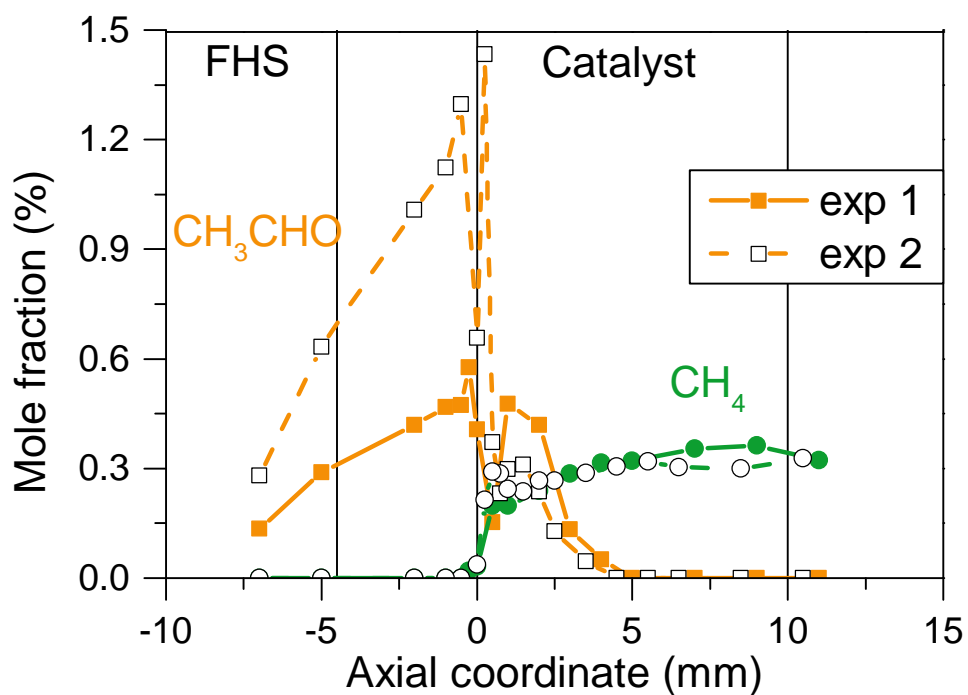
The thermal efficiency (see Section 3.5.3) of the reactor is 91 %, which indicates that the reactor operates in a nearly adiabatic regime. This is in line with values reported in the literature for similar CPOX conditions [67, 162, 163].

The measurements were reproduced on the same catalyst. As plotted in Figure 4.20, some deviations on the species profiles are apparent in the gap between the catalyst and the front inert monolith. The standard deviation of the mole fraction of the reactants and the main products is 3 %, while that of the by-products is 6 %. Aside from experimental errors (see Section 3.4), such variations can be explained by the facts that radial gradients of composition are present in this zone (as discussed in Section 4.2.3) and that an accurate control of the radial position of the capillary tip is difficult to achieve because of its high flexibility. On the contrary, while measuring within a honeycomb channel, the capillary tip leans against the channel wall, and a very good reproducibility of species profiles is observed.

In accordance with the spatial profiles in autothermal reformers previously reported by other laboratories [12, 28–30, 34, 71, 121], both the temperature and the concentration profiles confirm that the CPOX of ethanol proceeds according to a reaction mechanism similar to that of the CPOX of light hydrocarbons. In fact, the reactor can be divided in two zones: an oxy-reforming zone (0 – 2 mm) and a consecutive reforming zone (2 – 10 mm). This is similar to the catalytic zones described for methane in Section 4.1. In the first part, total oxidation occurs along with partial oxidation and/or steam reforming, leading to more exo- than endothermic reactions which are responsible for the surface



(a) Mole fractions of ethanol and hydrogen



(b) Mole fractions of acetaldehyde and methane

Figure 4.20: Mole fractions of ethanol (EtOH) and hydrogen (a), as well as acetaldehyde and methane (b) as a function of the axial coordinate for two different measurements for CPOX of C_2H_5OH over Rh/Al_2O_3 at $C/O = 0.75$.

4. CPOX of Methane and Ethanol over Rh/Al₂O₃

hot-spot temperature and the peak of the mole fraction of water. In the subsequent zone, ethanol is further converted at the expense of water, while hydrogen and carbon monoxide are produced. Analogous to methane, syngas formation seems to occur as a combination of direct and indirect routes (see Section 2.2.1.1) for ethanol CPOX. However, the radial concentration gradients in the gas-phase make it unfeasible to draw a conclusion on the concentrations close to the surface of the catalyst from the measured concentrations (see Section 2.2.1.1).

In line with previous experimental and modeling studies [15, 43, 67, 164, 165], the WGS reaction seems to take place, as indicated by the slight increase of carbon dioxide in the second part of the catalyst. Along with the main reaction pathway, by-product formation can be due to surface reactions as well as homogeneous chemistry. This is a major difference to the mechanism of methane CPOX, in which no gas-phase reactions occur at ambient pressure (see Section 4.1, [6, 32, 69, 70]). Liguras et al. [165] proposed that ethylene and acetaldehyde are formed by heterogeneous dehydration and dehydrogenation of ethanol. This was also supported by other studies in literature which revealed that ethanol dehydration to ethylene can be catalyzed by the γ -Al₂O₃ washcoat [96, 166–168]. Furthermore, (oxidative) dehydrogenation of ethanol may take place as a heterogeneous reaction, in which the γ -Al₂O₃ washcoat plays an important role [167, 168]. On the opposite, Salge et al. [43] suggested that surface reactions are not likely to form products more complex than C1 species. Our experimental results suggest the hypothesis that both pathways can be responsible for by-product formation. On the one hand, a significant contribution to ethylene production may be due to the acidic properties of the γ -Al₂O₃ washcoat. On the other hand, the formation of by-products via homogeneous chemistry takes place upstream of the catalyst ($z < 0$ mm). Additionally, in a previous study on C₃H₈ CPOX [71], the formation of intermediate hydrocarbons within the first millimeters of the catalytic monolith was shown. It occurred whenever the temperature was high enough for the onset of gas-phase

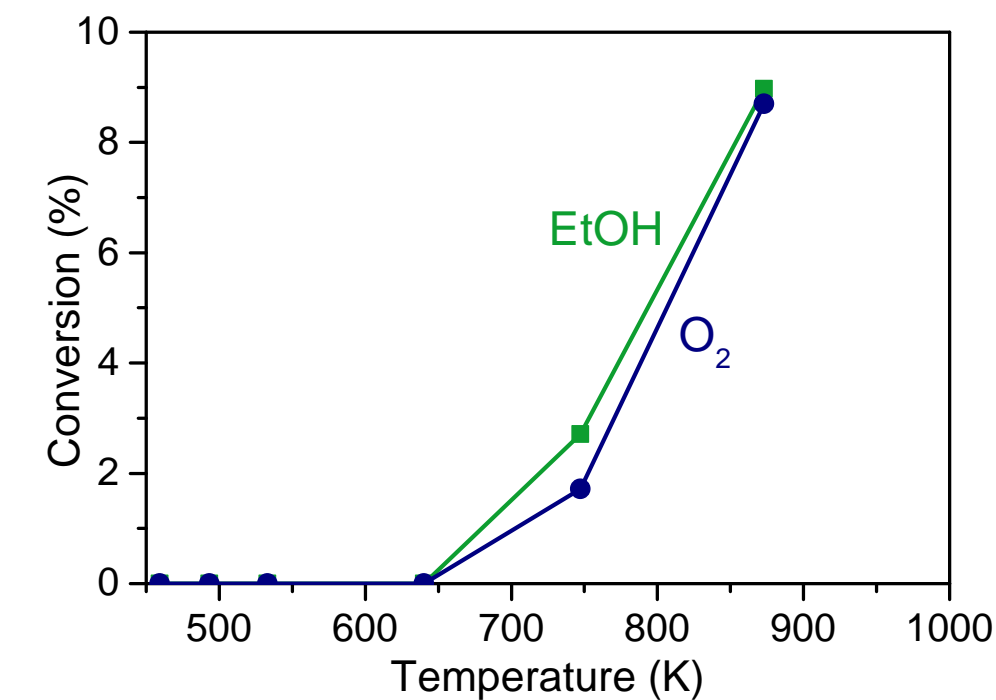
reactions. A similar reaction path may occur in the CPOX of ethanol because ethanol is a more reactive hydrocarbon than propane.

To better understand the significance of gas-phase reactions in the ethanol CPOX system, a *blank* measurement was performed by replacing the catalytic monolith with an uncoated one. Isothermal operation was carried out at the same inlet conditions as the catalytic tests, using a C/O ratio of 0.75 (see Section 3.3.3) at temperatures in the range of $T = 473 - 873$ K. The gases were sampled at an axial position of ~ 20 cm downstream of the mixing point, which corresponds to the entrance of the catalytic monolith. Ethanol and oxygen conversion and the product distribution of the *blank* measurements are reported in Figure 4.21. Activation of gas-phase reactions is found for temperatures higher than 640 K and, in line with the spatially resolved measurements, upstream of the catalyst (Figure 4.19). Oxidative dehydrogenation of ethanol leads to noticeable amounts of acetaldehyde and water (Equation (2.11)), while dehydration to ethylene (Equation (2.12)) occurs to a lesser extent. However, it has to be taken into account that the complete reactor tube is heated by the furnace in the *blank* measurements. This means that the reactive gas is heated over a length of 20 cm until the sampling capillary is reached. In the catalytic experiments, the gas-phase temperature starts to increase in the front heat shield, i.e. only 1.5 cm upstream of the catalyst inlet. Additionally, the possibility of a catalytic activity of the FHS due to acid sites in the cordierite cannot be completely ruled out. In previous studies on the homogeneous combustion of oxygenated hydrocarbons [169, 170], selective dehydration activity was observed at low temperatures; this was due to the silica walls of the reactor. However, such a reactivity is not observed at the operating conditions examined in the present study.

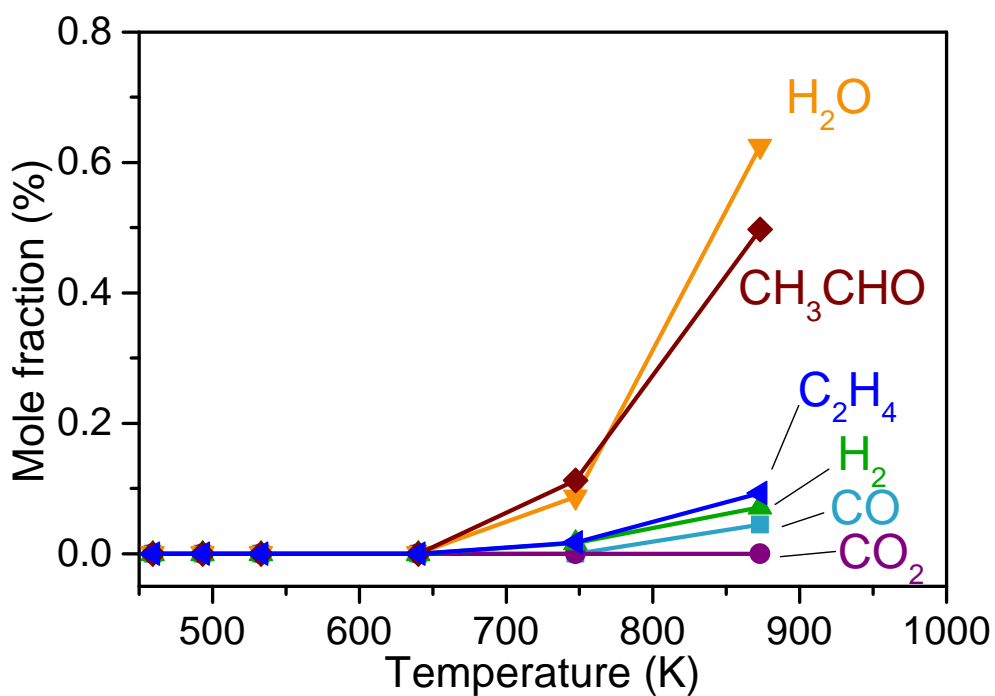
4.2.2 Effect of C/O on Spatial Profiles

The influence of the C/O ratio on the axial profiles of gas composition and temperature was studied at C/O ratios from 0.65 to 0.85 in a central channel

4. CPOX of Methane and Ethanol over Rh/Al₂O₃



(a) Conversion of ethanol and O₂



(b) Mole fractions of products

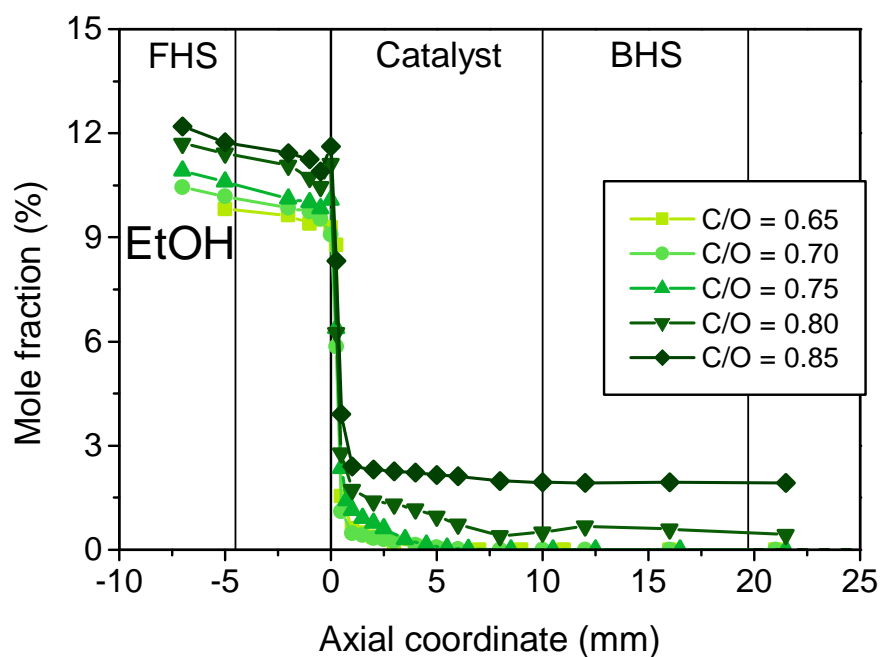
Figure 4.21: Conversion of ethanol (EtOH) and oxygen as a function of temperature (a), and mole fractions of products as a function of temperature (b) for *blank* isothermal measurements for C₂H₅OH and oxygen at C/O = 0.75.

of the catalytic monolith Rh₆₀₀ (see Section 3.3.3 for detailed operating conditions). All measurements were performed under oxygen-rich conditions to limit by-product formation. Previous investigations showed that by-product formation in CPOX of ethanol starts already at oxygen-rich conditions with an increase in the concentration of by-products going to fuel-rich conditions [15, 16]. A technical system would only be feasible for oxygen-rich conditions as coke precursors are not acceptable in the feed for the fuel cell.

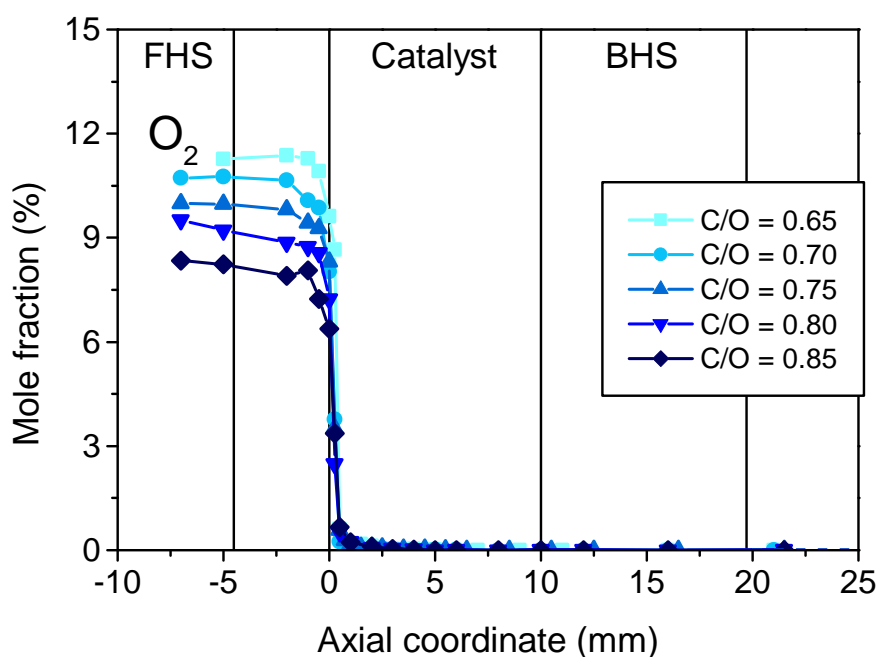
The axial profiles of the reactants, ethanol and molecular oxygen, are displayed in Figure 4.22 (a) and (b), respectively. Oxygen is completely converted at all investigated C/O ratios. The length of the catalyst-coated channel, over which oxygen is completely consumed, is not affected by the change in the C/O ratio. This indicates a pure mass-transfer limitation of oxygen consumption in the catalyst. Similar findings are reported in literature for the CPOX of methane [29, 32, 164] and propane [71]. Contrary to that of oxygen, the length over which ethanol consumption occurs increases with rising C/O ratios. At $C/O \leq 0.75$, ethanol, Figure 4.22 (a), is completely consumed. At the higher C/O ratios, $C/O = 0.80$ and 0.85 , an incomplete ethanol conversion is observed, with a higher mole fraction at the catalyst outlet ($z = 10$ mm) at $C/O = 0.85$. Thermodynamic equilibrium calculations, Figures 4.22 and 4.25 (b), predict a full consumption of ethanol at all examined C/O ratios. Therefore, ethanol conversion is, at least partially, kinetically controlled. For hydrocarbon fuels, such as propane [34], complete conversion and syngas yields close to thermodynamic equilibrium concentrations are reached at the stoichiometric composition of partial oxidation. However, for ethanol, an excess of oxygen is needed to achieve complete conversion and high hydrogen yields. These findings indicate that the oxygen within the hydroxyl group of ethanol is not as effective for oxidation as the molecular oxygen.

Generally, the investigated range of C/O ratios can be separated into two different sections. From $C/O = 0.65$ to 0.75 , an increase in steam reforming is observed. For C/O ratios > 0.75 , steam reforming proceeds to a lower extent.

4. CPOX of Methane and Ethanol over Rh/Al₂O₃

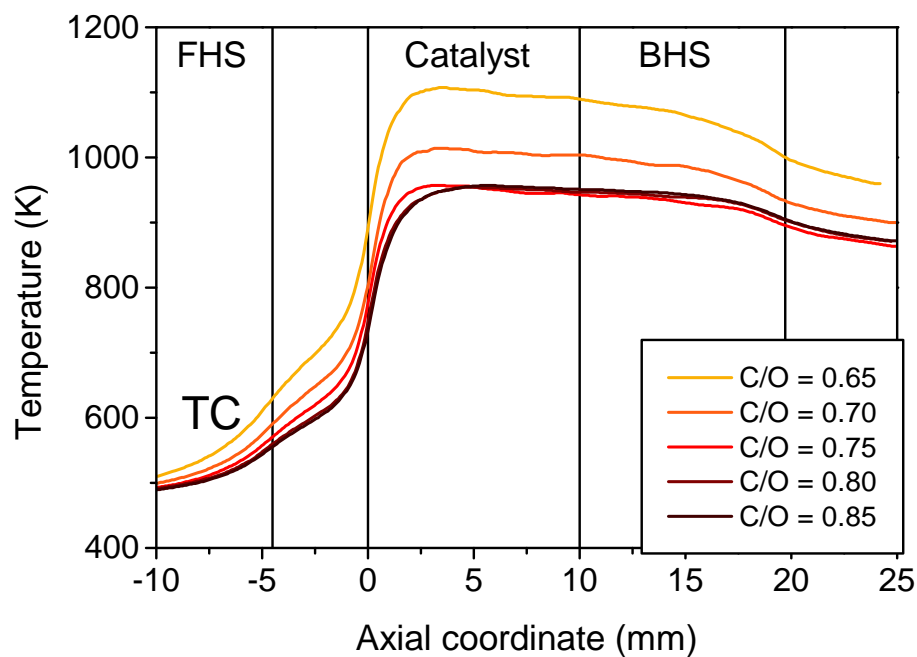


(a) Mole fraction of ethanol

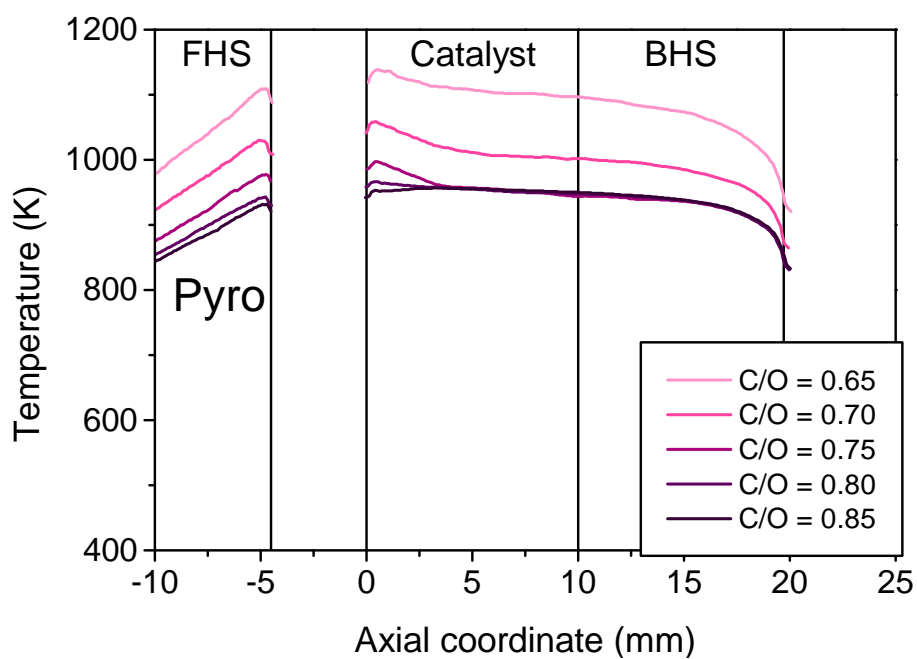


(b) Mole fraction of oxygen

Figure 4.22: Mole fractions of the reactants ethanol (EtOH) (a), and oxygen (b), gas-phase temperature (c), and surface temperature (d) as a function of the axial coordinate for CPOX of C₂H₅OH over Rh/Al₂O₃ at different C/O ratios. Equilibrium concentrations are zero for ethanol and oxygen for all investigated C/O ratios.



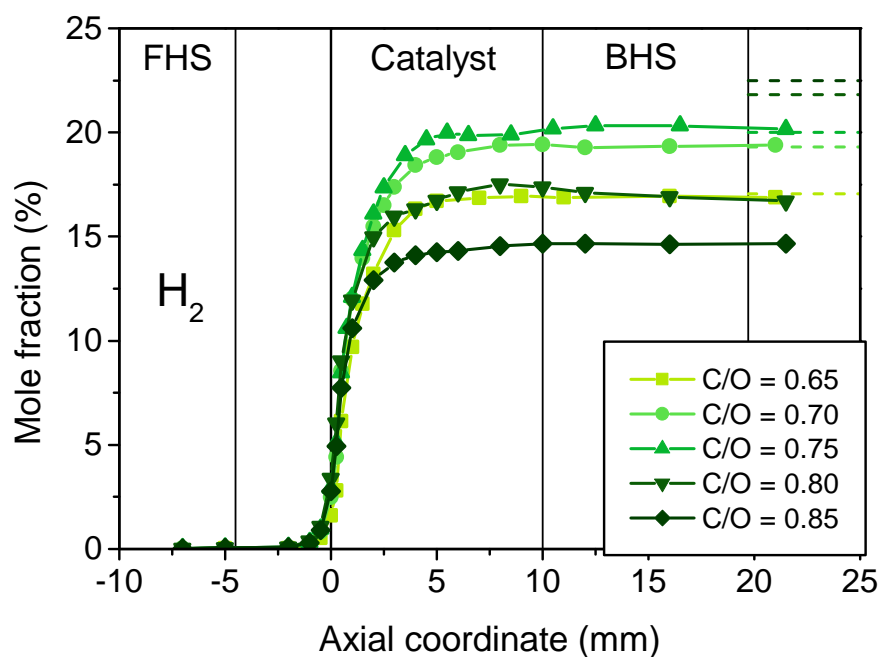
(c) Gas-phase temperature



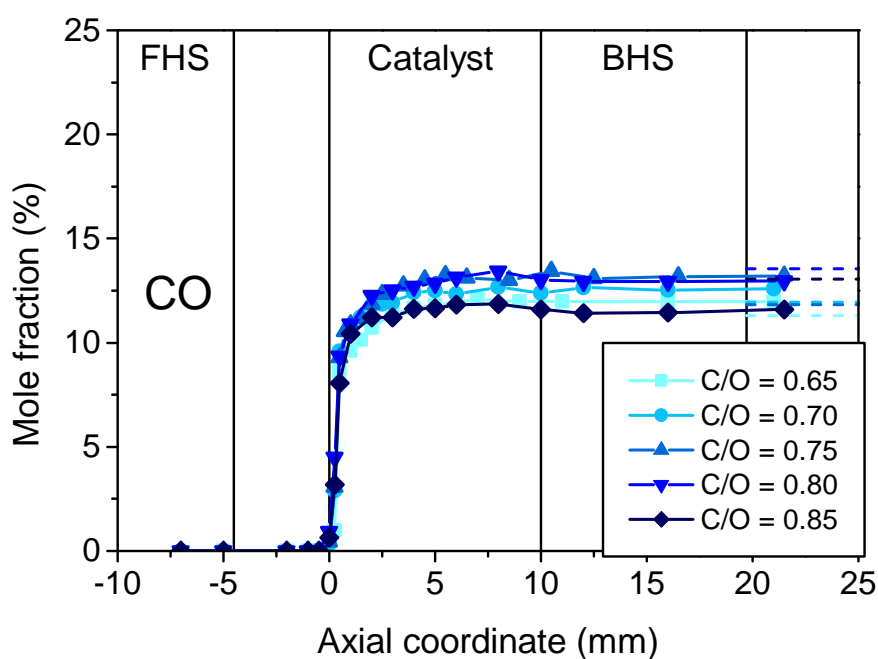
(d) Surface temperature

Figure 4.22: Continued.

4. CPOX of Methane and Ethanol over Rh/Al₂O₃



(a) Mole fraction of H₂



(b) Mole fraction of CO

Figure 4.23: Mole fractions of the main products hydrogen (a), carbon monoxide (b), water (c), and carbon dioxide (d) as a function of the axial coordinate for CPOX of C₂H₅OH over Rh/Al₂O₃ at different C/O ratios. Dashed lines show thermodynamic equilibrium composition.

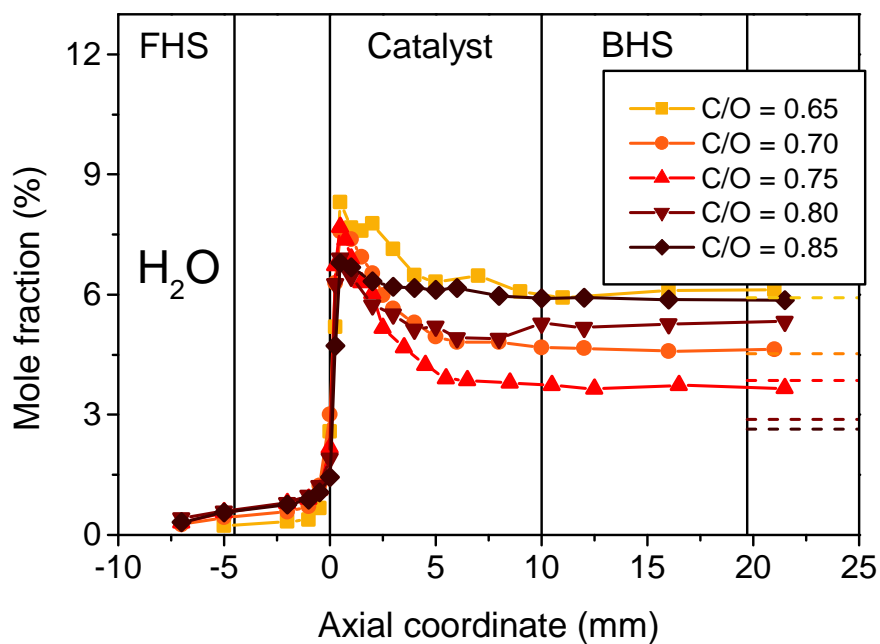
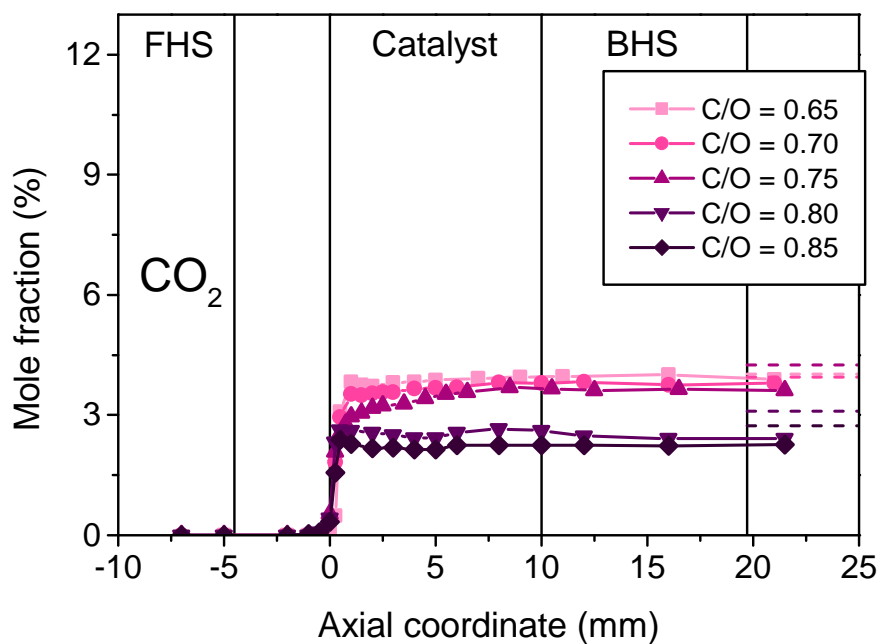
(c) Mole fraction of H_2O (d) Mole fraction of CO_2

Figure 4.23: Continued.

4. CPOX of Methane and Ethanol over Rh/Al₂O₃

This effect is noticeable in the products, the temperature profiles, and also in the consumption of ethanol. For this reason, the following discussion is also separated for the two operating ranges.

4.2.2.1 C/O = 0.65 – 0.75

Figure 4.22 (c) and (d) show the gas-phase and the wall temperature, respectively. For the gas temperature as well as for the wall temperature, a decrease in temperature with increasing C/O ratios is observed. For the wall temperature, a hot spot is visible at the catalyst entrance ($z \approx 0.5$ mm). The height of the hot spot decreases with the rising C/O ratio ($T_{\text{wall}} = 1137$ K for C/O = 0.65 compared to $T_{\text{wall}} = 997$ K for C/O = 0.75). From a thermodynamic point of view, the decline in surface temperature is due to the decreasing amount of molecular oxygen in the feed that is connected to a rise in the C/O ratio. Hence, total oxidation of ethanol, a highly exothermic reaction ($\Delta_{\text{R}}H^{\ominus} = -1278$ kJ mol⁻¹), proceeds to a lesser extent and less heat is released at the catalyst entrance. From C/O = 0.65 to C/O = 0.75, the overall surface temperature decreases at all positions. This is also observed for the surface hot spot. At the same time, the decline in temperature becomes steeper after the maximum. The maximum water consumption is observed at C/O = 0.75. At the same C/O ratio, the highest mole fraction of hydrogen, Figure 4.23 (a), is detected. The decrease in total oxidation products with a simultaneous increase in steam reforming products is also predicted by the thermodynamic calculations (see dashed lines in Figure 4.23 and Figure 4.25 (a)).

The mole fractions of the by-products are displayed as a function of the axial coordinate in Figure 4.24. The formation of methane, Figure 4.24 (a), starts at the catalyst inlet ($z = 0$ mm). Up to a C/O ratio of 0.75, the mole fraction of methane passes through a local maximum within the first millimeter of the channel, followed by a drop in the mole fraction and another rise. Also, for CPOX of C₃H₈, a similar formation pattern of methane was observed,

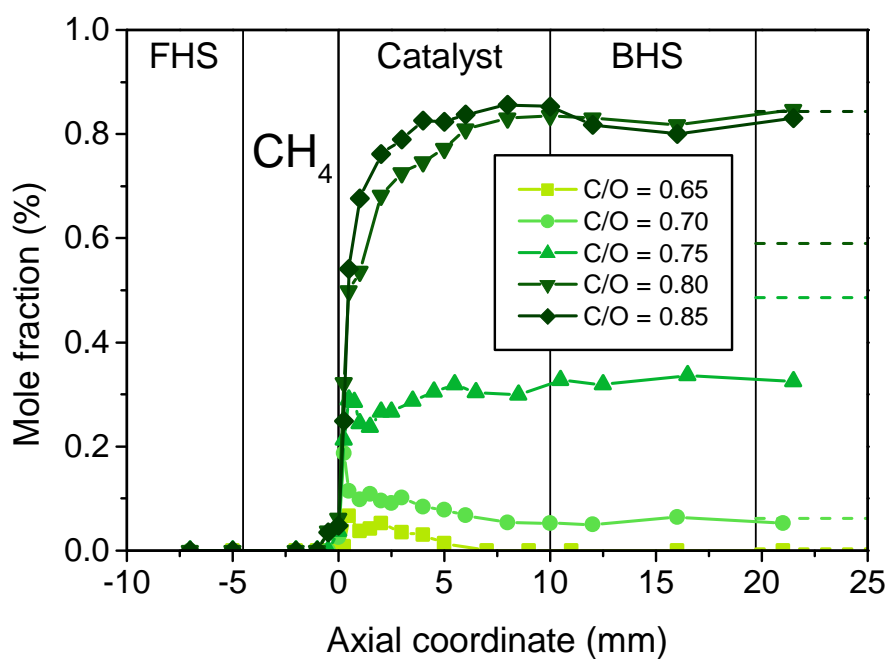
including homogeneous formation, heterogeneous consumption by steam reforming, and formation by heterogeneous methanation [71]. Different reaction pathways may lead to the formation of methane in the channel of the honeycomb catalyst during CPOX of ethanol as well. The initial formation could have been caused by homogeneous cracking reactions that are caused by the high temperature within the first two millimeters of the catalyst. A consumption of methane is most likely due to heterogeneous steam reforming. This may cause the drop after the initial formation at $C/O = 0.65 - 0.75$ and the complete and partial consumption at $C/O = 0.65$ and 0.70 , respectively. The second rise in methane concentration after the drop in the mole fraction is probably due to heterogeneous reactions, e.g. methanation [12] of synthesis gas (Equation (2.7)) or acetaldehyde decomposition (Equation (2.14)) [100] to methane and carbon monoxide.

The amount of ethylene formed in the gas phase upstream of the catalyst is small (mole fraction $< 0.01\%$). Inside the catalyst-coated channel, the mole fraction of ethylene increases within the first millimeters of the channel. At $C/O \leq 0.75$, ethylene is again completely consumed in steam reforming, so that no ethylene is detected at the catalyst outlet ($z = 10$ mm).

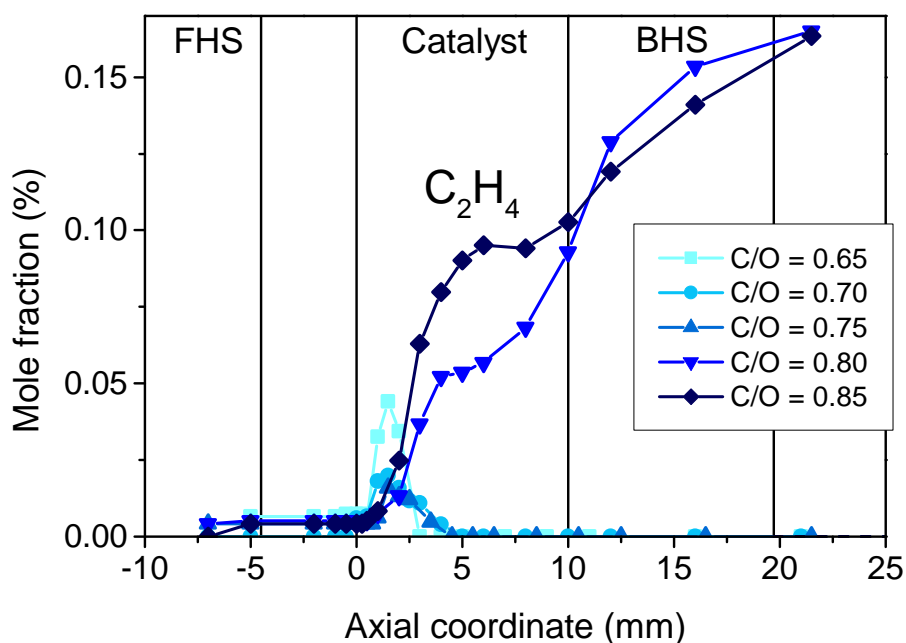
Contrary to ethylene, the mole fraction of acetaldehyde, Figure 4.24 (c), reaches high values up to 1.5% upstream of the catalyst ($z < 0$ mm) by oxidative dehydrogenation of ethanol. The higher the C/O ratio, i.e. the higher the ethanol concentration in the reactant stream, the higher the acetaldehyde formation in homogeneous gas-phase reactions. The temperature upstream of the catalyst, Figure 4.22 (c) and (d), decreases with increasing C/O ratios, which is also favorable for exothermic oxidative dehydrogenation of ethanol from a thermodynamic point of view.

Acetaldehyde consumption occurs in the channel of the catalyst-coated monolith, which is probably due to total oxidation within the first millimeter. At the same time, acetaldehyde is probably formed by dehydrogenation.

4. CPOX of Methane and Ethanol over Rh/Al₂O₃



(a) Mole fraction of CH₄



(b) Mole fraction of C₂H₄

Figure 4.24: Mole fractions of the by-products methane (a), ethylene (b), and acetaldehyde (c) as a function of the axial coordinate for CPOX of C₂H₅OH over Rh/Al₂O₃ at different C/O ratios. Dashed lines show thermodynamic equilibrium composition. For ethylene and acetaldehyde, equilibrium concentration is zero at all investigated C/O ratios.

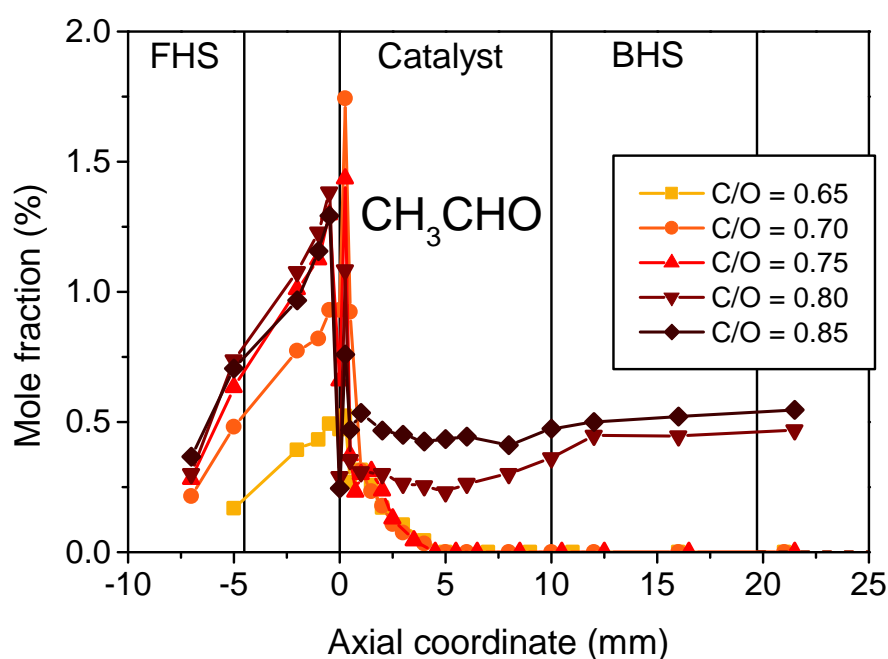
(c) Mole fraction of CH_3CHO

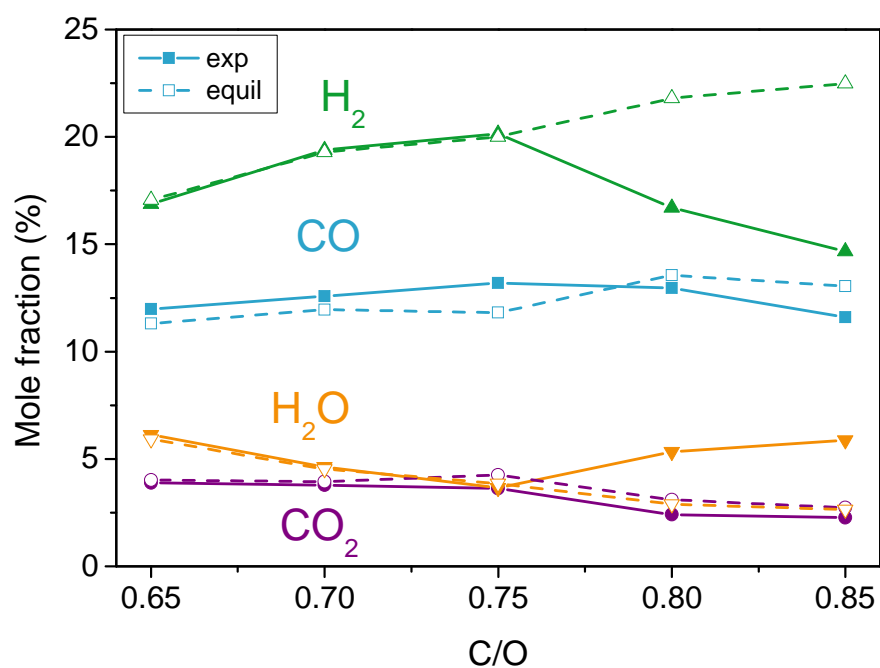
Figure 4.24: Continued.

Acetaldehyde is also consumed in steam reforming, leading to a complete consumption for $z > 5$ mm at $\text{C/O} = 0.65 - 0.75$.

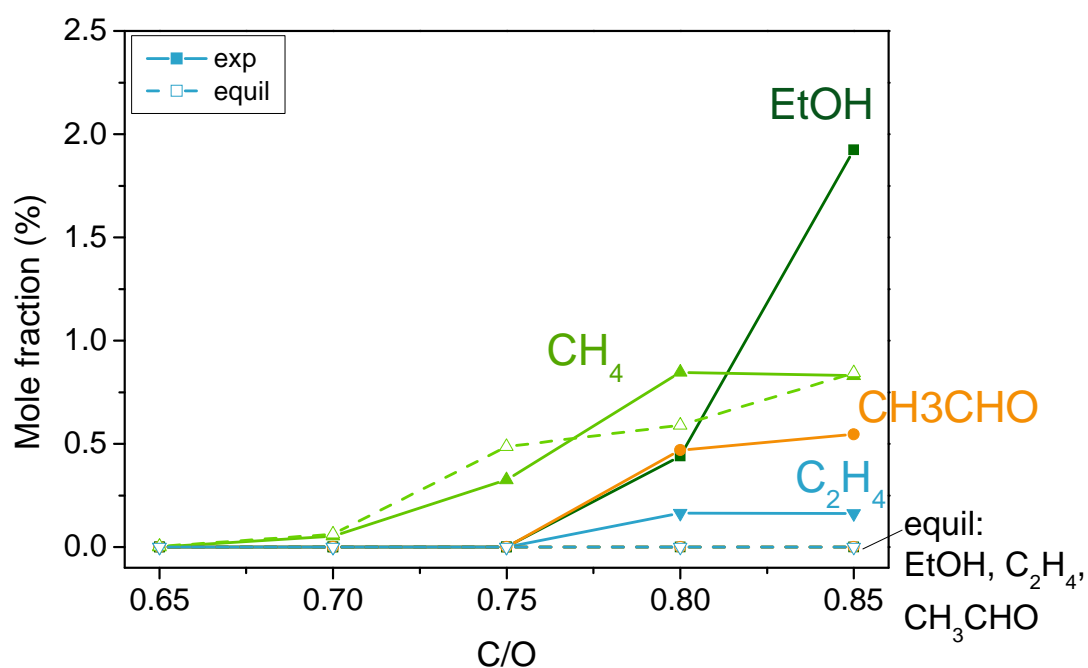
At the catalyst entrance, several reactions seem to take place simultaneously within the first millimeter. This leads to large changes in the gas composition within less than 0.25 mm, which causes difficulties in completely resolving the axial profile with a resolution of 0.25 mm. Furthermore, radial and even axial diffusion needs to be taken into account in this area, leading to an additional influence on the concentration profiles in addition to the ongoing reactions.

A comparison of the experimental mole fractions at the catalyst outlet ($z = 10$ mm) with calculated mole fractions at the thermodynamic equilibrium is shown in Figure 4.25. At $\text{C/O} \leq 0.75$, the thermodynamic equilibrium for the main products is reached at the catalyst outlet (Figure 4.25 (a)). The experimentally observed complete conversion of ethanol and the formation of methane as by-product agree with the thermodynamic equilibrium (Figure 4.25 (b)).

4. CPOX of Methane and Ethanol over Rh/Al₂O₃



(a) Mole fractions of main products



(b) Mole fractions of by-products and ethanol

Figure 4.25: Mole fractions of the main products (a) as well as the by-products and ethanol (EtOH) (b) at the catalyst outlet ($z = 10$ mm) as a function of the C/O ratio for experiments (exp, solid lines) and isothermal thermodynamic calculations (equil, dashed lines) based on CPOX of C₂H₅OH.

4.2.2.2 C/O = 0.80 – 0.85

At $C/O \geq 0.80$, the hot spot disappears and endothermic steam reforming proceeds to a lesser extent (Figure 4.23 (c)). Thus, the decrease in surface temperature in the axial direction after the hot spot diminishes with rising C/O ratios. An ethanol breakthrough is observed for $C/O \geq 0.80$ (Figure 4.22 (a)). Furthermore, a lower mole fraction of hydrogen and a higher mole fraction of water are observed. Also, the length over which hydrogen is formed decreases. This is partly caused by the temperature, as endothermic steam reforming is less favored at decreasing temperatures. Another possible aspect is coking of the catalytic surface due to the detected ethylene, Figure 4.24 (b), which is known as a coke precursor [171–173]. The mole fraction of carbon monoxide, Figure 4.23 (b), is not as strongly affected by a change in the C/O ratio as the mole fraction of hydrogen. By looking at the stoichiometry of steam reforming of ethanol, one reaction turnover yields 4 molecules of hydrogen and 2 molecules of carbon monoxide. The related decrease in hydrogen concentration is steeper than the one in carbon monoxide concentration, which can be explained by the above-mentioned stoichiometry of the steam reforming of ethanol. Another possibility is that, as for methane CPOX [120, 164], CO and H₂ formation are limited by different rate-determining steps, and thus, are differently influenced by a change in the C/O ratio. Furthermore, reactions independent of hydrogen formation, e.g. the decomposition of acetaldehyde, Figure 4.24 (c), to methane and carbon monoxide, could contribute to the mole fraction of carbon monoxide.

At higher C/O ratios of 0.80 and 0.85, only a steep increase of the mole fraction of the by-product methane up to 0.9 % is observed within the first few millimeters of the catalyst (Figure 4.24 (a)). Due to lower temperatures, the heterogeneous formation of methane is favored at $C/O \geq 0.80$ because methanation as well as acetaldehyde decomposition are exothermic reactions. Furthermore, a consumption of methane is not observed.

4. CPOX of Methane and Ethanol over Rh/Al₂O₃

The mole fraction of ethylene in the channel of the catalyst shows an increase, passes through a local plateau and through a further rise for the C/O ratios of 0.80 and 0.85. Ethylene is still formed in the back heat shield. This shape of ethylene profile is probably the result of an overlapping of heterogeneous and homogeneous formation of ethylene and the consumption by heterogeneous steam reforming inside the channel of the catalyst. In the back heat shield, ongoing exothermic, homogeneous dehydration of ethanol is probably responsible for the further increase in ethylene concentration in the axial direction. C/O = 0.80 and 0.85 are the only investigated C/O ratios with unconverted ethanol and ethylene in the back heat shield, which supports the assumption that ethylene is formed by dehydration of ethanol. In contrast to ethylene, acetaldehyde formation increases upstream of the catalyst with rising C/O ratios. For C/O = 0.80 and 0.85, only a partial consumption of acetaldehyde in the channel of the monolith is observed. This further supports the assumption that endothermic steam reforming occurs to a lesser extent for these C/O ratios.

The equilibrium calculations show an increasing deviation of the product composition from the one at thermodynamic equilibrium for C/O \geq 0.80. Carbon dioxide is the only main product that still reaches thermodynamic equilibrium. The mole fraction of hydrogen shows the largest difference ($\Delta x = 8$ percentage points) between experimental and thermodynamic equilibrium values. Furthermore, a breakthrough of ethanol as well as the presence of ethylene and acetaldehyde at the catalyst outlet ($z = 10$ mm) are observed in the experiments. This breakthrough does not agree with the thermodynamically equilibrated composition. Steam reforming is thermodynamically favored, but it is kinetically limited at C/O \geq 0.80. The kinetic limitation causes the breakthrough of ethanol and the by-products. It is questionable whether the gas composition would reach thermodynamic equilibrium with longer residence times or catalysts. Some of the by-products formed, such as ethylene, may not equilibrate, but rather form polycyclic hydrocarbons and coke farther downstream. In the equilibrium calculations, solid carbon was included in the form of graphite

(Section 3.5.1). Graphite is only present for $C/O \geq 0.85$ ($Y_{\text{Graphite}}^C = 5.1\%$) for thermodynamic equilibrium. It was not possible to detect carbon formation with the applied analytics. Nevertheless, only small amounts of carbon formation would be possible during the experiments as the C balance closes within $\pm 5\%$.

4.2.3 Influence of Radial Position of Channel

The spatially resolved measurements reveal that temperature and composition strongly vary along the axial coordinate of a central channel of the catalytic monolith. Consequently, the behavior of channels located at different radial positions may not be the same as that of the inner ones, which has important consequences on the overall fuel conversion and hydrogen yield. This phenomenon is observed for methane CPOX, as described above (Section 4.1.2). For this reason, experiments are also performed for ethanol CPOX to investigate the presence of radial differences of temperature and composition over the honeycomb catalyst. Spatial profiles were collected in three differently-located channels across the monolith: one central channel (referred to as “central”), one channel intermediately positioned between the center and the periphery of the monolith (“middle”), and one channel close to the periphery of the monolith (“outer”). The experiments were performed at $C/O = 0.75$ (see Section 3.3.3 for operating conditions).

Figure 4.26 shows the axial profiles of concentration for ethanol and oxygen ((a) and (b)) and those of temperature for the gas phase and the surface ((c) and (d)), measured in the three investigated channels. Upstream of the monolith ($z < 0$ mm), the temperature measured by the thermocouple at the radial position of the outer channel is approximately 50 K higher than that measured in the channels located closer to the center. The higher temperature is probably caused by the higher residence time of the flow stream close to the reactor wall. The higher residence time is due to the boundary layer which develops upstream of

4. CPOX of Methane and Ethanol over Rh/Al₂O₃

the FHS close to the reactor wall. In line with the higher temperature, a higher consumption of the reactants, Figure 4.26 (a) and (b), and a higher selectivity towards acetaldehyde and ethylene, Section 4.2.3 (b) and (c), are observed. This may be related to the onset of gas-phase reactions upstream of the catalyst entrance ($z < 0$ mm). It was confirmed by CFD simulations (not shown) that the C/O ratio at the inlet of the front heat shield ($z = -15$ mm) is the same for all investigated channels.

The spatial profiles in Figure 4.26 show that the catalytic section of the reactor can be split in two zones: as long as oxygen is present in the gas phase (0–2 mm), similar values are observed on the concentration profiles of the reactants as well as on the temperature profiles measured by the thermocouple. This is very similar to the behavior seen in methane CPOX (Section 4.1.2). Only in the outer channel, a decrease of 10 K on the hot-spot temperature measured by the pyrometer is noticed, which is likely due to radial heat losses, as discussed below. When oxygen is completely consumed (after 2 mm), analogous trends on the species profiles in the central and the middle channels are observed, whereas the outer channel shows an incomplete consumption of ethanol. In addition to this, the decreasing trend of the temperature measured by both the pyrometer and the thermocouple becomes steeper from the center to the periphery of the monolith. The temperature difference between the central and the middle channel is ~ 8 K and the difference of central to outer channel is ~ 30 K at the monolith outlet ($z = 10$ mm). Thus, endothermic steam reforming is less favored in the outer channel, resulting in an ethanol conversion of 91 %. The higher residence time in the outer channel due to the boundary layer close to the reactor wall seems to be outweighed by the lower temperature. The same is observed for methane CPOX (Section 4.1.2).

The concentration profiles of the main products are illustrated in Figure 4.27. As previously discussed for the mole fractions of ethanol and oxygen, no significant changes are detected for the entire length of the concentration profiles in the central and the middle channel. The same is observed for the

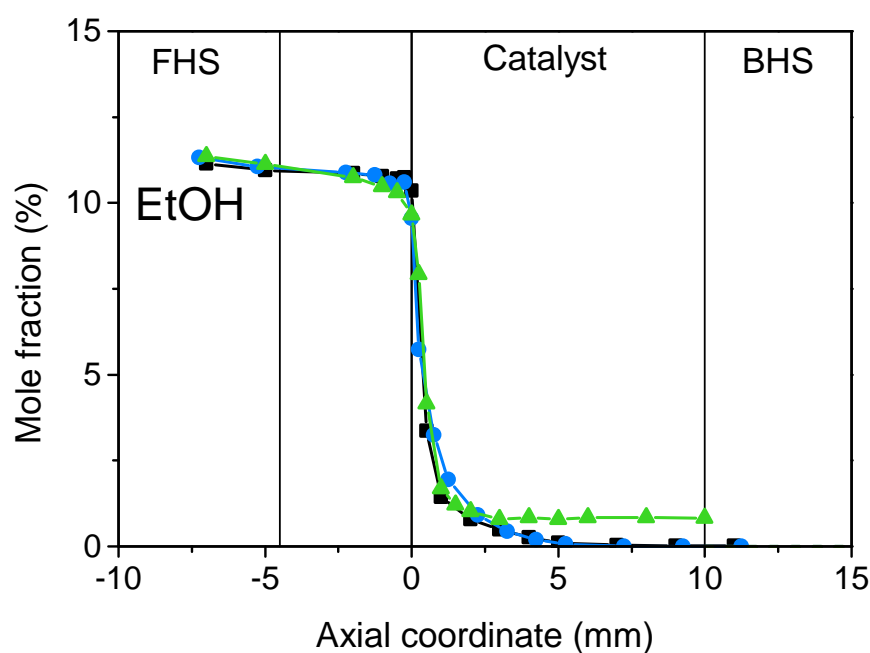
outermost channel up to 2 mm. For an axial coordinate $z > 2$ mm, the mole fraction of hydrogen is 3 percentage points lower than in the inner channels, and there is an increase in the water content. This further indicates that steam reforming of ethanol occurs to a lesser extent in the outer channel.

For ethanol CPOX, the CO concentration stays nearly constant whereas the CO₂ concentration is considerably lower ($x_{\text{CO}_2} = 3.7\%$ for central and middle channel compared to $x_{\text{CO}_2} = 2.4\%$ for outer). In contrast to these values, for methane CPOX, CO concentration is lower for the outer ($x_{\text{CO}} = 4.0\%$ at $z = 11$ mm) than for central and middle channel ($x_{\text{CO}} = 6.1\%$ at $z = 11$ mm), whereas the CO₂ concentration stays constant (see Section 4.1.2). Different reactions seem to be affected by the changed conditions in the outer channel for ethanol and methane CPOX.

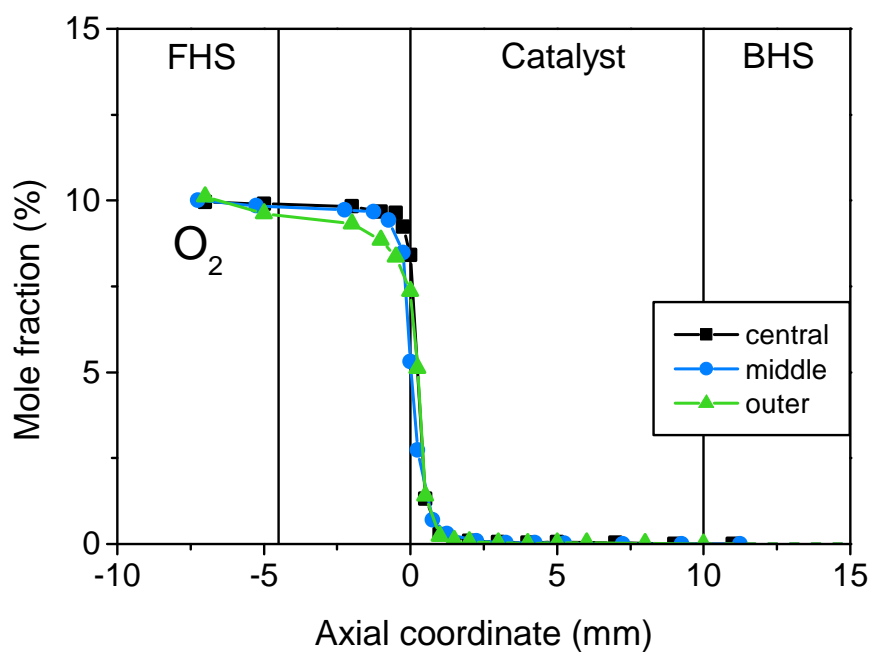
The lack of reforming activity results in higher amounts of by-products. Also, the higher residence time is favorable for side-product formation. The concentration profiles of methane, ethylene, and acetaldehyde are plotted in Section 4.2.3. Compared to the inner channel, the catalyst is not capable of efficiently converting acetaldehyde and ethylene to syngas, and a breakthrough of such species is observed at the catalyst outlet ($z = 10$ mm) for the outer channel. As previously discussed for the effect of the C/O ratio, ethylene production due to ethanol dehydration on the acid sites of the stabilized γ -Al₂O₃ washcoat as well as gas-phase reactions cannot be ruled out. In line with CO_x methanation, which is more favored due to the lower temperature, the mole fraction of methane progressively increases from the central to the most peripheral channel.

The decrease of temperature and, consequently, the loss of reforming activity are primarily due to radial heat loss, which becomes very important in the outer channels. There is a large difference in temperature between the outer channel and the furnace ($\Delta T > 400$ K), which does not exist in this way for the central and middle channel. Therefore, the thermal efficiency decreases from 91% in the central channel to 77% in the outer channel. It is worth noting

4. CPOX of Methane and Ethanol over Rh/Al₂O₃

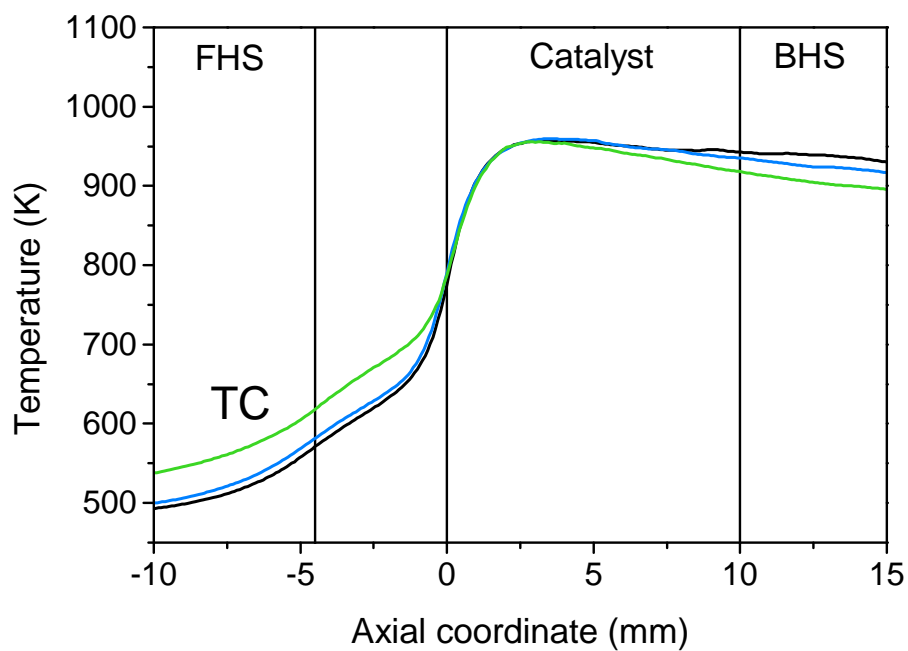


(a) Mole fraction of ethanol

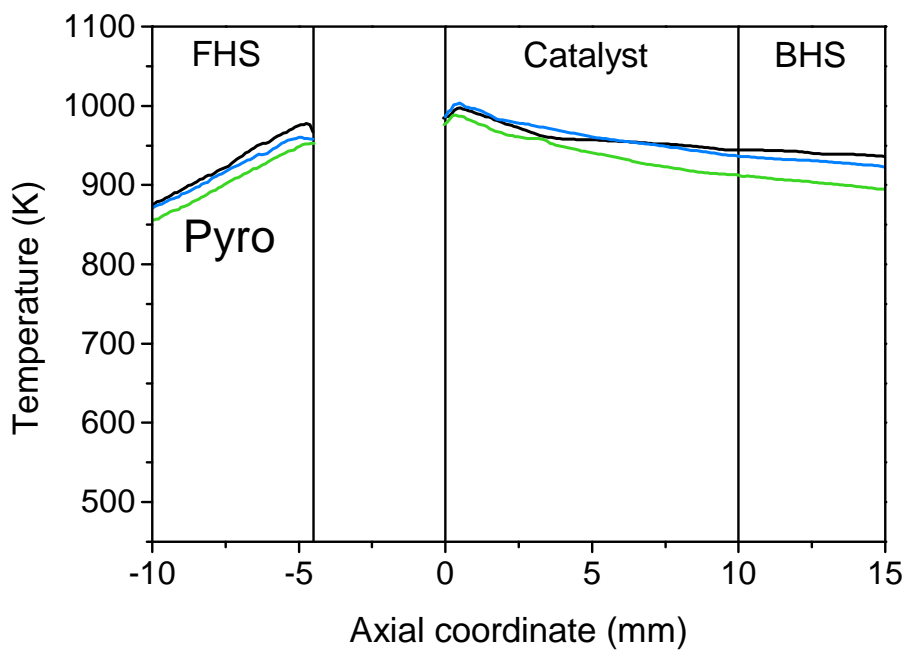


(b) Mole fraction of O₂

Figure 4.26: Mole fractions of the reactants C₂H₅OH (EtOH) (a) and O₂ (b), gas-phase temperature (c), and surface temperature (d) as a function of the axial coordinate for CPOX of C₂H₅OH over Rh/Al₂O₃ at C/O = 0.75 in three channels, with different positions across the monolith. Same explanation of the channel position as in Figure 4.3. Equilibrium values are zero for ethanol and oxygen for all investigated channels.



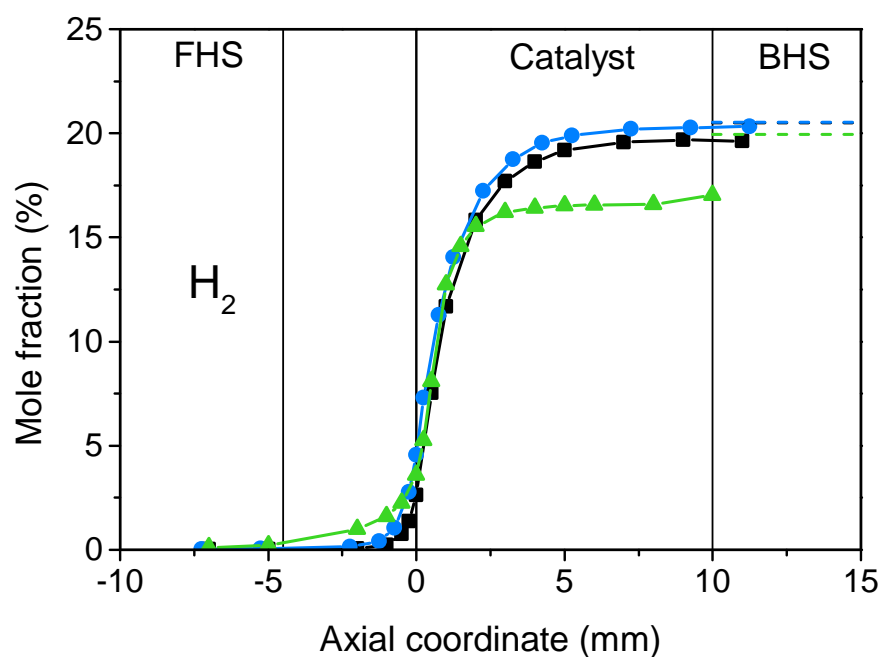
(c) Gas-phase temperature



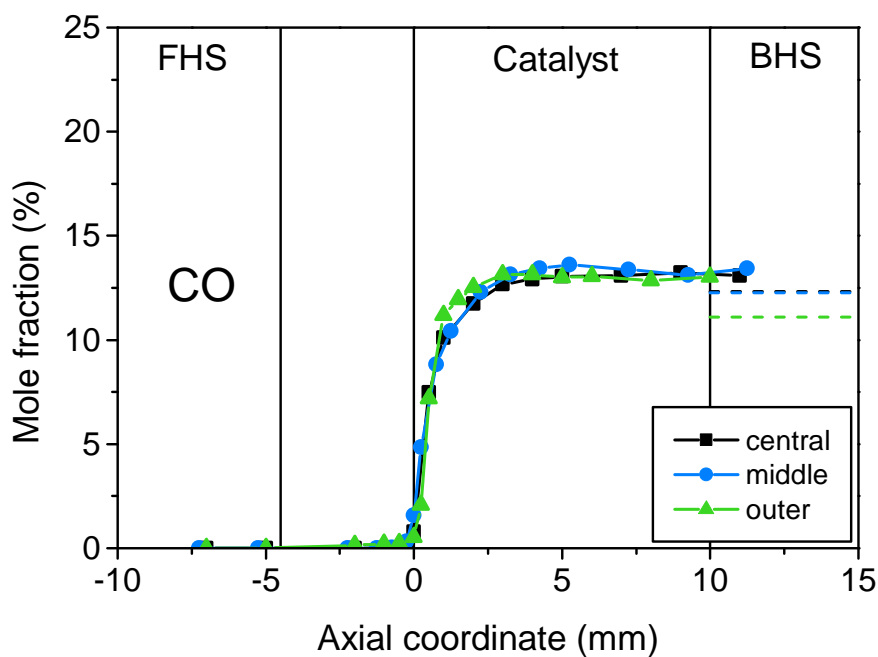
(d) Surface temperature

Figure 4.26: Continued.

4. CPOX of Methane and Ethanol over Rh/Al₂O₃



(a) Mole fraction of H₂



(b) Mole fraction of CO

Figure 4.27: Mole fractions of the main products hydrogen (a), carbon monoxide (b), water (c), and carbon dioxide (d) as a function of the axial coordinate for CPOX of C₂H₅OH over Rh/Al₂O₃ at C/O = 0.75 in three differently-positioned channels. See Figure 4.3 for explanation of the channel positions. Dashed lines show the equilibrium composition.

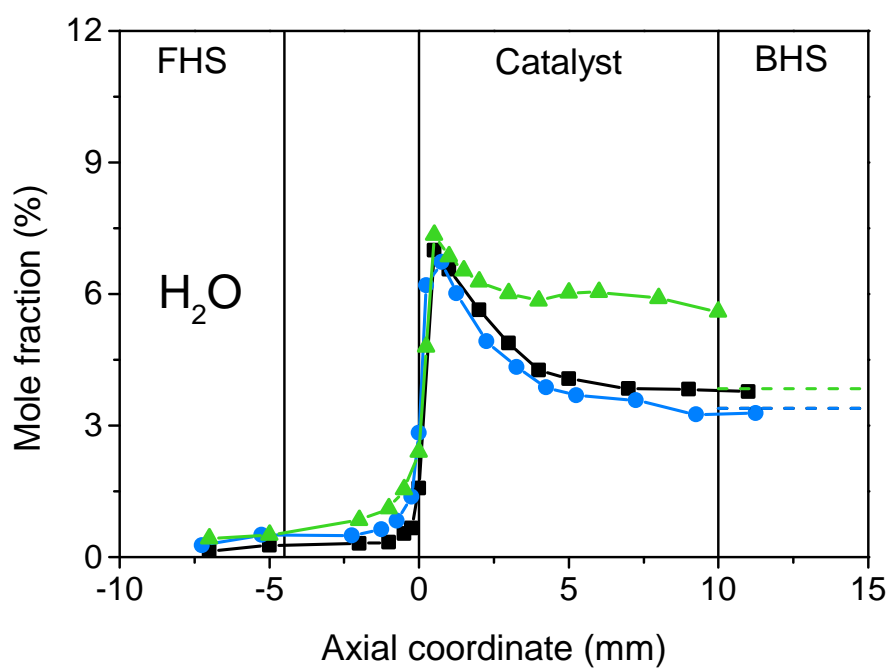
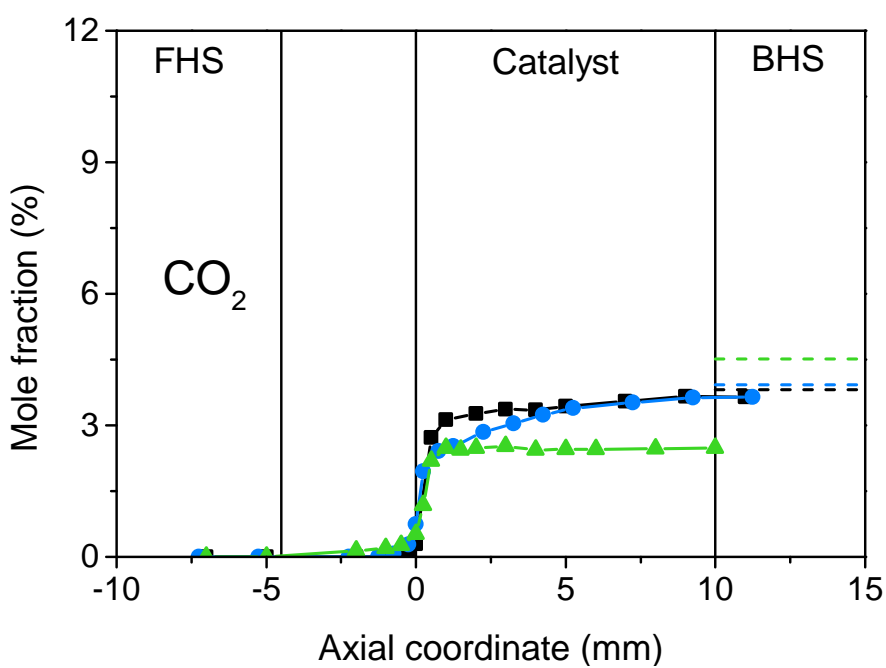
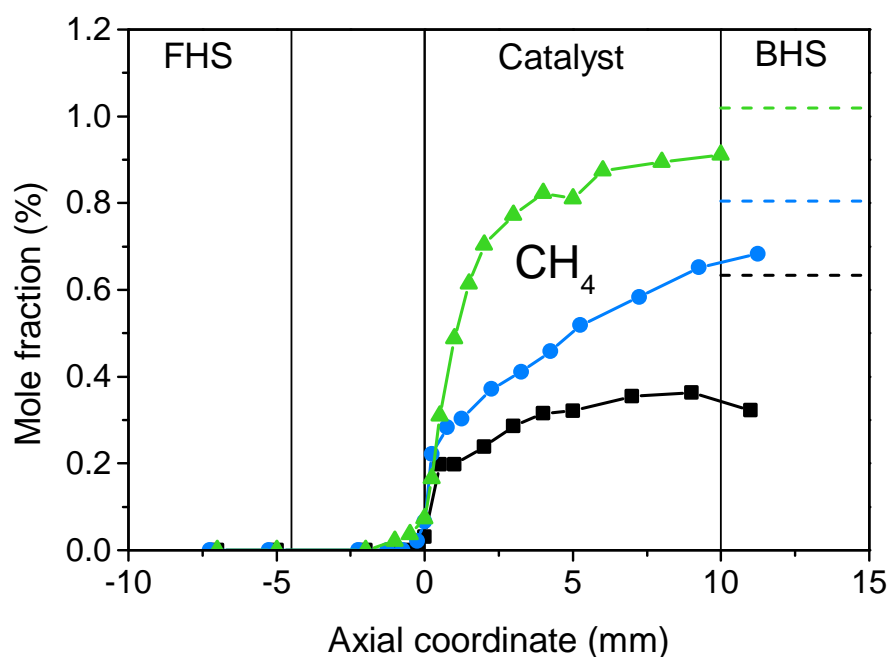
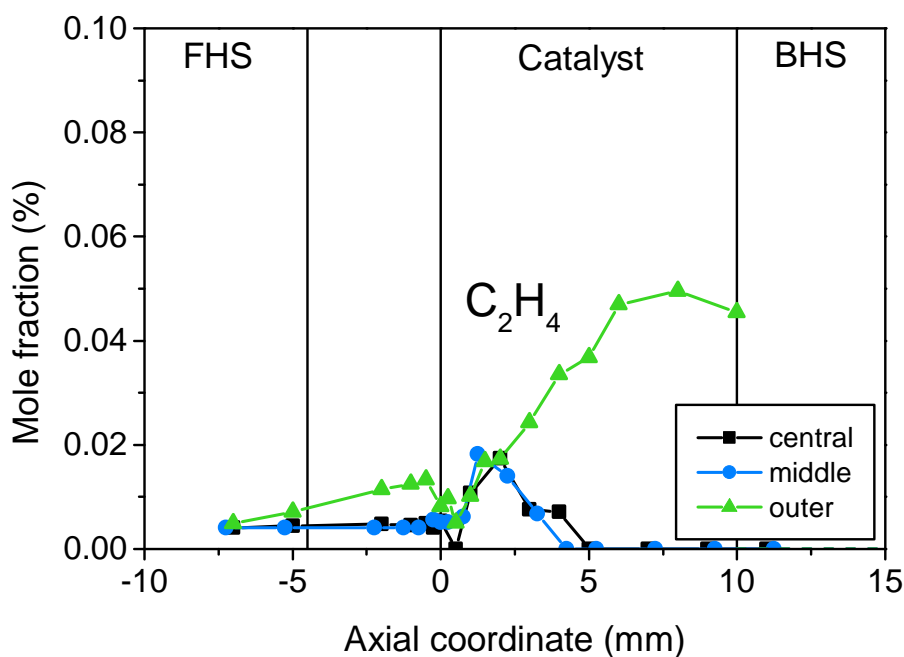
(c) Mole fraction of H_2O (d) Mole fraction of CO_2

Figure 4.27: Continued.

4. CPOX of Methane and Ethanol over Rh/Al₂O₃



(a) Mole fraction of CH₄



(b) Mole fraction of C₂H₄

Figure 4.28: Mole fractions of the by-products methane (a), ethylene (b), and acetaldehyde (c) as a function of the axial coordinate for CPOX of C₂H₅OH over Rh/Al₂O₃ at C/O = 0.75 in three differently-positioned channels. See Figure 4.3 for explanation of the channel positions. Dashed lines show the equilibrium composition. For C₂H₄ and CH₃CHO, equilibrium concentration is zero.

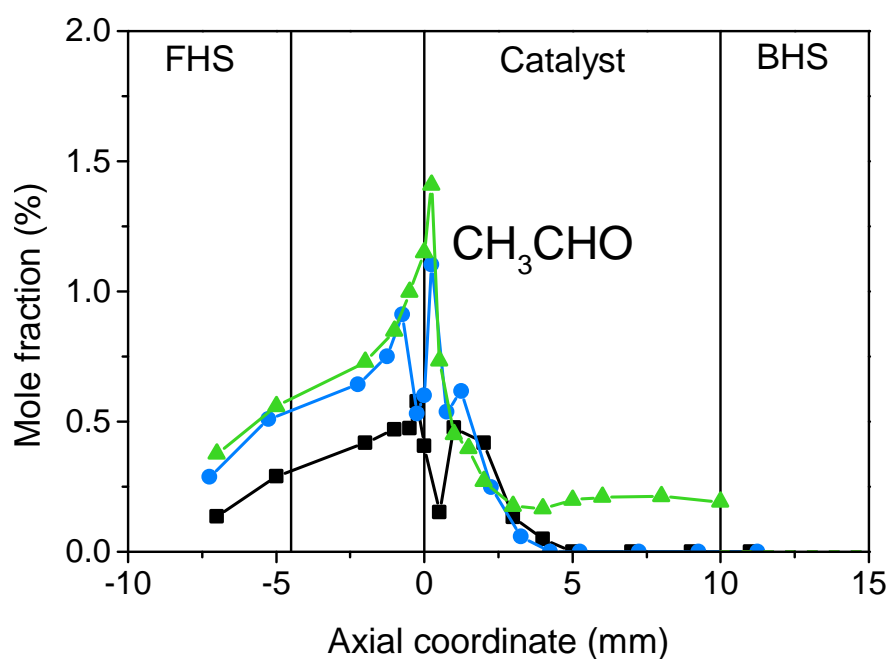
(c) Mole fraction of CH_3CHO

Figure 4.28: Continued.

that another explanation for the reduction of reforming activity may be catalyst coking. Coke formation could be relevant under the operating conditions tested herein, as high amounts of soot precursors, such as ethylene, are observed. To evaluate the influence of coke formation, further investigations would be necessary.

4.2.4 Summary for Ethanol

Investigations for a range of C/O ratios from 0.65 to 0.85 by means of the in-situ sampling technique clearly show the influence of the reactant feed on the reaction network in the CPOX reformer. With the increasing C/O ratio, by-product formation rises, especially upstream of the catalyst ($z < 0$ mm). The exothermic formation of by-products from ethanol decomposition is favored for increasing C/O ratios as these lead to higher ethanol concentrations and lower temperatures at $z < 0$ mm. At $\text{C/O} \geq 0.80$, the mole fraction of hydrogen decreases.

4. CPOX of Methane and Ethanol over Rh/Al₂O₃

In addition, the conversion of ethanol is incomplete and other by-products besides methane are detected at the catalyst outlet ($z = 10$ mm), which is due to undesired side-reactions. The comparison with calculated mole fractions at the thermodynamic equilibrium reveals that the deviation from equilibrium increases with rising C/O ratios for $C/O \geq 0.80$.

The investigation of a range of C/O ratios in partial oxidation of ethanol reveals that the highest hydrogen yield with a low by-product formation is achieved at $C/O = 0.75$. Also, complete ethanol consumption is observed at this C/O. The temperature even at the hot spot does not exceed 1000 K. This is favorable for stability of catalyst performance as deactivation by sintering will occur only to a small extent at these temperatures [174]. Ethanol can be used as a fuel for a CPOX reformer under these operating conditions.

The investigations in three-differently-positioned channels reveal that radial heat loss has a strong impact on the reactor performance even for a small diameter of the honeycomb monolith (diameter = 10 mm). A moderate temperature loss (30 K) largely affects the product distribution leading to lower H₂ yields and to noticeable quantities of ethylene and acetaldehyde at the catalyst outlet for peripheral channels. The breakthrough of by-products and a reduced hydrogen yield represent crucial issues and need to be taken into account when designing CPOX reformers. Heat losses can be minimized by thick layers of thermal insulation but cannot be completely eliminated. With respect to APU (Auxiliary Power Unit) technology, integrated reformer/fuel cell devices can represent a promising solution because of a more favorable thermal management. The adoption of systems with shell-and-tube configuration allows an accurate control of the reformer tube temperature. This is done by heat recovery from exhaust gases coming from the downstream SOFC (Solid-Oxide Fuel Cell), which, furthermore, causes an increase in the overall thermal efficiency [175, 176].

Chapter 5

CPOX of Ethanol-Blended Gasoline Over Rh/Al₂O₃

The mobile application of APUs is based on the use of widely available automotive fuels with an already existing infrastructure. For the operation of a CPOX reformer with commercial fuels, the performance of these fuels in a reformer must be known. Commercial fuels are complex mixtures as they consist of hundreds of different hydrocarbon species, e.g. alkanes, alkenes, cycloalkanes, and aromatic compounds [105]. The composition can only be expressed as an averaged molecular composition. Furthermore, the concentrations of the different species in commercial fuels vary, depending on the origin of the fuel and the region, where the fuel is sold. Regulations for the properties of the fuels differ for many countries.

To investigate the performance of commercial fuels in CPOX reformers and to understand ongoing processes, such as catalyst aging, reproducibility of the experiments is important. Thus, model fuels, also called “surrogates”, are applied to achieve reproducibility and to be able to understand the reaction network. The model fuels contain only a small number of components,

5. CPOX of Ethanol-Blended Gasoline Over Rh/Al₂O₃

generally one or two, in known amounts. The components are chosen to represent the dominating species of the commercial fuel. For example, for gasoline, iso-octane (2,2,4-trimethylpentane) [19–22] or a blend of iso-octane and toluene [23, 24] is used to investigate the performance of gasoline in CPOX reformers.

In this work, the CPOX of the commercial fuels 95 RON gasoline (“Super Benzin”) and E 85 was studied. Both of these logistic fuels contain ethanol. In 95 RON gasoline, ethanol is only a fuel additive with a concentration of 5 vol-%; in E 85, it is the main component with 85 vol-%. These fuels were chosen to cover the complete range of ethanol-blended gasoline. E 85 is an alternative fuel which can be used in flexible fuel vehicles (FFV) or in gasoline engines after modification. The model surrogates used in this study consist of ethanol/iso-octane blends with 5 vol-% and 85 vol-% ethanol, respectively. All these fuels were investigated on Rh₉₀₀ for C/O = 0.6 – 1.5. Ex-situ measurements were performed with the setup CPOX 1 (see Section 3.3.4 for detailed operating conditions).

Figure 5.1 shows the yielded amounts of the main products and methane as a function of the C/O ratio for commercial fuels and surrogates. For 95 RON gasoline and its surrogate, no yields are shown for methane at C/O > 1.0 as the values were outside of the calibration range of the FTIR. Further by-products, such as ethylene, are also formed, but exceeded the calibration range of the FTIR as well. Reactant conversion cannot be followed during the experiments for the commercial fuels as too many components are present. The temperature that was detected in the gas phase downstream of the catalyst is displayed in Figure 5.1 (f). Each of the following two sections focuses on one of the commercial fuels.

5.1 Gasoline with 5 % Ethanol¹

For 95 RON gasoline, the hydrogen yield passes through a maximum at $C/O = 0.81$ ($Y_{H_2}^H = 0.79$). A steep decrease with increasing C/O ratio is observed ($Y_{H_2}^H = 0.42$ at $C/O = 1.44$). For the surrogate, a higher hydrogen yield ($Y_{H_2}^H = 0.89$) is observed at a slightly higher C/O ratio of 0.9.

This shift is probably due to the other hydrocarbon species in commercial, e.g. aromatic compounds. The chain lengths of the hydrocarbons vary, and the C/O ratio is calculated based on an averaged composition. Thus, for the same calculated C/O ratio, the actual C/O ratio for a short-chain hydrocarbon is lower than the calculated C/O ratio, while the C/O ratio for long-chain hydrocarbon is higher than the calculated one [24].

In addition, some hydrocarbon species are preferentially converted and consume the available oxygen, thus leading to higher C/O ratios for the remaining species [22]. A favored conversion of ethanol compared to iso-octane is observed for ethanol/iso-octane blends [16], and this effect is probably stronger for commercial fuels than for two-component mixtures as much more than two different species are present in commercial fuels.

Nevertheless, the same trends are noticeable for commercial and model fuels, with hydrogen showing a maximum value below $C/O = 1.0$ and a distinct decline with increasing C/O ratio after the maximum.

For water, Figure 5.1 (a), an opposing trend is visible compared to hydrogen. A minimum is observed, which is more pronounced for the model than for the commercial fuel. As for the CPOX of single-component fuels on Rh/Al_2O_3 (Chapter 4), steam reforming will most likely play an important role

¹Parts of this section have been taken from [16]. Reprinted (adapted) from Catalysis Today, 197, C. Diehm, T. Kaltschmitt and O. Deutschmann, Hydrogen production by partial oxidation of ethanol/gasoline blends over Rh/Al_2O_3 , 90-100, Copyright (2012), with permission from Elsevier.

5. CPOX of Ethanol-Blended Gasoline Over Rh/Al₂O₃

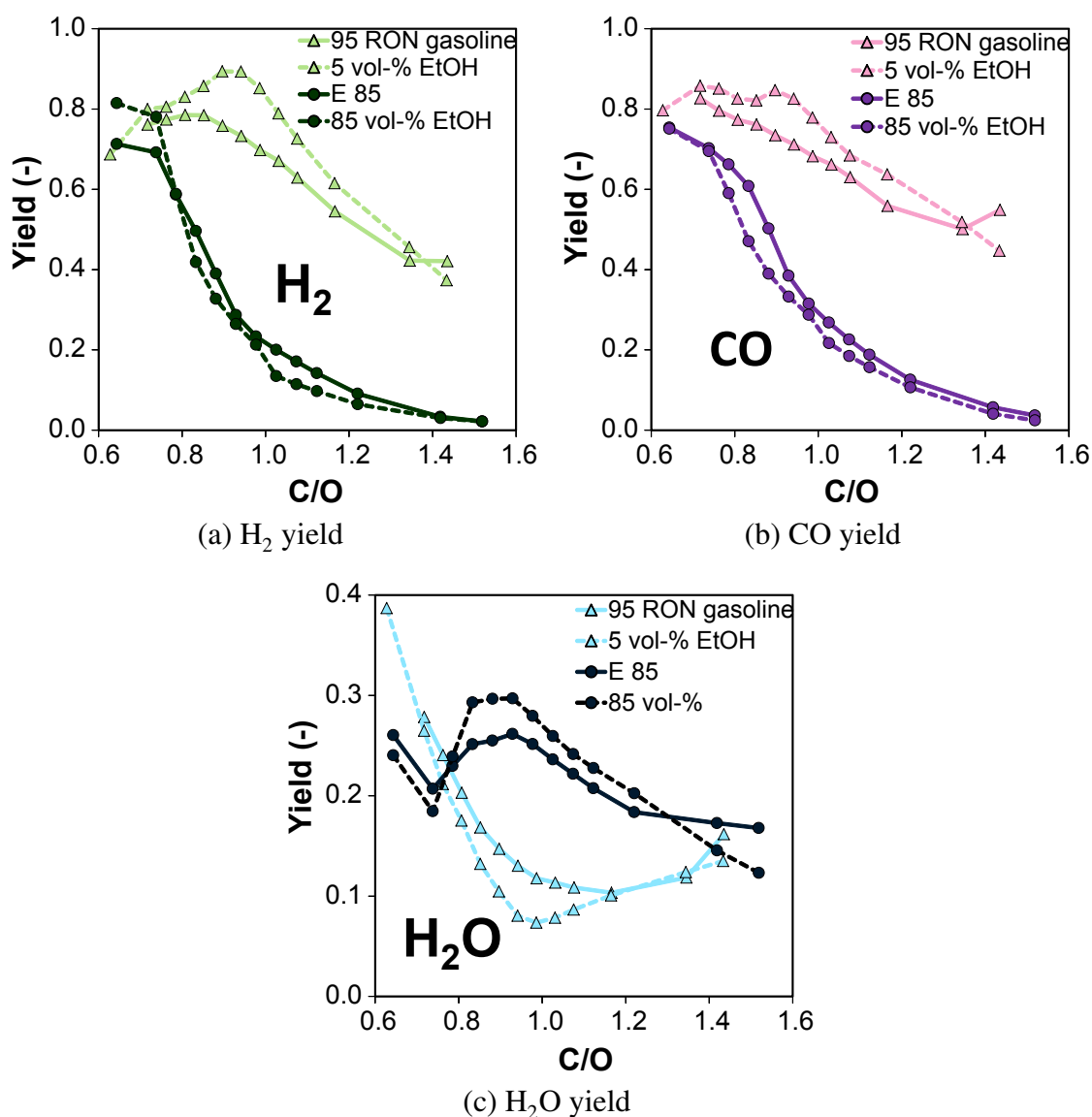


Figure 5.1: Yielded amount of hydrogen (a), CO (b), water (c), CO₂ (d), and CH₄ (e), as well as the gas-phase temperature downstream of the catalyst (f) as a function of the C/O ratio for CPOX of commercial and model fuels over Rh/Al₂O₃. Volume percent refers to the concentration of ethanol in the ethanol/iso-octane blends. No yields are shown for methane at C/O > 1.0 for 95 RON gasoline and its surrogate as the values exceeded the calibration range.

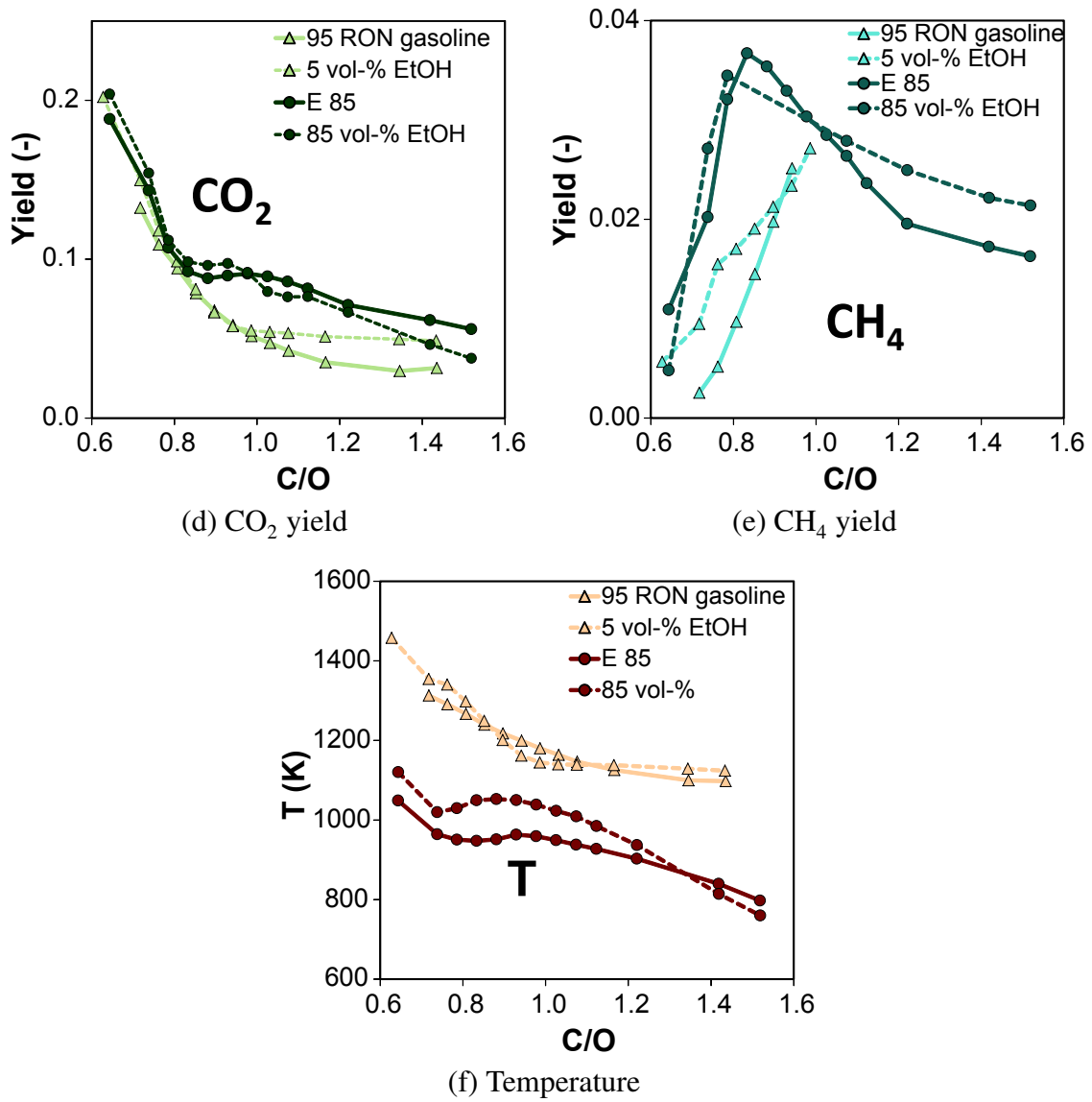


Figure 5.1: Continued.

5. CPOX of Ethanol-Blended Gasoline Over Rh/Al₂O₃

in the formation of hydrogen. This would also explain the correlation of low water yields with high hydrogen yields observed for $C/O < 1.0$.

CO and CO₂ showed a decrease with rising C/O ratio for 95 RON gasoline. For the surrogate, two maxima are observed for CO at $C/O < 1.0$, and the decrease in CO₂ yield is not as strong as for the commercial fuel.

The methane formation for both model and commercial fuel increases strongly with C/O ratio reaching $Y_{CH_4}^C = 0.03$ already at $C/O = 0.9$. For higher C/O ratios, a further increase of methane yield is detected, the values are not shown, as they lay outside the calibration range of the FTIR. By-product formation increases due to the presence of unconverted fuel.

The temperature, Figure 5.1 (f), is very high at low C/O ratios, 1312 K for 95 RON gasoline. With increasing C/O ratios, the temperature decreases. Nevertheless the temperature is above 1050 K for all investigated C/O ratios. This high temperature is also favorable for by-product formation. Additionally, it has to be taken into account that this temperature is the gas-phase temperature downstream of the catalyst.

From the investigations on the single-component fuels (Chapter 4), even higher temperatures are expected at the catalytic surface, especially throughout the first millimeter of the catalyst. Such high temperatures lead to faster catalyst aging due to sintering. Also, these high temperatures mean a high thermal stress for all the reactor parts. Furthermore, coking on the catalyst surface could occur due to the fact that coke-precursors, such as ethylene, contribute to catalyst deactivation.

5.2 Gasoline with 85 % Ethanol²

For E 85, the hydrogen yield, Figure 5.1 (a), decreases steeply from $Y_{\text{H}_2}^{\text{H}} = 0.71$ at $\text{C/O} = 0.64$ to $Y_{\text{H}_2}^{\text{H}} = 0.02$ at $\text{C/O} = 1.52$. The ethanol/iso-octane blend containing 85 vol-% ethanol also shows a very similar trend, as higher hydrogen yields are only observed at low C/O ratios ($Y_{\text{H}_2}^{\text{H}} = 0.81$ at $\text{C/O} = 0.64$). For the model fuel, the conversion of ethanol and iso-octane is only complete at $\text{C/O} = 0.64$. The conversion decreases to $X_{\text{EtOH}} = 0.25$ at $\text{C/O} = 1.52$ (not shown) [16]. Conversion of iso-octane does not occur at $\text{C/O} = 1.52$.

The carbon monoxide yield declines strongly, similar to the hydrogen yield, for the commercial fuel as well as for the surrogate. A local minimum in the water yield is observed at $\text{C/O} = 0.74$, followed by a maximum at $\text{C/O} = 0.93$ and a further decrease with increasing C/O ratio for both fuels.

A similar shaped curve is observed for the temperature, Figure 5.1 (f). For both fuels, the highest temperature $T \approx 1100$ K occurs at $\text{C/O} = 0.64$, followed by a decline, a local maximum, and a further decrease with rising C/O ratios. Steam reforming seems to proceed to a lower extent with increasing C/O ratios, leading to higher water yields and lower hydrogen yields, despite the local temperature maximum around $\text{C/O} = 0.9$. For C/O ratios > 0.9 , a decrease in all product yields is observed for commercial fuel and model fuel, which correlates with the strong decrease in conversion for these C/O ratios.

For CO_2 , the yield detected for E 85 decreases steeply from $\text{C/O} = 0.64$ ($Y_{\text{CO}_2}^{\text{C}} = 0.19$) to $\text{C/O} = 0.83$ ($Y_{\text{CO}_2}^{\text{C}} = 0.10$), followed by a slower decline with rising C/O ratios to $Y_{\text{CO}_2}^{\text{C}} = 0.06$ at $\text{C/O} = 1.52$. For the surrogate, only minor deviations to this behavior are observed for the CO_2 yield.

²Parts of this section have been taken from [16]. Reprinted (adapted) from Catalysis Today, 197, C. Diehm, T. Kaltschmitt and O. Deutschmann, Hydrogen production by partial oxidation of ethanol/gasoline blends over Rh/Al₂O₃, 90-100, Copyright (2012), with permission from Elsevier.

5. CPOX of Ethanol-Blended Gasoline Over Rh/Al₂O₃

For both logistic and model fuel, the by-product methane runs through a maximum ($Y_{\text{CH}_4}^{\text{C}} = 0.04$) at $\text{C/O} = 0.83$. The high temperatures and unconverted fuel favor the formation of by-products in cracking reactions. In contrast to methane, acetaldehyde formation (not shown) increases, which is most likely due to oxidative dehydrogenation of ethanol in the gas phase over the entire range of investigated C/O ratios. This is also observed for ethanol as a single-component fuel in *blank* experiments without any catalyst for temperatures > 640 K (Section 4.2.1).

5.3 Summary

Overall, the shape of the product yields as a function of the C/O ratio is very similar for 95 RON gasoline and the ethanol/iso-octane blend containing 5 vol-% ethanol. This blend can be employed as a model fuel for 95 RON gasoline. This is a surprising result as the performance of ethanol-blended gasoline, a mixture composed of hundreds of different hydrocarbons, can be reproduced with high accuracy by means of a two-component blend. Hence, the model system simplifies the complex reaction system. The performance of the complex commercial fuel in a CPOX reformer can be investigated more closely and under reproducible conditions using the surrogate. The study of the ethanol/iso-octane blends with an in-situ technique would lead to a deeper insight into the reaction network.

A very close match is observed between yields and temperature for CPOX of commercial E 85 and the mixture of ethanol and iso-octane with 85 vol-% ethanol. Thus, the blend can be used as a surrogate for further studies on the performance of ethanol-blended gasoline with high ethanol content in a CPOX reformer. Reproducible experiments and spatially resolved in-situ measurements with this surrogate can contribute extensively to the understanding of the reaction network.

Compared to 95 RON gasoline and its surrogate, the agreement of E 85 and its surrogate is higher. This similarity between commercial fuel and model system for E 85 is comprehensible as 85 vol-% of both fuels are ethanol. Thus, solely 15 vol-% are different hydrocarbon species. The CPOX of the commercial fuel and the model system with high ethanol content seems to be primarily influenced by ethanol as the main component.

From the investigations shown here, it can be concluded that the highest syngas yields and lowest by-product yields are achieved at $C/O = 0.8-0.9$ for ethanol-blended gasoline with a low percentage of ethanol. For E 85, clearly fuel-lean conditions ($C/O = 0.64$) have to be chosen. These inlet conditions show the highest hydrogen yield, and complete conversion is expected based on the conversion observed for the model fuel (not shown) [16]. Nevertheless, the formation of by-products, such as ethylene, already occurs at these fuel-lean conditions. This by-product formation makes the application of a gas-cleaning step, e.g. selective oxidation [177], downstream of the reformer necessary to avoid coke formation. This step would be important in APUs as coke formation can easily occur in fuel cells [178].

Chapter 6

CPOX of CH₄ Over Staged Pd-Rh Catalyst

The investigations in Section 4.1 provide an insight into the catalytic partial oxidation of methane on Rh. The reaction sequence in a channel of the catalyst can be split into an oxy-reforming and a reforming zone. Based on this, a two-stage catalyst was studied for methane CPOX. It consisted of Pd₆₀₀ and Rh₆₀₀. A thin slice of Pd ($L = 2$ mm), which is a good catalyst for total oxidation [151], followed by a larger slice of Rh ($L = 8$ mm) was employed.

The direct effect of the staged catalyst on the axial temperature and concentration profiles can be observed with the in-situ sampling technique. Palladium is expected to favor total oxidation, which will probably yield a pure oxidation zone instead of an oxy-reforming zone. The reforming activity of Rh is expected to be similar to the one observed for a single slice of Rh catalyst in the reforming zone.

The impact on the performance of methane as a fuel in a CPOX reformer will contribute to the identification of new catalysts and catalyst combinations.

6. CPOX of CH₄ Over Staged Pd-Rh Catalyst

The results of these investigations are shown in this chapter. Furthermore, they are compared to the results for a Rh catalyst ($L = 11$ mm).

6.1 Spatial Profiles in a Single Channel for Pd-Rh

The catalytic partial oxidation of methane was investigated with the in-situ sampling technique for $C/O = 1.0$ in a central channel (see Section 3.3.2). The obtained axial temperature and concentration profiles are shown in Figures 6.1 and 6.2. The oxygen mole fraction shown was calculated based on the O balance because of problems with the IMR-MS. Oxygen is completely consumed at $z = 1.25$ mm. Thus, no more oxygen is available in the second stage of the catalyst, where Rh is the catalytically active material. Methane mole fraction decreases steeply from 13.3 % at $z = -0.25$ mm to 6.5 % at $z = 2.75$ mm, followed by a slow decline to 5.4 % at the catalyst outlet.

The total oxidation products water and CO₂ are formed mainly in the Pd stage. After the initial increase to 1.5 % at $z = 0.75$ mm, CO₂ shows only a slight increase of 0.7 percentage points to 2.2 % at the end of the catalyst. The H₂O mole fraction reaches its highest value of 7.7 % close to the end of the Pd stage. In the Rh stage, steam reforming occurs, which consumes water until a steady value of 4.5 % is maintained at 8.75 mm.

Hydrogen is produced, starting from $z = 0.75$ mm. Hydrogen formation continued in the Rh stage ($z = 2 - 10$ mm), where steam reforming is most likely the dominating reaction. The onset of carbon monoxide formation is at 0.25 mm, upstream of the one for hydrogen. Probably, as for methane CPOX on Rh [120], H₂ and CO formation are controlled by two different rate-determining steps. After a slight increase of CO in the Rh stage to 4.9 % at $z = 2.75$ mm, a nearly constant CO concentration is observed in the Rh stage.

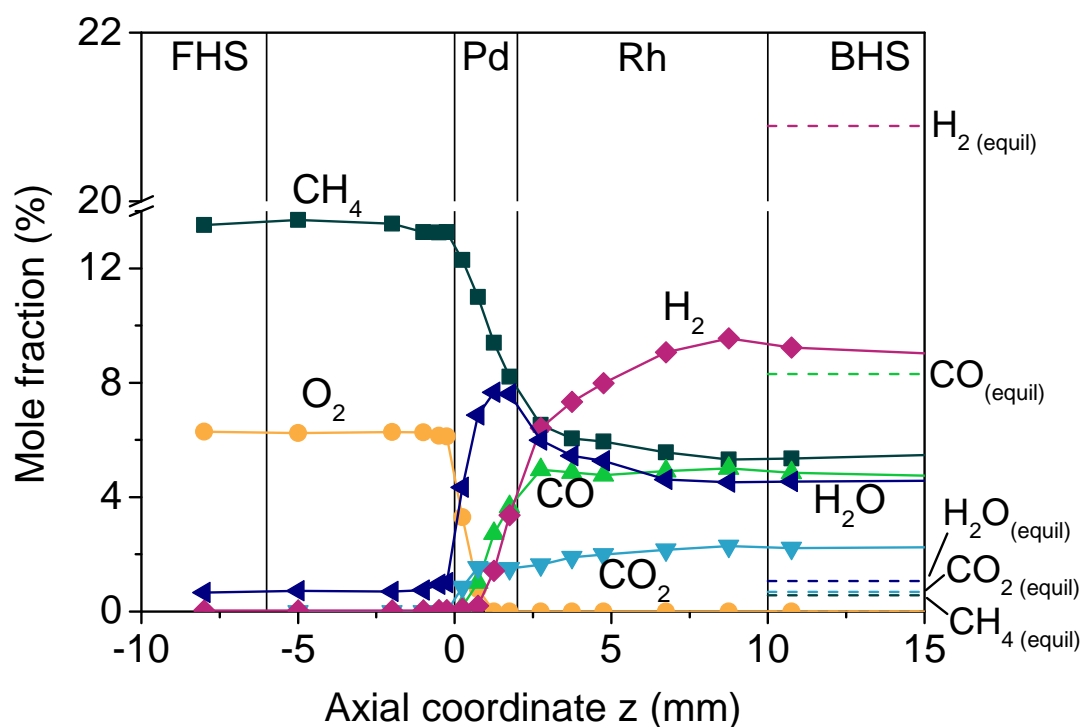


Figure 6.1: Mole fractions of CH_4 , O_2 , H_2 , H_2O , CO , and CO_2 as a function of the axial coordinate for CPOX of CH_4 over Pd-Rh catalyst at $\text{C}/\text{O} = 1.0$. Oxygen is calculated from the O balance. Dashed lines represent thermodynamic equilibrium values.

For the two-stage catalyst, the gas-phase temperature profile is shown in Figure 6.2. The surface temperature is not measured due to problems with the optical fiber. A maximum temperature of 1000 K is detected for the gas phase. The position of the gas-phase maximum is located in the Rh stage of the two-stage catalyst ($z = 3.8$ mm). Towards the end of the channel, a decrease in gas-phase temperature is detected ($T = 977$ K at $z = 10$ mm).

Due to highly exothermic total oxidation, which is the predominant reaction in this zone, the surface hot spot is expected to be in the Pd stage. Also, for methane CPOX on Rh, a downstream shift of the highest gas temperature compared to the surface hot spot is observed (Section 4.1.1). Also, the decrease in the temperature of the gas phase will most likely be a result of a decline in surface temperature similar to the behavior observed for methane CPOX on Rh. This decrease is caused by endothermic reforming reactions.

6. CPOX of CH₄ Over Staged Pd-Rh Catalyst

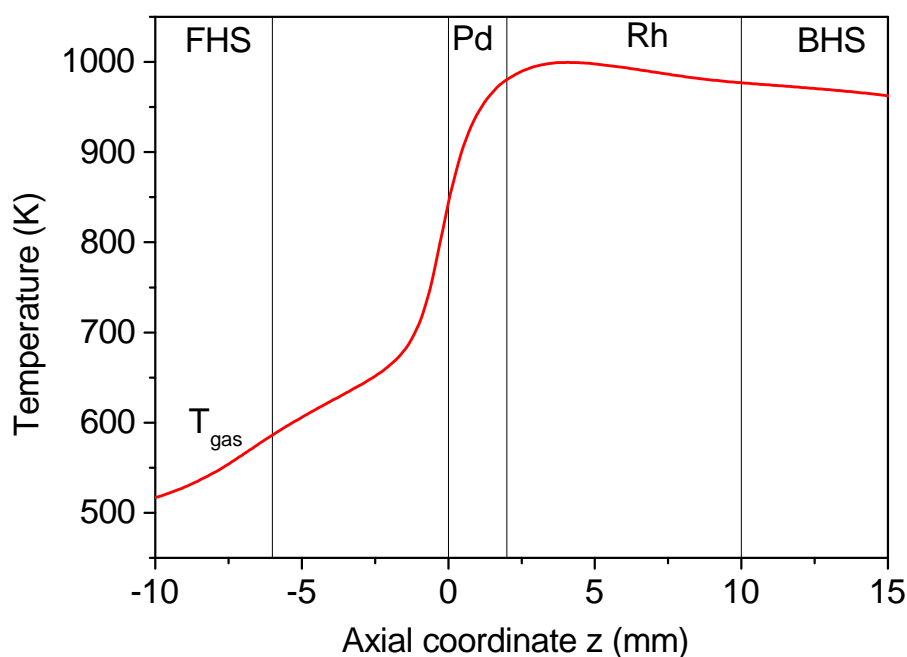


Figure 6.2: Measured temperature of the gas phase as a function of the axial coordinate for CPOX of CH₄ over Pd-Rh catalyst at C/O = 1.0.

The comparison of the measured values with the composition at thermodynamic equilibrium (dashed lines in Figure 6.1) reveals that the system is far away from the thermodynamic equilibrium. Higher methane conversion and significantly larger syngas yields ($\Delta x_{\text{H}_2} = 11.7$ percentage points) are present at equilibrium. This leads to the assumption that methane conversion is to some extent limited by kinetic effects. Steam reforming is favored from a thermodynamic point of view, but is kinetically limited. At equilibrium, solid carbon (in the form of graphite) is formed with a yield of 14.7%. The carbon formation could not be monitored in the shown experiments, but the carbon balance closes within $\pm 10\%$, suggesting only small amounts of solid carbon.

Concerning the Pd stage, compared to the formation of water and carbon dioxide, the downstream shift of the formation of hydrogen and carbon monoxide is not expected from mechanisms suggested for CPOX of methane on Pd in literature. The mechanism commonly proposed in literature [48,49,83] consists of a direct route of syngas formation, i.e. H₂O, CO₂, H₂, and CO are formed

simultaneously (see Sections 2.2.1.1 and 2.2.1.2). However, these conclusions were based on ex-situ measurements. The results from in-situ measurements shown here lead to the assumption that an indirect route to syngas is more likely. First, the total oxidation products H_2O and CO_2 are formed, followed by the formation of H_2 and CO in reforming reactions, i.e. steam and dry reforming. Nevertheless, it has to be born in mind that it is not possible to deduce the concentrations of the species close to the catalytic surface from the measurement of the concentration profiles with the in-situ technique (see Section 2.2.1.1).

All molecular oxygen is consumed in the Pd stage. At the entrance of the Rh stage, mainly methane and water are present at a $\frac{\text{H}_2\text{O}}{\text{C}}$ ratio of 0.93, which is close to the stoichiometric composition for methane steam reforming ($\frac{\text{H}_2\text{O}}{\text{C}} = 1.0$). Steam reforming also seems to be the predominant reaction. Additionally, the WGS reaction could occur, as an increase in CO_2 concentration is observed. In accordance with the findings on catalysts with Rh as only catalytically active metal [10, 12, 37, 120], dry reforming is not expected.

6.2 Pd-Rh vs. Rh

The comparison of the measured values for the two-stage catalyst Pd-Rh with the single-slice Rh catalyst is shown in Figures 6.3 and 6.4. The total length of the combination of Pd and Rh slices is 10 mm compared to 11 mm of the single Rh slice. The oxygen mole fraction, Figure 6.3 (b), is similar for both catalysts, whereas the methane mole fraction, (a), is significantly lower for Rh than for Pd-Rh. A much steeper decrease in methane concentration is detected within the first millimeter of the Rh catalyst. At $z = 0.5$ mm, $x_{\text{CH}_4} = 7.8\%$ for Rh and $x_{\text{CH}_4} = 11.7\%$ for Pd-Rh are observed. The difference in methane concentration at the catalyst outlet amounts to 1.5 percentage points.

6. CPOX of CH₄ Over Staged Pd-Rh Catalyst

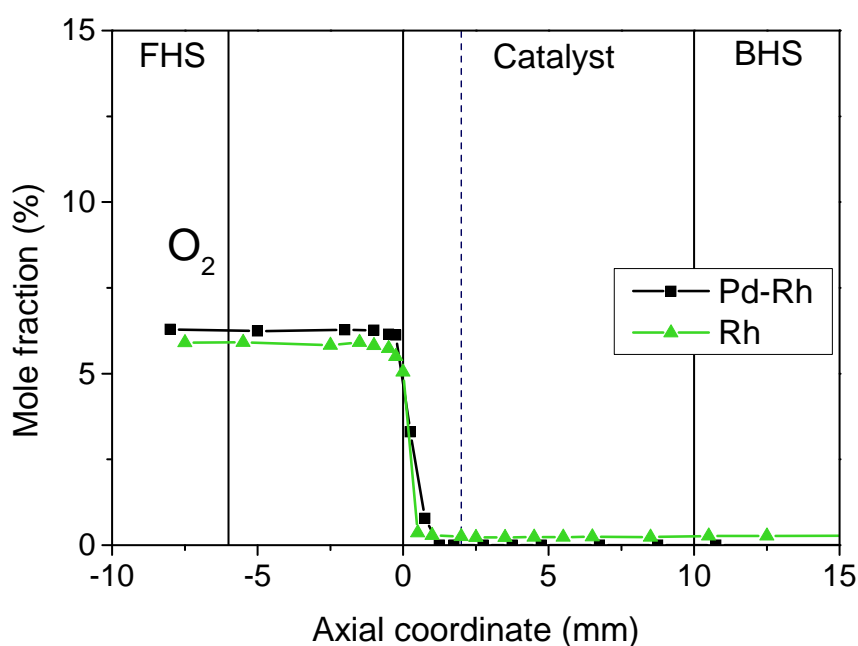
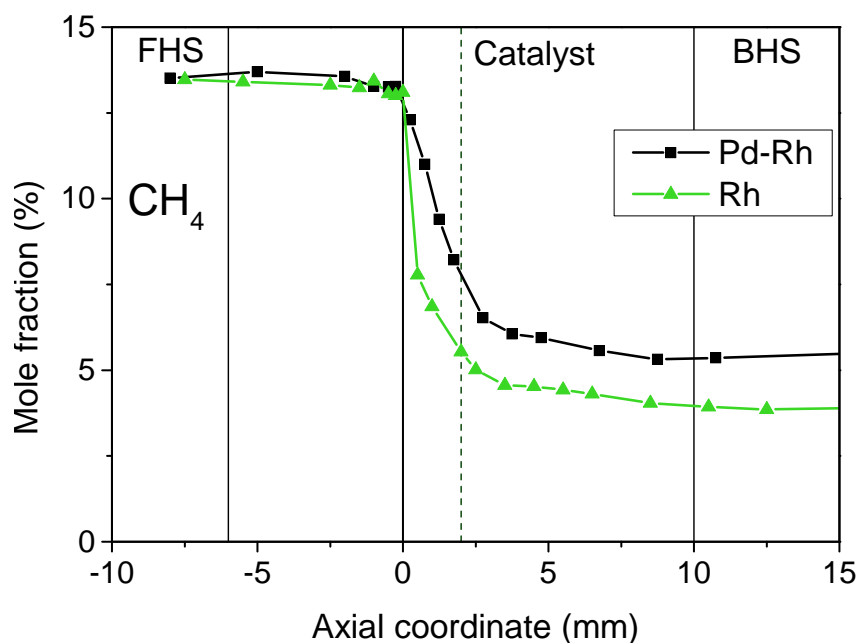
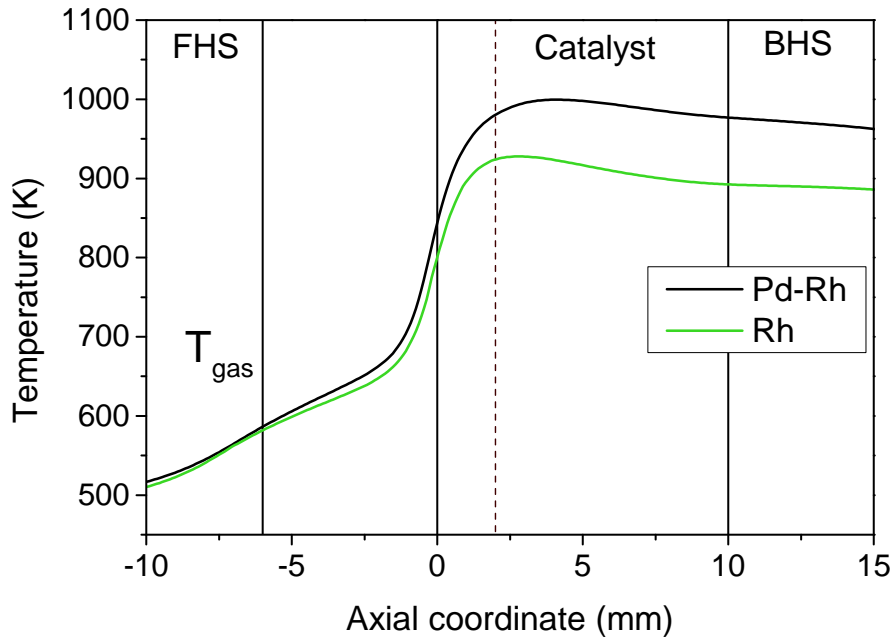
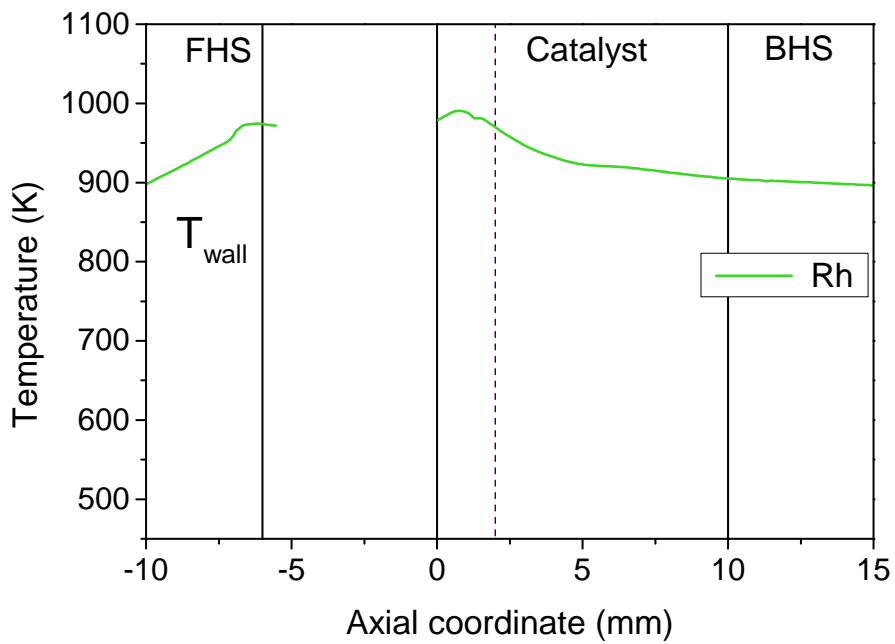


Figure 6.3: Mole fractions of the reactants, CH₄ (a) and O₂ (b), gas-phase temperature (c), and surface temperature (d) as a function of the axial coordinate for CPOX of CH₄ over a Rh catalyst and a two-stage Pd-Rh catalyst at C/O = 1.0. The concentration of O₂ for Pd-Rh is calculated from the O balance. The vertical dashed line represents the end of the Pd and beginning of the Rh stage of the staged catalyst. The end of the Pd-Rh catalyst is shown at $z = 10$ mm, and the Rh catalyst end is not shown ($z = 11$ mm).



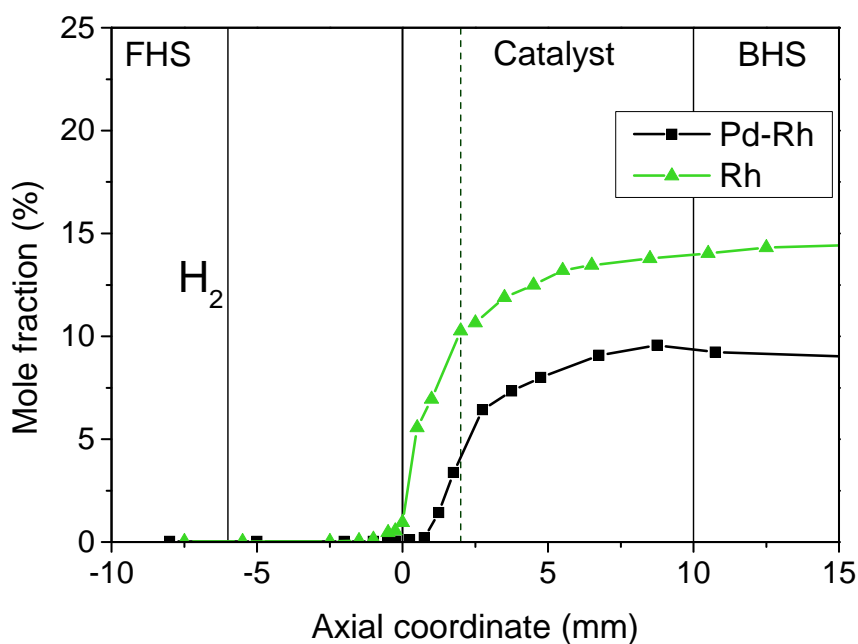
(c) Gas-phase temperature



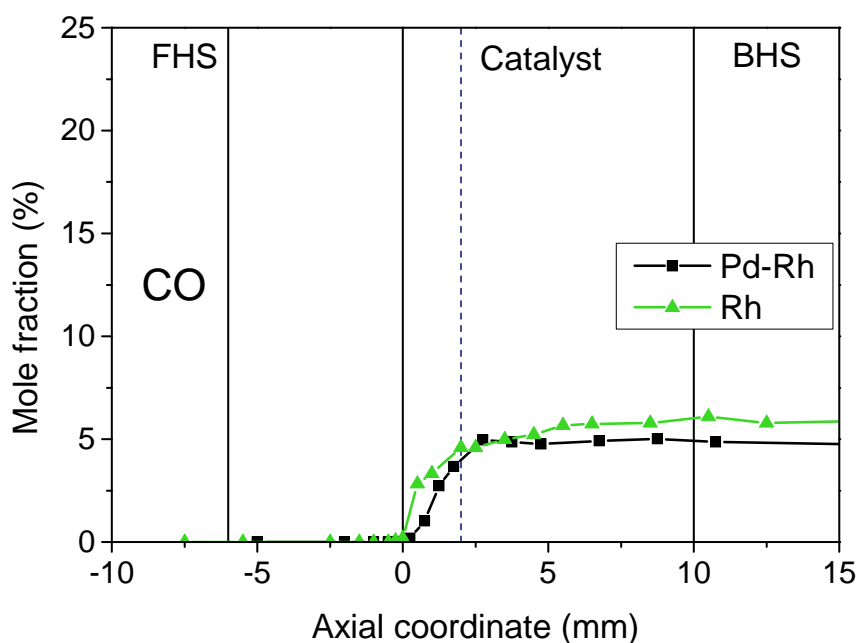
(d) Surface temperature

Figure 6.3: Continued.

6. CPOX of CH₄ Over Staged Pd-Rh Catalyst



(a) Mole fraction of H₂



(b) Mole fraction of CO

Figure 6.4: Mole fraction of the main products hydrogen (a), carbon monoxide (b), water (c), and carbon dioxide (d) as a function of the axial coordinate for CPOX of CH₄ over a Rh catalyst and a two-stage Pd-Rh catalyst at C/O = 1.0. The vertical dashed line represents the end of the Pd and beginning of the Rh stage for the staged catalyst. The end of the Pd-Rh catalyst is shown at $z = 10$ mm, the Rh catalyst end is not shown ($z = 11$ mm).

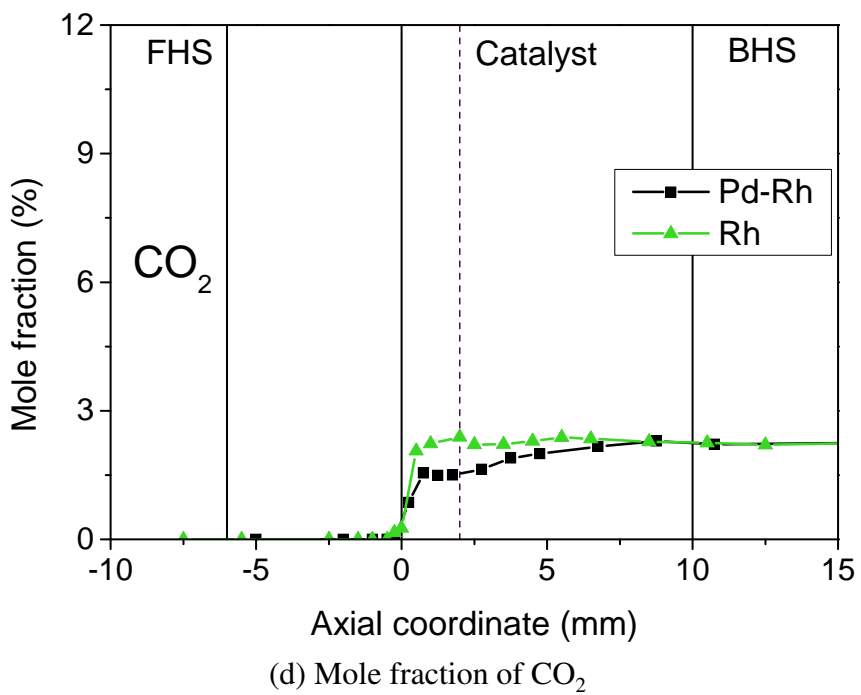
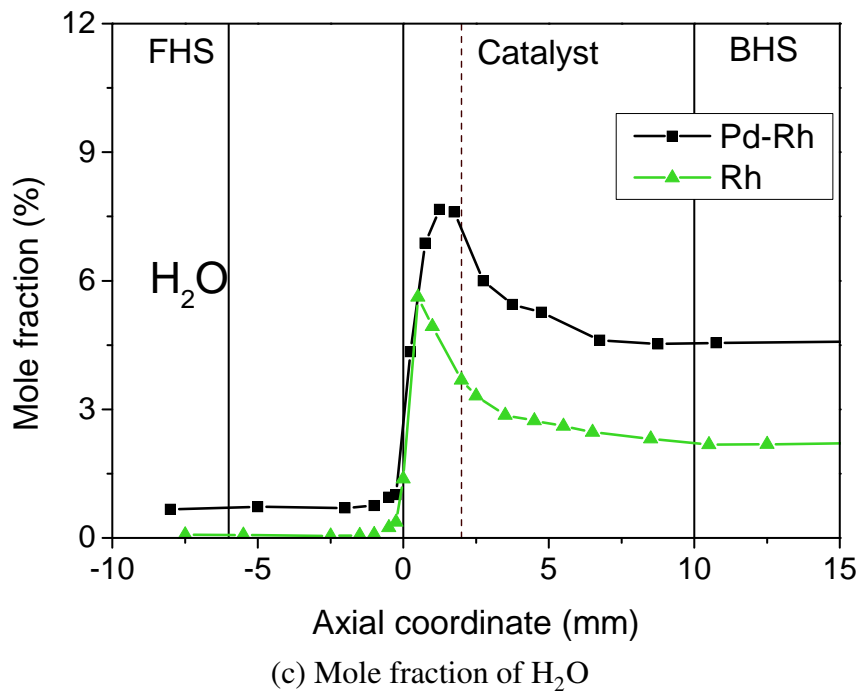


Figure 6.4: Continued.

6. CPOX of CH₄ Over Staged Pd-Rh Catalyst

For the partial oxidation products H₂ and CO, Figure 6.4 (a) and (b), a clear difference is observed in axial position at which formation of each product sets in. In the Rh catalyst, H₂ and CO are already formed right at the catalyst entrance. In the Pd-Rh catalyst, the formation of H₂ and CO starts at 0.75 mm and 0.25 mm, respectively. In contrast to this, H₂O and CO₂ are produced at $z = 0$ mm for both catalysts.

Additionally, when comparing the Rh with the Pd-Rh catalyst, the hydrogen concentration is higher by 4.8 percentage points and the water concentration is lower by 2.4 percentage points (both at $z = 10$ mm) for the single-stage Rh catalyst. For CO mole fractions, a difference of 1.2 percentage points is detected at the catalyst outlet. For CO₂, the mole fractions measured for Rh and Pd-Rh are very similar at the catalyst outlet. A difference is only visible in the first half of the channel.

The gas-phase temperature shows significant differences. The maximum temperature is shifted 1.6 mm downstream for Pd-Rh and it is 72 K higher. At the catalyst outlet, $\Delta T = 83$ K is detected, as the gas-phase temperature decreases more strongly for Rh than for Pd-Rh.

From these observations, different conclusions can be drawn. Firstly, steam reforming occurs to a lesser extent for Pd-Rh than for Rh, even though the temperature is higher in the former one by $\Delta T_{\text{gas}} \geq 80$ K. Secondly, the mechanism of syngas formation is different in Pd-Rh, which is due to the presence of Pd that is lacking in the Rh catalyst. In Rh, a combination of direct and indirect routes is assumed [12], with the formation of hydrogen and carbon monoxide occurring directly at the catalyst entrance when oxygen is still present, and further downstream by means of steam reforming (Section 2.2.1.1).

For the Pd stage of Pd-Rh, an indirect route for syngas formation seems to be more realistic. In this case, methane is first converted to H₂O and CO₂ in total oxidation, and H₂ and CO are formed in the reforming step after all oxygen has been consumed. However, it has to be taken into consideration that,

as discussed in Section 2.2.1.1, it is not possible to draw a conclusion on the concentrations of the species close to the surface of the catalyst.

Additionally, in the comparison of the formation of syngas on the employed Pd-Rh and Rh catalyst, the ratio of catalytic to geometric surface area, $F_{\text{cat,geo}}$, has to be taken into consideration. $F_{\text{cat,geo}}$ is significantly higher for the applied Rh catalyst ($F_{\text{cat,geo}} \approx 185$) than for the Pd stage ($F_{\text{cat,geo}} \approx 33$). Thus, the Rh catalyst provides more catalytically active surface area than the Pd stage for the same geometric surface area, leading to a higher activity. Assuming that the indirect route to syngas formation occurs for both metals, the difference in activity could be an explanation for the deviations in the measured concentration profiles. For Rh, the oxygen concentration close to the catalyst might be zero due to the high catalytic activity, even though oxygen is still observed with the sampling technique. Thus, syngas formation only proceeds in the absence of oxygen. For Pd, higher oxygen concentrations might occur close to the surface, due to the lower activity. Therefore, the syngas formation is delayed (in terms of the z position) until the oxygen concentration decreases to zero close to the catalyst.

Deeper insight could be gained from investigating a single Pd slice with a length of 10 mm and a $F_{\text{cat,geo}}$ comparable to the one for Rh. These investigations would make it possible to determine if the deviation in the measured concentration profiles for Rh and Pd-Rh is due to different catalytic activities or is caused by the different noble metals.

6.3 Summary

A staged catalytic reactor containing Pd and Rh was examined with an in-situ sampling technique. For the first time, in-situ investigations on a Pd honeycomb monolith are presented in this work, to the best of the author's knowledge. For the Pd-Rh catalyst, a lower syngas yield than for Rh is observed. Thus, the

6. CPOX of CH₄ Over Staged Pd-Rh Catalyst

Pd-Rh catalyst is not beneficial as a catalyst combination in a CPOX reformer. However, a lower ratio of catalytic to geometric surface area for the Pd stage compared to the Rh catalyst needs to be taken into consideration for the interpretation of the measured concentration profiles.

Other combinations, such as Pt and Ni or Rh and Ni, could be attractive due to the low price of Ni compared to noble metals. Platinum is also studied as a catalyst in partial oxidation processes [29, 179]. A short slice of Pt or Rh could be used for the oxy-reforming zone and a longer slice of Ni for the reforming zone. In literature, in-situ investigations for a Pt-Ni foam catalyst showed promising results [180, 181]. Further investigations are necessary to evaluate the potential of Pt-Ni and Rh-Ni honeycomb catalysts for usage in CPOX reformers.

Chapter 7

CPOX of Propane at Elevated Pressures over Rh/Al₂O₃

In small-scale applications, e.g. mobile APUs, space and weight are the main limiting factors. An operation at elevated pressures provides the opportunity to reach a higher molar flow rate for the same volume. Thus, a higher throughput is achieved. Also, for decentralized applications, operation of CPOX reformers at elevated pressures could be beneficial as connected process steps might employ pressurized conditions [80].

However, with operation at elevated pressures, certain challenges have to be faced. Gas-phase reaction rates increase with a rise in pressure. Therefore, undesired by-product formation, e.g. of coke precursors, is more likely [6]. Increased formation of carbon deposits can be a result, which would also be undesirable for the downstream equipment. Additionally, rising temperatures due to higher pressures could lead to faster aging of the catalyst.

7.1 Operation at 2-4 bar¹

The catalytic partial oxidation of propane was investigated at elevated pressures ranging from 2 – 4 bar on Rh₄₀₀ ($L = 26$ mm) at $C/O = 0.8$ and a constant molar flow rate (see Section 3.3.5 for detailed operating conditions).

Spatial concentration and temperature profiles for propane CPOX are shown in Figures 7.1 to 7.3. It has to be kept in mind that the experiments were performed for a constant molar flow rate. Hence, the volumetric flow rate decreases with increasing pressure. This leads to a doubling of the residence time from 2 to 4 bar.

For oxygen, Figure 7.1 (b), the increase in pressure has no influence on the length of the part of the channel, in which it is consumed. Oxygen consumption is mass-transfer limited [71] at ambient pressure and also at elevated pressures. The diffusion coefficient is proportional to p^{-1} and the density is proportional to p . Therefore, the diffusion rate, which is a product of diffusion coefficient and density, is independent of the pressure.

Propane consumption, on the other hand, is moderately dependent on the pressure. The position at which complete propane consumption is detected shifts towards the catalyst inlet for an increase in pressure. An overall offset to higher temperatures is observed for surface as well as gas-phase temperatures rising from 2 bar ($T_{\text{gas}} = T_{\text{wall}} = 1078$ K at $z = 21$ mm) to 4 bar ($T_{\text{wall}} = 1132$ K, $T_{\text{gas}} = 1120$ K at $z = 21$ mm).

For hydrogen, Figure 7.2 (a), as well as for CO, (b), very similar mole fractions are detected for all three investigated pressures. Slightly lower hydrogen mole fractions are observed at the catalyst outlet at 4 bar ($x_{\text{H}_2} = 21.8\%$) compared to 2 and 3 bar ($x_{\text{H}_2} = 22.8\%$ and 22.6% , respectively). The water peak, which is detected for all investigated pressures at $z \approx 1.5$ mm, is con-

¹Measurements have been performed at Politecnico di Milano. Results shown in this section have been published in [81].

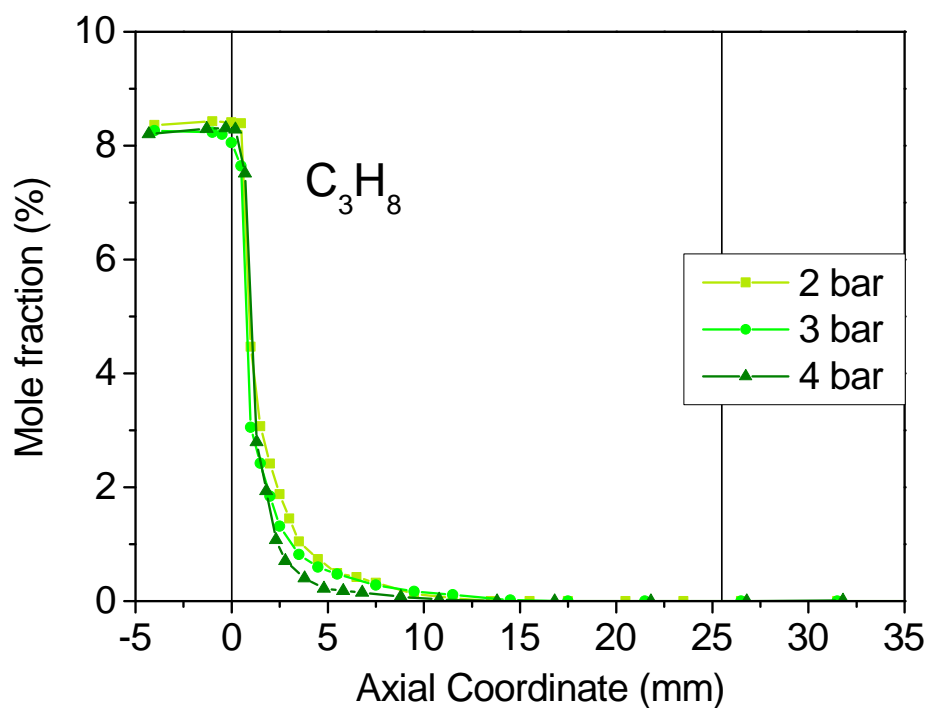
siderably higher at 4 bar with 8.6 % compared to 5.4 % at 2 bar and 5.1 % at 3 bar. Also, at the catalyst outlet, a larger water concentration is observed for 4 bar than for the other two pressure levels. Nevertheless, the values at the catalyst outlet show a difference of only 0.6 percentage points. Thus, at 4 bar, more water is formed in the oxy-reforming zone but a majority is consumed again in the reforming zone. CO_2 shows very similar mole fractions for 2 – 4 bar, and only for operation at 4 bar is a peak observed at $z = 1.3 \text{ mm} - 1.8 \text{ mm}$. The decrease in CO_2 mole fraction might be due to dry reforming or reverse WGS, whereas endothermic dry reforming would be favored thermodynamically at the high temperatures observed for 4 bar. Overall, a low dependency of the main product formation on pressure is observed, leading to the assumption that the heterogeneous reactions are mainly independent of pressure.

For all main products, the observed mole fractions at the catalyst outlet are close to the values of the thermodynamic equilibrium.

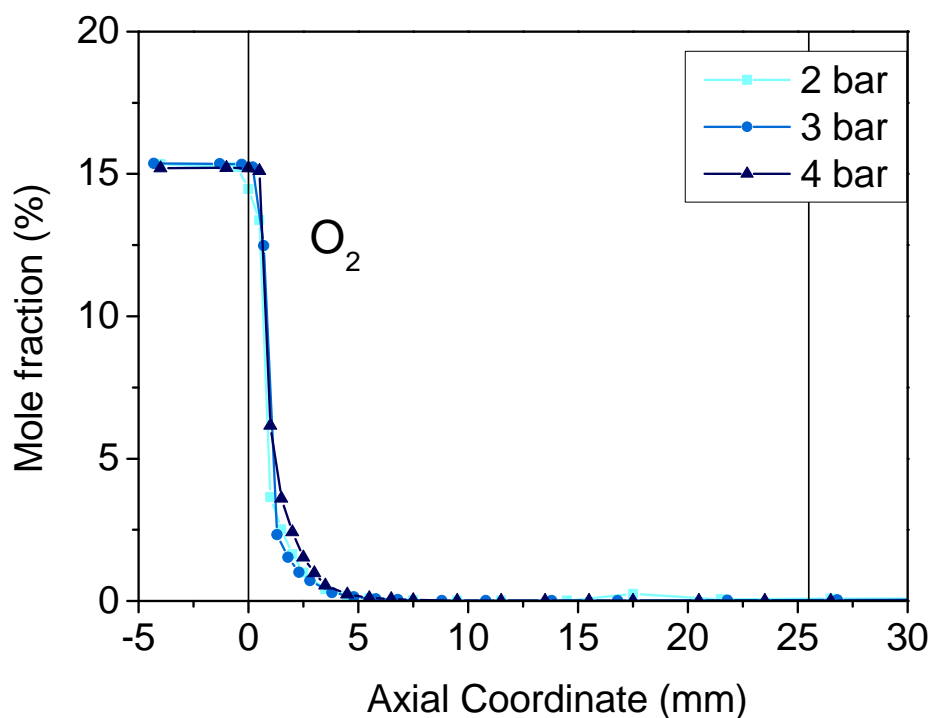
The by-products, Figure 7.3, are formed within the first few millimeters of the catalyst by means of gas-phase cracking of propane (see Section 2.2.2.2). This was also observed for propane CPOX at ambient pressure [71]. It is clearly noticeable that the formation of the by-products in homogeneous gas-phase reactions increases with a rise in pressure. Thus, the increased conversion of propane at elevated pressures within the first millimeters of the catalyst is due to these homogeneous reactions. The increased pressure is accompanied by a higher temperature and residence time, which are both favorable factors for the by-product formation originating from propane cracking.

Except for methane, the side-products are consumed again at all pressures. This consumption is due to heterogeneous reforming reactions, mainly steam reforming. This also correlates with the consumption of water, which is observed from $z = 1.3 \text{ mm}$ to $z \sim 15 \text{ mm}$ along the channel of the catalyst and which is highest at 4 bar, for which the largest by-product yields are detected. Methane, Figure 7.3 (a), is the only by-product still present at the reactor outlet.

7. CPOX of Propane at Elevated Pressures over Rh/Al₂O₃

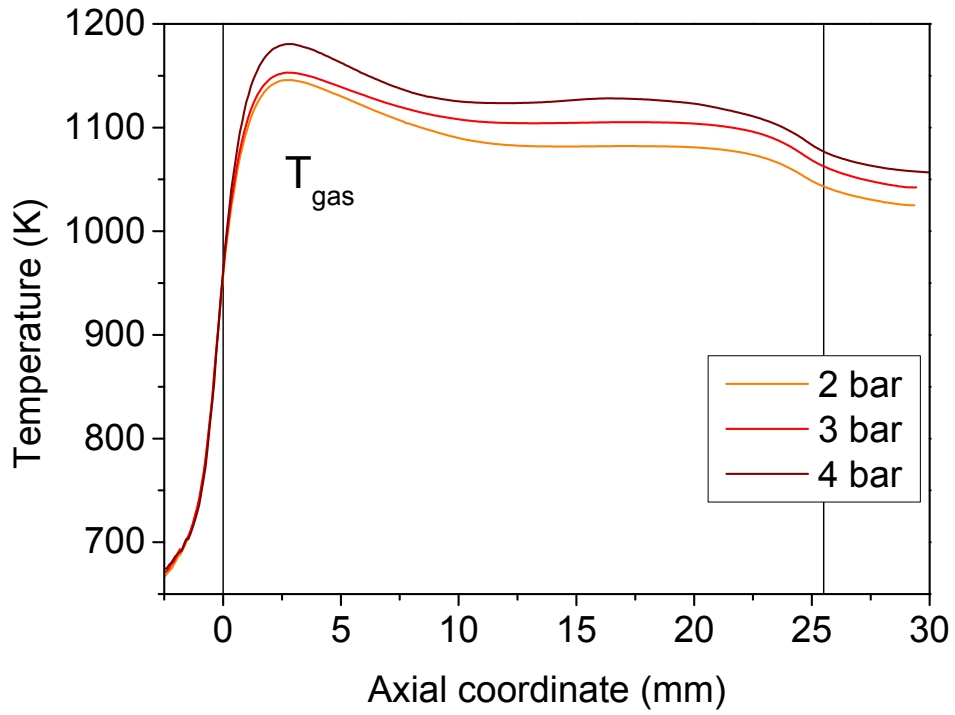


(a) Mole fraction of propane

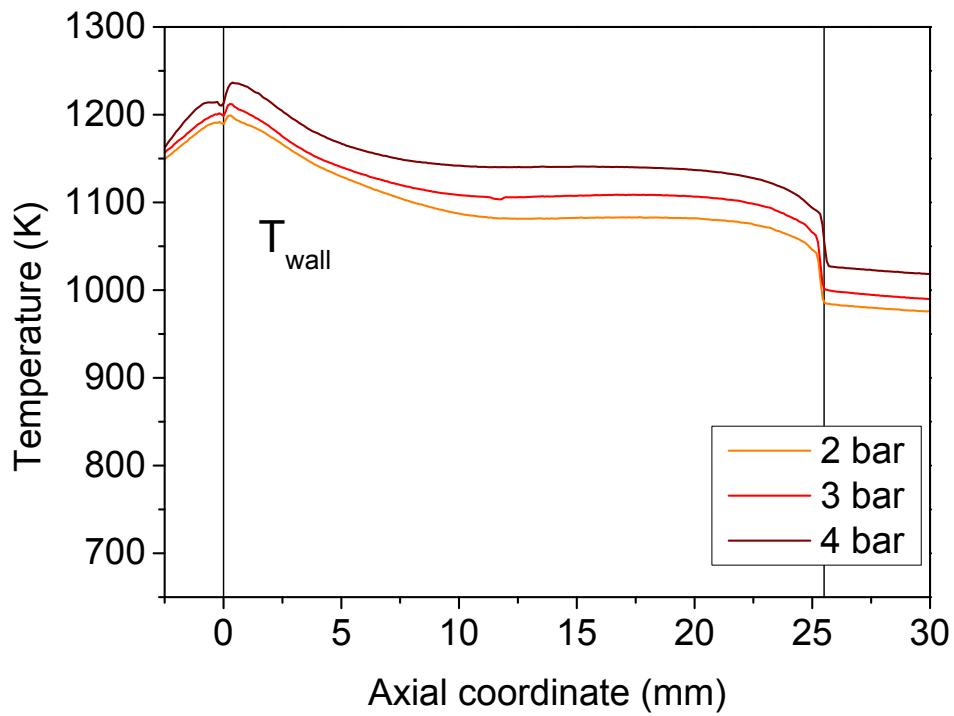


(b) Mole fraction of O_2

Figure 7.1: Mole fraction of the reactants propane (a) and O_2 (b), gas-phase temperature (c), and surface temperature (d) as a function of the axial coordinate for CPOX of C_3H_8 at $C/O = 0.8$ for three different pressures ranging from 2 to 4 bar. Thermodynamic equilibrium values are zero for C_3H_8 and O_2 at all pressures.



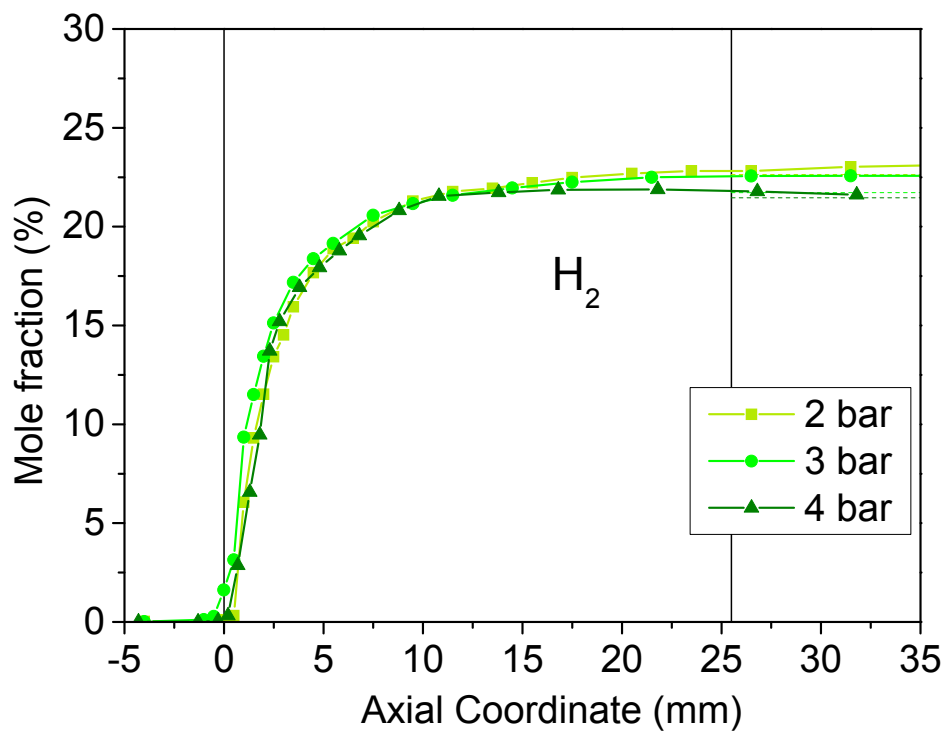
(c) Gas-phase temperature



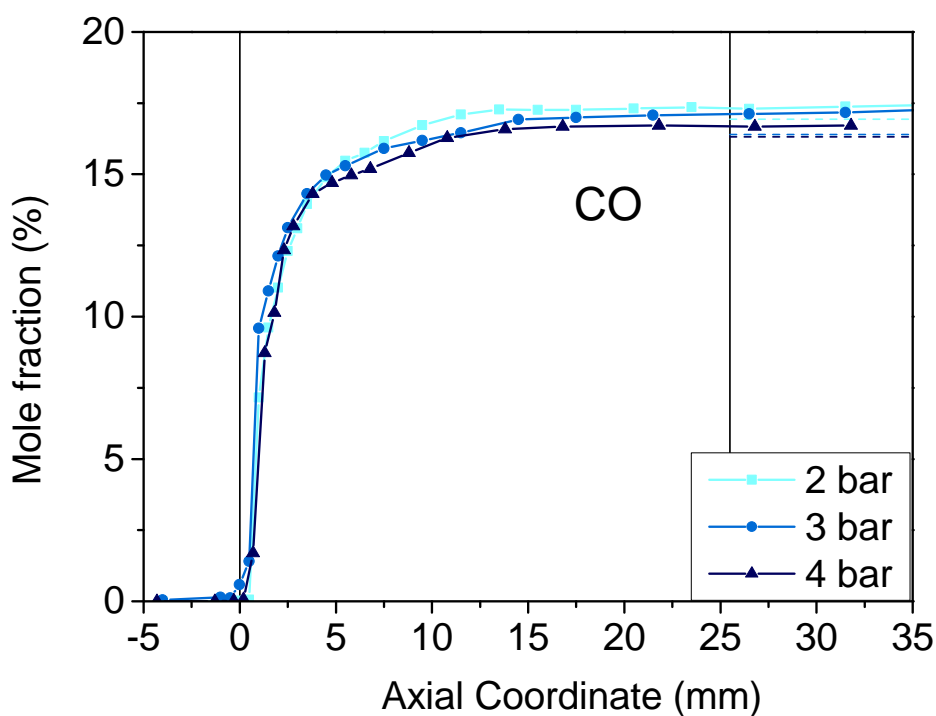
(d) Surface temperature

Figure 7.1: Continued.

7. CPOX of Propane at Elevated Pressures over Rh/Al₂O₃



(a) Mole fraction of H₂



(b) Mole fraction of CO

Figure 7.2: Mole fraction of the main products hydrogen (a), carbon monoxide (b), water (c), and carbon dioxide (d) as a function of the axial coordinate for CPOX of C₃H₈ at C/O = 0.8 for three different pressures ranging from 2 to 4 bar. Dashed lines show thermodynamic equilibrium values.

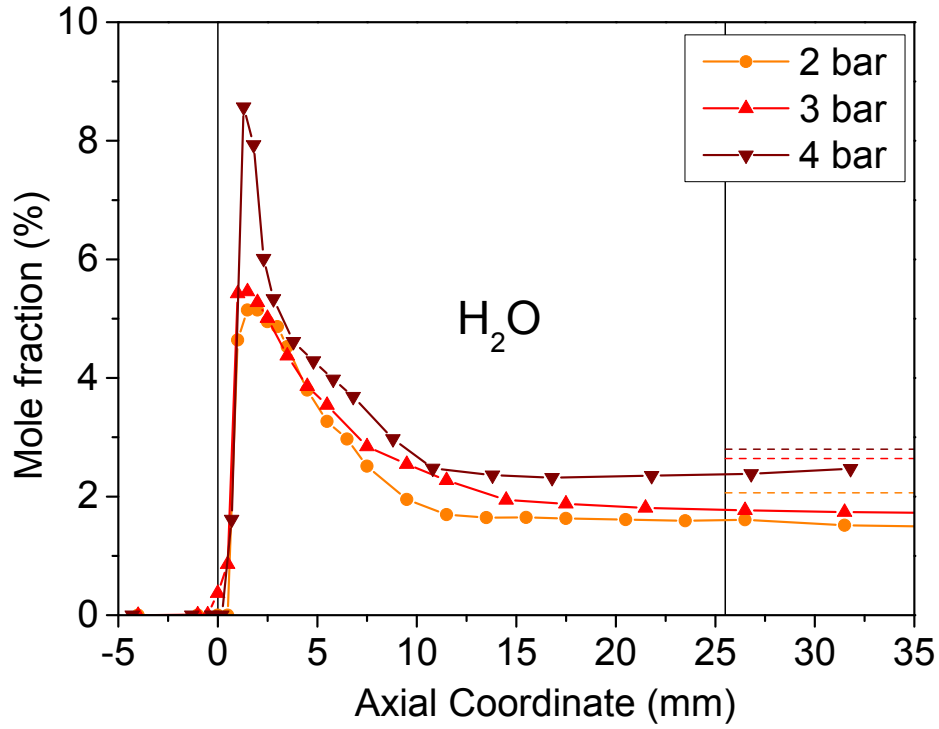
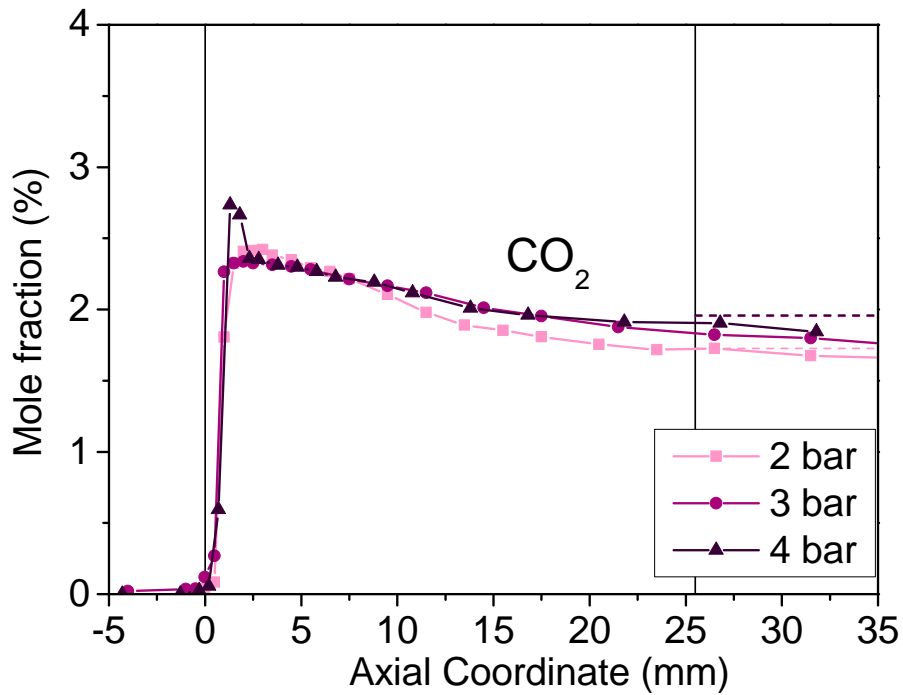
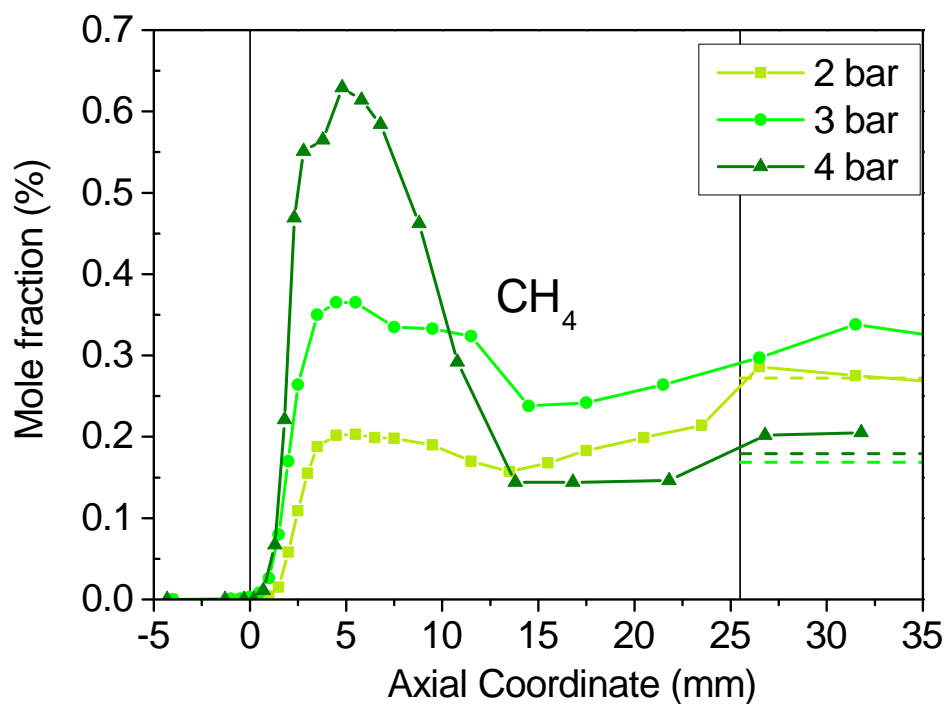
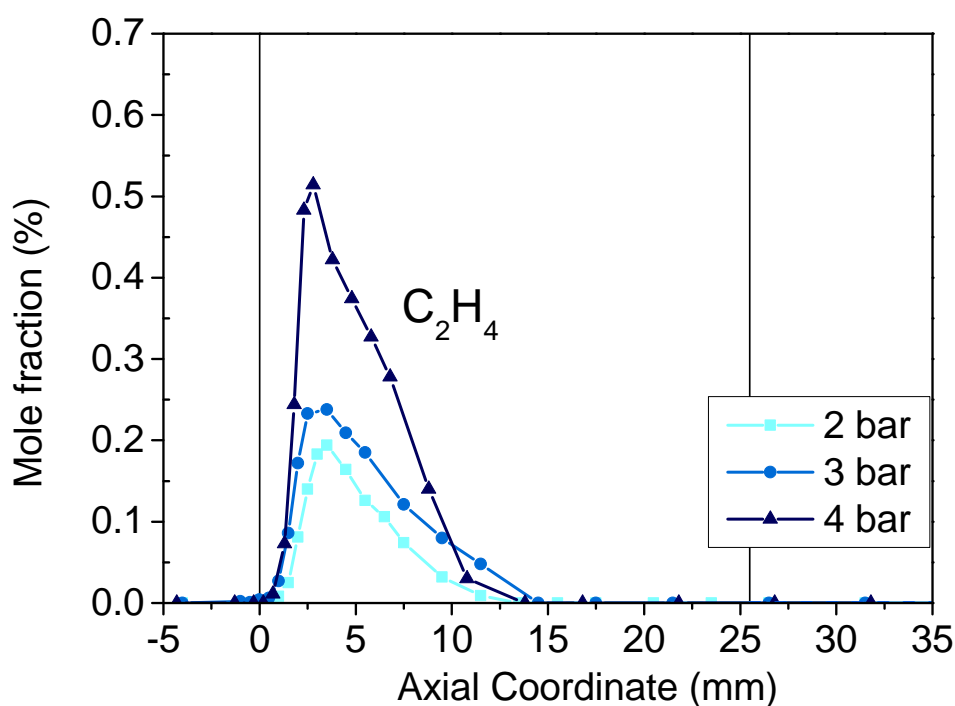
(c) Mole fraction of H_2O (d) Mole fraction of CO_2

Figure 7.2: Continued.

7. CPOX of Propane at Elevated Pressures over Rh/Al₂O₃



(a) Mole fraction of CH₄



(b) Mole fraction of C₂H₄

Figure 7.3: Mole fraction of the by products methane (a), ethylene (b), ethane (c), and propylene (d) as a function of the axial coordinate for CPOX of C₃H₈ at C/O = 0.8 for three different pressures ranging from 2 to 4 bar. Dashed lines show thermodynamic equilibrium values. For C₂H₄, C₂H₆, and C₃H₆, equilibrium values are zero.

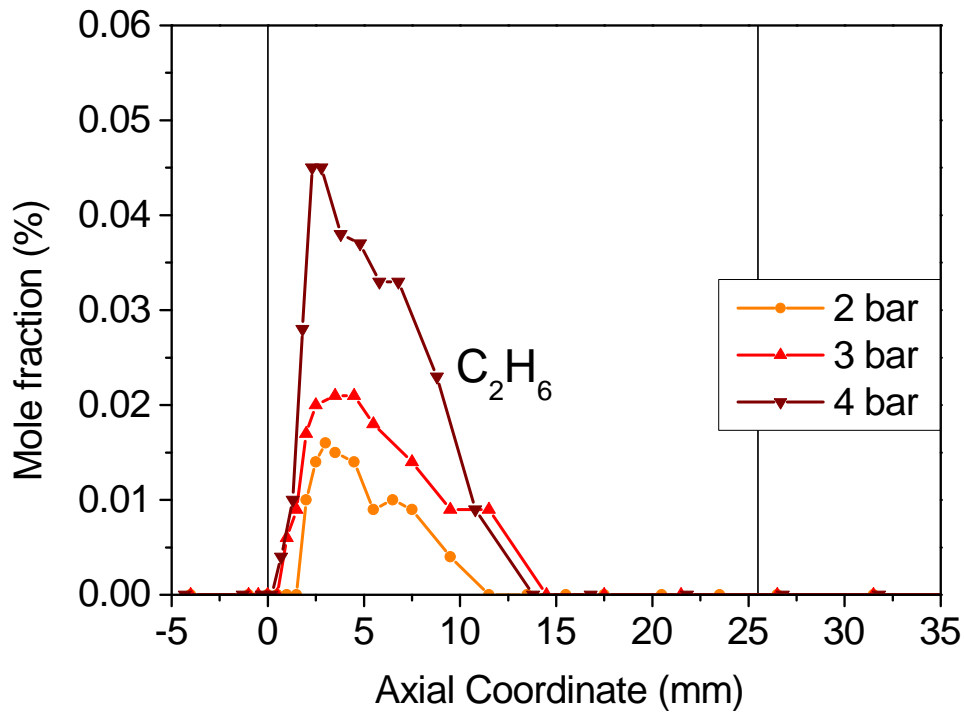
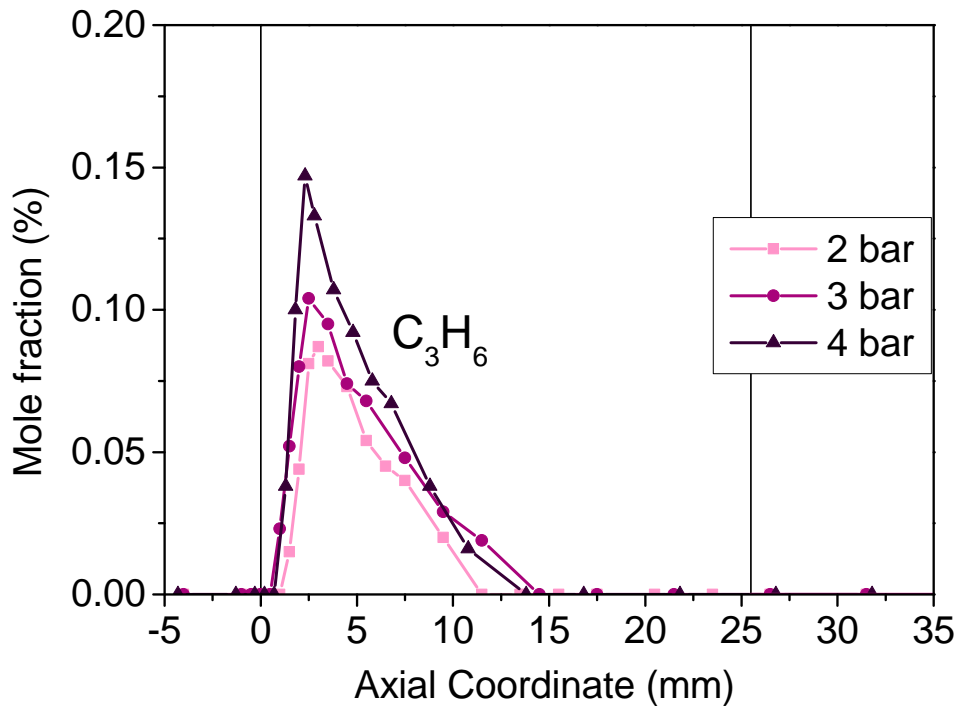
(c) Mole fraction of C_2H_6 (d) Mole fraction of C_3H_6

Figure 7.3: Continued.

7. CPOX of Propane at Elevated Pressures over Rh/Al₂O₃

After the initial formation in homogeneous cracking reactions and the following drop of the methane mole fraction due to heterogeneous reforming, another increase is visible. This is most likely due to methanation, Equation (2.7), as described in [71] for CPOX of C₃H₈ at ambient pressure. Methanation is an exothermic reaction; hence, it is favored at lower temperatures. During operation at 4 bar, which exhibits the highest temperature of all investigated pressures, the lowest methane concentration ($x_{\text{CH}_4} = 0.20\%$) is discovered at the catalyst outlet (compared to $x_{\text{CH}_4} = 0.29\%$ for 2 bar and $x_{\text{CH}_4} = 0.30\%$ for 3 bar). However, the methane mole fraction is higher at the catalyst outlet for 3 bar than for 2 bar even though the temperature is higher. The thermodynamic equilibrium composition contains methane, with the lowest value for 3 bar ($x_{\text{CH}_4} = 0.17\%$) and the highest for 2 bar $x_{\text{CH}_4} = 0.27\%$.

7.1.1 Summary for Operation at Elevated Pressures

Overall, similar mole fractions of the main products are detected at the catalyst outlet for the investigated pressures. Also, the rate of heterogeneous consumption seems to be unaffected by a pressure increase. The effect of pressure on the catalytic partial oxidation of propane is mainly visible in the by-products, which are formed from propane in homogeneous cracking reactions. The increase in residence time, which is due to a constant molar flow rate, favors these reactions. The side-products, except for methane, are consumed again in heterogeneous reforming reactions for all pressures. However, the higher temperatures at elevated pressures could lead to faster aging of the catalyst due to sintering and thermal stress.

In the study shown above, it was only possible to collect spatial profiles in a central channel. Thus, the dependency of the radial channel position is not known. For the studies on methane and ethanol CPOX at ambient pressure, Sections 4.1.2 and 4.2.3, radial gradients across the monolith are observed, showing lower fuel conversion and, for ethanol, a breakthrough of by-products in an

outer channel. Higher conversion and no breakthrough are detected for the central channel at the same operating conditions. Similar behavior is also possible in the case of propane CPOX at ambient as well as elevated pressures. This has to be taken into account when designing a CPOX reformer for this system from the data presented in this work.

7.2 Coke Formation at 4 bar

During the experiments for CPOX of propane at 4 bar, a blocking of a metering valve downstream of the reactor occurred. Carbon particles were found in the valve, which led to the assumption that the operating conditions at 4 bar favor the formation of solid carbon, i.e. coke or soot. To further investigate the kind of carbon formed and the underlying formation process, different types of filters were inserted into the reactor downstream of the catalyst to collect carbon samples (see Section 3.3.5). Four different filter types were used. With regard to the filter material, three of the filters were based on the same material, a FeCrAlloy[®] mesh (see Section 3.3.5 for details). By calcination at 1223 K, 1373 K, and coating with γ -Al₂O₃, three differently inertized filters were obtained. The calcination causes the formation of an Al₂O₃-layer on the fibers of the mesh, employing aluminium from the alloy itself and oxygen from the calcination atmosphere. The fourth filter type was glass fabric tape. For each filter type, an experiment was performed for at least 6 h for C₃H₈ CPOX at 4 bar (10 Nl min⁻¹, C/O = 0.80). Three filters of one type were placed closely spaced in the reactor tube downstream of the BHS (see Figure 3.13).

Figure 7.4 shows the four different filter types after the experiments. For all filter types, out of the three filters present in the reactor, the one with the largest deposition of carbon is shown. For (a), the first of the three filters is shown, for (b) the second, for (c) the third, and for (d) the first filter. The ordinal number refers to the arrangement of the filters in the reactor tube related to the gas flow.

7. CPOX of Propane at Elevated Pressures over Rh/Al₂O₃

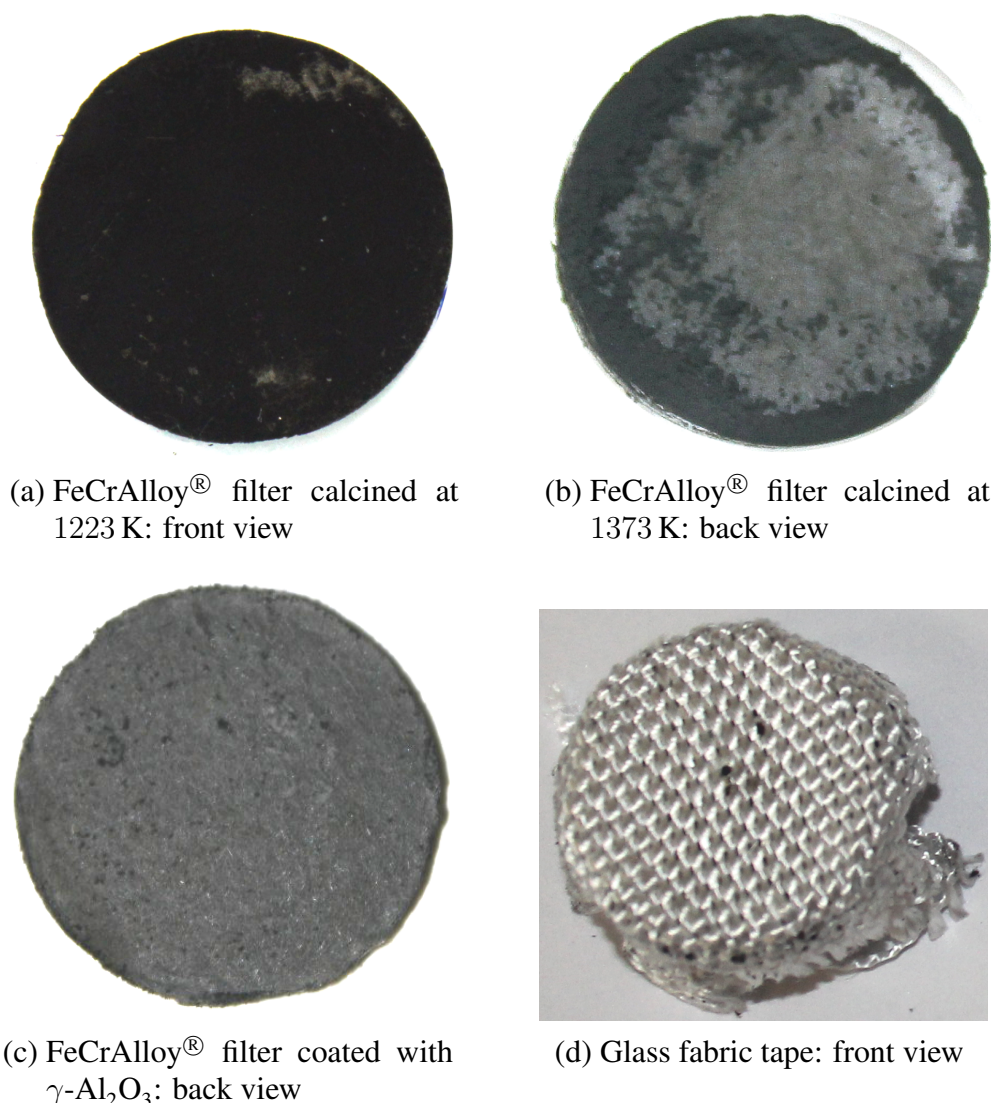


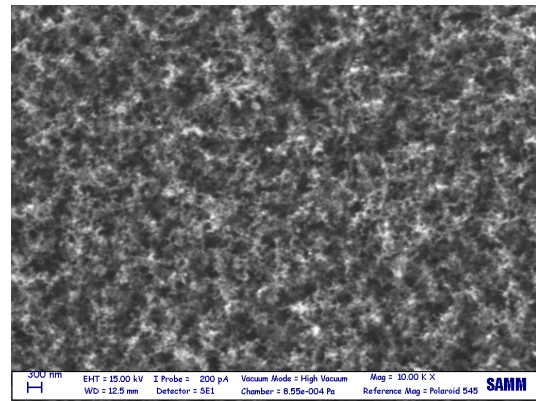
Figure 7.4: FeCrAlloy[®] filter calcined at 1223 K (a), at 1373 K (b), and filter coated with γ -Al₂O₃ (c) as well as glass fabric tape (d) after CPOX of propane at C/O = 0.8 and $p = 4$ bar after 6 h. Front view corresponds to the side of the filter, on which the gas flow hits the filter. Back view is the rear side, where the gas flow leaves the filter after passing through.

Comparing the deposition on the different filters, the highest amount of coke is found on the filter calcined at 1223 K, whereas nearly no coke is deposited on the glass fabric tape. As the operating conditions are the same for all four filter types during the experiments, the carbon formation seems to be

dependent on the material of the filter. Glass fabric tape is inert, whereas one or more components of the FeCrAlloy[®] seem to be catalyzing the formation of coke. The inertization of the FeCrAlloy[®] increases with calcination temperature and even more strongly by coating the FeCrAlloy[®] fibers of the mesh with γ -Al₂O₃. For the filter calcined at 1373 K and the one coated with γ -Al₂O₃, the carbon formation occurs mainly at the edge of the filter disk. This is most likely due to the mounting of the filters in the reactor tube, where some of the interizing Al₂O₃-layer is scratched off on the edges.



(a) 40 x enlarged with optical microscope



(b) SEM image

Figure 7.5: Image taken with 40 x enlargement in optical microscope (a) and with SEM (b) of FeCrAlloy[®] filter calcined at 1223 K after CPOX of propane at $C/O = 0.8$ and $p = 4$ bar.

The components of the FeCrAlloy[®], which are catalytically active, are probably Fe and Ni. These are both known to catalyze the formation of coke [39, 182–184]. Concerning the source of carbon, the outlet composition for CPOX of C₃H₈ contains methane and CO as probable carbon sources. The reactions responsible for carbon formation from these species would be methane decomposition (reverse reaction of Equation (2.8)) and the Boudouard reaction (Equation (2.9)). Taking into consideration the partial pressures of the species CH₄ and H₂ for Equation (2.8) as well as CO and CO₂ for Equation (2.9) and also the temperature at the catalyst outlet, the Boudouard reaction is favored

7. CPOX of Propane at Elevated Pressures over Rh/Al₂O₃

from a thermodynamic point of view, whereas methane decomposition is not proceeding.

In addition to these considerations, it needs to be taken into account that the composition at the catalyst outlet could vary across the monolith as observed for methane and ethanol CPOX at ambient pressure (see Sections 4.1.2 and 4.2.3, respectively). A breakthrough of by-products, e.g. ethylene, would open up additional pathways for carbon formation such as deposition of olefins and PAHs from the gas phase [20, 40–42, 171–173].

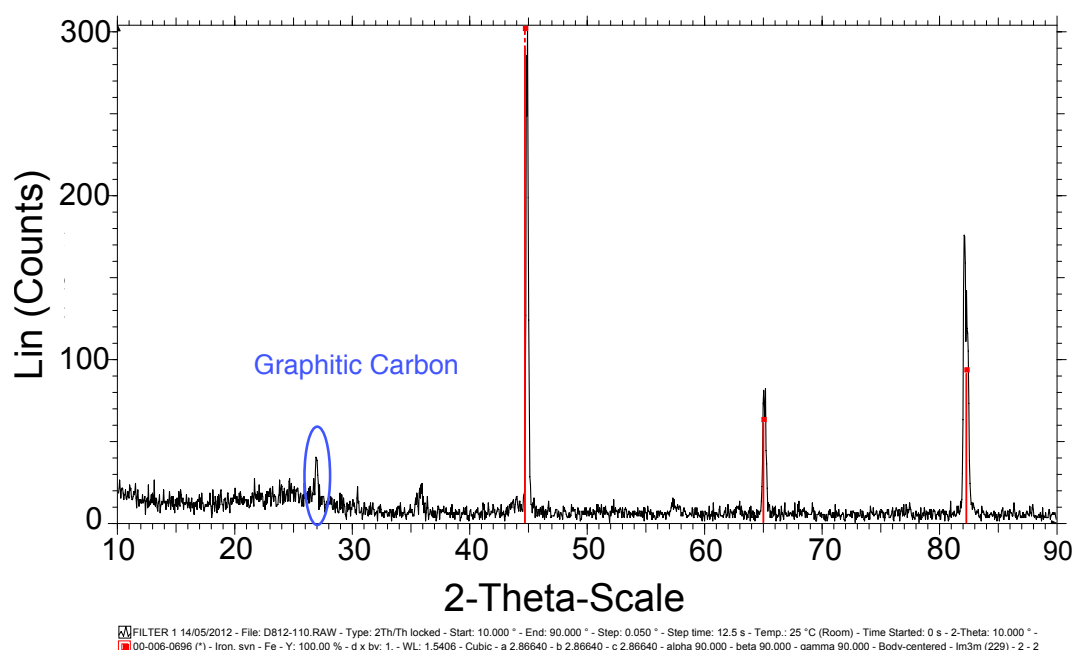


Figure 7.6: XRD spectrum (black) of FeCrAlloy[®] filter calcined at 1223 K (Figure 7.4 (a)). In red, the reference for synthetic iron is shown. The peak that results from graphitic carbon is highlighted with a blue ellipse around it.

Optical microscopy, SEM (Scanning Electron Microscopy), X-ray diffraction, and Raman spectroscopy were employed to characterize the carbon deposit formed on the filters. Figures 7.5 to 7.7 show the images and spectra obtained for the filter calcined at 1223 K (Figure 7.4 (a)). The picture enlarged forty times, Figure 7.5 (a), of the surface reveals a smooth layer of coke on the filter disc, with “fingers” sticking out. The surface structure of the coke layer and the

fingers is compared by SEM. The SEM measurements were performed at the Department of Chemistry, Materials and Chemical Engineering of Politecnico di Milano. A very similar structure, shown in Figure 7.5 (b), is detected for both positions.

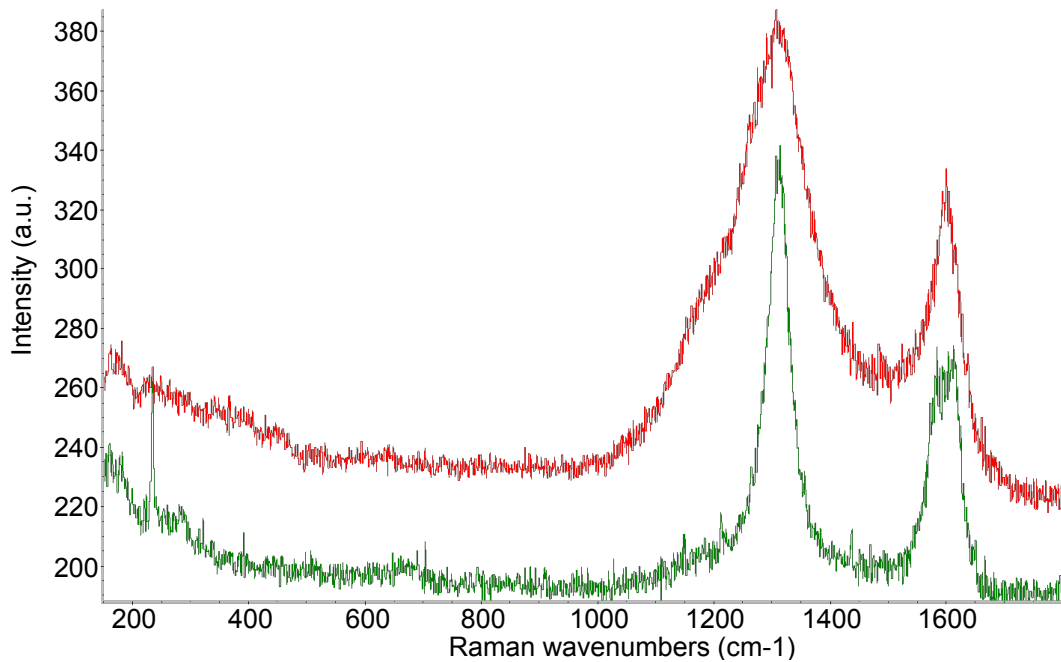


Figure 7.7: Raman spectra of two different positions on FeCrAlloy[®] filter calcined at 1223 K (Figure 7.4 (a)). The green spectrum represents a position on the filter at which carbon nanotubes are present. The red spectrum represents a position at which amorphous carbon is present.

An X-ray diffraction (XRD) spectrum, Figure 7.6, was recorded for the filter to gain knowledge about the allotrope of carbon in the deposit. The XRD measurement was also performed at the Department of Chemistry, Materials and Chemical Engineering of Politecnico di Milano. Due to the thin layer of deposit and the higher scattering factor of heavier elements, the pattern of the underlying FeCrAlloy[®] mesh is mainly visible. Only the small peak at $2\theta = 27^\circ$ fits the graphite pattern.

Additionally, Raman spectroscopy is performed at two different positions of the filter calcined at 1223 K, yielding the spectra in Figure 7.7. The measure-

7. CPOX of Propane at Elevated Pressures over Rh/Al₂O₃

ments and interpretation of the spectra were carried out by Andrea Lucotti. The green curve shows the radial breathing mode (RBM) at $\approx 250 \text{ cm}^{-1}$, which is typical for carbon nanotubes [185]. The assumption of the existence of nanotubes on the sample is supported by the splitting of the G mode ($\approx 1600 \text{ cm}^{-1}$) into a doublet, which is also characteristic for nanotubes [185]. The second investigated position produced the Raman spectrum displayed in red. Here, essential differences are visible compared to the other spectrum. There is no RBM and the G mode is not a doublet. Thus, at this position, no carbon nanotubes are present. The spectrum is more similar to ones obtained for amorphous carbon and soot [186]. From the investigations, the structure of the coke deposited on catalytically active filters is not completely clear. A mixture of different allotropes, such as graphite, amorphous carbon, and carbon nanotubes, seems to be present.

7.2.1 Summary for Coke Formation

The carbon formation during CPOX of C₃H₈ at 4 bar seems to be catalyzed by Fe or Ni. These metals are also components of stainless steel, which is used in the downstream equipment of APUs. The probability of coke formation on steel rises with increasing aging of the steel [187]. During operation at 4 bar, high gas-phase temperatures ($T = 1070 \text{ K}$) are reached at the catalyst outlet. Therefore, high temperatures are still maintained in the downstream equipment, which could be sufficient for catalyzed carbon formation. Considering the composition at the catalyst outlet, coke deposition due to the Boudouard reaction is favored from a thermodynamic point of view, whereas methane deposition seems unlikely. The formed coke seems to be a mixture of amorphous carbon, graphitic carbon, and carbon nanotubes, whereas the percentage of the allotropes in the mixture is not determinable from the investigations presented in this work.

To avoid the formation of solid carbon, one possibility would be to quench the ongoing reactions by a fast cool down of the reactive gases as close to the catalyst outlet as possible. However, this solution is only reasonable if downstream processes do not require high temperatures of the feed gas. Additionally, in areas where high temperatures cannot be avoided, inertized materials should be used for tubing to avoid the presence of compounds which could act as catalysts in coke formation. If the carbon formation is attributed to coke-precursors such as ethylene, selective oxidation of the coke-precursors by oxygen, which is added to the gas composition downstream of the catalyst, could be a possibility [177].

Chapter 8

Conclusion

Scope of This Work

Hydrogen is employed in a broad range of applications, e.g. as a basic material for the chemical industry and as a fuel in mobile power generation. Due to the different kinds of applications, a wide variety of feedstocks are reformed to hydrogen and carbon monoxide (synthesis gas). Catalytic partial oxidation is a promising possibility for on-site hydrogen generation because of autothermal operation. Furthermore, only fuel and air are necessary for the operation of a CPOX reformer.

For the design of a CPOX reformer, many aspects need to be taken into account. Operating conditions need to be adapted to the employed fuel and the downstream process. Many different fuels are applicable in CPOX reformers for hydrogen production, e.g. natural gas, LPG, logistic and renewable fuels. Every fuel has its own characteristic behavior and reaction network. In addition to a variation in fuels, a change in catalytically active material highly influences the ongoing reactions. A deeper understanding of the reaction sequence is useful for the design and optimization of a CPOX reformer.

8. Conclusion

The use of in-situ sampling techniques make it possible to collect axial concentration and temperature profiles inside one channel of a honeycomb catalyst. These techniques supply very detailed information on the reaction network along the channel of the catalyst, which is crucial for the development of detailed mechanisms and beneficial for reformer design. However, the measured spatially-resolved profiles are influenced by the sampling probe inside the channel.

Setup of In-Situ Sampling Technique

During this work, an experimental setup was designed and constructed for the investigation of CPOX on honeycomb monoliths. The included in-situ sampling technique makes it possible to measure axial concentration and temperature profiles inside one channel of a honeycomb. For the concentration profiles, a capillary is inserted into the channel. A constant gas flow is sucked from the channel at the position of the capillary tip. The analysis of the gas composition is performed using an FTIR spectroscope and two mass spectrometers. An axial resolution of 0.25 mm can be achieved. For the temperature profiles, two different methods are employed. A thermocouple is used to measure the gas-phase temperature; an optical fiber connected to a pyrometer is applied for the detection of the temperature at the channel wall.

Evaluation of Sampling Technique

In this work, CFD simulations were performed to investigate the effect of the sampling capillary on the axial profiles. The simulations revealed a distinct difference between a channel with and without a capillary. The deviation increased the further the probe was inserted into the channel. For the same axial position in a channel without and a channel with a probe, the residence time is larger for the channel with the probe. Thus, an upstream shift of the concentration profiles

is observed for the channel with the capillary. Experimental values for methane CPOX and 3D CFD simulations for a channel with a capillary showed an agreement, whereas a distinct deviation was observed between the experiments and the simulation values for a channel without a capillary.

The main finding is that CFD simulations are essential for the interpretation of the measured axial profiles. Furthermore, by using CFD simulations, effects like diffusion can be identified as being responsible for specific experimentally observed phenomena. Performing CFD simulations for all experimentally investigated systems is beyond the scope of this work. Nevertheless, the deviations were taken into account for the interpretation of the experimental data.

Investigated Systems: CH₄, C₂H₅OH, C₃H₈, and Ethanol-Blended Gasoline

Different systems were studied in this work to cover a variety of applications of CPOX reformers. Table 8.1 gives an overview of the investigated systems, each of which is presented with the major aspect on which the investigations focused.

Oxy-Reforming and Reforming Zone

For all fuels investigated on Rh/Al₂O₃, the reaction sequence in the channel can be split into two zones, the oxy-reforming zone and the reforming zone. In the oxy-reforming zone, total oxidation and steam reforming are the predominant reactions. All oxygen is consumed in this region, i.e. within the first millimeters of the catalyst. The reforming zone, in which there is no oxygen present anymore, is mainly influenced by steam reforming.

8. Conclusion

Fuel	Catalytically active material	Investigated aspect
Methane	Rh	Radial heat loss
	Pd-Rh	Two-stage catalyst
Ethanol	Rh	Feed composition $C/O = 0.65 - 0.85$
	Rh	Radial heat loss
95 RON gasoline	Rh	Feed composition $C/O = 0.6 - 1.5$
	Rh	Model fuel
E 85	Rh	Feed composition $C/O = 0.6 - 1.5$
	Rh	Model fuel
Propane	Rh	Pressure 2 – 4 bar

Table 8.1: Overview of systems investigated in this work.

Even though no in-situ measurements were performed for the commercial fuels 95 RON gasoline and E 85, the separation of the catalyst into the two zones is expected due to the results obtained for the single-component fuels.

Effect of Feed Composition on Ethanol

The study on ethanol CPOX included the collection of axial profiles for different C/O ratios, i.e. ethanol and oxygen concentrations in the feed, in a central channel. The chosen C/O ratios of $C/O = 0.65 - 0.85$ were all in the fuel-lean region. Former studies for ethanol CPOX revealed by-product formation al-

ready at fuel-lean conditions and that the amount of by-products increases with rising ethanol concentrations in the feed [15, 16]. Under technically relevant conditions, the formation of coke-precursors has to be avoided due to possible damage to the downstream fuel cell.

Under the employed operating conditions, the C/O ratio of 0.75 showed the best results, with complete ethanol conversion, the highest hydrogen yield of all investigated C/O ratios, and methane as the only by-product at the catalyst outlet. Additionally, only temperatures below 1000 K were observed. Therefore, catalyst aging by sintering would be low under these conditions [174]. For $C/O = 0.80 - 0.85$, thermodynamic equilibrium showed complete ethanol conversion and high hydrogen formation. Nevertheless, steam reforming seems to be kinetically limited under the given conditions, which is why the equilibrium composition is not reached. Consequently, for a CPOX reformer employing ethanol as a fuel, a C/O ratio of $C/O \leq 0.75$ should be chosen.

Influence of the Radial Position of the Probed Channel

For methane and ethanol, profiles were collected in three channels positioned across the monolith. One of the channels was positioned in the center of the monolith (“central”), one in the middle between center and edge of the monolith (“middle”), and one close to the edge of the monolith (“outer”). For ethanol, the C/O ratio ($C/O = 0.75$) with the best performance in the central channel, i.e. high hydrogen yield and low by-product formation, was chosen. The stoichiometric composition for partial oxidation ($C/O = 1.0$) was applied in methane CPOX.

For both fuels, it became apparent that radial heat loss plays an important role for the channels close to the reactor wall, leading to lower gas and surface temperatures. Close to the reactor wall, a boundary layer develops, which causes a larger residence time in the outer channel. This should be favorable

8. Conclusion

for reforming reactions, but the lower surface temperature seems to outweigh this effect. The heat dissipation leads to less steam reforming along the channel, causing lower rates of conversion and hydrogen yield. Additionally, for ethanol, the undesired by-products ethylene and acetaldehyde were present at the catalyst outlet of the outer channel. From these investigations, it is clear that the evaluation of the performance needs to be based on investigations in more than only the central channel of a monolithic catalyst.

For the design of a CPOX reformer, the observed heat losses need to be taken into account to avoid the loss in performance in the outer channels. A thick thermal insulation can minimize the heat dissipation even though complete prevention is not possible this way. Another approach could be the combination of the heat management of reformer and fuel cell. A shell-and-tube configuration might be a solution, in which hot exhaust gas from the SOFC flows counter-currently to the reactive flow inside the reactor tube. This reactor design would also increase the overall thermal efficiency of the APU [175, 176]. Furthermore, for methane, a C/O ratio lower than 1.0, probably around $C/O = 0.8$, would be chosen in a CPOX reformer to achieve higher rates of conversion and syngas formation as observed in [29].

Surrogates for Commercial Fuels

The investigations on commercial fuels and surrogates revealed that the CPOX of complex mixtures, such as 95 RON gasoline and E 85, can be closely reproduced by two-component ethanol/iso-octane blends with ethanol concentrations similar to those of the commercial fuels. From the studies shown in this work, the C/O ratios of 0.80 – 0.90 for 95 RON gasoline and 0.64 for E 85 can be identified as preferable inlet conditions for a CPOX reformer.

However, formation of by-products such as ethylene cannot be avoided for these fuels. To avoid coking in the downstream fuel cell, a gas-cleaning

step needs to be interposed in a technical application. Selective oxidation of the by-products in the hot outlet gas of the reactor by adding oxygen would be a possibility for removing undesired by-products. Further studies, such as in-situ investigations, need to be performed with the surrogates to gain a deeper insight into the reaction network and to discover additional methods to decrease by-product formation.

Staged Catalytic Reactor with Pd-Rh

The approach of using two different metals was based on the observation of the two zones, oxy-reforming and reforming zone, along the channel in a Rh catalyst. The comparison of the spatially-resolved profiles for methane CPOX on the Pd-Rh catalyst and a single-slice Rh catalyst with a similar length revealed different profiles for syngas formation on the Pd stage of Pd-Rh.

For Rh, a combination of direct and indirect routes is the expected mechanism, with syngas formation starting directly at the catalyst inlet, while oxygen is still present [12]. For the Pd stage of Pd-Rh, an indirect route seems to apply. Hydrogen is produced in steam reforming and the production starts when molecular oxygen is depleted. In the Rh stage of the Pd-Rh catalyst, no more oxygen is present and steam reforming is the predominant reaction.

In-situ studies on a longer, single-stage Pd catalyst would lead to a further insight into the formation of syngas on Pd. However, as discussed in Section 2.2.1.1, it is not possible to extrapolate from the measured gas composition to the concentrations at the catalytic surface. Thus, the surface mechanism cannot be concluded from the collected axial profiles.

Additionally, the influence of diffusion has to be taken into account for the Pd-Rh catalyst. This makes it difficult to assign the processes to the catalytically active material. Nevertheless, for the Pd-Rh catalyst, lower rates of methane conversion and syngas formation were observed than for the Rh

8. Conclusion

catalyst. Additionally, higher temperatures were detected. Thus, the application of a Pd-Rh catalyst in a CPOX reformer would not be beneficial. Further investigations on staged catalysts, employing cheaper catalytically active material, e.g. Ni, in the reforming zone, could lead to a substitute for the expensive Rh catalyst.

Investigations at 2 to 4 bar

Investigations for C_3H_8 CPOX on Rh/Al₂O₃ at 2 to 4 bar using an in-situ sampling technique showed similar concentration profiles for reactants and main products. Only the by-product formation due to gas-phase reactions increased with rising pressure inside the channel of the catalyst. However, due to heterogeneous steam reforming of the by-products, only methane was detected at the catalyst outlet of the central channel. Consequently, CPOX reformers could also be operated at elevated pressures with C_3H_8 without major drawbacks such as a distinctly lower syngas formation. Nevertheless, further studies in the outer channels of the catalyst are necessary to exclude the breakthrough of the coke precursors, such as ethylene.

Additionally, studies on coke formation at 4 bar revealed that Fe and Ni promote coke formation, which is probably due to the Boudouard reaction that occurs at the catalyst outlet under the given conditions. Therefore, only inertized materials should be used in CPOX reformers and the downstream areas with high temperatures. Another possibility would be to cool down the reactive gases to quench undesired reactions. However, this approach is only reasonable for downstream processes which do not require the feed gas to have high temperatures.

Outlook

Based on the knowledge obtained from the investigations performed for this work, further steps can be taken. One step would be the design of a CPOX reformer with high thermal efficiency, probably based on the use of heat recovery from the hot exhaust gas of an SOFC. This reformer could be tested with artificial hot exhaust gas at the constructed setup CPOX 3. The extent of radial heat loss in the newly designed reformer could be validated directly. Furthermore, a comparison between a reformer with thick insulation and one with heat provided by the SOFC exhaust gas could be accomplished. As another important parameter, different materials for the reactor tube could be tested to avoid coke formation in the operating reformer.

The in-situ sampling technique makes it possible to gain important insights into the reaction sequence of many different catalytic processes. This technique is not limited to catalytic partial oxidation; with the presented setup, an in-situ study in the area of automotive exhaust-gas after-treatment for diesel engines was successfully performed, and the results were employed to verify a recently developed mechanism [188]. Also, for methanation on a Ni catalyst, concentration and temperature profiles were collected [189]. Especially in the field of exhaust-gas after-treatment, where honeycomb catalysts are widely employed, the in-situ technique is a powerful tool to evaluate processes and mechanism and to develop new ones. In CPOX, mechanisms can be evaluated on the basis of the axial resolution of the profiles, and the development of new mechanisms can be based on those experimental data. Catalytically active material, such as Pd, for which in-situ investigations are scarce, or combinations of different catalysts, e.g. two- or multiple-stage catalysts, would help to verify mechanisms and to evaluate the performance of different materials under operating conditions. Moreover, studying two- or multi-stage catalysts, including Ni or other low-priced metals, could lead to the discovery of catalysts with a lower price than Rh catalysts, which would be desirable for the technical application of CPOX reformers.

References

- [1] Schobert, H. H., *Chemistry of Fossil Fuels and Biofuels*, Cambridge University Press, **2013**.
- [2] Ahmed, K.; Foeger, K., *Fuel Processing for High-Temperature High-Efficiency Fuel Cells*, *Industrial & Engineering Chemistry Research* **2010**, *49*(16), 7239–7256.
- [3] Krumpelt, M.; Krause, T. R.; Carter, J. D.; Kopasz, J. P.; Ahmed, S., *Fuel processing for fuel cell systems in transportation and portable power applications*, *Catalysis Today* **2002**, *77*, 3–16.
- [4] Deutschmann, O., *Catalytic reforming of logistic fuels at high-temperatures*, in *Catalysis*, vol. 24, The Royal Society of Chemistry, **2012**, pp. 48–82.
- [5] Enger, B. C.; Lodeng, R.; Holmen, A., *A review of catalytic partial oxidation of methane to synthesis gas with emphasis on reaction mechanisms over transition metal catalysts*, *Applied Catalysis A: General* **2008**, *346*(1 - 2), 1 – 27.
- [6] Deutschmann, O.; Schmidt, L. D., *Modeling the Partial Oxidation of Methane in a Short-Contact-Time Reactor*, *AIChE Journal* **1998**, *44*, 2465–2477.
- [7] Hannemann, S.; Grunwaldt, J.-D.; van Vegten, N.; Baiker, A.; Boye, P.;

- Schroer, C. G., *Distinct spatial changes of the catalyst structure inside a fixed-bed microreactor during the partial oxidation of methane over Rh/Al₂O₃*, *Catalysis Today* **2007**, *126*, 54–63.
- [8] Maestri, M.; Vlachos, D.; Beretta, A.; Forzatti, P.; Groppi, G.; Tronconi, E., *Dominant Reaction Pathways in the Catalytic Partial Oxidation of CH₄ on Rh*, *Topics in Catalysis* **2009**, *52*, 1983–1988.
- [9] Schmidt, L. D.; Huff, M., *Partial oxidation of CH₄ and C₂H₆ over noble metal-coated monoliths*, *Catalysis Today* **1994**, *21*, 443–454.
- [10] Schwiedernoch, R.; Tischer, S.; Correa, C.; Deutschmann, O., *Experimental and numerical study on the transient behavior of partial oxidation of methane in a catalytic monolith*, *Chemical Engineering Science* **2003**, *58*, 633–642.
- [11] Bodke, A.; Bharadwaj, S.; Schmidt, L. D., *The Effect of Ceramic Supports on Partial Oxidation of Hydrocarbons over Noble Metal Coated Monoliths*, *Journal of Catalysis* **1998**, *179*, 138.
- [12] Horn, R.; Williams, K. A.; Degenstein, N. J.; Schmidt, L. D., *Syngas by catalytic partial oxidation of methane on rhodium: Mechanistic conclusions from spatially resolved measurements and numerical simulations*, *Journal of Catalysis* **2006**, *242*, 92–102.
- [13] Silberova, B.; Venvik, H. J.; Walmsley, J. C.; Holmen, A., *Small-scale hydrogen production from propane*, *Catalysis Today* **2005**, *100*(3 - 4), 457 – 462.
- [14] Aartun, I.; Gjervan, T.; Venvik, H.; Goerke, O.; Pfeifer, P.; Fathi, M.; Holmen, A.; Schubert, K., *Catalytic conversion of propane to hydrogen in microstructured reactors*, *Chemical Engineering Journal* **2004**, *101*(1 – 3), 93–99.
- [15] Hebben, N.; Diehm, C.; Deutschmann, O., *Catalytic partial oxidation of*

- ethanol on alumina-supported rhodium catalysts: An experimental study*, Applied Catalysis A: General **2010**, 388, 225–231.
- [16] Diehm, C.; Kaltschmitt, T.; Deutschmann, O., *Hydrogen production by partial oxidation of ethanol/gasoline blends over Rh/Al₂O₃*, Catalysis Today **2012**, 197, 90–100.
- [17] Costa, L.; Vasconcelos, S.; Pinto, A.; Silva, A.; Mattos, L.; Noronha, F.; Borges, L., *Rh/CeO₂ catalyst preparation and characterization for hydrogen production from ethanol partial oxidation*, Journal of Materials Science **2008**, 43(2), 440–449.
- [18] Hohn, K. L.; Lin, Y.-C., *Catalytic Partial Oxidation of Methanol and Ethanol for Hydrogen Generation*, ChemSusChem **2009**, 2, 927–940.
- [19] Hartmann, M.; Maier, L.; Deutschmann, O., *Hydrogen production by catalytic partial oxidation of iso-octane at varying flow rate and fuel/oxygen ratio: From detailed kinetics to reactor behavior*, Applied Catalysis A: General **2011**, 391, 144–152.
- [20] Hartmann, M.; Maier, L.; Minh, H. D.; Deutschmann, O., *Catalytic partial oxidation of iso-octane over rhodium catalysts: An experimental, modeling, and simulation study*, Combustion and Flame **2010**, 157, 1771–1782.
- [21] Panuccio, G.; Williams, K.; Schmidt, L., *Contributions of heterogeneous and homogeneous chemistry in the catalytic partial oxidation of octane isomers and mixtures on rhodium coated foams*, Chemical Engineering Science **2006**, 61(13), 4207 – 4219.
- [22] Subramanian, R.; Panuccio, G. J.; Krummenacher, J. J.; Lee, I. C.; Schmidt, L. D., *Catalytic partial oxidation of higher hydrocarbons: reactivities and selectivities of mixtures*, Chemical Engineering Science **2004**, 59, 5501–5507.

- [23] O'Connor, R. P.; Klein, E. J.; Schmidt, L. D., *High yields of synthesis gas by millisecond partial oxidation of higher hydrocarbons*, *Catalysis Letters* **2000**, *70*, 99–107.
- [24] Hartmann, M., *Erzeugung von Wasserstoff mittels katalytischer Partialoxidation hoeherer Kohlenwasserstoffe an Rhodium*, Ph.D. thesis, Department of Chemistry and Biosciences, Karlsruhe Institute of Technology (Germany), **2009**.
- [25] Bobrova, L.; Zolotarsky, I.; Sadykov, V.; Sobyenin, V., *Hydrogen-rich gas production from gasoline in a short contact time catalytic reactor*, *International Journal of Hydrogen Energy* **2007**, *32*, 3698–3704.
- [26] Wang, L.; Murata, K.; Inaba, M., *Highly efficient conversion of gasoline into hydrogen on Al₂O₃-supported Ni-based catalysts: Catalyst stability enhancement by modification with W*, *Applied Catalysis A: General* **2009**, *358*, 264–268.
- [27] Nilsson, M.; Karatzas, X.; Lindstroem, B.; Pettersson, L. J., *Assessing the adaptability to varying fuel supply of an autothermal reformer*, *Chemical Engineering Journal* **2008**, *142*, 309–317.
- [28] Dalle Nogare, D.; Degenstein, N. J.; Horn, R.; Canu, P.; Schmidt, L. D., *Modeling spatially resolved profiles of methane partial oxidation on a Rh foam catalyst with detailed chemistry*, *Journal of Catalysis* **2008**, *258*, 131–142.
- [29] Horn, R.; Williams, K. A.; Degenstein, N. J.; Bitsch-Larsen, A.; Nogare, D. D.; Tupy, S. A.; Schmidt, L. D., *Methane catalytic partial oxidation on autothermal Rh and Pt foam catalysts: Oxidation and reforming zones, transport effects, and approach to thermodynamic equilibrium*, *Journal of Catalysis* **2007**, *249*, 380–393.
- [30] Donazzi, A.; Maestri, M.; Michael, B. C.; Beretta, A.; Forzatti, P.;

- Groppi, G.; Tronconi, E.; Schmidt, L. D.; Vlachos, D. G., *Microkinetic modeling of spatially resolved autothermal CH₄ catalytic partial oxidation experiments over Rh-coated foams*, Journal of Catalysis **2010**, 275, 270–279.
- [31] Beretta, A.; Groppi, G.; Lualdi, M.; Tavazzi, I.; Forzatti, P., *Experimental and modeling analysis of methane partial oxidation: transient and steady-state behavior of Rh-coated honeycomb monoliths*, Industrial & Engineering Chemistry Research **2009**, 48, 3825–3836.
- [32] Beretta, A.; Donazzi, A.; Livio, D.; Maestri, M.; Groppi, G.; Tronconi, E.; Forzatti, P., *Optimal design of a CH₄ CPO-reformer with honeycomb catalyst: Combined effect of catalyst load and channel size on the surface temperature profile*, Catalysis Today **2011**, 171, 79–83.
- [33] Donazzi, A.; Livio, D.; Beretta, A.; Groppi, G.; Forzatti, P., *Surface temperature profiles in CH₄ CPO over honeycomb supported Rh catalyst probed with in situ optical pyrometer*, Applied Catalysis A: General **2011**, 402, 41–49.
- [34] Livio, D.; Donazzi, A.; Beretta, A.; Groppi, G.; Forzatti, P., *Experimental and modeling analysis of the thermal behavior of an autothermal C₃H₈ catalytic partial oxidation reformer*, Industrial and Engineering Chemistry Research **2012**, 51, 7573–7583.
- [35] Kahle, L. C. S., *Reaktionskinetik der Oxidation und Reformierung von H₂, CO und CH₄ über Platinkatalysatoren*, Ph.D. thesis, Department of Chemistry and Biosciences, Karlsruhe Institute of Technology (Germany), **2013**.
- [36] Roussiere, T., *Catalytic Reforming of Methane in the Presence of CO₂ and H₂O at High Pressure*, Ph.D. thesis, Department of Chemistry and Biosciences, Karlsruhe Institute of Technology (Germany), **2013**.

- [37] Donazzi, A.; Beretta, A.; Groppi, G.; Forzatti, P., *Catalytic partial oxidation of methane over a 4% Rh/ γ -Al₂O₃ catalyst Part II: Role of CO₂ reforming*, *Journal of Catalysis* **2008**, *255*, 259–268.
- [38] Linstrom, P.; Mallard, W. (Editors), *NIST Chemistry WebBook, NIST Standard Reference Database Number 69*, National Institute of Standards and Technology, Gaithersburg (USA), <http://webbook.nist.gov> (retrieved October 20, 2013).
- [39] Claridge, J. B.; Green, M. L.; Tsang, S. C.; York, A. P.; Ashcroft, A. T.; Battle, P. D., *A study of carbon deposition on catalysts during the partial oxidation of methane to synthesis gas*, *Catalysis Letters* **1993**, *22*(4), 299–305.
- [40] Li, A.; Norinaga, K.; Zhang, W.; Deutschmann, O., *Modeling and simulation of materials synthesis: Chemical vapor deposition and infiltration of pyrolytic carbon*, *Composites Science and Technology* **2008**, *68*(5), 1097 – 1104.
- [41] Norinaga, K.; Deutschmann, O.; Saegusa, N.; Hayashi, J.-i., *Analysis of pyrolysis products from light hydrocarbons and kinetic modeling for growth of polycyclic aromatic hydrocarbons with detailed chemistry*, *Journal of Analytical and Applied Pyrolysis* **2009**, *86*(1), 148 – 160.
- [42] Kaltschmitt, T.; Maier, L.; Hartmann, M.; Hauck, C.; Deutschmann, O., *Influence of gas-phase reactions on catalytic reforming of isooctane*, *Proceedings of the Combustion Institute* **2011**, *33*, 3177–3183.
- [43] Salge, J. R.; Deluga, G. A.; Schmidt, L. D., *Catalytic partial oxidation of ethanol over noble metal catalysts*, *J. Catal.* **2005**, *235*, 69–78.
- [44] Schwank, J. W.; Tadd, A. R., *Catalytic reforming of liquid hydrocarbons for on-board solid oxide fuel cell auxiliary power units*, in *Catalysis*, vol. 22, The Royal Society of Chemistry, **2010**, pp. 56–93.

- [45] Vernon, P. D.; Green, M. L.; Cheetham, A. K.; Ashcroft, A., *Partial oxidation of methane to synthesis gas*, *Catalysis Letters* **1990**, *6*(2), 181–186.
- [46] Ahn, K.; Chung, Y.-C.; Oh, J. H.; Hari Prasad, D.; Kim, H.; Kim, H.-R.; Son, J.-W.; Lee, H.-W.; Lee, J.-H., *A Comparative Study of Catalytic Partial Oxidation of Methane Over CeO₂ Supported Metallic Catalysts*, *Journal of Nanoscience and Nanotechnology* **2011**, *11*, 6414–6419.
- [47] Haynes, D. J.; Campos, A.; Berry, D. A.; Shekhawat, D.; Roy, A.; Spivey, J. J., *Catalytic partial oxidation of a diesel surrogate fuel using an Ru-substituted pyrochlore*, *Catalysis Today* **2010**, *155*, 84–91.
- [48] Feio, L.; Hori, C.; Mattos, L.; Zanchet, D.; Noronha, F.; Bueno, J., *Partial oxidation and autothermal reforming of methane on Pd/CeO₂-Al₂O₃ catalysts*, *Applied Catalysis A: General* **2008**, *348*(2), 183 – 192.
- [49] Rodrigues, L. M.; Silva, R. B.; Rocha, M. G.; Bargiela, P.; Noronha, F. B.; Brandao, S. T., *Partial oxidation of methane on Ni and Pd catalysts: Influence of active phase and CeO₂ modification*, *Catalysis Today* **2012**, *197*(1), 137 – 143.
- [50] Rodrigues, C. P.; Schmal, M., *Nickel-alumina washcoating on monoliths for the partial oxidation of ethanol to hydrogen production*, *International Journal of Hydrogen Energy* **2011**, *36*, 10709–10718.
- [51] Cai, W.; Wang, F.; Zhan, E.; Veen, A. V.; Mirodatos, C.; Shen, W., *Hydrogen production from ethanol over Ir/CeO₂ catalysts: A comparative study of steam reforming, partial oxidation and oxidative steam reforming*, *Journal of Catalysis* **2008**, *257*(1), 96 – 107.
- [52] Heitnes, K.; Lindberg, S.; Rokstad, O. A.; Holmen, A., *Catalytic partial oxidation of methane to synthesis gas using monolithic reactors*, *Catal. Today* **1994**, *21*, 471–480.

- [53] Hu, Y. H.; Ruckenstein, E., *Catalyst Temperature Oscillations during Partial Oxidation of Methane*, *Industrial & Engineering Chemistry Research* **1998**, *37*, 2333–2335.
- [54] Huff, M.; Torniainen, P.; Schmidt, L., *Partial oxidation of alkanes over noble metal coated monoliths*, *Catalysis Today* **1994**, *21*(1), 113 – 128.
- [55] Liguras, D. K.; Goundani, K.; Verykios, X. E., *Production of hydrogen for fuel cells by catalytic partial oxidation of ethanol over structured Ni catalysts*, *Journal of Power Sources* **2004**, *130*, 30–37.
- [56] Choudhary, V.; Rane, V.; Rajput, A., *Selective oxidation of methane to CO and H₂ over unreduced NiO-rare earth oxide catalysts*, *Catalysis Letters* **1993**, *22*(4), 289–297.
- [57] York, A. P.; Xiao, T.; Green, M. L., *Brief Overview of the Partial Oxidation of Methane to Synthesis Gas*, *Topics in Catalysis* **2003**, *22*(3-4), 345–358.
- [58] Dissanayake, D.; Rosynek, M. P.; Kharas, K. C.; Lunsford, J. H., *Partial oxidation of methane to carbon monoxide and hydrogen over a Ni/Al₂O₃ catalyst*, *Journal of Catalysis* **1991**, *132*(1), 117 – 127.
- [59] Zhu, H.; Kee, R. J.; Engel, J. R.; Wickham, D. T., *Catalytic partial oxidation of methane using RhSr- and Ni-substituted hexaaluminates*, *Proceedings of the Combustion Institute* **2007**, *31*, 1965–1972.
- [60] Haynes, D. J.; Berry, D. A.; Shekhawat, D.; Spivey, J. J., *Catalytic partial oxidation of n-tetradecane using pyrochlores: Effect of Rh and Sr substitution*, *Catalysis Today* **2008**, *136*, 206–213.
- [61] York, A. P.; Claridge, J. B.; Brungs, A. J.; Tsang, S. C.; Green, M. L., *Molybdenum and tungsten carbides as catalysts for the conversion of methane to synthesis gas using stoichiometric feedstocks*, *Chemical Communications* **1997**, 39–40.

- [62] Hartmann, M.; Kaltschmitt, T.; Deutschmann, O., *Catalytic partial oxidation of higher hydrocarbon fuel components on Rh/Al₂O₃ coated honeycomb monoliths*, *Catalysis Today* **2009**, *147*, 204–209.
- [63] Tomasic, V.; Jovic, F., *State-of-the-art in the monolithic catalysts/reactors*, *Applied Catalysis A: General* **2006**, *311*(0), 112 – 121.
- [64] Williams, J. L., *Monolith structures, materials, properties and uses*, *Catalysis Today* **2001**, *69*(1 - 4), 3–9.
- [65] Dautzenberg, F.; Mukherjee, M., *Process intensification using multifunctional reactors*, *Chemical Engineering Science* **2001**, *56*(2), 251 – 267.
- [66] Panuccio, G. J.; Dreyer, B. J.; Schmidt, L. D., *A comparison of the catalytic partial oxidation of C₁ to C₁₆ normal paraffins*, *AIChE Journal* **2007**, *53*(1), 187–195.
- [67] Donazzi, A.; Michael, B. C.; Schmidt, L. D., *Chemical and geometric effects of Ce and washcoat addition on catalytic partial oxidation of CH₄ on Rh probed by spatially resolved measurements*, *Journal of Catalysis* **2008**, *260*, 270–275.
- [68] Degenstein, N.; Subramanian, R.; Schmidt, L., *Partial oxidation of n-hexadecane at short contact times: Catalyst and washcoat loading and catalyst morphology*, *Applied Catalysis A: General* **2006**, *305*(2), 146 – 159.
- [69] Bitsch-Larsen, A.; Horn, R.; Schmidt, L. D., *Catalytic partial oxidation of methane on rhodium and platinum: Spatial profiles at elevated pressure*, *Applied Catalysis A: General* **2008**, *348*, 165–172.
- [70] Veser, G.; Frauhammer, J., *Modelling steady state and ignition during catalytic methane oxidation in a monolith reactor*, *Chemical Engineering Science* **2000**, *55*, 2271–2286.

- [71] Donazzi, A.; Livio, D.; Maestri, M.; Beretta, A.; Groppi, G.; Tronconi, E.; Forzatti, P., *Synergy of Homogeneous and Heterogeneous Chemistry Probed by In Situ Spatially Resolved Measurements of Temperature and Composition*, *Angewandte Chemie International Edition* **2011**, *50*, 3943–3946.
- [72] Seyed-Reihani, S. A.; Jackson, G. S., *Catalytic partial oxidation of n-butane over Rh catalysts for solid oxide fuel cell applications*, *Catalysis Today* **2010**, *155*, 75–83.
- [73] Torniainen, P.; Chu, X.; Schmidt, L., *Comparison of monolith-supported metals for the direct oxidation of methane to syngas*, *Journal of Catalysis* **1994**, *146*(1), 1 – 10.
- [74] Tavazzi, I.; Beretta, A.; Groppi, G.; Forzatti, P., *Development of a molecular kinetic scheme for methane partial oxidation over a Rh/ α -Al₂O₃ catalyst*, *Journal of Catalysis* **2006**, *241*(1), 1–13.
- [75] Wang, D.; Dewaele, O.; Groote, A. M.; Froment, G. F., *Reaction Mechanism and Role of the Support in the Partial Oxidation of Methane on Rh/Al₂O₃*, *Journal of Catalysis* **1996**, *159*(2), 418–426.
- [76] Hofstad, K. H.; Hoebink, J.; Holmen, A.; Marin, G., *Partial oxidation of methane to synthesis gas over rhodium catalysts*, *Catalysis Today* **1998**, *40*(2 - 3), 157 – 170.
- [77] Mallens, E.; Hoebink, J.; Marin, G., *The Reaction Mechanism of the Partial Oxidation of Methane to Synthesis Gas: A Transient Kinetic Study over Rhodium and a Comparison with Platinum*, *Journal of Catalysis* **1997**, *167*(1), 43 – 56.
- [78] Weng, W.; Yan, Q.; Luo, C.; Liao, Y.; Wan, H., *The concentration of oxygen species over SiO₂-supported Rh and Ru catalysts and its rela-*

- tionship with the mechanism of partial oxidation of methane to synthesis gas*, Catalysis Letters **2001**, 74(1-2), 37–43.
- [79] Deutschmann, O.; Schwiedernoch, R.; Maier, L. I.; Chatterjee, D., *Natural gas conversion in monolithic catalysts: Interaction of chemical reactions and transport phenomena*, in *Studies in Surface Science and Catalysis* (Edited by J. J. S. E. Iglesia; T. H. Fleisch), vol. 136, Elsevier, Amsterdam, NL, **2001**, pp. 251–258.
- [80] Lyubovsky, M.; Roychoudhury, S.; LaPierre, R., *Catalytic partial oxidation of methane to syngas at elevated pressures*, Catalysis Letters **2005**, 99(3-4), 113–117.
- [81] Donazzi, A.; Livio, D.; Diehm, C.; Beretta, A.; Groppi, G.; Forzatti, P., *Effect of pressure in the autothermal catalytic partial oxidation of CH₄ and C₃H₈: Spatially resolved temperature and composition profiles*, Applied Catalysis A: General **2014**, 469(0), 52–64.
- [82] Hu, Y. H.; Ruckenstein, E., *Catalytic Conversion of Methane to Synthesis Gas by Partial Oxidation and CO₂ Reforming*, in *Advances in Catalysis*, vol. 48 of *Advances in Catalysis*, Academic Press, **2004**, pp. 297–345.
- [83] Nakagawa, K.; Ikenaga, N.; Kobayashi, T.; Suzuki, T., *Transient response of catalyst bed temperature in the pulsed reaction of partial oxidation of methane to synthesis gas over supported group VIII metal catalysts*, Catalysis Today **2001**, 64, 31–41.
- [84] Fujimoto, K.; Ribeiro, F. H.; Avalos-Borja, M.; Iglesia, E., *Structure and Reactivity of PdO_x/ZrO₂ Catalysts for Methane Oxidation at Low Temperatures*, Journal of Catalysis **1998**, 179(2), 431 – 442.
- [85] Mattos, L. V.; Noronha, F. B., *The influence of the nature of the metal on the performance of cerium oxide supported catalysts in the partial oxidation of ethanol*, Journal of Power Sources **2005**, 152, 50–59.

- [86] York, A. P. E.; Xiao, T.; Green, M. L. H.; Claridge, J. B., *Methane Oxidation for Synthesis Gas Production*, *Catalysis Reviews: Science & Engineering* **2007**, *49*(4), 511–560.
- [87] Kimmerle, B.; Baiker, A.; Grunwaldt, J.-D., *Oscillatory behaviour of catalytic properties, structure and temperature during the catalytic partial oxidation of methane on Pd/Al₂O₃*, *Physical Chemistry Chemical Physics* **2010**, *12*, 2288–2291.
- [88] Stoetzel, J.; Frahm, R.; Kimmerle, B.; Nachttegaal, M.; Grunwaldt, J.-D., *Oscillatory Behavior during the Catalytic Partial Oxidation of Methane: Following Dynamic Structural Changes of Palladium Using the QEXAFS Technique*, *The Journal of Physical Chemistry C* **2012**, *116*(1), 599–609.
- [89] Bychkov, V. Y.; Tyulenin, Y. P.; Slinko, M. M.; Shashkin, D. P.; Korchak, V. N., *The study of the oscillatory behavior during methane oxidation over Pd catalysts*, *Journal of Catalysis* **2009**, *267*(2), 181 – 187.
- [90] Krummenacher, J. J.; West, K. N.; Schmidt, L. D., *Catalytic partial oxidation of higher hydrocarbons at millisecond contact times: decane, hexadecane, and diesel fuel*, *Journal of Catalysis* **2003**, *215*, 332–343.
- [91] Wanat, E. C.; Suman, B.; Schmidt, L. D., *Partial oxidation of alcohols to produce hydrogen and chemicals in millisecond-contact time reactors*, *Journal of Catalysis* **2005**, *235*, 18–27.
- [92] Silva, A. M.; Farias, A. M. D. d.; Costa, L. O. O.; Barandas, A. P. M. G.; Mattos, L. V.; Fraga, M. A.; Noronha, F. B., *Partial oxidation and water-gas shift reaction in an integrated system for hydrogen production from ethanol*, *Applied Catalysis A: General* **2008**, *334*, 179–186.
- [93] Schmal, M.; Cesar, D. V.; Souza, M. M. V. M.; Guarido, C. E., *Drifts and TPD analyses of ethanol on Pt catalysts over Al₂O₃ and ZrO₂ - par-*

- tial oxidation of ethanol*, The Canadian Journal of Chemical Engineering **2011**, 89(5), 1166–1175.
- [94] de Lima, S. M.; Colman, R. C.; Jacobs, G.; Davis, B. H.; Souza, K. R.; de Lima, A. F. F.; Appel, L. G.; Mattos, L. V.; Noronha, F. B., *Hydrogen production from ethanol for PEM fuel cells. An integrated fuel processor comprising ethanol steam reforming and preferential oxidation of CO*, Catalysis Today **2009**, 146, 110–123.
- [95] Mavrikakis, M.; Barteau, M. A., *Oxygenate reaction pathways on transition metal surfaces*, Journal of Molecular Catalysis A: Chemical **1998**, 131(1 - 3), 135 – 147.
- [96] Fatsikostas, A. N.; Verykios, X. E., *Reaction network of steam reforming of ethanol over Ni-based catalysts*, Journal of Catalysis **2004**, 225, 439–452.
- [97] Chen, G.; Li, S.; Jiao, F.; Yuan, Q., *Catalytic dehydration of bioethanol to ethylene over TiO₂/γ-Al₂O₃ catalysts in microchannel reactors*, Catalysis Today **2007**, 125, 111–119.
- [98] Bichon, P.; Haugom, G.; Venvik, H. J.; Holmen, A.; Blekkan, E. A., *Steam reforming of ethanol over supported Co and Ni catalysts*, Topics in Catalysis **2008**, 49, 38–45.
- [99] Erdohelyi, A.; Rasko, J.; Kecskes, T.; Toth, M.; Doemoek, M.; Baan, K., *Hydrogen formation in ethanol reforming on supported noble metal catalysts*, Catalysis Today **2006**, 116, 367–376.
- [100] Houtman, C. J.; Barteau, M. A., *Divergent pathways of acetaldehyde and ethanol decarbonylation on the Rh(111) surface*, Journal of Catalysis **1991**, 130, 528–546.
- [101] Marinov, N. M., *A detailed chemical kinetic model for high temperature*

- ethanol oxidation*, International Journal of Chemical Kinetics **1999**, *31*, 183–220.
- [102] Livio, D.; Diehm, C.; Donazzi, A.; Beretta, A.; Deutschmann, O., *Catalytic partial oxidation of ethanol over Rh/Al₂O₃: Spatially resolved temperature and concentration profiles*, Applied Catalysis A: General **2013**, *467*(0), 530 – 541.
- [103] Beretta, A.; Forzatti, P., *Partial oxidation of light paraffins to synthesis gas in short contact-time reactors*, Chemical Engineering Journal **2004**, *99*(3), 219 – 226.
- [104] Livio, D.; Donazzi, A.; Beretta, A.; Groppi, G.; Forzatti, P., *Optimal Design of A CPO-Reformer of Light Hydrocarbons with Honeycomb Catalyst: Effect of Frontal Heat Dispersions on the Temperature Profiles*, Topics in Catalysis **2011**, *54*(13-15), 866–872.
- [105] Battin-Leclerc, F., *Detailed chemical kinetic models for the low-temperature combustion of hydrocarbons with application to gasoline and diesel fuel surrogates*, Progress in Energy and Combustion Science **2008**, *34*, 440–498.
- [106] Dietz, I., A.G.; Schmidt, L., *Effect of pressure on three catalytic partial oxidation reactions at millisecond contact times*, Catalysis Letters **1995**, *33*(1-2), 15–29.
- [107] Fichtner, M.; Mayer, J.; Wolf, D.; Schubert, K., *Microstructured Rhodium Catalysts for the Partial Oxidation of Methane to Syngas under Pressure*, Industrial & Engineering Chemistry Research **2001**, *40*(16), 3475–3483.
- [108] Hong, J. K.; Zhang, L.; Thompson, M.; Wei, W.; Liu, K., *Effect of Sulfur Poisoning in High Pressure Catalytic Partial Oxidation of Methane over*

- Rh-Ce/Al₂O₃ Catalyst*, *Industrial & Engineering Chemistry Research* **2011**, *50*(8), 4373–4380.
- [109] Kado, S.; Imagawa, K.; Kiryu, A.; Yagi, F.; Minami, T.; Kawai, H.; Kawazuishi, K.; Tomishige, K.; Nakamura, A.; Suehiro, Y., *Syngas production from natural gas via catalytic partial oxidation using ceramic monolith catalyst at short contact time and elevated pressure*, *Catalysis Today* **2011**, *171*(1), 97 – 103.
- [110] Quiceno, R.; Perez-Ramirez, J.; Warnatz, J.; Deutschmann, O., *Modeling the high-temperature catalytic partial oxidation of methane over platinum gauze: Detailed gas-phase and surface chemistries coupled with 3D flow field simulations*, *Applied Catalysis A: General* **2006**, *303*(2), 166 – 176.
- [111] Mantzaras, J., *New Directions in Advanced Modeling and in Situ Measurements Near Reacting Surfaces*, *Flow, Turbulence and Combustion* **2013**, *90*(4), 681–707.
- [112] Reinke, M.; Mantzaras, J.; Schaeren, R.; Bombach, R.; Kreutner, W.; Inauen, A., *Homogeneous ignition in high-pressure combustion of methane/air over platinum: Comparison of measurements and detailed numerical predictions*, *Proceedings of the Combustion Institute* **2002**, *29*(1), 1021 – 1029.
- [113] Schneider, A.; Mantzaras, J.; Jansohn, P., *Experimental and numerical investigation of the catalytic partial oxidation of mixtures diluted with and in a short contact time reactor*, *Chemical Engineering Science* **2006**, *61*(14), 4634 – 4649.
- [114] Schneider, A.; Mantzaras, J.; Bombach, R.; Schenker, S.; Tylli, N.; Jansohn, P., *Laser induced fluorescence of formaldehyde and Raman measurements of major species during partial catalytic oxidation of methane*

with large H_2O and CO_2 dilution at pressures up to 10 bar, Proceedings of the Combustion Institute **2007**, 31(2), 1973 – 1981.

- [115] Zellner, A.; Suntz, R.; Deutschmann, O., *In-situ investigations of catalytic gas-phase reactions inside an optically accessible flow reactor: NO reduction with H_2 over Pt/Al_2O_3* , Chemie Ingenieur Technik **2013**, submitted.
- [116] Grunwaldt, J.-D.; Hannemann, S.; Schroer, C. G.; Baiker, A., *2D-Mapping of the Catalyst Structure Inside a Catalytic Microreactor at Work: Partial Oxidation of Methane over Rh/Al_2O_3* , The Journal of Physical Chemistry B **2006**, 110(17), 8674–8680.
- [117] Grunwaldt, J.-D.; Baiker, A., *Axial variation of the oxidation state of $Pt-Rh/Al_2O_3$ during partial methane oxidation in a fixed-bed reactor: An in situ X-ray absorption spectroscopy study*, Catalysis Letters **2005**, 99(1-2), 5–12.
- [118] Schmeisser, V.; de Riva Perez, J.; Tuttlies, U.; Eigenberger, G., *Experimental results concerning the role of Pt, Rh, Ba, Ce and Al_2O_3 on NO_x -storage catalyst behaviour*, Topics in Catalysis **2007**, 42-43(1-4), 15–19.
- [119] Horn, R.; Degenstein, N. J.; Williams, K. A.; Schmidt, L. D., *Spatial and temporal profiles in millisecond partial oxidation processes*, Catalysis Letters **2006**, 110, 169–178.
- [120] Horn, R.; Williams, K. A.; Degenstein, N. J.; Schmidt, L. D., *Mechanism of H_2 and CO formation in the catalytic partial oxidation of CH_4 on Rh probed by steady-state spatial profiles and spatially resolved transients*, Chemical Engineering Science **2007**, 62, 1298–1307.
- [121] Michael, B. C.; Nare, D. N.; Schmidt, L. D., *Catalytic partial oxidation of ethane to ethylene and syngas over Rh and Pt coated monoliths:*

- Spatial profiles of temperature and composition*, Chemical Engineering Science **2010**, *65*, 3893–3902.
- [122] Horn, R.; Korup, O.; Geske, M.; Zavyalova, U.; Oprea, I.; Schloegl, R., *Reactor for in situ measurements of spatially resolved kinetic data in heterogeneous catalysis*, Review of Scientific Instruments **2010**, *81*, 6.
- [123] Korup, O.; Mavlyankariev, S.; Geske, M.; Goldsmith, C. F.; Horn, R., *Measurement and analysis of spatial reactor profiles in high temperature catalysis research*, Chemical Engineering and Processing: Process Intensification **2011**, *50*, 998–1009.
- [124] Korup, O.; Goldsmith, C. F.; Weinberg, G.; Geske, M.; Kandemir, T.; Schloegl, R.; Horn, R., *Catalytic partial oxidation of methane on platinum investigated by spatial reactor profiles, spatially resolved spectroscopy, and microkinetic modeling*, Journal of Catalysis **2013**, *297*, 1–16.
- [125] Partridge, W. P.; Storey, J. M.; Lewis, S.; Smithwick, R.; DeVault, G. L.; Cunningham, M. J.; Currier, N.; Yonushonis, T. M., *Time-Resolved Measurements of Emission Transients By Mass Spectrometry*, SAE Paper 2000-01-2952 **2000**.
- [126] Choi, J.-S.; Partridge, W. P.; Daw, C. S., *Spatially resolved in situ measurements of transient species breakthrough during cyclic, low-temperature regeneration of a monolithic Pt/K/Al₂O₃ NO_x storage-reduction catalyst*, Applied Catalysis A: General **2005**, *293*(0), 24–40.
- [127] HIDEN Analytical Ltd., www.hidenanalytical.com.
- [128] Sa, J.; Fernandes, D. L. A.; Aiouache, F.; Goguet, A.; Hardacre, C.; Lundie, D.; Naeem, W.; Partridge, W. P.; Stere, C., *SpaciMS: spatial and temporal operando resolution of reactions within catalytic monoliths*, Analyst **2010**, *135*, 2260–2272.

- [129] Hettel, M.; Diehm, C.; Torkashvand, B.; Deutschmann, O., *Critical evaluation of in situ probe techniques for catalytic honeycomb monoliths*, *Catalysis Today* **2013**, 216(0), 2 – 10.
- [130] Karakaya, C., *A Novel, Hierarchically Developed Surface Kinetics for Oxidation and Reforming of Methane and Propane over Rh/Al₂O₃*, Ph.D. thesis, Department of Chemistry and Biosciences, Karlsruhe Institute of Technology (Germany), **2012**.
- [131] Karakaya, C.; Deutschmann, O., *Kinetics of hydrogen oxidation on Rh/Al₂O₃ catalysts studied in a stagnation-flow reactor*, *Chemical Engineering Science* **2013**, 89(0), 171 – 184.
- [132] Baer, J. N.; Karakaya, C.; Deutschmann, O., *Catalytic ignition of light hydrocarbons over Rh/Al₂O₃ studied in a stagnation-point flow reactor*, *Proceedings of the Combustion Institute* **2013**, 34, 2313–2320.
- [133] Karadeniz, H.; Karakaya, C.; Tischer, S.; Deutschmann, O., *Numerical modeling of stagnation-flows on porous catalytic surfaces: CO oxidation on Rh/Al₂O₃*, *Chemical Engineering Science* **2013**, 104, 899 – 907.
- [134] Baerns, M.; Behr, A.; Brehm, A.; Gmehling, J.; Hofmann, H.; Onken, U.; Renken, A., *Technische Chemie*, Wiley-VCH, Weinheim, **2006**.
- [135] Chorkendorff, I.; Niemantsverdriet, J. W., *Concepts of modern catalysis and kinetics*, Wiley-VCH, Weinheim, 2nd edn., **2007**.
- [136] Atkins, P. W.; De Paula, J., *Physikalische Chemie*, Wiley-VCH, Weinheim, 4th edn., **2006**.
- [137] Deutschmann, O., *Computational Fluid Dynamics Simulation of Catalytic Reactors*, in *Handbook of Heterogeneous Catalysis* (Edited by H. K. G. Ertl; F. Schüth; J. Weitkamp), Wiley-VCH, Weinheim, **2008**, pp. 1811–1828.

- [138] Kee, R. J.; Coltrin, M. E.; Glarborg, P., *Chemically Reacting Flow: Theory and Practice*, Wiley-Interscience, **2003**.
- [139] Deutschmann, O.; Tischer, S.; Kleditzsch, S.; Janaradhanan, V. M.; Correa, C.; Chatterjee, D.; Mladenov, N.; Minh, H. D.; Karadeniz, H., *DETCHEMTM software package*, 2.4a edn., **2013**, www.detchem.com.
- [140] Raja, L. L.; Kee, R. J.; Deutschmann, O.; Warnatz, J.; Schmidt, L. D., *A critical evaluation of Navier-Stokes, boundary-layer, and plug-flow models of the flow and chemistry in a catalytic-combustion monolith*, *Catalysis Today* **2000**, 59(1 - 2), 47 – 60.
- [141] Deutschmann, O.; Tischer, S.; Kleditzsch, S.; Janardhanan, V.; Correa, C.; Chatterjee, D.; Mladenov, N.; Minh, H. D.; Karadeniz, H., *DETCHEMTM User Manual*, 2.4 edn., **2012**, www.detchem.com.
- [142] *OpenFOAM*, www.openfoam.org.
- [143] Kaltschmitt, T., *Catalytic Partial Oxidation of higher Hydrocarbon Fuels for Hydrogen Production - Process Investigation with regard to the Concept of an Auxiliary Power Unit*, Ph.D. thesis, Department of Chemistry and Biosciences, Karlsruhe Institute of Technology (Germany), **2012**.
- [144] Skoog, D. A.; Holler, F. J.; Crouch, S. R., *Principles of instrumental analysis*, Thomson Brooks/Cole, Belmont, California, 6th edn., **2007**.
- [145] Schwedt, G., *Analytische Chemie : Grundlagen, Methoden und Praxis*, Thieme, Stuttgart, **1995**.
- [146] Hoffmann, J. (Editor), *Taschenbuch der Messtechnik*, Fachbuchverlag Leipzig im Carl-Hanser-Verlag, Munich, Vienna, Leipzig, 3rd edn., **2002**.
- [147] V & F, *PDF Brochure for H-sense*, www.vandfna.com/H-Sense.pdf.
- [148] V & F, *PDF Brochure for Airsense*, **2011**,

<http://www.vandf.com/service-support/document-downloads/product-flyer.html>.

- [149] Hartmann, M.; Lichtenberg, S.; Hebben, N.; Zhang, D.; Deutschmann, O., *Experimental investigation of catalytic partial oxidation of model fuels under defined constraints*, *Chemie Ingenieur Technik* **2009**, *81*, 909–919.
- [150] VICI® Valco Instruments Co. Inc., http://www.vici.com/support/images/template_6-port.gif (retrieved September 11, 2013).
- [151] Anderson, R. B.; Stein, K. C.; Feenan, J. J.; Hofer, L. J. E., *Catalytic Oxidation of Methane*, *Industrial & Engineering Chemistry* **1961**, *53*(10), 809–812.
- [152] Bogotto, M.; Dellavedova, M., *Experimental and modeling analysis of the catalytic partial oxidation of light hydrocarbons at 1-4 bar*, Master's thesis, Department of Energy, Politecnico di Milano (Italy), **2012**.
- [153] Zabetakis, M. G., *Flammability characteristics of combustibles gas and vapors*, Bulletin 627, U.S. Department of Interior - Bureau of Mines, Washington, **1965**.
- [154] Novati, D.; Perico, A., *Caratterizzazione dello scambio di materia in filtri metallici utilizzati come supporti per catalizzatori strutturati*, Master's thesis, Department of Energy, Politecnico di Milano (Italy), **2010**.
- [155] Boothe, B. J.; Shih, A. J.; Kong, J.; Roberts, W. L., *Goniometric characteristics of optical fibres for temperature measurement in diesel engine exhaust filters*, *Measurement Science and Technology* **2003**, *14*(5), 563.
- [156] Burcat, A.; Ruscic, B., *Third Millennium Ideal Gas and Condensed Phase Thermochemical Database for Combustion with updates from Active Thermochemical Tables*, Tech. Rep., ANL-05/20 and TAE 960

Technion-IIT, Aerospace Engineering, and Argonne National Laboratory, Chemistry Division, **2005**.

- [157] Nakamura, I.; Kobayashi, Y.; Hamada, H.; Fujitani, T., *Adsorption behavior and reaction properties of NO and CO on Rh(111)*, *Surface Science* **2006**, *600*, 3235–3242.
- [158] ANSYS[®] Academic Research, Release 13.0.
- [159] Maier, L.; Schadel, B.; Delgado, K. H.; Tischer, S.; Deutschmann, O., *Steam Reforming of Methane Over Nickel: Development of a Multi-Step Surface Reaction Mechanism*, *Topics in Catalysis* **2011**, *54*, 845–858.
- [160] Habisreuther, P.; Philipp, M.; Eickhoff, H.; Leuckel, W., *Mathematical Modeling of Turbulent Swirling Flames*, in *High Intensity Combustors - Steady Isobaric Combustion* (Edited by S. Wittig; O. Voehringer; S. Kim), Wiley-VCH, Weinheim, **2005**, pp. 156–175.
- [161] Golovitchev, V.; Tao, F.; Chomiak, J., *Numerical Evaluation of Soot Formation Control at Diesel-Like Conditions by Reducing Fuel Injection Timing*, SAE Paper 1999-01-3552 **1999**.
- [162] Michael, B. C.; Donazzi, A.; Schmidt, L. D., *Effects of H₂O and CO₂ addition in catalytic partial oxidation of methane on Rh*, *Journal of Catalysis* **2009**, *265*, 117–129.
- [163] Kaltschmitt, T.; Diehm, C.; Deutschmann, O., *Catalytic Partial Oxidation of Isooctane to Hydrogen on Rhodium Catalysts: Effect of Tail-Gas Recycling*, *Industrial & Engineering Chemistry Research* **2012**, *51*, 7536–7546.
- [164] Nogare, D. D.; Degenstein, N. J.; Horn, R.; Canu, P.; Schmidt, L. D., *Modeling spatially resolved data of methane catalytic partial oxidation on Rh foam catalyst at different inlet compositions and flowrates*, *Journal of Catalysis* **2011**, *277*, 134–148.

- [165] Liguras, D. K.; Kondarides, D. I.; Verykios, X. E., *Production of hydrogen for fuel cells by steam reforming of ethanol over supported noble metal catalysts*, *Applied Catalysis B: Environmental* **2003**, *43*, 345–354.
- [166] Cavallaro, S., *Ethanol Steam Reforming on Rh/Al₂O₃ Catalysts*, *Energy & Fuels* **2000**, *14*, 1195–1199.
- [167] Mattos, L. V.; Jacobs, G.; Davis, B. H.; Noronha, F. B., *Production of hydrogen from ethanol: Review of reaction mechanism and catalyst deactivation*, *Chemical Reviews* **2012**, *112*, 4094–4123.
- [168] Basagiannis, A. C.; Panagiotopoulou, P.; Verykios, X. E., *Low temperature steam reforming of ethanol over supported noble metal catalysts*, *Topics in Catalysis* **2008**, *51*, 2–12.
- [169] Haas, F. M.; Chaos, M.; Dryer, F. L., *Low and intermediate temperature oxidation of ethanol and ethanol-PRF blends: An experimental and modeling study*, *Combustion and Flame* **2009**, *156*, 2346–2350.
- [170] Lefkowitz, J. K.; Heyne, J. S.; Won, S. H.; Dooley, S.; Kim, H. H.; Haas, F. M.; Jahangirian, S.; Dryer, F. L.; Ju, Y., *A chemical kinetic study of tertiary-butanol in a flow reactor and a counterflow diffusion flame*, *Combustion and Flame* **2012**, *159*, 968–978.
- [171] Yoon, S.; Kang, I.; Bae, J., *Effects of ethylene on carbon formation in diesel autothermal reforming*, *International Journal of Hydrogen Energy* **2008**, *33*, 4780–4788.
- [172] Joensen, F.; Rostrup-Nielsen, J. R., *Conversion of hydrocarbons and alcohols for fuel cells*, *Journal of Power Sources* **2002**, *105*(2), 195 – 201.
- [173] Webb, G., *The formation and role of carbonaceous residues in metal-catalysed reactions of hydrocarbons.*, *Catalysis Today* **1990**, *7*(2), 139 – 155.

- [174] Ding, S.; Yang, Y.; Jin, Y.; Cheng, Y., *Catalyst Deactivation of Rh-Coated Foam Monolith for Catalytic Partial Oxidation of Methane*, Industrial & Engineering Chemistry Research **2009**, 48(6), 2878–2885.
- [175] Goldin, G.; Zhu, H.; Kattke, K.; Dean, A. M.; Braun, R.; Kee, R. J.; Zhang, D.; Maier, L.; Deutschmann, O., *Coupling complex reformer chemical kinetics with three-dimensional computational fluid dynamics*, ECS Transactions **2009**, 25, 1253–1262.
- [176] Kattke, K. J.; Braun, R. J.; Colclasure, A. M.; Goldin, G., *High-fidelity stack and system modeling for tubular solid oxide fuel cell system design and thermal management*, Journal of Power Sources **2011**, 196, 3790–3802.
- [177] Villano, S. M.; Hoffmann, J.; Carstensen, H. H.; Dean, A. M., *Selective Removal of Ethylene, a Deposit Precursor, from a "Dirty" Synthesis Gas Stream via Gas-Phase Partial Oxidation*, Journal of Physical Chemistry A **2010**, 114, 6502–6514.
- [178] McEvoy, A. J., *Innovations for anodes – catalysis and direct oxidation*, Materialwissenschaft und Werkstofftechnik **2002**, 33, 331–334.
- [179] Geske, M.; Pelzer, K.; Horn, R.; Jentoft, F. C.; Schloegl, R., *In-situ investigation of gas phase radical chemistry in the catalytic partial oxidation of methane on Pt*, Catalysis Today **2009**, 142, 61–69.
- [180] Tong, G. C. M.; Flynn, J.; Leclerc, C. A., *A dual catalyst bed for the autothermal partial oxidation of methane to synthesis gas*, Catalysis Letters **2005**, 102, 131–137.
- [181] Bell, C. J.; Leclerc, C. A., *Effect of Relative Bed Lengths on a Platinum/Nickel Stratified Dual Bed Catalyst for the Catalytic Partial Oxidation of Methane at Millisecond Contact Times*, Energy & Fuels **2007**, 21, 3548–3554.

- [182] Audier, M.; Guinot, J.; Coulon, M.; Bonnetain, L., *Formation and characterization of catalytic carbons obtained from CO disproportionation over an iron nickel catalyst – II: Characterization*, Carbon **1981**, 19(2), 99–105.
- [183] Audier, M.; Oberlin, A.; Oberlin, M.; Coulon, M.; Bonnetain, L., *Morphology and crystalline order in catalytic carbons*, Carbon **1981**, 19(3), 217–224.
- [184] Guinot, J.; Audier, M.; Coulon, M.; Bonnetain, L., *Formation and characterization of catalytic carbons obtained from CO disproportionation over an iron nickel catalyst – I: Fragmentation and rates of carbon deposition*, Carbon **1981**, 19(2), 95 – 98.
- [185] Dresselhaus, M. S.; Dresselhaus, G.; Jorio, A., *Raman Spectroscopy of Carbon Nanotubes in 1997 and 2007*, The Journal of Physical Chemistry C **2007**, 111(48), 17887–17893.
- [186] Escribano, R.; Sloan, J.; Siddique, N.; Sze, N.; Dudev, T., *Raman spectroscopy of carbon-containing particles*, Vibrational Spectroscopy **2001**, 26(2), 179 – 186.
- [187] Zimmermann, G.; Zychlinski, W.; Woerde, H. M.; van den Oosterkamp, P., *Absolute Rates of Coke Formation: A Relative Measure for the Assessment of the Chemical Behavior of High-Temperature Steels of Different Sources*, Industrial & Engineering Chemistry Research **1998**, 37(11), 4302–4305.
- [188] Chan, D.; Tischer, S.; Heck, J.; Diehm, C.; Deutschmann, O., *Correlation between catalytic activity and catalytic surface area of a Pt/Al₂O₃ DOC: An experimental and microkinetic modeling study*, Applied Catalysis B: Environmental **2013**, *submitted*.
- [189] Schollenberger, D., *Nutzung von Wabenreaktoren zur Methanisierung*

bei PtG-Prozessen, Master's thesis, Department of Chemistry and Biosciences, Karlsruhe Institute of Technology (Germany), **2013**.

Appendices

Curriculum Vitae

Personal Details

Name	Claudia Melanie Diehm
Date of Birth	03.05.1986
Place of Birth	Karlsruhe, Germany
Nationality	German
Marital Status	single

Professional Experience

Since 12 / 2012	Research Scientist , Group leader “In-Situ Reaction Measurement Technique” Institute of Catalysis Research and Technology Karlsruhe Institute of Technology (KIT)
03 / 2012 - 06 / 2012	Guest Scientist Laboratory of Catalysis and Catalytic Processes Department of Energy, Politecnico di Milano, Milan, Italy
10 / 2010 - 12 / 2012	Research Assistant Institute for Chemical Technology and Polymer Chemistry Karlsruhe Institute of Technology (KIT)

Education

11 / 2010 - 12 / 2013	Member of the Helmholtz Research School “Energy-Related Catalysis” Karlsruhe Institute of Technology (KIT)
-----------------------	--

- 11 / 2010 - 12 / 2013 **PhD student**
Institute for Chemical Technology and Polymer
Chemistry
Karlsruhe Institute of Technology (KIT)
- 08 / 2010 **Diplom** in Chemistry
Karlsruhe Institute of Technology (KIT)
Thesis: Katalytische Partialoxidation von
ethanolhaltigen Kraftstoffen an Rhodium
Advisor: Prof. Dr. Olaf Deutschmann
- 07 / 2005 **Abitur**
Humboldt-Gymnasium, Karlsruhe
- 01 / 2003 - 04 / 2003 **Exchange Student**
Bodmin Community College, Bodmin,
Great Britain

Accomplishments

- 07 / 2013 **Young Researcher** at the 63rd Lindau Nobel
Laureate Meeting 2013 (Chemistry)
- 03 / 2012 - 06 / 2012 **Foreign Exchange Scholarship** by Helmholtz
Research School "Energy-Related Catalysis"
- 07 / 2011 - 07 / 2013 **PhD student speaker** of the Helmholtz Research
School "Energy-Related Catalysis"
- 02 / 2011 **Sparkassenpreis** of the Sparkasse Karlsruhe and
Karlsruhe Institute of Technology for Diploma
theses with topics concerning the environment
- 10 / 2009 - 07 / 2010 **Scholarship** of the Karlsruher
Universitätsgesellschaft e.V.

Personal Interests

Singing and Voice Training

Photography

List of Publications

Publications

- [1] Chan, D.; Tischer, S.; Heck, J.; Diehm, C. and Deutschmann, O., *Correlation between catalytic activity and catalytic surface area of a Pt/Al₂O₃ DOC: An experimental and microkinetic modeling study*, Applied Catalysis B: Environmental **2013**, *accepted*
- [2] Donazzi, A.; Livio, D.; Diehm, C.; Beretta, A.; Groppi, G. and Forzatti, P., *Effect of Pressure in the Autothermal Catalytic Partial Oxidation of CH₄ and C₃H₈: spatially resolved temperature and composition profiles*, Applied Catalysis A: General **2013**, *469*, 52-64
- [3] Livio, D.; Diehm, C.; Donazzi, A.; Beretta, A. and Deutschmann, O., *Catalytic Partial Oxidation of Ethanol over Rh/Al₂O₃: Spatially Resolved Temperature and Concentration Profiles*, Applied Catalysis A: General **2013**, *467*, 530-541
- [4] Hettel, M.; Diehm, C.; Torkashvand, B. and Deutschmann, O., *Critical evaluation of in situ probe techniques for catalytic honeycomb monoliths*, Catalysis Today **2013**, *216*, 2-10
- [5] Diehm, C.; Kaltschmitt, T. and Deutschmann, O., *Hydrogen production by partial oxidation of ethanol/gasoline blends over Rh/Al₂O₃*, Catalysis Today **2012**, *197*, 90-100
- [6] Kaltschmitt, T.; Diehm, C. and Deutschmann, O., *Catalytic Partial Oxidation of Isooctane to Hydrogen on Rhodium Catalysts: Effect of Tail-Gas Recycling*, Industrial & Engineering Chemistry Research **2012**, *51*, 7536-7546
- [7] Hebben, N.; Diehm, C. and Deutschmann, O., *Catalytic partial oxidation of ethanol on alumina-supported*

rhodium catalysts: An experimental study, Applied Catalysis A: General **2010**, 388, 255-231

Oral Presentations

- [1] Diehm, C.; Livio, D.; Hettel, M.; Torkashvand, B. and Deutschmann, O., *Partial Oxidation of Methane and Ethanol on Rh/Al₂O₃ Coated Monoliths Studied by an In-Situ Probe Technique*
23rd North American Meeting of the North American Catalysis Society **June 2-7, 2013**
Louisville, USA
- [2] Diehm, C.; Livio, D.; Hettel, M. and Deutschmann, O., *Partial Oxidation of Ethanol and Methane on Rh/Al₂O₃ - Spatially-Resolved Concentration and Temperature Profiles*
Jahrestreffen Reaktionstechnik **May 6-8, 2013**
Wuerzburg, Germany
- [3] Diehm, C.; Livio, D. and Deutschmann, O., *Untersuchung der katalytischen Partialoxidation von Ethanol anhand orts aufgelöster Konzentrations- und Temperaturprofile*
ProcessNet-Jahrestagung und 30. DECHEMA-Jahrestagung der Biotechnologen **September 10-13, 2012**
Karlsruhe, Germany
- [4] Diehm, C.; Kaltschmitt, T. and Deutschmann, O., *Catalytic Partial Oxidation of Ethanol Blended Fuel on Rh Coated Catalysts*
22nd North American Meeting of the North American Catalysis Society **June 5-10, 2011**
Detroit, USA

Poster Presentations

- [1] Diehm, C.; Kaltschmitt, T. and Deutschmann, O.,
Catalytic Partial Oxidation of Ethanol/Gasoline Blends over
Rh/Al₂O₃
45. Jahrestreffen Deutscher Katalytiker **March 14-16, 2012**
Weimar, Germany
- [2] Diehm, C.; Kaltschmitt, T. and Deutschmann, O.,
Catalytic Partial Oxidation of Ethanol Blended Fuels
8th ECCE **September 25-29, 2012**
Berlin, Germany
- [3] Diehm, C.; Kaltschmitt, T. and Deutschmann, O.,
Catalytic Partial Oxidation of Ethanol Blended Fuels
EUROPACAT X August 28 - September 2, 2011
Glasgow, Great Britain
- [4] Diehm, C.; Kaltschmitt, T. and Deutschmann, O.,
Catalytic Partial Oxidation of Ethanol Blended Fuels
44. Jahrestreffen Deutscher Katalytiker mit Jahrestreffen
Reaktionstechnik **March 16-18, 2011**
Weimar, Germany

